sPH-PPG-2023-002
v5.0
March 10, 2025

$\mathrm{dN_{ch}/d}\eta$ at sPHENIX in Run 24 Au+Au collisions with the INTT

Joseph Bertaux[1], Cameron Dean[2], Takashi Hachiya[3], Misaki Hata[3], Jaein Hwang[4], Hao-Ren Jheng[2], Tomoya Kato[5], Chia-Ming Kuo[6], Itaru Nakagawa[7], Genki Nukazuka[7], Michael Peters[2], Gunther Roland[2], Cheng-Wei Shih[6], Maya Shimomura[3], and Yuka Sugiyama[3]

[1] *Purdue University*
[2] *Massachusetts Institute of Technology*
[3] *Nara Women University*
[4] *Korea University*
[5] *Rikkyo University*
[6] *National Central University*
[7] *RIKEN/RBRC*

Abstract

The pseudorapidity distribution of charged hadrons produced in Au+Au collisions at a center-of-mass energy of $\sqrt{s_{NN}} = 200\,\mathrm{GeV}$ is measured using data collected by the sPHENIX detector. Charged hadron yields are extracted by counting cluster pairs in the inner and outer layers of the Intermediate Silicon Tracker, with corrections applied for detector acceptance and reconstruction efficiency. The measured distributions are consistent with previous experimental results from the Relativistic Heavy Ion Collider, with a [1.6][1] reduction in uncertainty for measurements using the tracklet method. This result features full azimuthal coverage at mid-rapidity and serves as a key commissioning benchmark by validating the performance of several new detector components, thereby supporting the broader sPHENIX physics program.

[1] This value is based on our current conservative estimate including all sources of uncertainty. The finalized number will be updated when the full set of uncertainties are evaluated and included.

Contents

1 Introduction

A hot medium of strongly interacting, deconfined quarks and gluons, known as the quark-gluon plasma (QGP), is formed in ultra-relativistic heavy-ion collisions [1]. The multiplicity and pseudorapidity (η) distributions of charged particles produced in these collisions are critical observables for characterizing the initial conditions and the subsequent hydrodynamic evolution of the QGP [2]. Furthermore, the dependence of charged-particle multiplicity on the colliding system, center-of-mass energy, and collision geometry provides insight into nuclear shadowing, gluon saturation effects [3], and the contributions and modeling of particle production from hard scattering and soft processes [4, 5]. Studying the charged-hadron multiplicity and its dependence on η is essential for understanding the formation and properties of the QGP in heavy-ion collisions.

At Relativistic Heavy-Ion Collider (RHIC), measurements of the system-size dependence of charged-particle η density, denoted as $\mathrm{dN_{ch}/d}\eta$, have been performed for copper-copper (Cu+Cu), gold-gold (Au+Au), and uranium-uranium (U+U) collisions at various center-of-mass energies. Similarly, the ALICE, ATLAS, and CMS experiments at Large Hadron Collider (LHC) have reported $\mathrm{dN_{ch}/d}\eta$ at mid-rapidity ($|\eta|< 0.5$), expressed as $\langle \mathrm{dN_{ch}/d}\eta \rangle$, for lead-lead (Pb+Pb) and xenon-xenon (Xe+Xe) collisions at TeV energy scales. These measurements, summarized in Table 1, have revealed several key empirical trends. (1) Charged–particle production approximately follows a power-law scaling with center-of-mass energy. (2) Central heavy-ion collisions show a steeper increase in $\langle \mathrm{dN_{ch}/d}\eta \rangle$ as a function of center-of-mass energy compared to proton-proton (p+p) and proton-nucleus (p+A) collisions. (3) The values of $\mathrm{dN_{ch}/d}\eta$, normalized by the number of participating nucleon pairs, N_{part}, have a non-linear increase. (4) The shapes of the N_{part} dependence remain consistent across different collision energies. These findings provide an opportunity to test scaling laws and models tuned to data from different energy regimes and evaluate their applicability to other collision systems.

This note describes the measurement of $\mathrm{dN_{ch}/d}\eta$ using data collected by the sPHENIX detector, specifically the Intermediate Silicon Tracker, INTT, and a minimum-bias trigger based on inputs from the Minimum-Bias (Min. Bias) Detector, MBD. The analysis depends on the synchronization and functionality of key detector components and the reconstruction chain, including triggering, synchronization across subdetectors, proper operation and coordination of readout servers within individual subdetectors, centrality determination, data readout, bad channel mapping, hit decoding and unpacking, clustering, vertex finding, and detector alignment. Consequently, this work is closely tied to the commissioning of the detector.

Two analysis approaches have been developed. The first, referred to as the combinatoric method, is based on techniques from the PHOBOS and PHENIX publications [10, 36], while the second, called the closest-match method, follows the CMS Run 2 Xe+Xe and Run 3 Pb+Pb analyses [33, 32]. Both approaches share common global objects, including tracking and calorimeter data storage tapes (DSTs), simulations, INTT calibrations, clusters, scaled trigger objects, Min. Bias classification based on the MBD and Zero-Degree Calorimeter (ZDC) information, centrality calibration, and truth-level definitions. However, the approaches differ in their methods for vertex reconstruction (Section 6.4), tracklet reconstruction and counting (Section 6.5), correction factors (Section 7), and systematic un-

Table 1: Selected measurements from previous and present experiments. Information not explicitly mentioned in the publication is marked as ”–”.

Experiment	Collision species	Center-of-mass energy	Number of analyzed events	Reference
PHENIX	Au+Au	130 GeV	∼ 137 k	[6]
		19.6 GeV 130 GeV 200 GeV	40 k 160 k 270 k	[7]
	U+U	193 GeV	–	[8]
PHOBOS	Au+Au	56 GeV 130 GeV	382 724	[9]
	Au+Au Cu+Cu d+Au p+p	19.6–200 GeV 22.4–200 GeV 200 GeV 200 and 410 GeV	–	[10]
BRAHMS	Au+Au	130 GeV 200 GeV	–	[11] [12]
STAR	Au+Au	130 GeV	60 k	[13]
ALICE	p+p	900 GeV	284	[14]
		900 GeV 2.36 TeV	150 k 40 k	[15]
		7 TeV	300 k	[16]
		13 TeV	∼ 1.5 M	[17]
		0.9, 2.36, 2.78, 7, and 8 TeV	40 k-343.7 M	[18]
		0.9, 7, and 8 TeV	7.4 k-61 M	[19]
		5.02, 7, and 13 TeV	–	[20]
	Pb+Pb	2.76 TeV	2711	[21]
		5.02 TeV	∼ 100 k	[22]
	Xe+Xe	5.44 TeV	∼ 1 M	[23]
CMS	p+p	0.9 and 10 TeV	∼ 5 k	[24]
		0.9 TeV 2.36 TeV	∼ 40.3 k ∼ 10.8 k	[25]
		7 TeV	∼ 55 k	[26]
		0.9, 2.36, and 7 TeV	12-442 k	[27]
		8 TeV	–	(With TOTEM) [28]
		13 TeV	11.5 M	[29]
	p+Pb	5.02 TeV 8.16 TeV	∼ 420 k ∼ 3 M	[30]
	Pb+Pb	2.76 TeV	∼ 100 k	[31]
		5.36 TeV	–	[32]
	Xe+Xe	5.44 TeV	∼ 1.36 M	[33]
ATLAS	p+Pb	5.02 TeV	∼ 2.1 M	[34]
	Pb+Pb	2.76 TeV	∼ 1.63 M	[35]

certainties (Section 8). The shared objects will be discussed jointly, while analysis methods are introduced and explained separately.

2 Detector - INTT

The INTT is a two-layer barrel strip tracker [37] with a clamshell structure, positioned between the Monolithic Active Pixel Sensor (MAPS)-based Vertex Detector, MVTX, and the Time Projection Chamber, TPC. Its primary objective is to provide the sPHENIX tracking system with the capability to associate reconstructed tracks to the RHIC bunch crossings with a single-bunch-crossing timing resolution, enabling effective out-of-time pileup discrimination and suppression. This is achieved through the high processing frequency of the INTT FPHX readout chip, which operates at 9.4 MHz [38] and synchronizes with the RHIC bunch-crossing frequency, resulting in a time resolution of $\mathcal{O}(100\,\mathrm{ns})$ as shown in Figure 1. In addition, by providing two additional spatial points, the INTT bridges the MVTX and TPC, improving the pattern recognition for track reconstruction.

The INTT is designed to provide hermetic 2π azimuthal coverage and a pseudorapidity range of $|\eta|\leq 1.1$ for collision vertices within ± 10 cm of the nominal interaction point along the beam axis. To fulfill these requirements, the detector consists of 24 silicon ladders in the inner barrel and 32 in the outer barrel. These ladders are arranged tangentially and evenly spaced around the beam pipe at radial positions of approximately 7.2, 7.8, 9.7, and 10.3 cm from the beam axis, as illustrated in Figure 2.

Each ladder has an active area of $2\times 46\,\mathrm{cm}^2$ [39]. Two types of silicon sensors, type-A and type-B, are employed. The type-A sensor features an active area of $128 \times 19.968\,\mathrm{mm}^2$ and is segmented into eight rows and two columns of blocks. Each block contains 128 strips with a 78µm pitch and a strip length of 16 mm, oriented in the longitudinal direction. Similarly, the type-B sensor has an active area of $100 \times 19.968\,\mathrm{mm}^2$, divided into five rows and two columns of blocks, with each block comprising 128 strips of the same 78µm pitch but with a strip length of 20 mm. This configuration yields a total of 6656 readout channels per ladder and 372736 channels across the entire INTT barrel. The radiation length of a single ladder is 1.14% X_0, minimizing material interference and preserving track reconstruction accuracy.

The INTT barrel is divided into two halves, referred to as the north and south barrels, with signals read out separately from each half. Figure 3 illustrates the full readout cable chain up to the INTT Read-Out Card (ROC). When a silicon channel is activated by its interaction with a charged particle, the analog signal is transmitted to the FPHX chip, where it is converted into a digital signal with an attached amplitude and bunch-crossing index. The digital signal is then received by the INTT ROC through High-Density Interconnects (HDI), the Bus Extender Cable (BEX), and a micro-coaxial conversion cable. The signal packet, assembled by the ROC, is subsequently transmitted to the INTT FELIX server [40] via a 60-meter-long optical fiber. The FELIX readout server correlates the received digital signals with Global Level-1 (GL1) trigger signals, storing hits associated with the same GL1 trigger within an event.

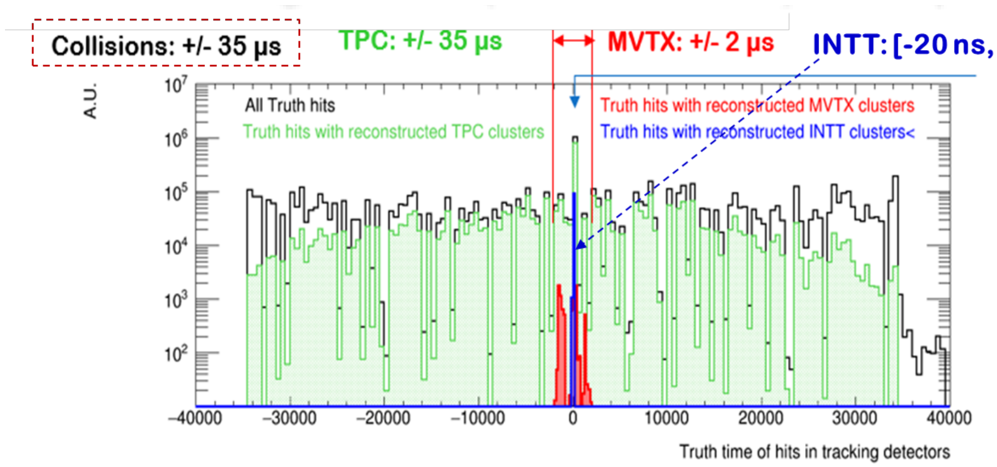

Figure 1: The timing resolution of sPHENIX tracking system based on simulation study.

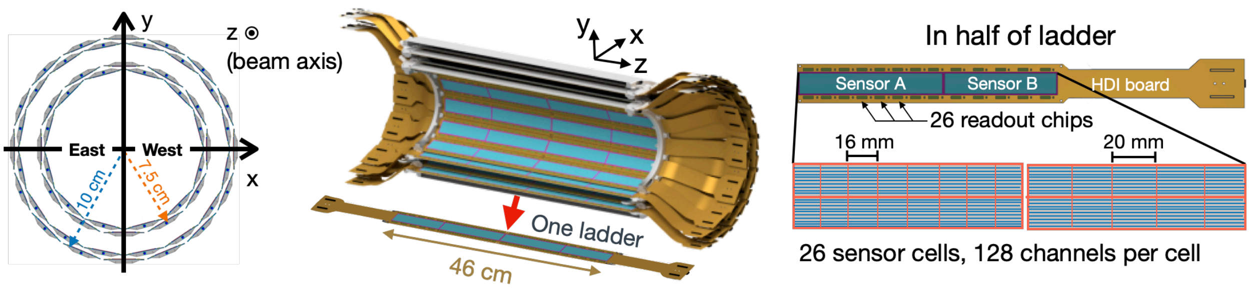

Figure 2: Left: the cross-section view of the INTT. Middle and Right: Schematic drawings of the INTT barrel and a INTT half ladder.

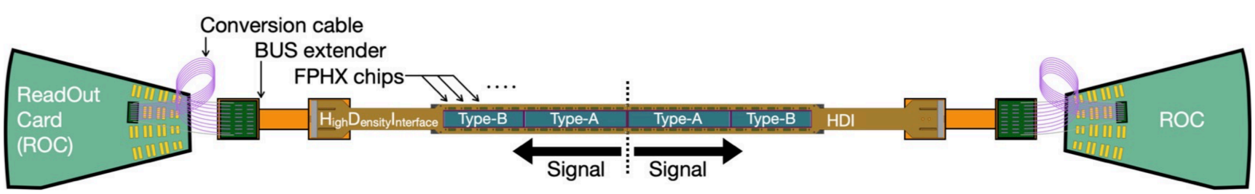

Figure 3: Schematic drawing of INTT silicon ladder, and the full readout cable chain up to read-out card.

3 Event selection

3.1 Data

The analysis uses Min. Bias (Section 3.1.5) Au+Au collision data collected on October 10, 2024, acquired without the sPHENIX magnetic field [41]. Table 2 summarizes the key properties of the analyzed data sample.

Table 2: Key properties of the analyzed data DSTs

Property	**Value**
Run number	54280
INTT calibration tag	ProdA_2024
Centrality calibration tag	
Calorimeter production software build	ana_441
INTT production software build	ana_464
Total number of events in analyzed DSTs	8.79 M
Total number of Min. Bias (Section 3.1.5) events	4.38 M

A specialized production macro has been set up to generate cluster DSTs, available at https://github.com/sPHENIX-Collaboration/ProdFlow/tree/ppg02-qm25-clustering. This macro includes the necessary settings and configurations for the hit unpacking procedure[2] carried out by the Fun4All module InttCombinedRawDataDecoder. The key configurations applied are:

- runInttStandalone = true: The time_bucket information of raw hits is not stored for further reconstruction
- set_triggeredMode = true: Data were collected with INTT operating in trigger mode
- set_bcoFilter = true: The hit BCO mask is applied
- writeInttEventHeader = true: The InttEventHeader node is stored in the output DST

With these settings, InttCombinedRawDataDecoder performs INTT calibrations, which are detailed in Sections 3.1.1–3.1.3.

3.1.1 INTT calibration – Hit BCO mask

During Run 2024 data taking, a firmware upgrade to FELIX enabled timing synchronization across all FELIX servers [42]. This synchronization was validated by the alignment of spikes in the hit time bucket distribution, the hit BCO relative to the GL1 BCO, across all FELIX servers, as shown in Figure 4.

For run 54280, the strobe length was set to 100 BCOs, allowing multiple collisions to occur within a single strobe length. To address this, a hit BCO filter is applied to include only hits recorded within ± 1 BCO relative to the GL1 BCO.

[2] Hit unpacking refers to the process of converting raw hit objects into TrkrHit objects, which are subsequently used for higher-level reconstructions.

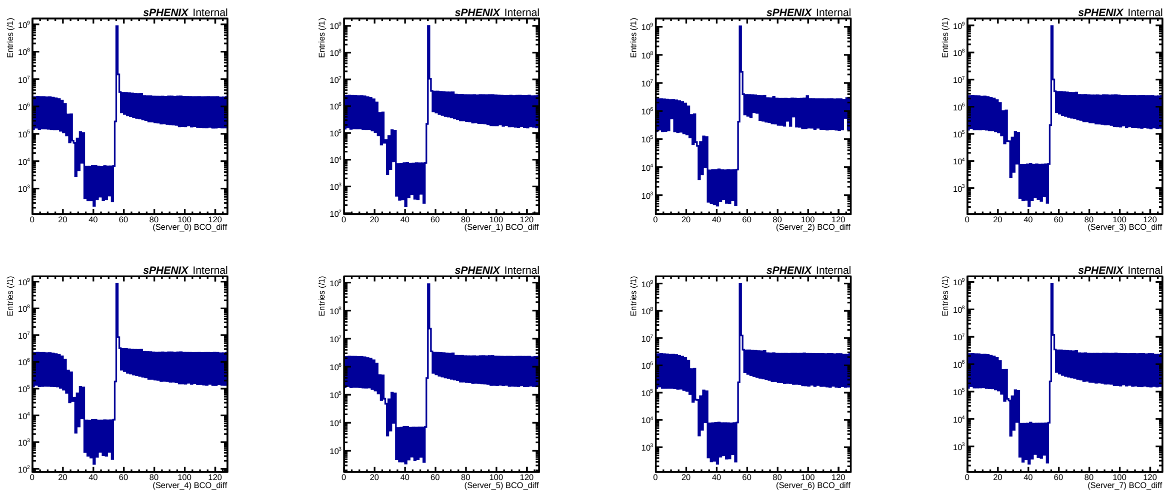

Figure 4: The hit time bucket distribution across all INTT FELIX servers (with the time bucket labeled as "BCO_diff" on the X-axis).

3.1.2 INTT calibration – Hot, dead, and cold channel masks

Hot, dead, and cold channels are identified using a data-driven method based on the first ten thousand events and masked during the hit unpacking process. For each channel in an INTT half-ladder, the hit rate, corrected for strip length and the radius of its position, is binned into a histogram, an example of which is shown in Figure 5. A Gaussian function is fitted to the distribution. Channels with hit rates exceeding the mean of the fitted Gaussian by 5σ are classified as hot channels, while those falling 3σ below the mean are classified as cold channels. Channels with hit rates of zero are identified as dead channels. Table 3 summarizes the classification results, and the hit distributions with bad channels masked are shown in Figure 6.

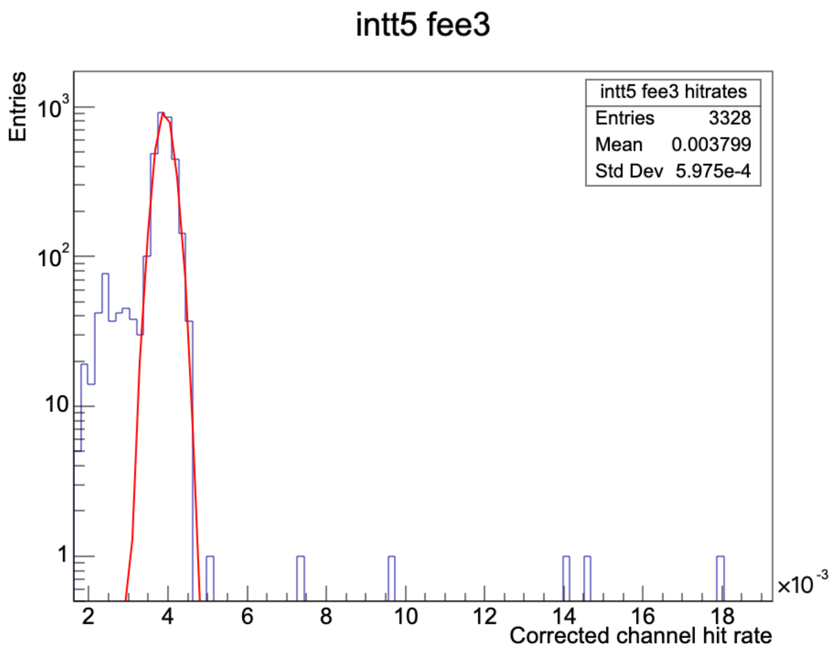

Figure 5: The corrected channel hit rate distribution of FELIX server 5 and FELIX channel 3.

Table 3: The summary of channel classification of run 54280.

Channel type	Number of channels	Ratio
Hot	36	0.01%
Dead	5547	1.49%
Cold	9119	2.45%
Good	358,034	96.06%

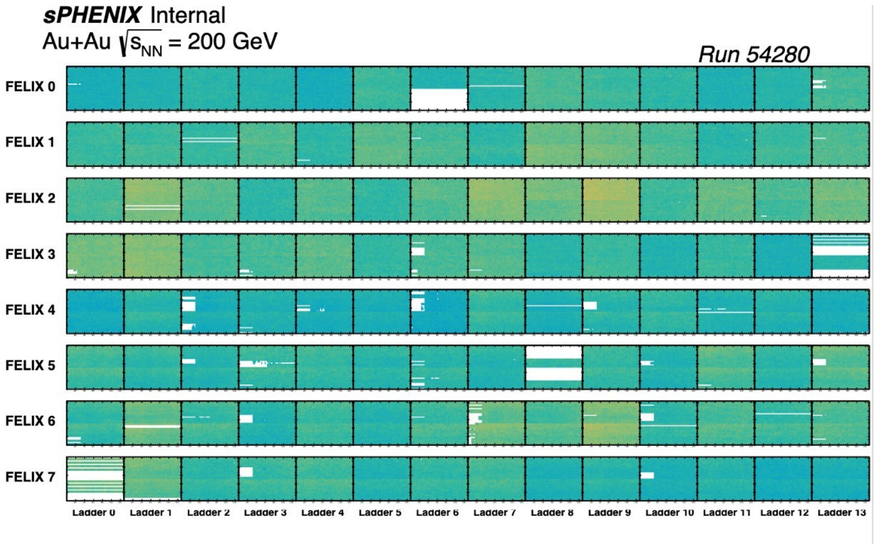

Figure 6: INTT hit map of run 54280 after applying the bad channel mask.

3.1.3 INTT calibration – Analog-to-digital conversion

The FPHX readout chip [38] used by INTT features a 3-bit analog-to-digital (ADC) converter with eight programmable signal amplitude comparators, whose threshold settings are listed in Equation 1 for the run 54280. When an analog signal is digitized, its amplitude is compared against these preset thresholds. The final digital signal amplitude is determined by the index of the comparator with the highest threshold that the signal exceeds. The digitized signal is discarded if its amplitude is below the first comparator's threshold (set to 35 for this run).

To determine the optimal threshold settings, the energy deposit distribution, measured in a beam test experiment with an 800 MeV positron beam, is used as a reference, as shown in Figure 7. The first comparator threshold of 35 effectively minimizes noise contamination while preserving the majority of the signal distribution. The remaining threshold values are evenly spaced for the most part, covering the full signal spectrum.

The INTT rawhit data store a 3-bit signal amplitude, which is mapped to the corresponding ADC threshold during the rawhit decoding process. These hit ADC values are then used in the clustering stage to determine the cluster position.

$$\text{Threshold setting} = [35, 45, 60, 90, 120, 150, 180, 210]. \tag{1}$$

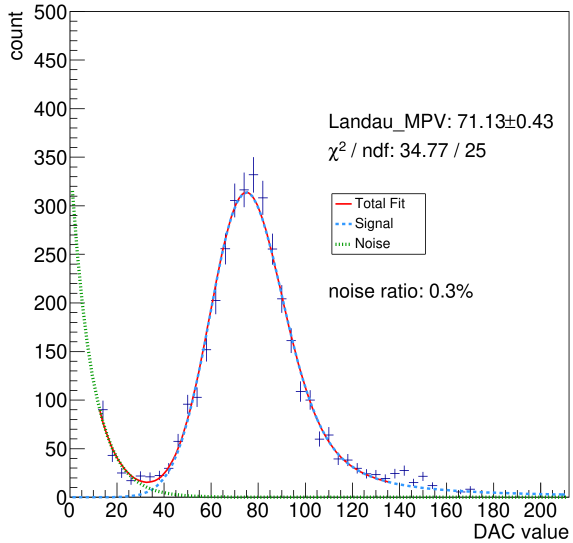

Figure 7: The energy deposit distribution of INTT ladder measured in beamtest.

3.1.4 Event BCO removal

Events with a BCO difference of less than 62 relative to their preceding event are discarded to mitigate the issue of incorrect hit association. This issue is identified as off-diagonal entries in the correlation between the number of inner and outer INTT clusters and the MBD charge sum, as shown in Figure 8. These off-diagonal events are not caused by the hit BCO or bad channel masks, as they persist even when these masks are disabled. Additionally, their presence in Min. Bias events suggests that they are unlikely to originate from collision-induced backgrounds.

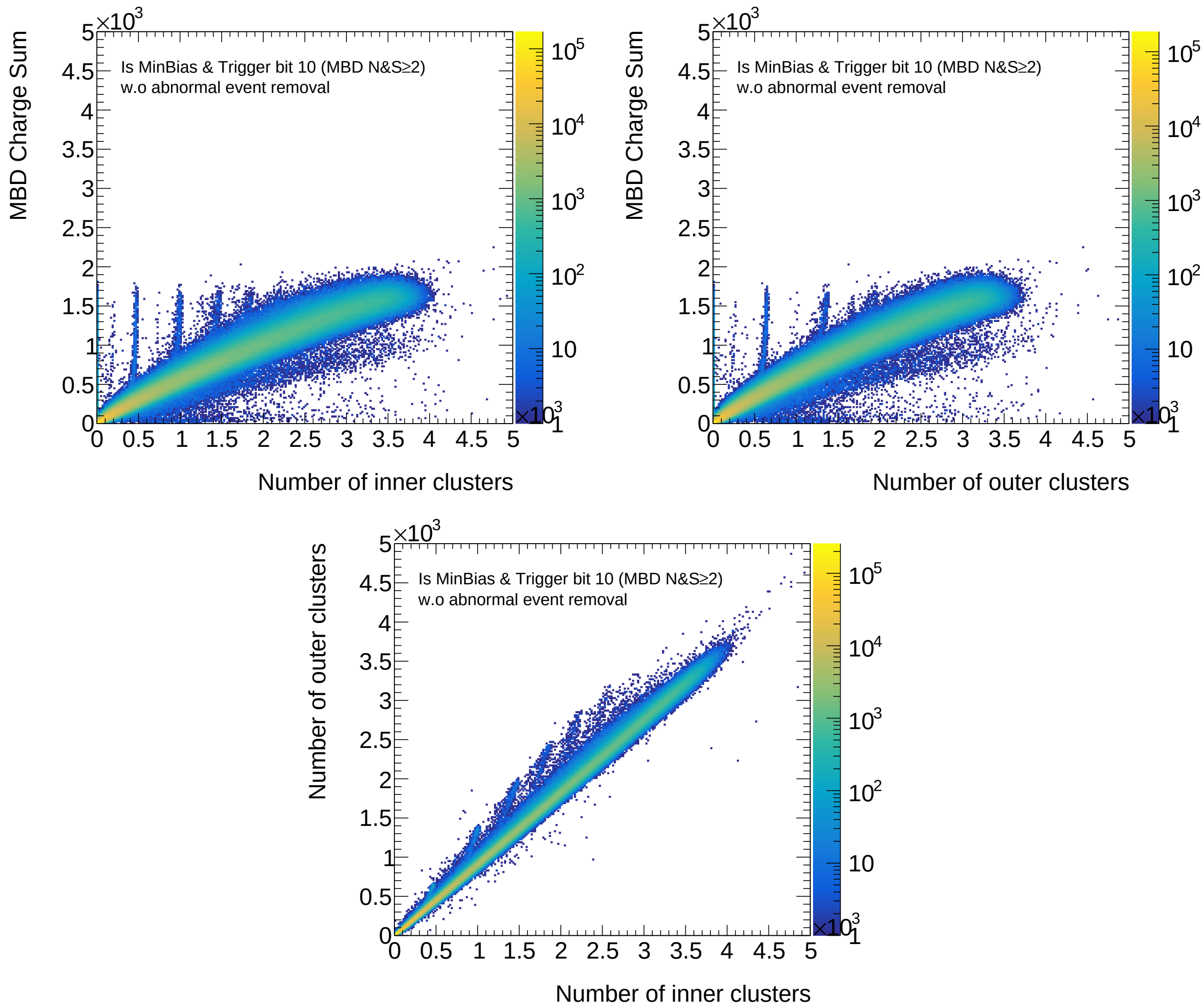

Figure 8: The correlation between the number of inner and outer INTT clusters and the MBD charge sum.

The left plot of Figure 9 shows the difference in event BCO between an off-diagonal event and its next adjacent event, demonstrating that, in most cases, the adjacent event occurs within 60 BCOs—the INTT "open_time" during which FELIX reads out hits from a given distinct BCO—of the event of interest. For comparison, the right plot of Figure 9 shows the event BCO difference across all events, extending up to 200 BCOs. This highlights an issue in INTT data acquisition, as illustrated in Figure 10 and detailed below.

When a trigger is fired, the INTT readout chip sends hits with the corresponding hit BCO to the INTT Read-Out Card (ROC). The INTT ROC then forwards the hits to the INTT FELIX server, which initiates a 60-BCO open_time upon receiving the first arriving hit. If another GL1 signal occurs within this 60-BCO window, the event header of hits associated with the previous GL1 will be overwritten. As a result, hits from the previous GL1 will be assigned to the later GL1 signal, effectively carrying them over to the next triggered event. Figure 11 provides additional evidence for this interpretation. The top two plots show two events: the event of interest (BCO 1029942106868, event ID 2452, left plot) and its subsequent event (BCO $10299421068\underline{94}$, event ID 2453, right plot). In the subsequent event, one spike appears at time bucket 55, corresponding to hits from the later GL1 signal. Another spike, occurring at time bucket 29, differs from the first spike by 26 time buckets, matching the BCO difference between the two events, $10299421068\underline{94}$ - $10299421068\underline{68}$ = 26. This alignment suggests that these hits were carried over from the previous event. The bottom plots compare the time buckets of hits from the event of interest (blue), the adjacent event (red), and the hits from the adjacent event recalculated relative to the event of interest (green). The overlap between the green and blue distributions shows that some hits from the next adjacent event share the same time bucket as the event of interest, providing clear evidence of incorrect hit assignment.

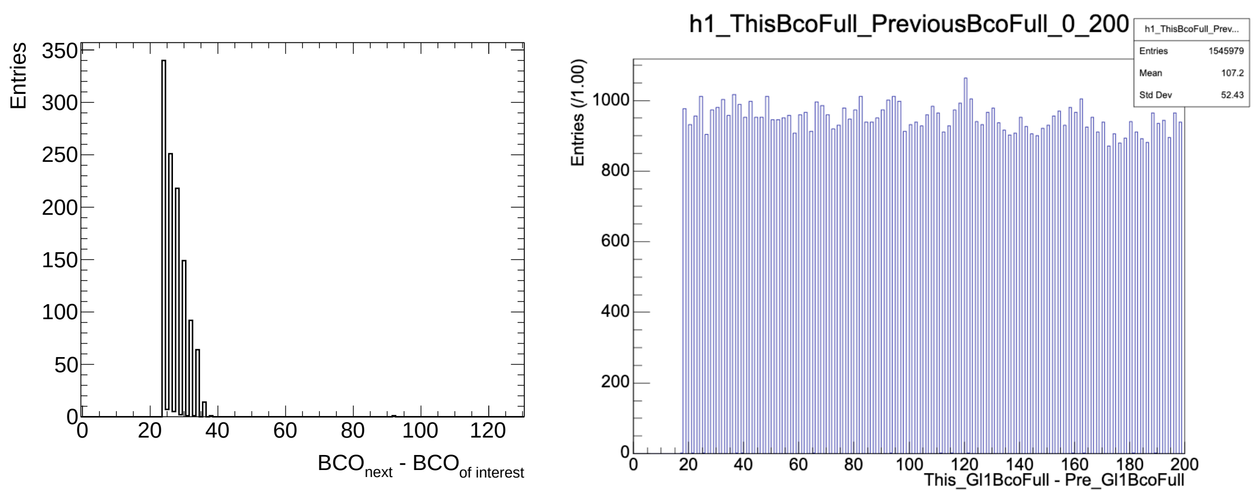

Figure 9: (Left) The difference in event BCO between the off-diagonal event (labeled as $\mathrm{BCO}_{\text{of interest}}$) and its next adjacent event (labeled as $\mathrm{BCO}_{\text{next}}$). (Right) The event BCO difference in all events.

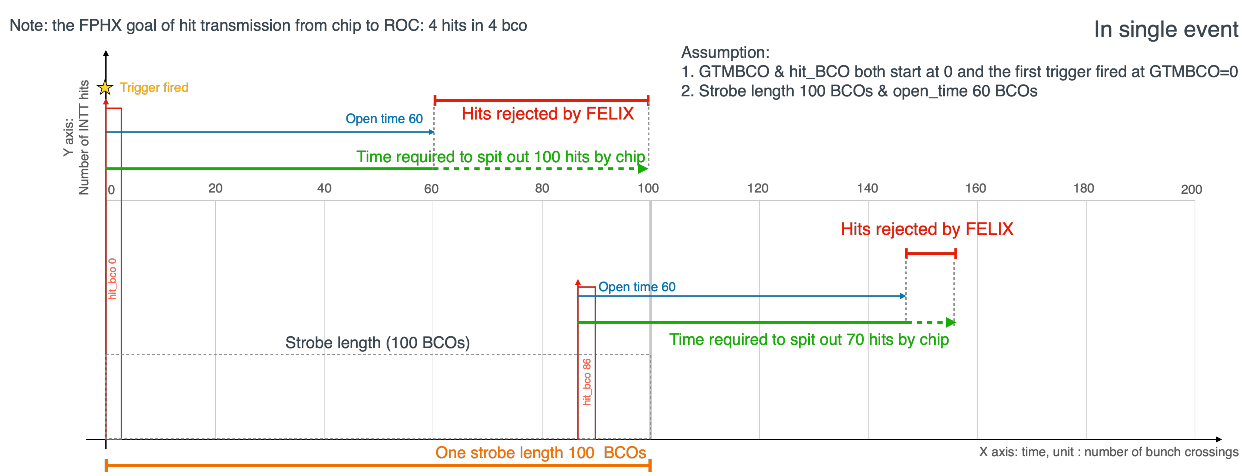

Figure 10: The data process logic of INTT in a single event.

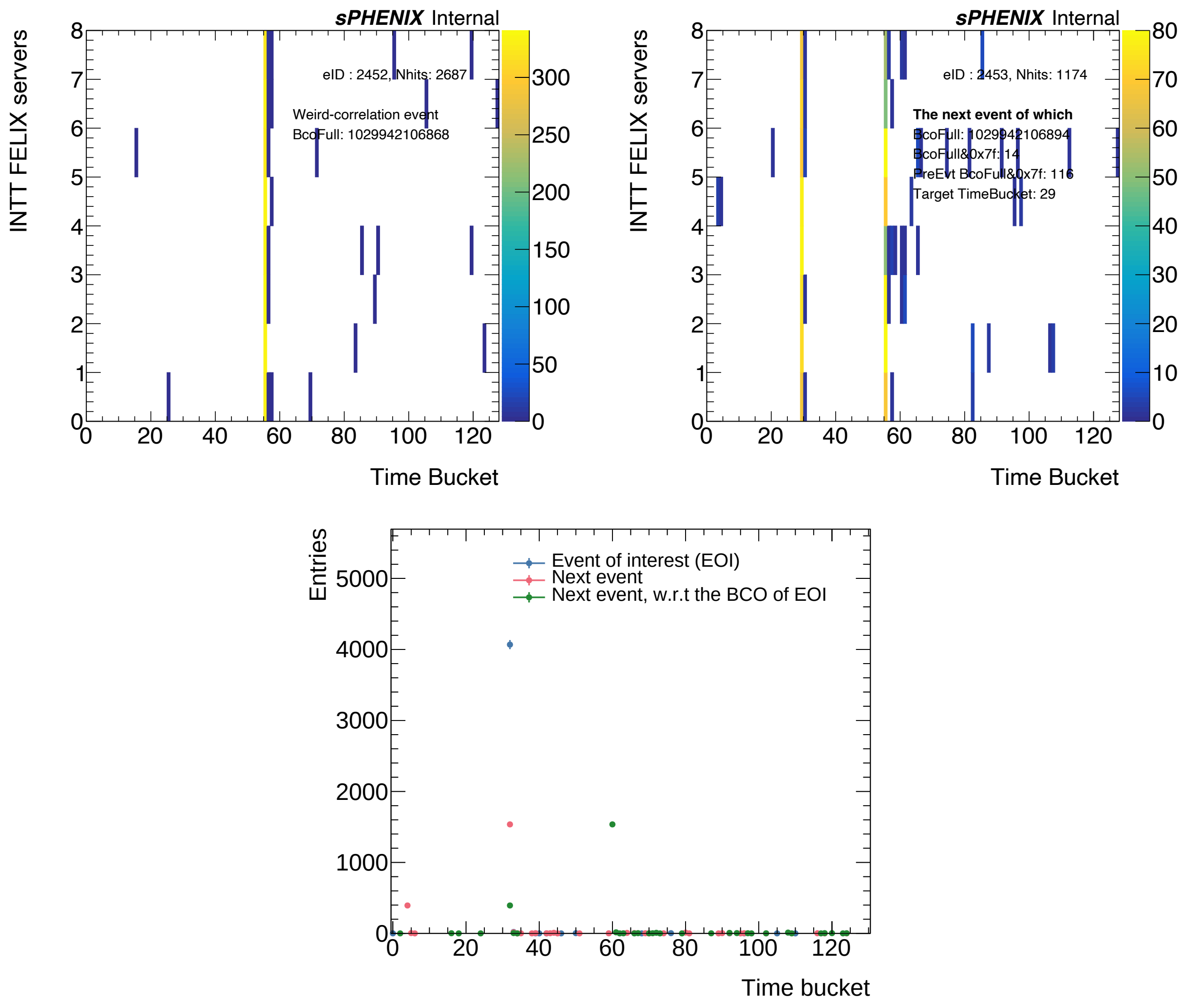

Figure 11: An example of the hit time bucket distributions for all eight INTT FELIX servers in the event of interest (top left) and its next event (top right). (Bottom) The time buckets of hits from the event of interest (blue), the adjacent event (red), and the time bucket of hits from the adjacent event recalculated relative to the event of interest (green).

Figure 12 shows the same correlations as Figure 8, but with the event BCO removal applied. After this removal process, approximately 1.3% of events were discarded, irrespective of the centrality intervals, as shown in Figure 13.

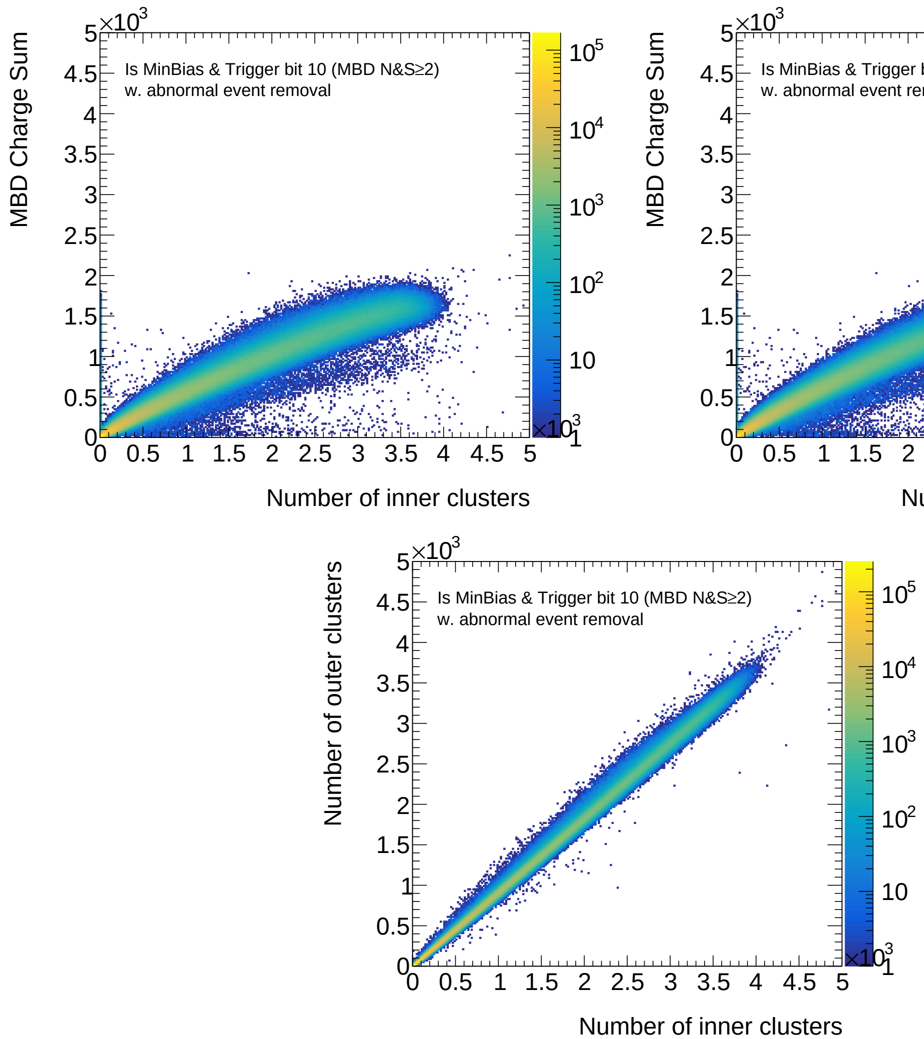

Figure 12: The correlation between the number of inner and outer INTT clusters and the MBD charge sum after the event BCO removal.

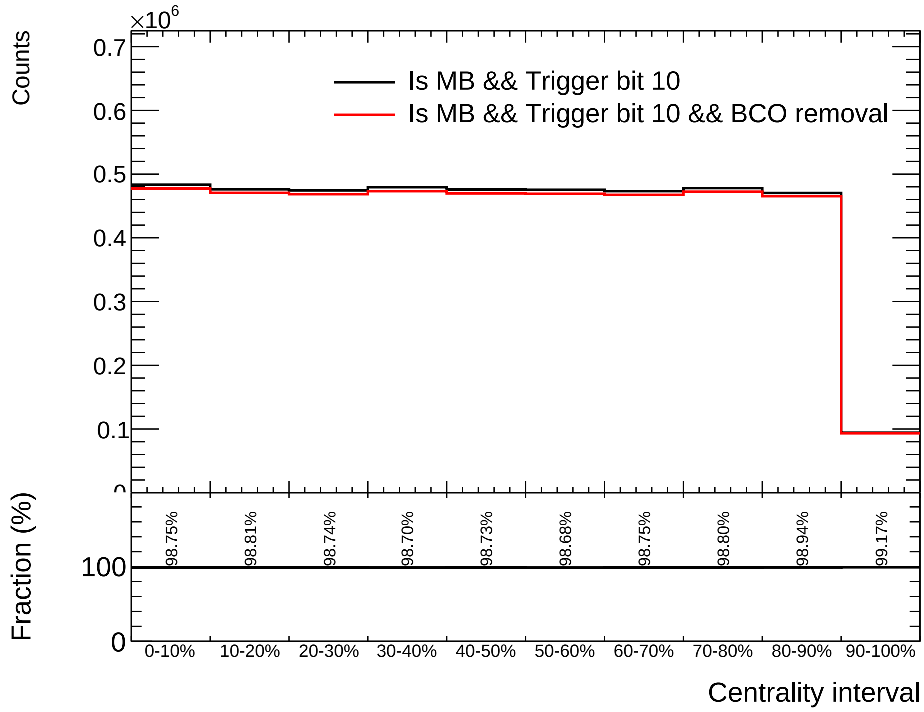

Figure 13: Fraction of events discarded by the event BCO removal as a function of centrality.

3.1.5 Min. Bias definition

The Min. Bias criteria are defined in Ref. [43]:

1. **The Level-1 trigger condition**: at least 2 hits above threshold in both the north and south MBD
2. **Background cleaning**: Events, where the charge signal in the south MBD exceeds that of the north MBD by more than 10 times, are discarded
3. **ZDC coincidence**: Coincidence of energy deposit greater than 40 GeV between the north and south ZDC. This significantly removes non-collision background at high luminosities
4. **MBD vertex cut**: $|z_{\mathrm{MBD}}| < 60\,\mathrm{cm}$

3.2 Offline selection

In addition to the Min. Bias definition, additional selections on global physics objects are applied offline for the analysis:

- **INTT vertex cut**: $-10\,\mathrm{cm} \leq$ Reconstructed vertex Z position ($\mathrm{vtx_Z}$) $\leq 10\,\mathrm{cm}$, discussed in Section 6.4.3
- **Centrality**: $0 - 70\%$

4 Monte Carlo

4.1 Standalone simulation framework

All simulations were produced using the Fun4All framework. As the analysis uses non-standard detector configurations (such as shifted vertex positions, summarized in Table 4 and no magnetic field), and only requires the beam pipe, MVTX, INTT, and MBD to be simulated for a small number of events, a standalone simulation setup is prepared for internal studies. This subsection serves as documentation for reference within the collaboration.

Table 4: Summary of vertex positions in simulation.

Parameter	Value
$\langle \mathrm{vtx_x} \rangle$	-0.022 cm
$\langle \mathrm{vtx_y} \rangle$	0.223 cm
$\langle \mathrm{vtx_z} \rangle$	-4.39 cm
$\sigma(\mathrm{vtx_z})$	9.39 cm

The framework of mass simulation production via framework and all user requests are handled via a top-level python script which creates a condor submission file and any required folders. The framework has options to run single particle events of any particle type, Pythia8, or read HepMC files. There are three different generators that have produced HepMC files; `HIJING`, `EPOS4`, and `AMPT`. All three generators are used in the analysis to verify the accuracy of the Monte Carlo samples.

To ensure the simulations are reproducible, all productions are generated using an `ana` build. An `ana` build is a permanently archived copy of the sPHENIX software stack that is created every Saturday at approximately 3 am. Using an `ana` build also ensures that simulations are performed with all calibrations, major reconstruction updates, detector geometries, and bug fixes synchronized with the simulation DSTs centrally produced by the sPHENIX software and production team.

Three methods are also used to track the production settings for each DST. The first method uses the folder structure of the file, which is the most user-friendly but the most susceptible to losing information as all a user has to do is move the file. Each DST is stored within subfolders that define the production information, for example:

```
/sphenix/tg/tg01/bulk/dNdeta_INTT_run2023/data/simulation/ana.399/EPOS/fullSim
/magOff/detectorAligned/dstSet_00000
```

All simulations appear in the directory `/sphenix/tg/tg01/bulk/dNdeta_INTT_run2023/data/simulation/` then subfolders define the software stack, generator, whether the Geant4 simulation of sPHENIX was enabled, whether the detectors were aligned in Geant4 and what DST revision you're looking at. DST revisions are automatically handled when the job launches. If a DST already exists with the same settings in storage then the new

DST is placed into a folder with one higher value that the latest stored file, so if an identically tagged file exists `dstSet_00000` then the new file will go to `dstSet_00001`. Further, while a DST is being produced, it will exist in a subfolder called `inProduction` and is automatically moved to the top folder when the job completes. This allows analysers to immediately use DSTs while condor is still producing the rest of the data set without worrying about using unreadable files.

The second method to store production data involves a text file that is written along side the DST. This text file contains all the production information as well as the seeds used for that production so each DST can be exactly recreated if needed. The form of the text file is

Listing 1: Example metadata file

```
====== Your production details ======
Production started: 2024/01/22 16:47
Production Host: spool1068.sdcc.bnl.gov
Folder hash: 281626f
Software version: ana.399
Output file: dNdeta-sim-EPOS-000-00000.root
Output dir: /sphenix/tg/tg01/bulk/dNdeta_INTT_run2023/data/simulation/
ana.399/EPOS/fullSim/magOff/detectorAligned
Number of events: 400
Generator: EPOS
fullSim: true
turnOnMagnet: false
idealAlignment: true
=====================================

Seeds:
PHRandomSeed::GetSeed() seed: 2677558228
PHRandomSeed::GetSeed() seed: 67770606
PHRandomSeed::GetSeed() seed: 2482422915
PHRandomSeed::GetSeed() seed: 969717365
PHRandomSeed::GetSeed() seed: 4082588279
PHRandomSeed::GetSeed() seed: 1008239460
PHRandomSeed::GetSeed() seed: 280233077
PHRandomSeed::GetSeed() seed: 527826680
PHG4MvtxDigitizer random seed: 527826680
PHRandomSeed::GetSeed() seed: 3802774622
PHG4InttDigitizer random seed: 3802774622
PHRandomSeed::GetSeed() seed: 1263913743
SEEDS: PHRandomSeed::GetSeed() seed: 2677558228
PHRandomSeed::GetSeed() seed: 67770606
PHRandomSeed::GetSeed() seed: 2482422915
PHRandomSeed::GetSeed() seed: 969717365
PHRandomSeed::GetSeed() seed: 4082588279
PHRandomSeed::GetSeed() seed: 1008239460
```

```
PHRandomSeed::GetSeed() seed: 280233077
PHRandomSeed::GetSeed() seed: 527826680
PHG4MvtxDigitizer random seed: 527826680
PHRandomSeed::GetSeed() seed: 3802774622
PHG4InttDigitizer random seed: 3802774622

md5sum:
5a3910480142d71865188235bce6bba1
```

The last method to maintain the metadata is the use of a storage node directly in the DST. This means that even if the DST is downloaded and renamed then a user can access this node and print out the production details, including the seeds.

The simulation framework along with the metadata class is stored on github. Before each production is launched, the changes to the repository are pushed to github as part of the metadata information is to record the git hash of simulation framework so that this can be checked out to exactly reproduce any DST at a later date. The framework can be found at `https://github.com/cdean-github/dNdeta_sPHENIX_simulations/`.

The beampipe, MBD, MVTX, and INTT were simulated using GEANT4 with modified geometry based on a preliminary alignment study [44, 45]. In particular, significant effort was made to update the INTT GEANT4 geometry according to the survey measurements, as detailed in Appendix B.

The three INTT calibrations – the hit BCO, hot/dead/cold channel masks, and the analog-to-digital conversion map – are centrally maintained in the sPHENIX Calibration Database. These calibrations are accessed by the simulation setup through the relevant production tag (Table 2).

4.2 Central simulation production

Table 5 summarizes the sPHENIX central production simulation samples used in this analysis.[3]

Table 5: Summary of simulation sample with production and CDB tag.

Generator	Production tag	CDB tag	Special configuration
HIJING	run 26, type 4, -nop	MDC2	-
	run 27, type 4, -nop		Enhanced strangeness by 40%
EPOS4	run 26, type 25, -nop		-
AMPT	run 26, type 24, -nop		-

[3] Table 5 will be updated and completed when all the requested simulation samples are available.

4.3 Primary charged hadron definition

In line with previous measurements at RHIC and LHC, the primary charged-hadrons are defined as prompt charged-hadrons and decay products of particles with proper decay length $c\tau < 1\,\mathrm{cm}$, where c is the speed of light in vacuum and τ is the proper lifetime of the particle. This definition excludes contributions from prompt leptons, decay products of particles with longer lifetimes, and secondary interactions. The selection criteria corresponding to the technical definition of primary charged hadrons are as follows:

1. The particle is a primary PHG4Particle, or equivalently, a final-state HepMC::GenParticle without a decay vertex, with a status of 1. Proper Lorentz rotation and boost are applied to account for the beam crossing and shifted vertex. This criterion excludes particles from secondary interactions.
2. The particle is stable.
3. The particle has a charge $\neq 0$.
4. The particle is classified as a meson or baryon.

Contributions from charged leptons to the tracklet counts are expected to be negligible. Figure 14 presents the number of charged particles, strange particles (which undergo weak decays), and charged leptons across 200 `HIJING` simulation events. Charged leptons are nearly two orders of magnitude less abundant than strange particles. Consequently, any variation from including charged leptons is negligible compared to the significantly larger effect of strangeness decays, for which a systematic uncertainty will be assigned.

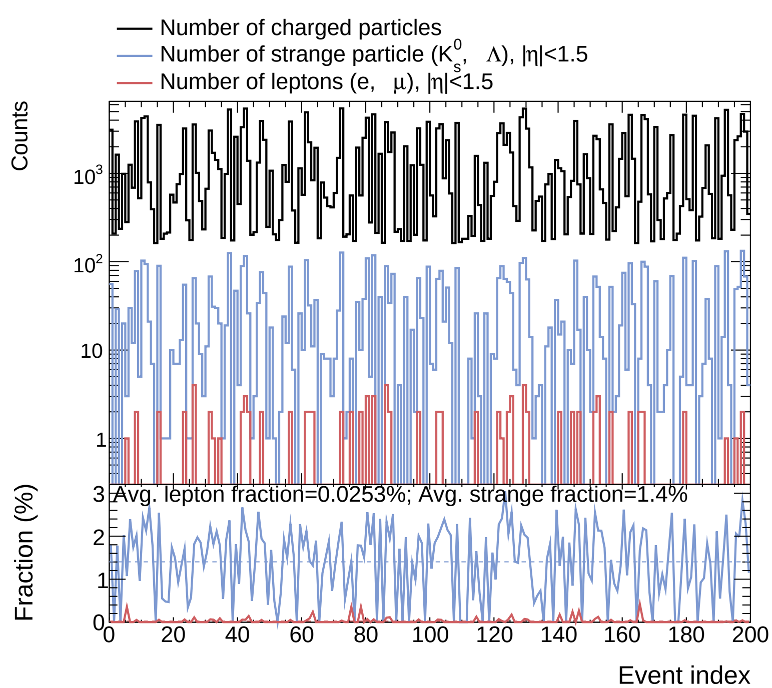

Figure 14: The number of charged particles, strange particles (which undergo weak decays), and charged leptons across 200 `HIJING` simulation events.

4.4 Z-vertex reweighting

Figure 15 shows the vertex Z position reconstructed by INTT tracklets, detailed in Section 6.4.3. The data-to-simulation ratio is used as a per-event weight and applied to the simulation, ensuring the vertex Z position matches that observed in the data. For events with $-10\,\mathrm{cm} \leq \mathrm{vtx_Z} \leq 10\,\mathrm{cm}$, the reweighting factors are consistent with 1.

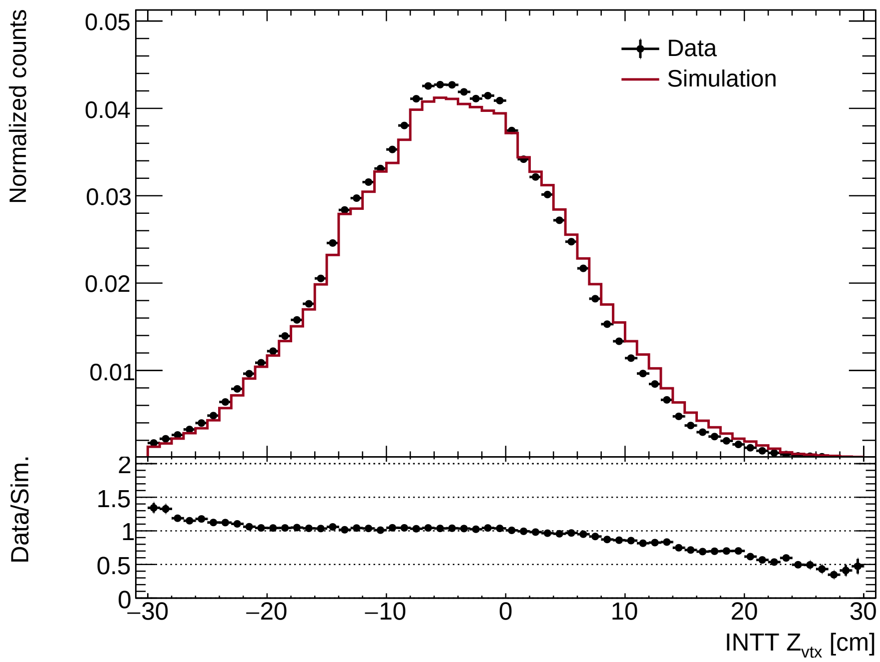

Figure 15: Distribution of the vertex Z position reconstructed by INTT tracklets in data and simulation (top panel), and the ratio of data to simulation (bottom panel).

5 Toolkit

The following list summarizes the analysis tools:

- dNdEta Fun4All ntuplizer: This Fun4All analysis module reads data and simulation DSTs and produces analysis ROOT trees. The module can be found at https://github.com/sPHENIX-Collaboration/analysis/tree/master/dNdEta_Run2023/dNdEtaINTT, while the corresponding Fun4All macros could be found at https://github.com/sPHENIX-Collaboration/analysis/tree/master/dNdEta_Run2023/macros.

- dNdEta analysis codes: The analysis codes perform the offline beamspot reconstruction, per-event vertex Z position reconstruction, tracklet reconstruction and counting, correction factor calculation and application, systematic uncertainty, and plotting utilities. The codes can be found at

  – The PHOBOS-approach analysis: https://github.com/sPHENIX-Collaboration/analysis/tree/master/dNdEta_Run2023/analysis_INTT_CW/NewCode2024

– The CMS-approach analysis: https://github.com/sPHENIX-Collaboration/analysis/tree/master/dNdEta_Run2023/analysis_INTT

6 Analysis

6.1 Centrality

The centrality determination used in this analysis was taken from the MBD and ZDC information. The sPHENIX Event Plane Detector (sEPD) was operational, but was not included in the current centrality definition. The information was taken from the centralised sPHENIX production area using the tags listed in table 2 and was calculated according to the procedure documented by Dan Lis and Jamie Nagle [43]. In this analysis, we have access to

- the MIN. BIAS trigger decision,
- the event number,
- the clock value,
- the front end module (FEM) clock value,
- the centrality,
- the Z vertex as determined by the MBD,
- the MBD north and south charge sums,
- the total MBD charge
- the MBD north/south charge asymmetry.

By requiring the MIN. BIAS and the scaled trigger bit, the centrality determination is stable up to the maximal centrality value derived, as can be seen in Figure 16. The centrality compared to the MBD Z vertex is shown in Figure 17, where no correlation between the two variables is found.

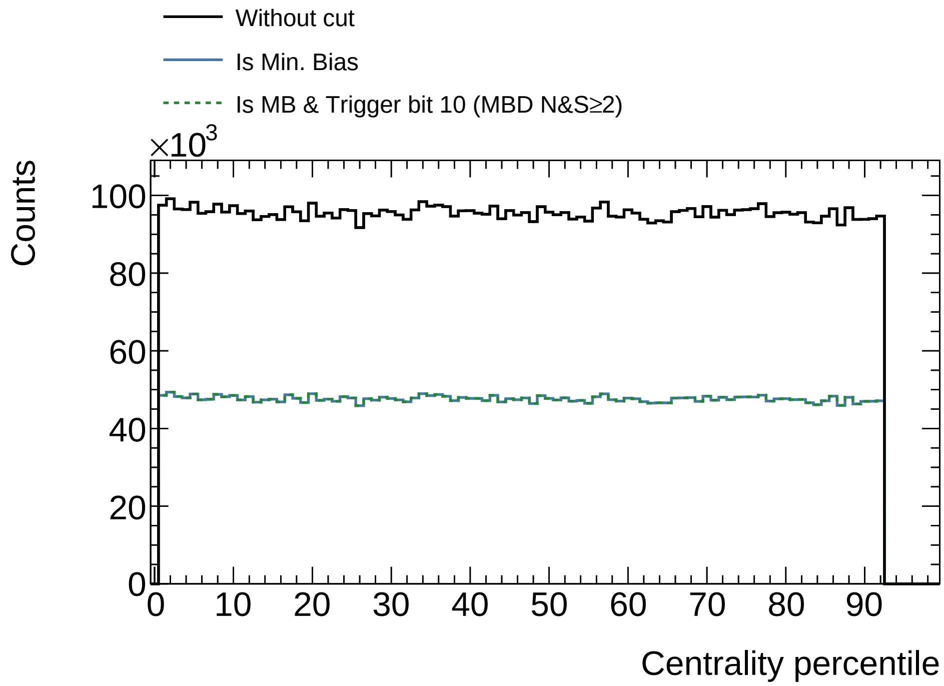

Figure 16: Centrality determined for run 54280 after applying the Min. Bias and the scale trigger bit.

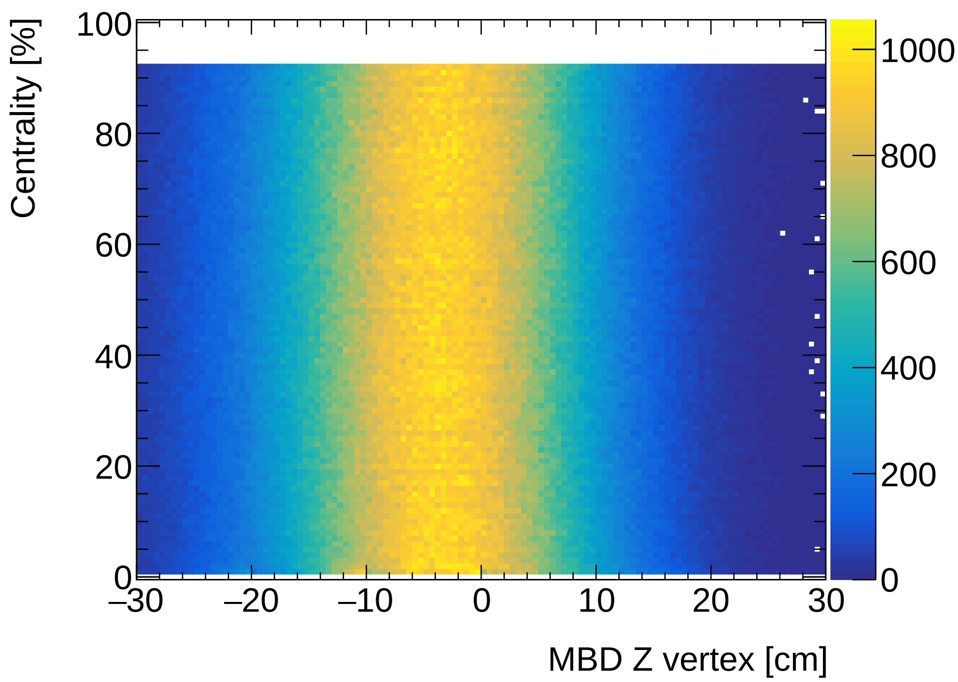

Figure 17: Centrality determined for run 54280 after applying the Min. Bias and the scale trigger bit, compared to the MBD-determined Z-vertex.

6.2 Cluster reconstruction

After the extraction of INTT hits from the event DST, the next step in reconstruction for this analysis is the formation of clusters of adjacent hits. These clusters ideally represent the full extent of the deposit of energy from a particular charged particle passing through a layer of the INTT, and contain information about that deposit's location, timing, size, and energy.

6.2.1 INTT clustering algorithm

The clustering of hits in the INTT is implemented using an adjacency graph, where each hit is represented as a node, and two nodes are connected by an edge if their corresponding hits are adjacent. The clusters then correspond to the connected components of this graph. Full implementation details can be found in `https://github.com/sPHENIX-Collaboration/coresoftware/blob/master/offline/packages/intt/InttClusterizer.cc`.

The characteristics of the clusters formed using this method depend on the criteria by which two hits are determined to be "adjacent." Several definitions were considered:

1. Standard clustering: two INTT hits are adjacent if and only if they are in the same column (corresponding to the same coordinate in z) and their edges touch in the ϕ direction. This is the current default definition in the INTT clusterizer.

2. Standard Z-clustering: two INTT hits are adjacent if and only if either the corners or the edges of their corresponding strips touch. In other words, hits are adjacent if and only if their row and column coordinates both differ by at most one. This is the definition currently used in the MVTX clusterizer and can be enabled in the INTT clusterizer.

3. Modified Z-clustering: two INTT hits are adjacent if and only if the edges of their corresponding strips touch. In other words, hits are adjacent if and only if their row and column coordinates differ by at most one, excluding the case where both differ by exactly one. (See Figure 18 for an example of how this differs from definition 2.)

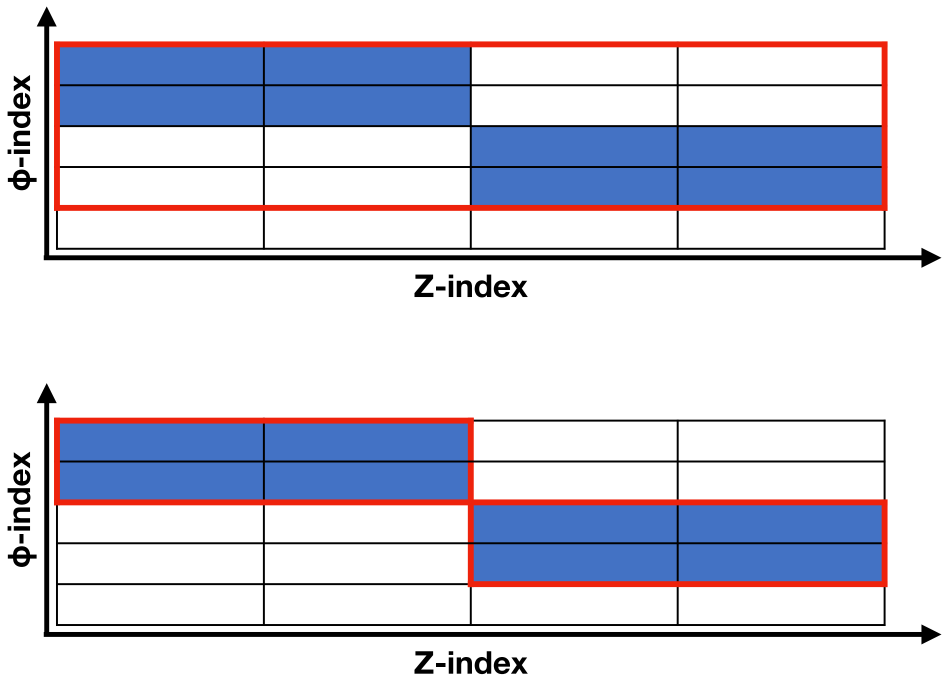

Figure 18: Illustration of one case in which the definitions of adjacency lead to differing results. In the top plot, the second definition of adjacency (including strip corners) is used, in which one cluster, outlined here in red, is formed. In the bottom plot, the third definition of adjacency (excluding strip corners) forms two clusters.

A comparison of the performance of each of these adjacency definitions required the development of a benchmark for clustering performance in simulation.

6.2.2 Clustering performance benchmarks

To objectively compare the effects of changes to the INTT clustering algorithm and its configurable settings, a method for evaluating the performance of the INTT clusterizer on simulated hits was developed. This method evaluates how well a clustering algorithm replicates the following two features of an ideal clustering algorithm:

1. All of the hits created by a given truth particle within a given layer are contained in exactly one reconstructed cluster, and
2. Each reconstructed cluster contains the hits created by exactly one truth particle.

These two features suggest two corresponding histograms as figures of merit:

1. The number of reconstructed clusters associated with the hits generated by a given truth particle, and

2. The number of truth particles associated with the hits contained in a given reconstructed cluster.

For an ideal clustering algorithm with a detector with an extremely fine-grained sensor layout, all entries in both histograms should be concentrated precisely at 1. Any deviations from this ideal scenario arise due to the sensor's granularity and potential limitations in the clustering algorithm. Given a fixed sensor layout, the relative differences between these histograms serve as a direct measure of clustering performance. Notably, if the clustering efficiency is imperfect, the number of clusters per truth particle will be less than one. In contrast, if the segmentation is too coarse or the multiplicity is too high, the number of truth particles per cluster will exceed one.

In order to make this comparison maximally compatible with the way that the INTT clusterizer operates, the reconstructed hits associated with each truth particle were grouped by TrkrHitSet, and the subsequent comparison with reconstructed clusters occurred only within the relevant TrkrHitSet. The method outlined here is implemented in the dNdEtaINTT Fun4All ntuplizer.

The results of this comparison, for hits simulated using the `HIJING` generator, applied to all three definitions of hit adjacency, are shown in Figure 19.

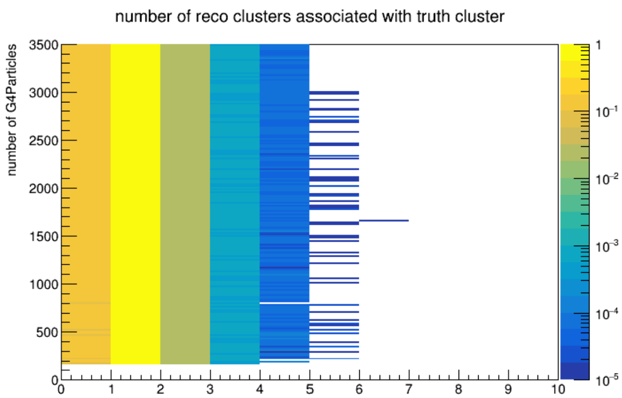

(a) Standard clustering, criterion 1

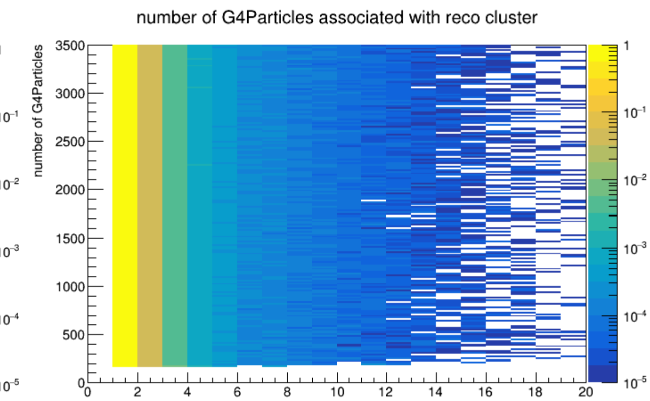

(b) Standard clustering, criterion 2

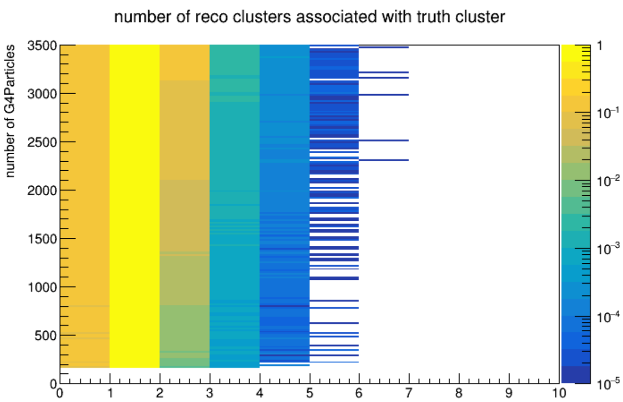

(c) Standard Z-clustering, criterion 1

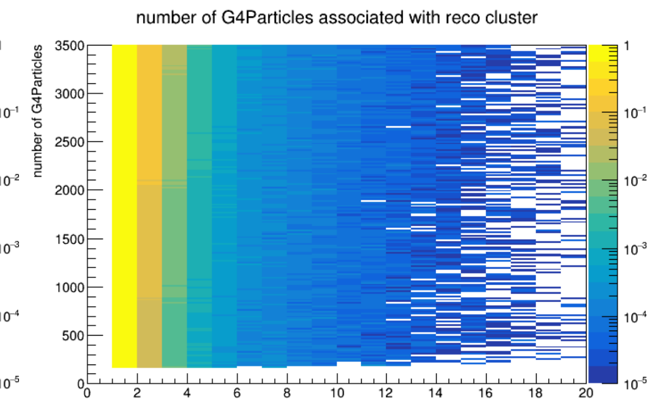

(d) Standard Z-clustering, criterion 2

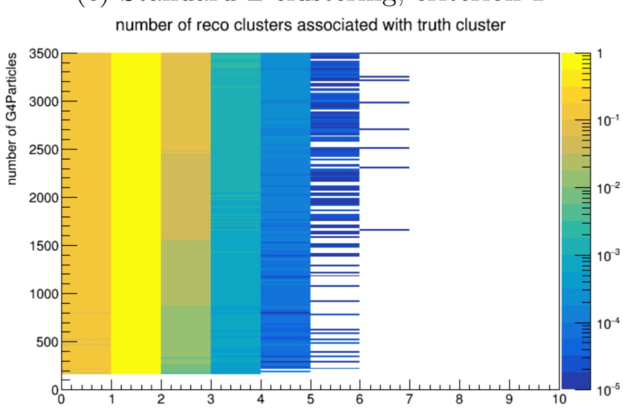

(e) Modified Z-clustering, criterion 1

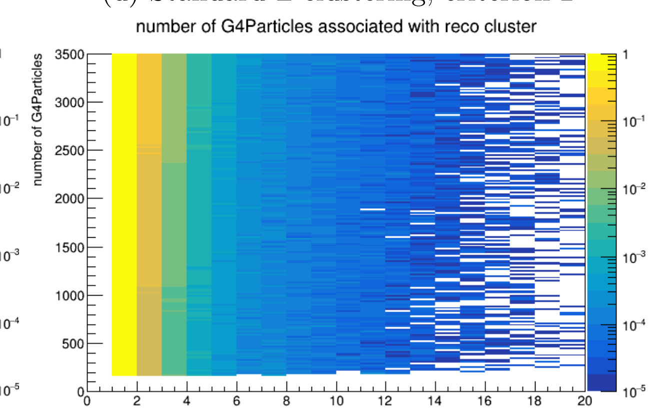

(f) Modified Z-clustering, criterion 2

Figure 19: Clustering performance comparison, differentially in occupancy, normalized within occupancy bins.

Since the latter two definitions are seen to have a multiplicity-dependent performance, they will not be used for further portions of this analysis; subsequent sections proceed with the standard definition of adjacency in the default INTT clusterizer, which fixes the INTT cluster size in the Z-axis to be 1. It is worth noting that the clustering algorithm implemented in MVTX follows the standard Z-clustering definition, where diagonally adjacent pixel hits are included as part of a cluster.

6.2.3 Background cluster removal/mitigation

A cluster ADC threshold of > 35 was applied to exclude single-hit clusters with minimal hit ADC values, as those clusters are assumed to be predominantly noise. Figure 20 shows the distribution of cluster ADC for clusters with a ϕ-size of 1. The $dN_{ch}/d\eta$ measurements with and without this cluster ADC requirement were compared, and the variation in the $dN_{ch}/d\eta$ distribution was quoted as a source of systematic uncertainty.

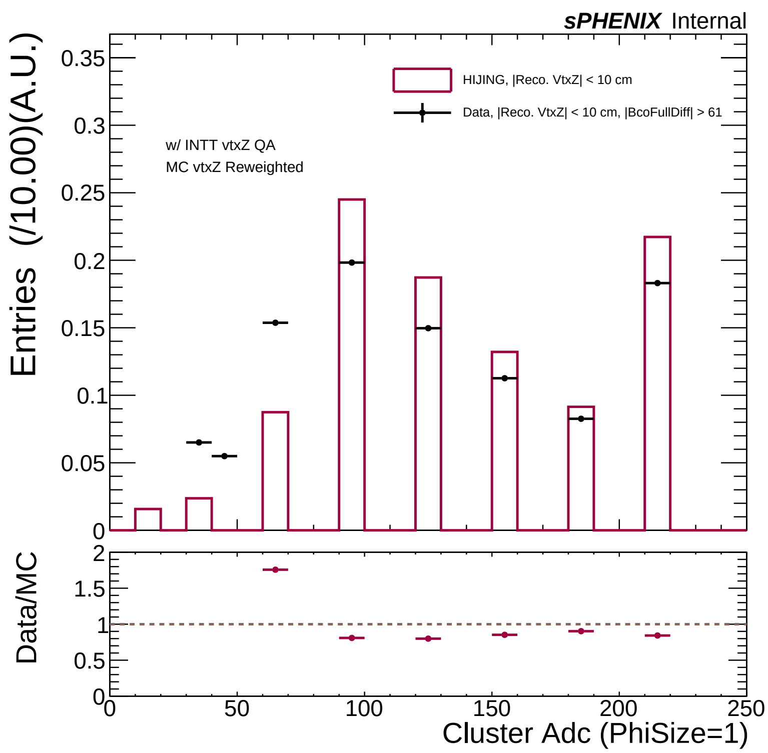

Figure 20: The cluster ADC distribution for clusters with a ϕ-size of 1.

6.2.4 Cluster distributions

The basic distributions of the clusters are shown in this section. Figure 21 shows the comparisons of the number of clusters in the INTT inner layer between data and `HIJING` simulation. The distributions shown are normalized to the number of events in data.

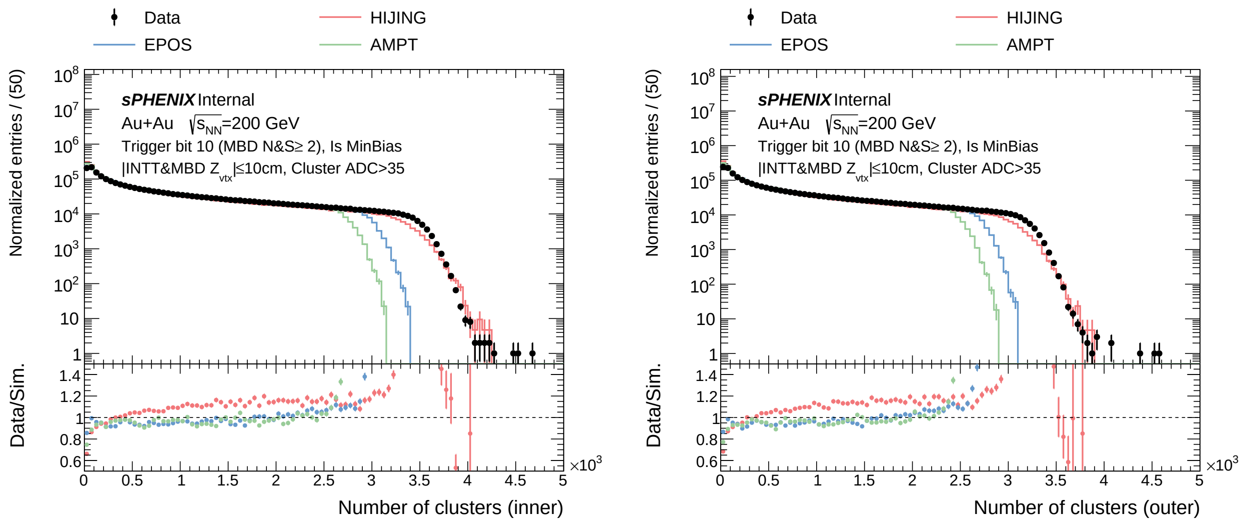

Figure 21: The number of clusters in the INTT inner (left) and outer (right) layer in data and `HIJING`, `EPOS4`, and `AMPT` simulations.

Figure 22 shows the cluster ϕ (left) and η (right) distributions in data and simulations, where ϕ and η are calculated with respect to the event vertex.

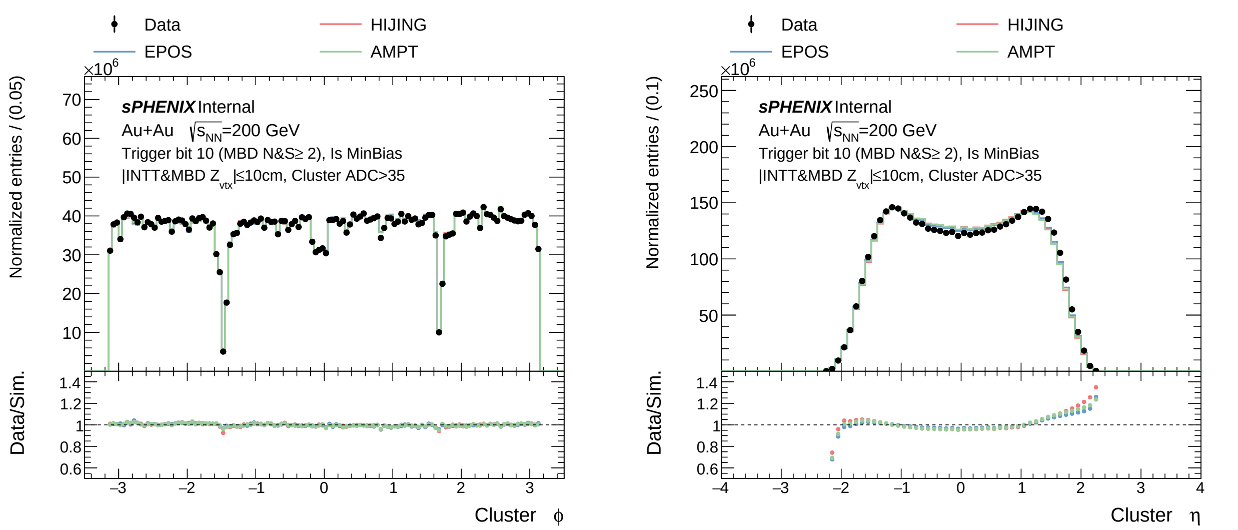

Figure 22: The cluster ϕ (left) and η (right) distribution in data and simulations.

Figure 23 shows the cluster ϕ-size (left), defined as the number of strips in the ϕ direction, and ADC (right) distribution in data and simulation. Discrepancies between data and simulation are seen in both variables. A dedicated study and an attempt to reproduce data distributions in simulation can be found in Appendix D. The impact of large ϕ-size clusters on tracklet reconstruction is studied by comparing the ϕ-sizes of constituent clusters in tracklets, detailed in Sec. 6.5.2. The discontinuity observed in the cluster ϕ-size around 50 and in the cluster ADC near 10×10^3 can be explained as follows: If a cluster has a sufficiently large energy deposit to extend over a range in the ϕ direction, it is more likely to span two or more strips in the Z direction (i.e., with a cluster Z-size ≥ 1). However, since Z-clustering is disabled by default, as explained in Sec. 6.2.1, this introduces a truncation effect in both variables at large values.

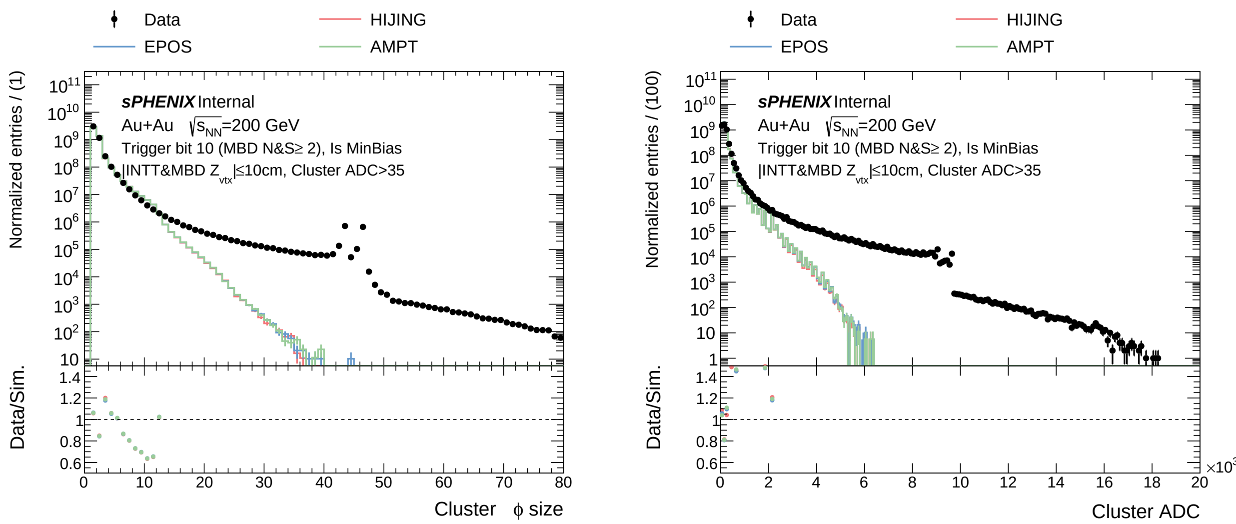

Figure 23: The cluster ϕ-size (left) and ADC (right) distribution in data and simulations.

The two distinct spikes observed in the distributions of cluster ϕ-size (ϕ-size $= 43$ and 46) and cluster ADC were investigated and found to be partially caused by the chip saturation issue. Figure 24 shows a cutoff in the tail of the distribution of the number of hits recorded by a single chip within one distinct hit BCO. This indicates that a chip can record a maximum of 73 hits per distinct hit BCO within the 60-BCO INTT open_time. Any hits from the given hit BCO that are not received by the INTT FELIX server within this 60-BCO window are dropped and cannot be recovered.

An example, illustrated in Figure 25, demonstrates this issue. In this scenario, 100 out of 128 channels on a chip are fired. The chip reads out these hits and sends them to the INTT ROC, which forwards them to the INTT FELIX server. When the FELIX server detects the first hit in the given hit BCO, it initiates the 60-BCO open_time window to collect subsequent hits from the same hit BCO. As mentioned above, only a maximum of 73 hits can be recorded within this window, meaning the remaining $100 - 73 = 27$ hits in this distinct hit BCO only arrive at the FELIX server after the predefined window. These 27 hits are unrecoverable and consequently dropped.

A distinct pattern is observed in the hit map of a chip experiencing saturation, as shown in Figure 26. When chip saturation occurs, it often results in a cluster with a large number of fired channels, while nearby channels fire in an alternating manner, meaning the channels with signals are evenly spaced (referred to as "zebra-like crossing"). Additionally, these clusters with a high number of fired channels most commonly have a cluster ϕ-size of 43 or 46 and predominantly appear at the edge of a chip. It remains unclear why the chip saturation issue specifically, or coincidentally, manifests at ϕ-size 43 or 46.

Figure 27 shows three pronounced spikes in the cluster ϕ-size distribution for saturated chips: the spike at 2 corresponds to the thickness of the alternating channels, while the spikes at 43 and 46 correspond to clusters with a large number of fired strips. Based on this analysis, we conclude that the two spikes at ϕ-size 43 and 46 are at least partially attributed to chip saturation.

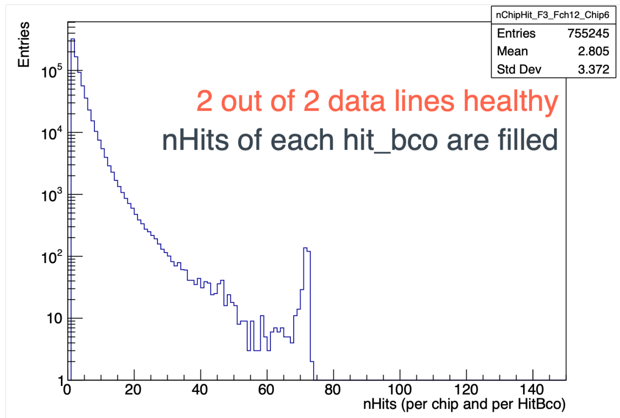

Figure 24: The number of hits of one chip in single BCO of one FUN4ALL event.

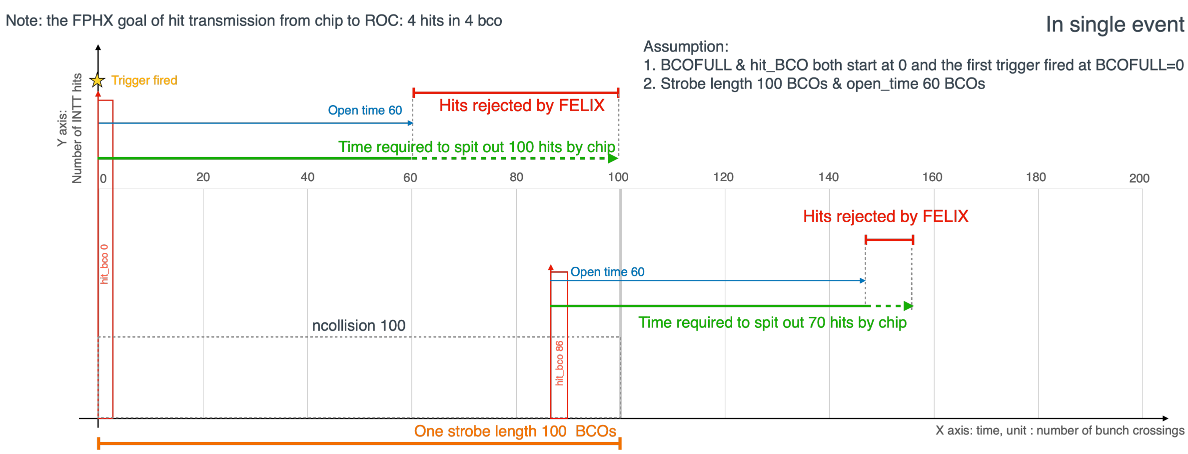

Figure 25: The illustration of INTT chip saturation issue.

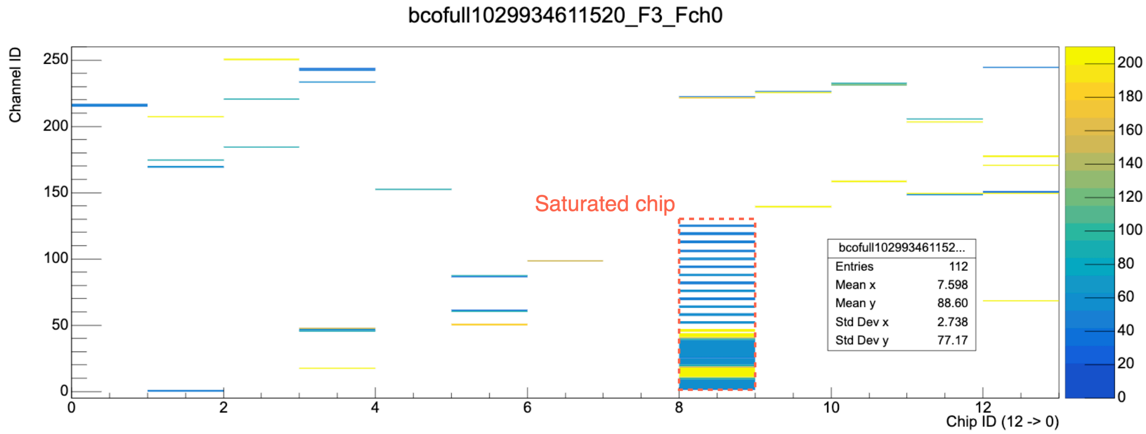

Figure 26: The hit map of one INTT half-ladder with chip saturated of one event.

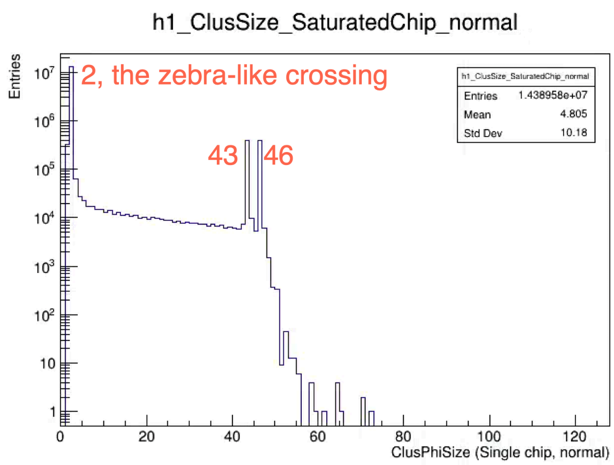

Figure 27: The cluster ϕ size distribution of the saturated chips.

The baseline analysis applies a cluster ϕ-size cut $\leq$ 40, which retains all clusters in simulation but excludes clusters with a large ϕ-size in data. The analysis is repeated without the cluster ϕ-size requirement and the resulting variation in the measured $\mathrm{dN_{ch}/d}\eta$ is used as a corresponding systematic uncertainty.

6.3 Tracklet analysis overview

Tracklets are defined as combinations of two clusters with a small angular separation in two detector layers. Clusters originating from a particle track associated with the event vertex exhibit small differences in pseudorapidity ($\Delta\eta$), azimuthal angle ($\Delta\phi$), and angular separation (ΔR). These three key quantities characterizing tracklets are defined as follows:

$$\Delta\eta = \eta_{\mathrm{inner}} - \eta_{\mathrm{outer}} \tag{2}$$

$$\Delta\phi = \phi_{\mathrm{inner}} - \phi_{\mathrm{outer}} \tag{3}$$

$$\Delta \mathrm{R} = \sqrt{(\Delta\eta)^2 + (\Delta\phi)^2} \tag{4}$$

Here, $\eta_{\text{inner(outer)}}$ and $\phi_{\text{inner(outer)}}$ represent the pseudorapidity and azimuthal angle of the cluster in the inner (outer) layer of the INTT, calculated with respect to the event vertex. Both vertex reconstruction and tracklet counting utilize the fact that tracklets associated with particles originating from the event vertex produce a coincidence peak in the $\Delta\eta$, $\Delta\phi$, and ΔR distributions. These processes are further detailed in the following subsections.

6.4 Vertex reconstruction using tracklets

The vertex reconstruction for the baseline tracklet analysis consists of two steps. The first step determines the beamspot position, defined as the average vertex position in the transverse plane over multiple events (v_x and v_y), while the second step reconstructs the per-event z-vertex position. The transverse vertex position varies by $\mathcal{O}(100)\,\mu$m, which is several orders of magnitude smaller than relevant length scales such as strip sizes and the radial distance between the INTT ladder and the beamline. In contrast, the z-vertex variation is significantly larger, approximately 5 cm. Event-by-event reconstruction of the z-vertex preserves fluctuations and maintains the sensitivity of the measurement as a function of η.

Two independent methods have been developed for beamspot determination, yielding consistent results.

6.4.1 Beam spot determination - DCA-ϕ fitter

The distance-of-closest-approach (DCA)-ϕ fitter closely follows Ref. [46]. This approach takes advantage of the fact that, for tracks originating from a beamspot at (x_0, y_0), the distance of closest approach to the origin follows a sinusoidal pattern with respect to the ϕ coordinate of the point of closest approach (PCA) to the origin (ϕ_{PCA}):

$$\text{DCA}(\phi_{\text{PCA}}) = R_0 \cos(\phi_{\text{PCA}} - \phi_0)$$

where $R_0 = \sqrt{x_0^2 + y_0^2}$ is the beamspot radial coordinate and $\phi_0 = \arctan\left(\frac{y_0}{x_0}\right)$ is the beamspot ϕ coordinate. Plotting the tracklet DCA and ϕ_{PCA}, as shown in Figure 28, and fitting the resulting sinusoidal ridge allows for the extraction of the two fit parameters R_0 and ϕ_0.

Data and simulation events are divided into sub-samples, and beamspot reconstruction is performed on events in each sub-sample with a cluster multiplicity of $20 < N_{\text{clusters}} < 350$. For each sub-sample, tracklets, constructed by pairs of clusters that pass the cluster ADC cut and with a $\Delta\phi < 0.122$ radians, are selected. Then, the sinusoidal correlation is extracted by profiling the noise-subtracted tracklet DCA and ϕ_{PCA} distribution, constructed by identifying the peak DCA for each slice of ϕ of the point of closest approach, ϕ_{PCA} and removing values less than 99.5% of this peak DCA. A graph is created with the cleaned sinusoidal correlation and fitted with the cosine function to extract R_0 and ϕ_0. Figure 28 and 29 show the tracklet DCA and ϕ_{PCA} distribution in one sub-sample, before the noise removal on the left and after on the right with the graph and cosine function fit, for simulation and data respectively. The final beamspot position is the average of PCA over all sub-samples.

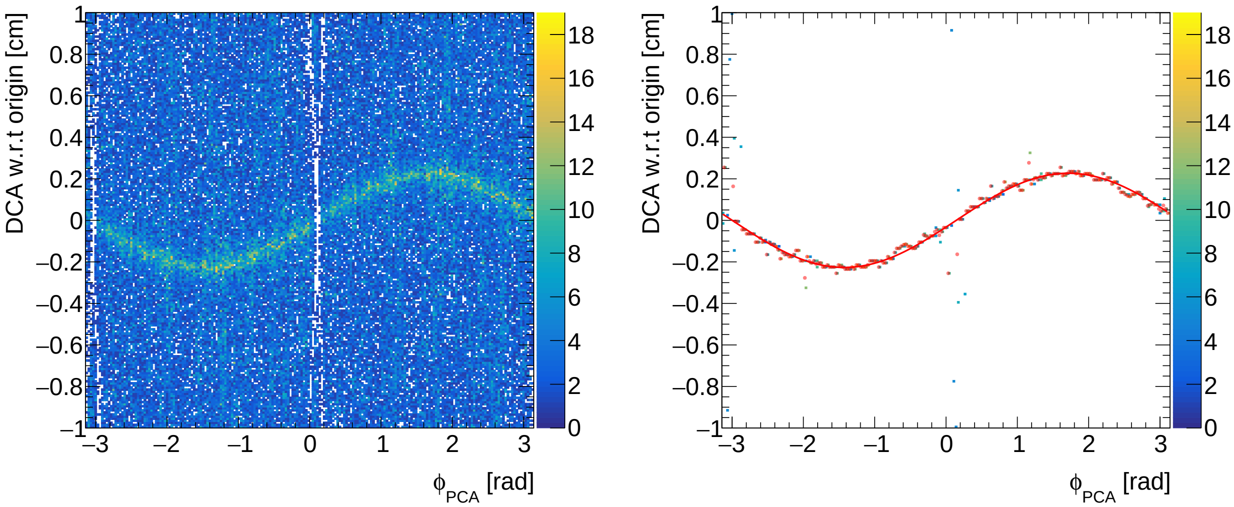

Figure 28: The DCA-ϕ method on simulation events. (Left) without noise removal; (right) after noise removal and the graph with the cleaned sinusoidal correlation and the fit.

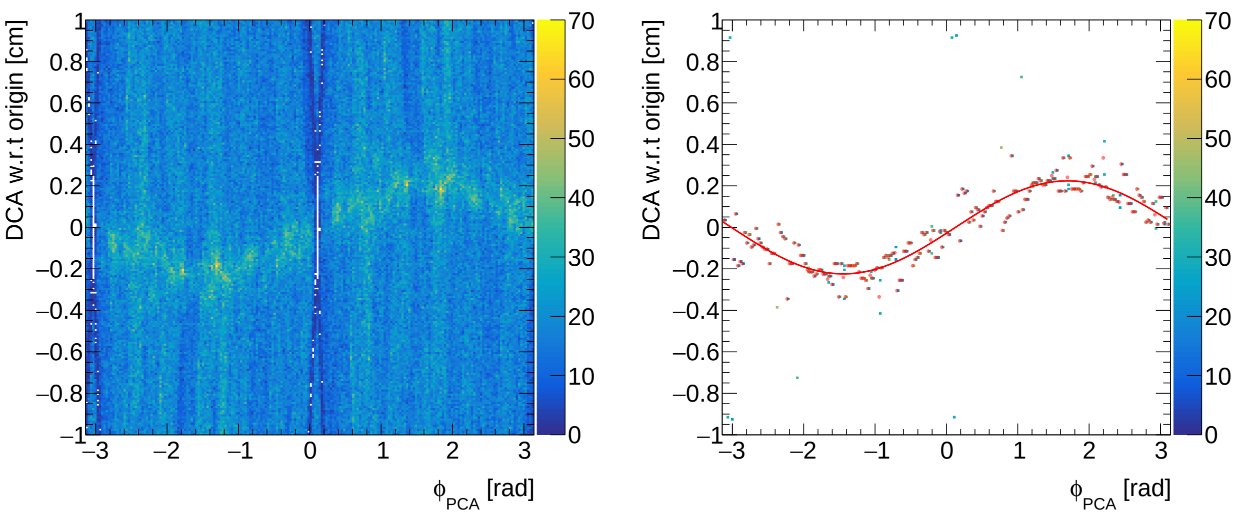

Figure 29: The DCA-ϕ in data. (Left) without noise removal; (right) after noise removal and the graph with the cleaned sinusoidal correlation and the fit.

Figure 30 shows the reconstructed beamspot position as a function of the sub-sample index for simulation events, consistent with the simulated truth vertex position $(v_x^{\mathrm{truth}}, v_y^{\mathrm{truth}}) = (-0.022, 0.223)\,\mathrm{cm}$. Figure 31 shows the beamspot position as a function of the median of INTT BCO of the sub-sample in data and indicates that the beamspot position is stable throughout run 54280.

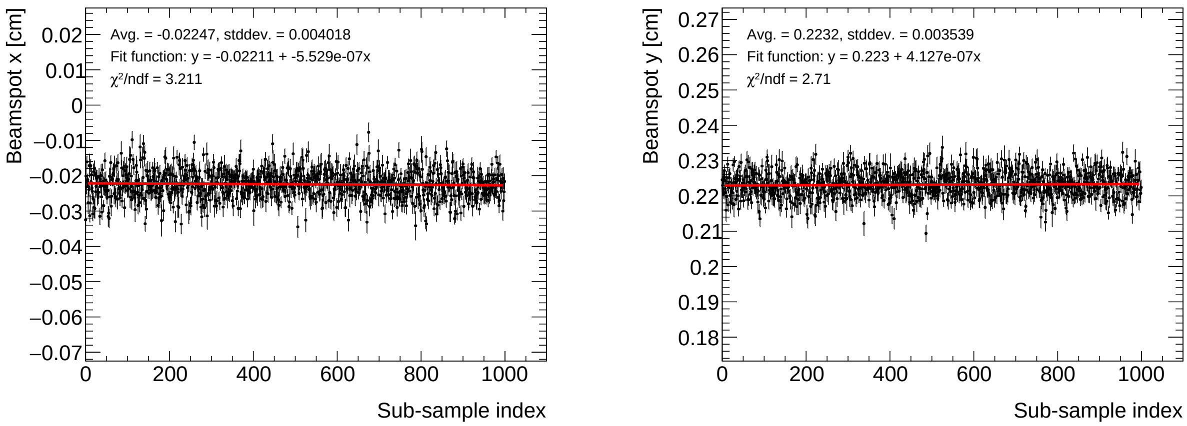

Figure 30: The reconstructed beamspot position as a function of the sub-sample index.

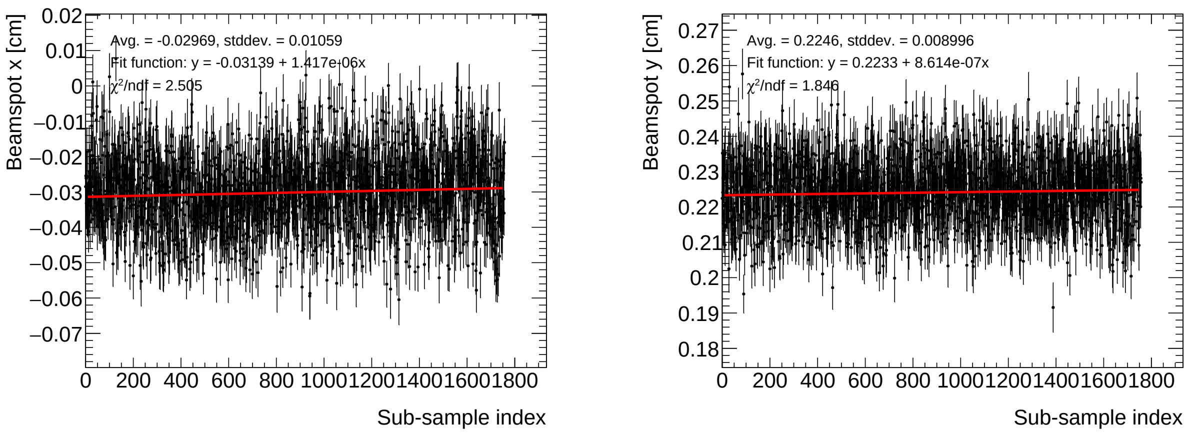

Figure 31: The beamspot position as a function of the median of INTT BCO of the sub-sample.

6.4.2 Beam spot determination - Iterative quadrant search and 2D tracklet fill

This approach involves two methods to reconstruct the averaged beam spot position. The derived final beam spot is used in the analysis of the combinatoric method.

The procedure of iterative quadrant search is detailed as follows and illustrated in Figure 32:

1. Events are divided into sub-samples, each containing 5000 events.

2. To make sure the sufficient number of tracks reconstructed while minimizing the combinatorial background, only the low-multiplicity events with the number of clusters more than 20 and less than 350 are included.

3. Within each event, start with a cluster in the inner layer and loop through the clusters in the outer layer. Cluster pairs with $\Delta\phi < 0.122$ radian are kept. This step is repeated for all events in a sub-sample.

4. A square of size 8×8 mm^2 centered at $(x, y) = (0, 0)$ is defined. The corners of the square are considered as vertex candidates. For each candidate, the DCA and $\Delta\phi$ of the cluster pairs are evaluated. An example 2D histogram of the inner cluster ϕ versus DCA and ϕ versus $\Delta\phi$ for one corner is shown in Figure 33.

5. For each corner, background removal is performed to exclude irrelevant entries. After background removal, the histograms are fitted with a Polynomial-0 function, as shown in Figure 34. A Polynomial-0 function is used because DCA and $\Delta\phi$ show no correlation with ϕ when tested against the true vertex, as demonstrated in Figure 35. This process is repeated for all four corners of the square.

6. The quadrant containing the corner with the smallest fit errors is selected. Steps 4 and 5 are repeated using a new square formed within the chosen quadrant, with its dimensions halved relative to the previous square.

7. The process is repeated until the size of the square reaches $30 \times 30\,\mu\text{m}^2$, comparable to the spatial resolution of INTT strips. The v_x and v_y for the sub-sample are calculated as the average positions of the corners and the center of the square from the final iteration.

8. The final values of v_x and v_y are obtained by averaging the v_x and v_y values across all sub-samples.

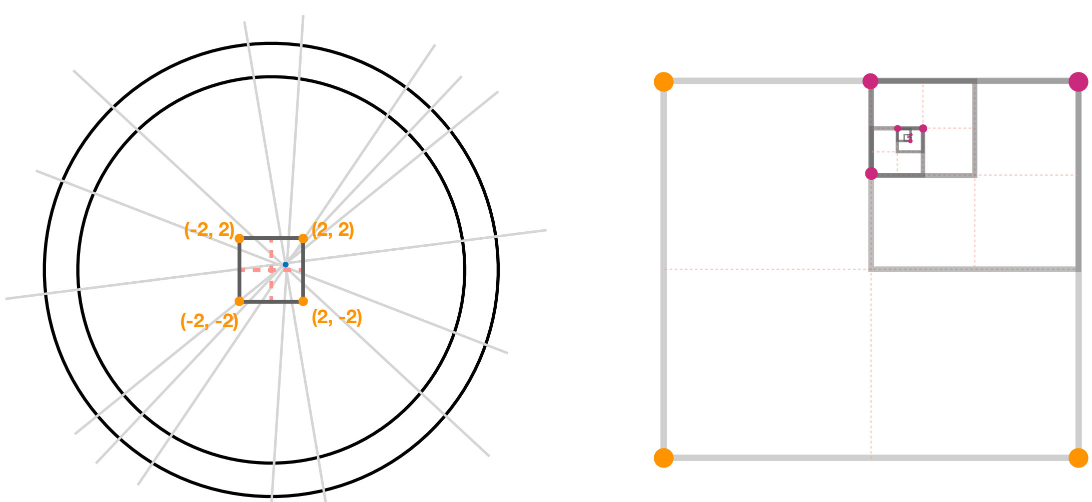

Figure 32: Iterative quadrant search

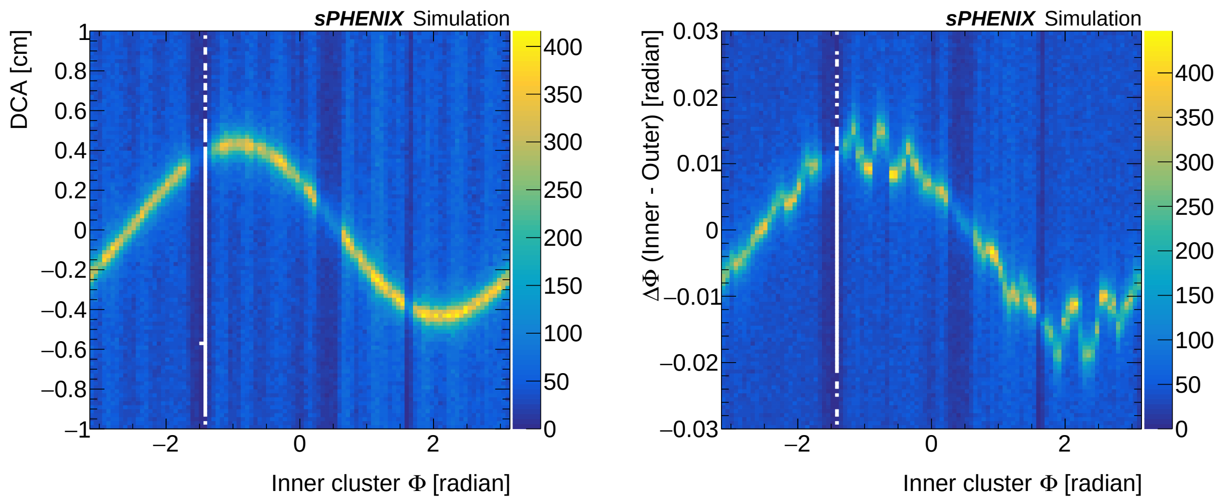

Figure 33: DCA (left) and cluster $\Delta\phi$ (right) as a function of inner cluster phi.

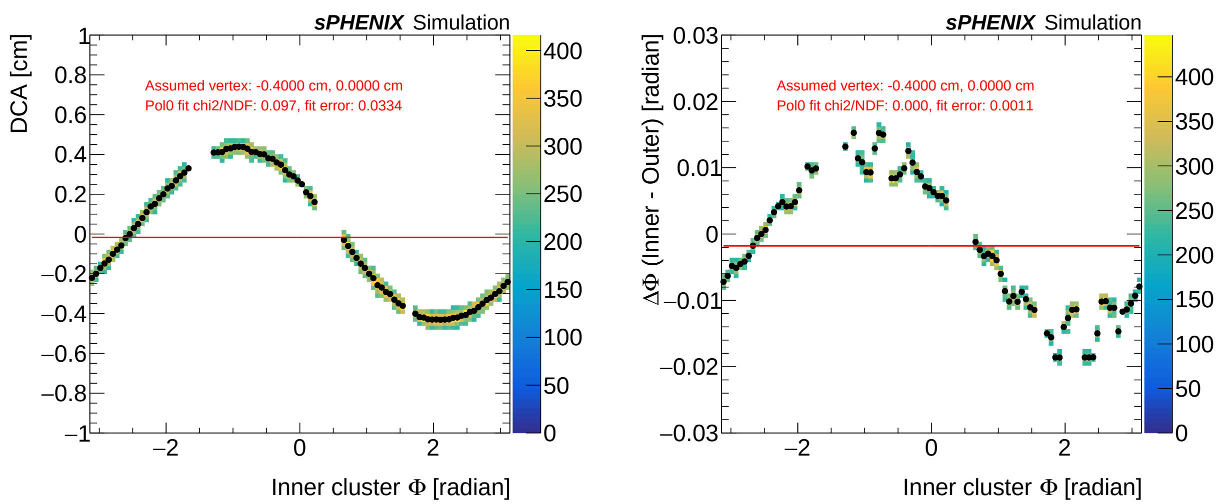

Figure 34: DCA (left) and cluster $\Delta\phi$ (right) as a function of inner cluster phi, post background removal.

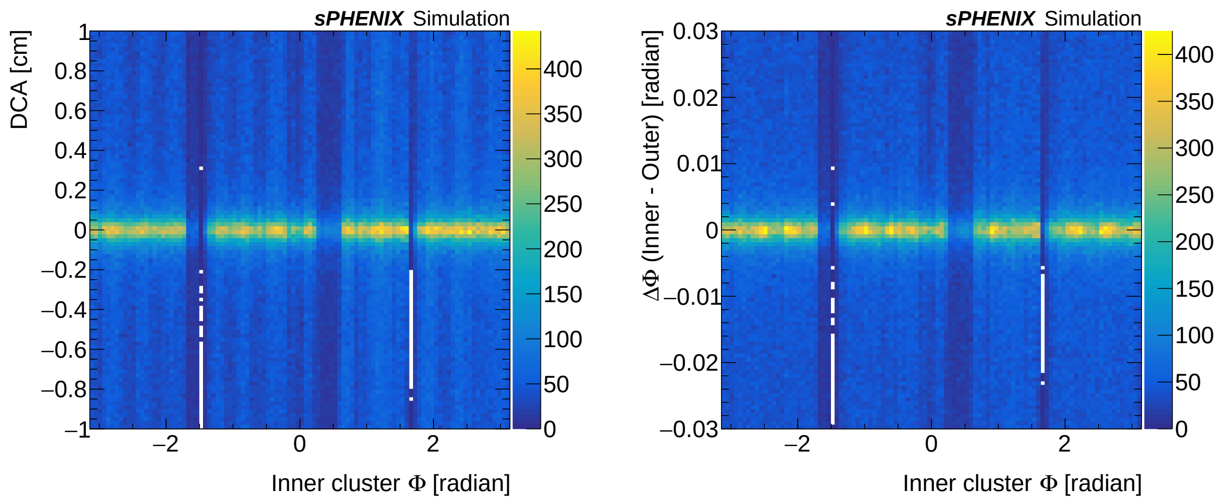

Figure 35: DCA (left) and cluster $\Delta\phi$ (right) as a function of inner cluster phi where the true vertex is taken as the tested vertex.

A closure test is performed in simulation, generated by `HIJING`, with the truth vertex position set at $(v_x, v_y) = (-0.02213\,\text{cm}, 0.2230\,\text{cm})$. A vertex of $(v_x, v_y) = (-0.02159\,\text{cm}, 0.2237\,\text{cm})$ is obtained from the method, in good agreement with the assigned position.

The 2D tracklet fill method complements the iterative quadrant search. The procedures are described as follows:

1. Define the dimensions and center of a finely-binned 2D histogram. The central point is determined by the vertex XY position acquired through Approach 2, which is (-0.02159 cm, 0.2237 cm) in the validation test. In the standard configuration, this corresponds to a $0.25\,\text{cm} \times 0.25\,\text{cm}$ square with bin sizes of $50\mu\text{m} \times 50\mu\text{m}$.

2. Populate the trajectories of the combinations outlined in step 1 of Approach 2 into the 2D histogram. The example is shown in Figure 36.

3. Remove the background of the histogram.

4. The v_x and v_y are obtained by taking the averages on both axes of the histogram, as shown in Figure 36. The vertex position (-0.02188 cm, 0.2232 cm) is obtained.

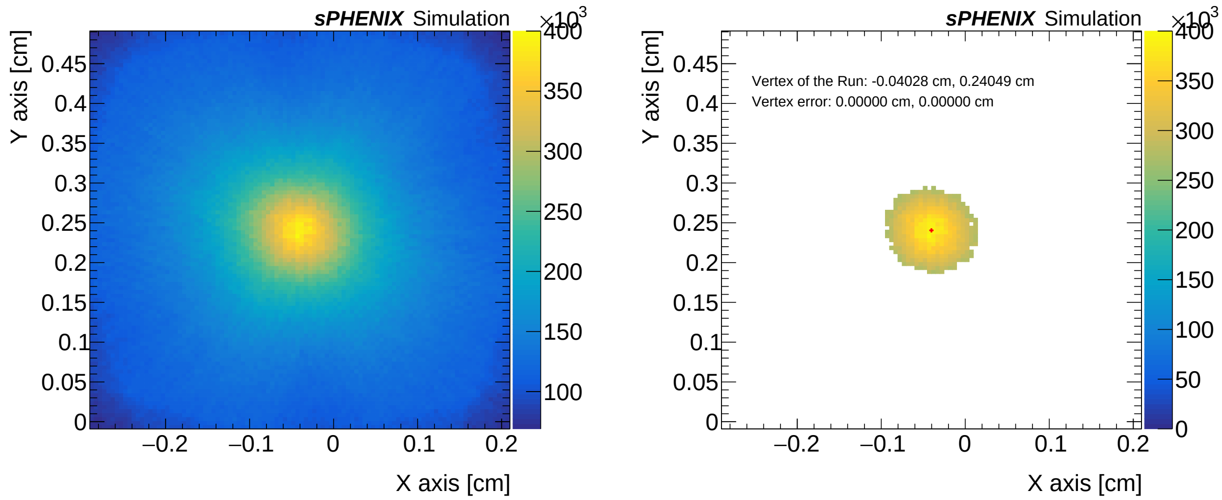

Figure 36: The 2D histogram filled by the trajectories of combinations before the background removal (left) and after background removal (right). The red full cross mark represents the reconstructed vertex in the transverse plane.

Figure 37 shows the full closure test of the methods in the simulation. The two methods agree in all the sub-samples. And the stability of the vertex X and Y positions in the data is evaluated. Figure 38 shows the average vertex X and Y positions calculated every five thousand events as a function of the averaged event ID in data, measured by the two approaches. The discrepancy between the measured vertices from the two approaches can be attributed to detector misalignment, as discussed in Section 8.1.1. The observed consistency in the vertex positions throughout the run indicates stable performance, supporting the adequacy of reconstructing the tracklets based on the average beam spot. In data, the final beam spot $(v_x, v_y) = (-0.02207\,\mathrm{cm}, 0.2230\,\mathrm{cm})$ was obtained and used in the analysis of the combinatoric method.

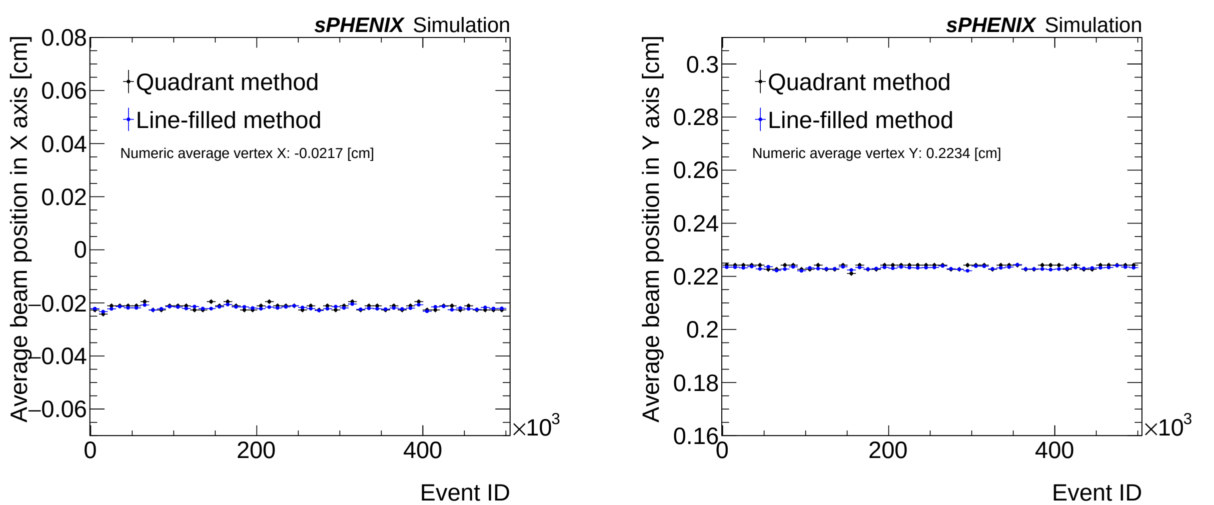

Figure 37: In simulation, vertex positions averaged over every five thousand events as a function of averaged event index for X position (left) and Y position (right).

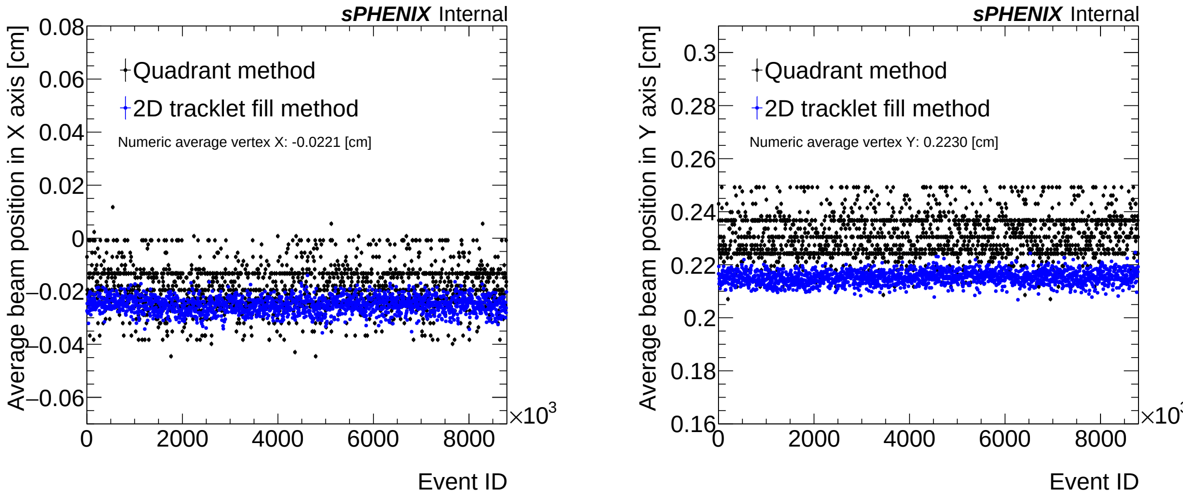

Figure 38: In data, vertex positions averaged over every five thousand events as a function of averaged event index for X position (left) and Y position (right).

6.4.3 Per-event z-vertex reconstruction

The lengths of the INTT strips, either 1.6 or 2.0 cm, inherently limit the precision of the z-vertex position. To address this, two reconstruction methods have been developed, both leveraging the fact that a single pair of inner and outer clusters defines only a range within which the vertex could potentially lie.

The first method, adopted in the analysis of the closest-match method, is described step-by-step below:

1. The cluster ϕ is calculated and updated relative to the beamspot coordinates v_x and v_y.

2. For each cluster in the inner layer, loop through the clusters in the outer layer. Cluster pairs that satisfy $\Delta\phi \leq \Delta\phi_{\text{cut}}$ and DCA $\leq$ DCA$_{\text{cut}}$ are retained, where DCA (Distance of Closest Approach) is defined as:

$$\mathrm{DCA} = \frac{|m \cdot v_x - v_y + b|}{\sqrt{m^2+1}} \tag{5}$$

$$m = \frac{y_{\text{outer}} - y_{\text{inner}}}{x_{\text{outer}} - x_{\text{inner}}} \tag{6}$$

$$b = y_{\text{inner}} - m \cdot x_{\text{inner}} \tag{7}$$

$$\tag{8}$$

   Here, $x_{\text{outer(inner)}}$ and $y_{\text{outer(inner)}}$ are the X and Y coordinates of the clusters in the outer (inner) layer. Repeat this process for all clusters in the inner layer.

3. Cluster pairs that pass the $\Delta\phi$ and DCA requirements form z-vertex candidates. Each candidate defines a range bounded by two edges, v_z^{edge1} and v_z^{edge2}, which are calculated

by linearly extrapolating from the paired clusters to the beamspot (v_x, v_y). These edges are defined as:

$$v_z^{\text{edge1}} = z_{\text{inner}}^{\text{edge1}} - \rho_{\text{inner}} \cdot \frac{z_{\text{outer}}^{\text{edge2}} - z_{\text{inner}}^{\text{edge1}}}{\rho_{\text{outer}} - \rho_{\text{inner}}} \tag{9}$$

$$v_z^{\text{edge2}} = z_{\text{inner}}^{\text{edge2}} - \rho_{\text{inner}} \cdot \frac{z_{\text{outer}}^{\text{edge1}} - z_{\text{inner}}^{\text{edge2}}}{\rho_{\text{outer}} - \rho_{\text{inner}}} \tag{10}$$

$$\rho_{\text{inner}} = \sqrt{(x_{\text{inner}} - v_x)^2 + (y_{\text{inner}} - v_y)^2} \tag{11}$$

$$\rho_{\text{outer}} = \sqrt{(x_{\text{outer}} - v_x)^2 + (y_{\text{outer}} - v_y)^2}. \tag{12}$$

4. The z-vertex candidate range is divided into fine segments, which are filled into a one-dimensional histogram. Examples of these histograms are shown in Figure 39.

5. The histogram is fitted with a combination of a Gaussian and a constant offset. The mean value of the Gaussian fit is taken as the reconstructed z-vertex position, vtx_z.

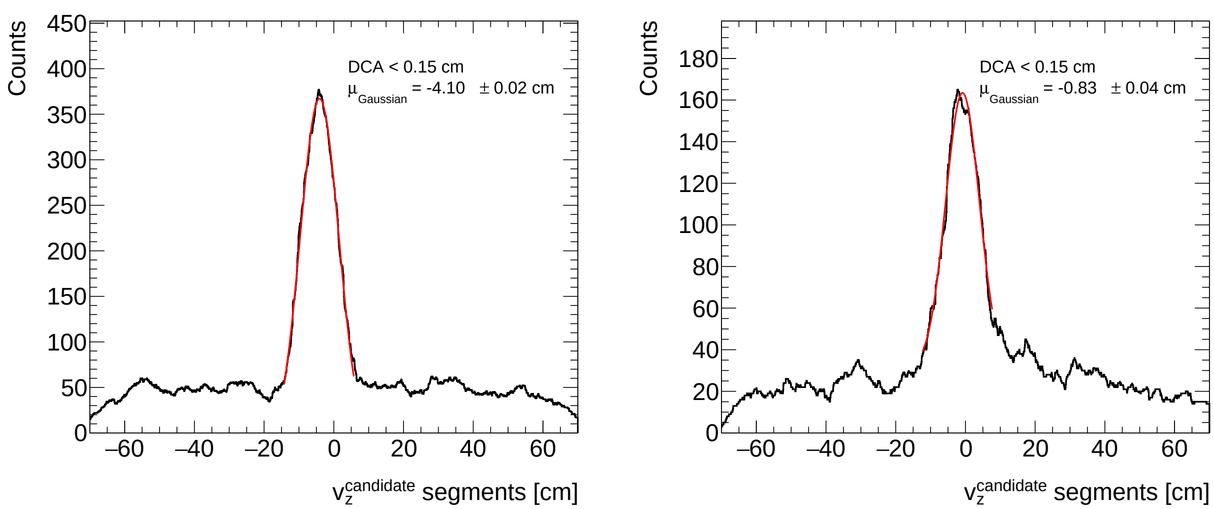

Figure 39: The histogram of segments in simulation (left) and in data (right).

The parameters $\Delta\phi_{\text{cut}}$ and DCA_{cut} are optimized by scanning across ranges of $\Delta\phi$ and DCA to achieve the best vertex reconstruction resolution. Figure 112 in Appendix F illustrates the vertex reconstruction resolution as a function of $\Delta\phi_{\text{cut}}$ and DCA_{cut}. The final selection criteria are determined to be $\Delta\phi_{\text{cut}} = 0.000523$ radians and $\text{DCA}_{\text{cut}} = 0.15\,\text{cm}$ for the analysis.

To quantify the vertex reconstruction bias and resolution, events are subdivided by centrality class. For each centrality interval, the difference between the reconstructed event vertex and the truth event vertex is fitted with a Gaussian distribution. The Gaussian fit's mean value quantifies the reconstruction bias, while the width represents the resolution. Figure 40 shows the bias and resolution of the vertex reconstruction as functions of centrality.

The resolution ranges from 0.188 cm for the most central events to 1.53 cm for the most peripheral events, while the bias remains below 0.02 cm across all centrality classes. Gaussian fits for all centrality classes are shown in Figure 115 in Appendix F.

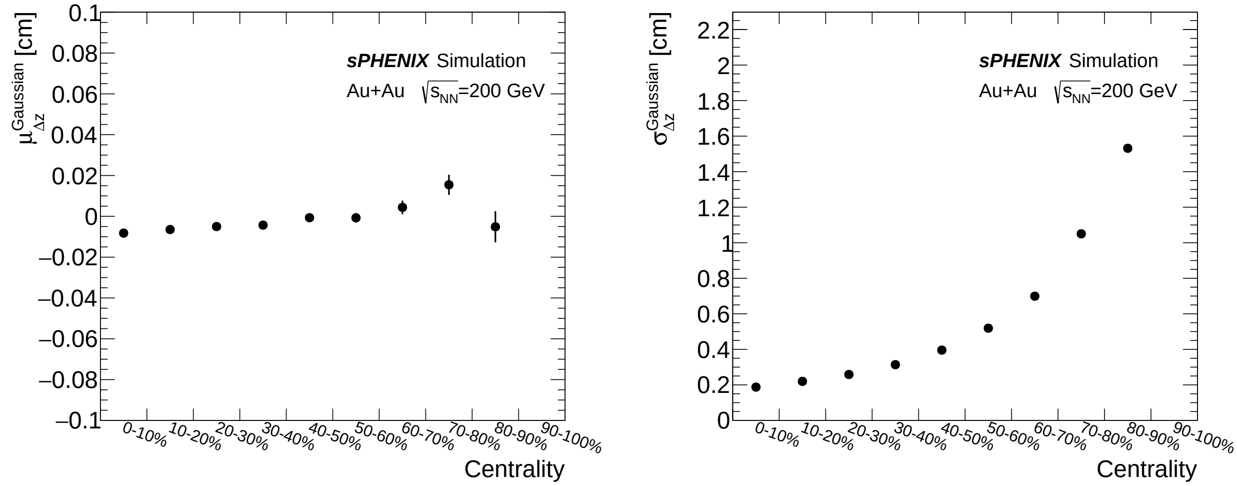

Figure 40: (Left) Z-vertex reconstruction bias as a function of centrality; (Right) z-vertex reconstruction resolution as a function of centrality.

The vertex reconstruction efficiency, $\epsilon_{\text{Reco. vertex}}$, defined in Equation 13, is shown as a function of centrality interval and $\text{vtx}_z^{\text{Truth}}$ in Figure 41, with a loose quality cut of $|\Delta(\text{vtx}_z^{\text{Reco}}, \text{vtx}_z^{\text{Truth}})| \leq 120\,\text{cm}$. This cut value is determined in accordance with the MBD Z-vertex criteria in the Min. Bias definition.

$$\epsilon_{\text{Reco. vertex}} = \frac{\text{Number of events with 1 reco. vertex with } |\Delta(\text{vtx}_z^{\text{Reco}}, \text{vtx}_z^{\text{Truth}})| \leq 120\,\text{cm}}{\text{Number of events with 1 truth vertex}} \tag{13}$$

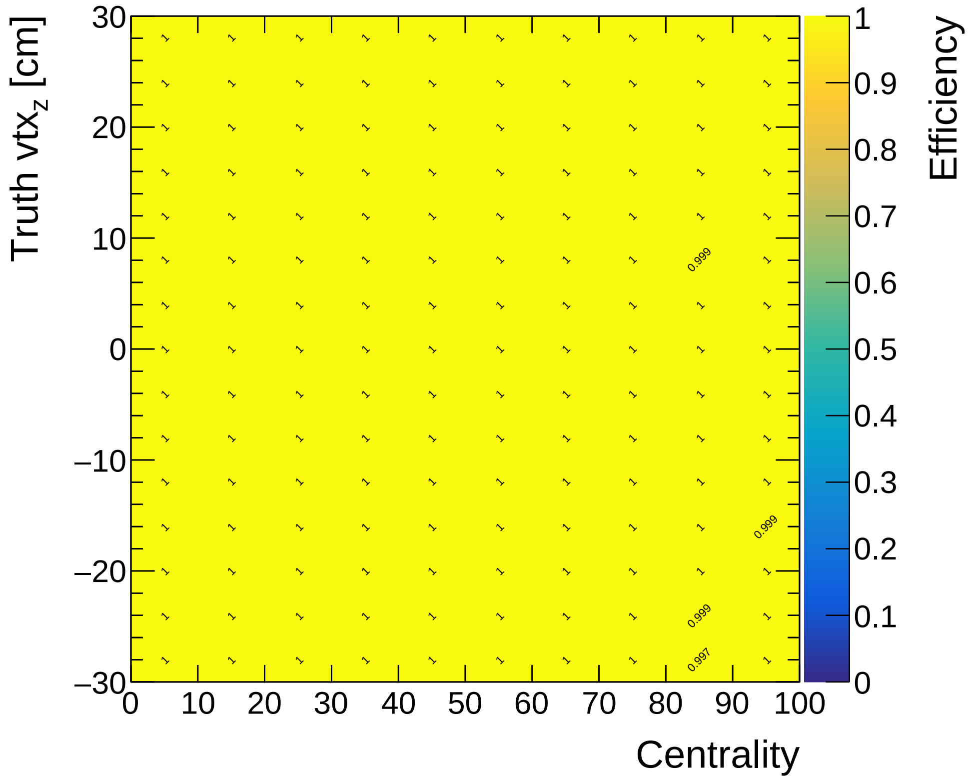

Figure 41: The vertex reconstruction efficiency as a function of centrality and vtx$_z^{\mathrm{Truth}}$.

Figure 15 in Section 4.4 presents the reconstructed z-vertex position in both data and simulation. The reconstructed vertex distributions for centrality intervals up to 70% are consistent, as shown in Figure 42.

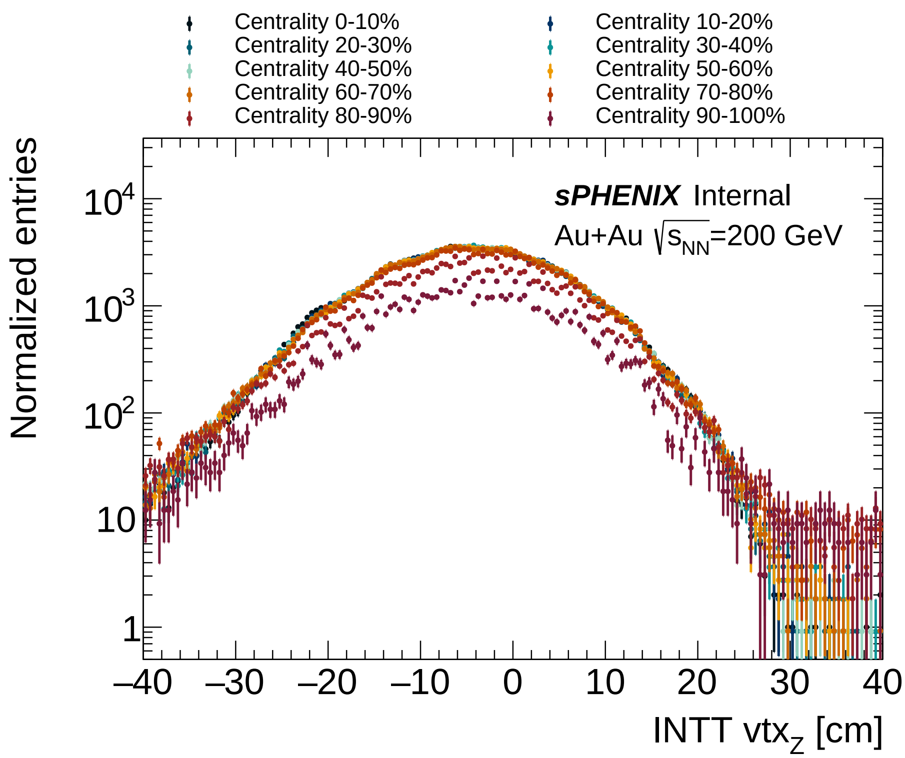

Figure 42: Reconstructed z-vertex position in different centrality intervals in data.

The reconstructed z-vertex distribution in both data and the simulation sample is fitted with a double-sided Crystal Ball (DBCB) function, as defined in Equation 14, and shown in Figure 43. In simulation, the fit results, particularly the mean and sigma values, are consistent, within uncertainties, with the initial vertex position settings. This confirms that the vertex reconstruction does not introduce a systematic bias in the vertex position.

The DBCB function is defined as:

$$\mathrm{DBCB}(z) = \begin{cases} e^{-\frac{1}{2}\cdot(\frac{z-\mu}{\sigma})^2} & , \ -a_L < \frac{z-\mu}{\sigma} < a_H \\ f \cdot (\frac{n_L}{a_L})^{n_L} \cdot e^{-\frac{a_L^2}{2}} \cdot \left[\frac{n_L}{a_L} - a_L - (\frac{z-\mu}{\sigma})\right]^{-n_L} + (1-f)\cdot e^{-\frac{1}{2}\cdot(\frac{z-\mu}{\sigma})^2} & , \ \frac{z-\mu}{\sigma} \le -a_L \\ (1-f)\cdot(\frac{n_H}{a_H})^{n_H} \cdot e^{-\frac{a_H^2}{2}} \cdot \left[\frac{n_H}{a_H} - a_H + (\frac{z-\mu}{\sigma})\right]^{-n_H} + f\cdot e^{-\frac{1}{2}\cdot(\frac{z-\mu}{\sigma})^2} & , \ \frac{z-\mu}{\sigma} \ge a_H \end{cases} \tag{14}$$

where μ is the peak position of the Gaussian component, a_L and a_H define the transitions to the power-law behavior on the low-z and high-z sides, and n_L and n_H are the exponents of the power-law tails.

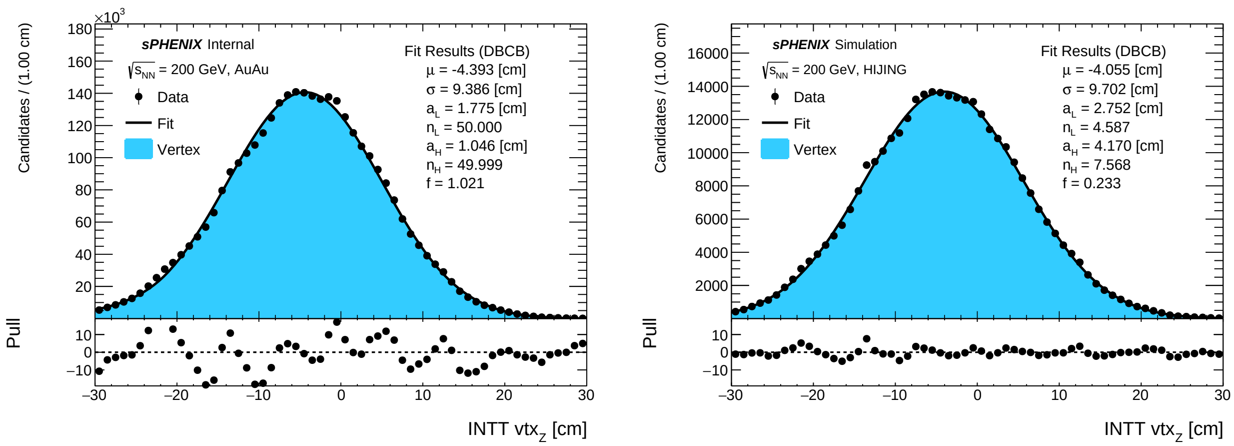

Figure 43: Double-side Crystal Ball fit to the reconstructed vertex in data (left) and simulation (right).

The INTT tracklet z-vertex reconstruction is compared to the MBD z-vertex calculation, as shown in Figure 44, using events from the 0–70% centrality intervals. The strong correlation indicates an agreement between the two independent measurements.

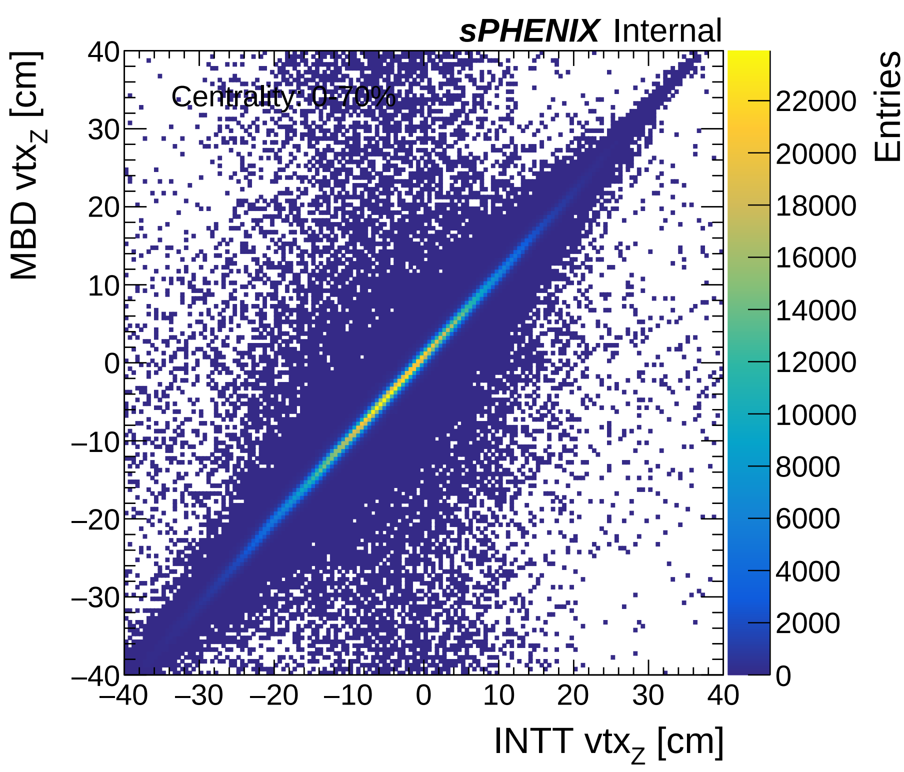

Figure 44: A comparison between the INTT tracklet z-vertex reconstruction and the MBD vertex determination.

The second approach, detailed in a separated internal note [47] and applied in the analysis of the combinatoric method, constructs vertex candidates as trapezoidal shapes by assuming a uniform distribution of particle hit positions along the Z-axis of a strip. Key quality checks are presented in Appendix E.1.

6.5 Tracklet reconstruction

Two approaches are developed for the tracklet reconstruction.

6.5.1 The combinatoric method

In this approach, one step prior to the tracklet reconstruction, the INTT column uniformity is checked. The procedures are described as follows:

1. INTT, the two-layer barrel strip tracker, can be considered as 26 chip rings, as illustrated in Figure 45. There are 56 columns in one chip ring.

2. In data and simulation, and in one chip ring, the number of clusters of each column corrected for strip length and its ϕ acceptance, is accumulated, and normalized by the column with highest count, as shown in Figure 46.

3. The corrected multiplicity of each column in data is divided by that of in simulation afterwards, as shown in the right plot of Figure 46. Most of the columns are with the ratios around 1 while a few of columns is with the ratio away from 1, which indicates the disagreement in the multiplicity uniformity between data and simulation. Note that the normalization is performed in each chip ring, and the ratio is calculated column by column. Therefore, this method is generator model and vertex Z distribution independent. The only assumption made is the uniformity of the particle emission along the azimuthal angle.

4. The steps 2 and 3 are repeated for all the chip rings, and the result is shown in Figure 47. The distribution peaked at one indicating a good column uniformity.

5. The columns with the ratios outside the range of 0.8 to 1.2 are discarded in both data and simulation. The map of the columns used in the following analysis is shown in Figure 48.

The column uniformity check serves as a direct tool to confirm the consistency of the map applied in both data and MC, and evaluate the performance of the data-driven bad channel identifier. The left plot of Figure 47 shows that the multiplicity ratios of all the columns are between 0.8 to 1.2, ensuring that the bad channels are all identified and they are masked in the analysis in both data and simulation. There is no additional column masked by this check.

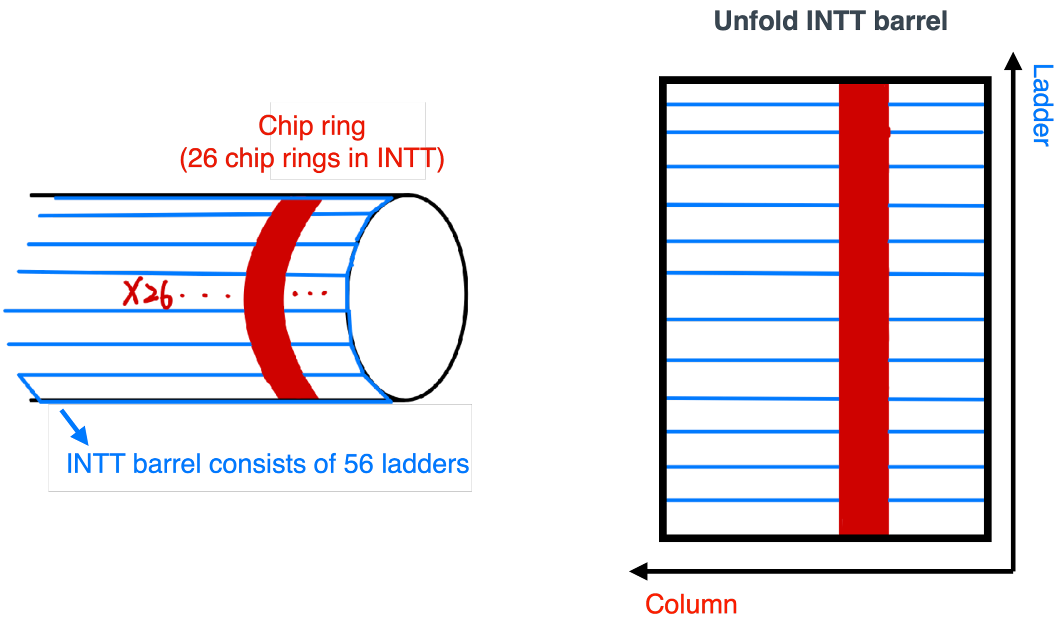

Figure 45: Cartoon showing the structure of INTT column ring.

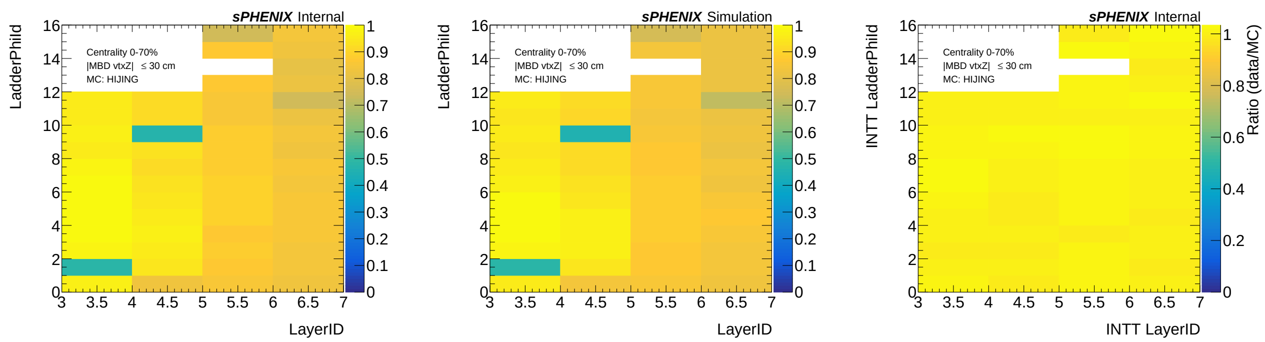

Figure 46: The corrected and normalized multiplicity of all 56 columns in one INTT chip ring in data (left) and simulation (middle). Right: The ratio between data and simulation.

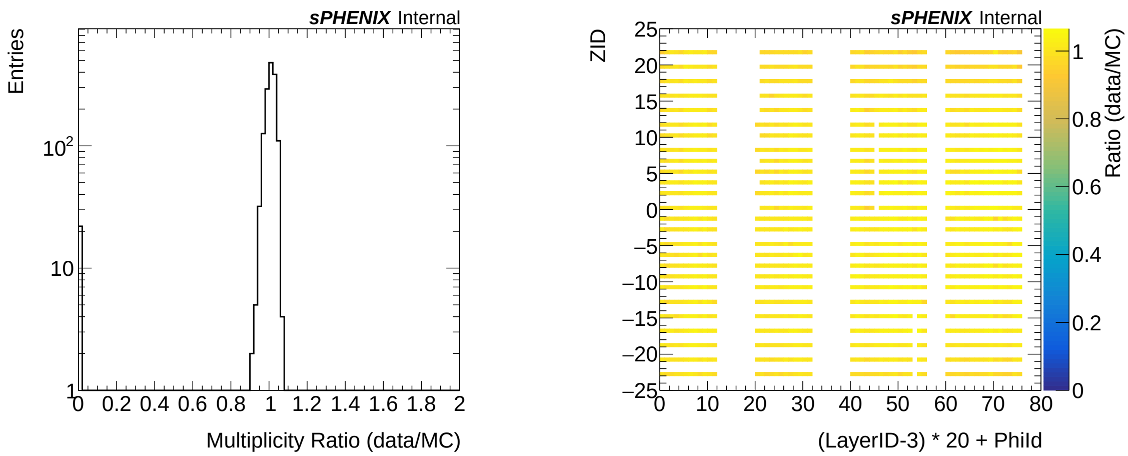

Figure 47: The ratio of the corrected multiplicity between data and simulation of each of all the 1456 INTT columns presented in 1D (left) and 2D (right).

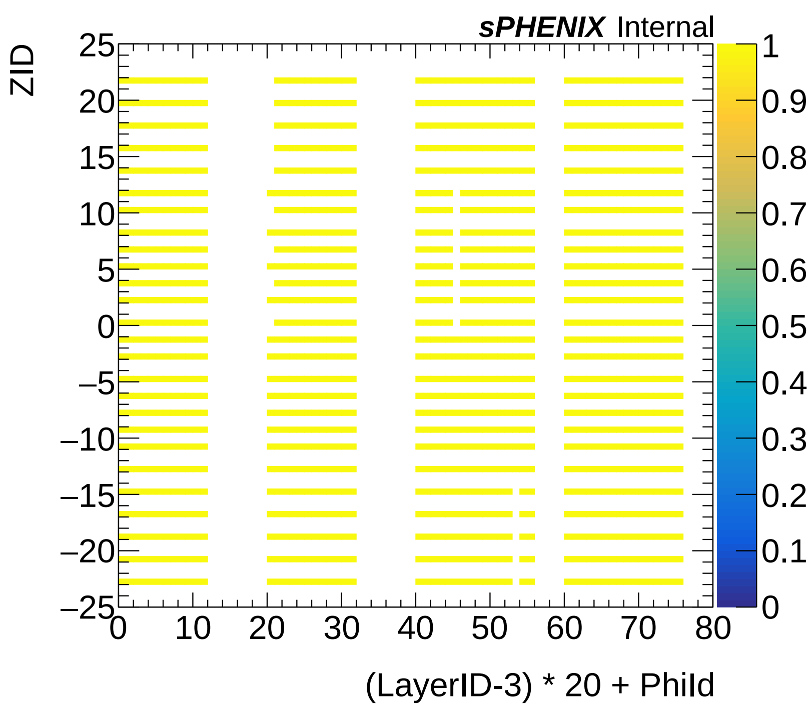

Figure 48: The column map used in the following analysis.

The combinatoric method allows an inner cluster to be paired with multiple outer pairs. The procedure are detailed as follows:

1. The cluster η and ϕ are updated based on the reconstructed event vertex.

2. In an event, all possible tracklets are formed by pairing one cluster in the inner barrel and one cluster in the outer barrel.

3. The extrapolated possible vertex Z range of a cluster pair not able to link to the reconstructed v_z is discarded, as demonstrated in Figure 49. Such requirement is equivalent to a cut $|\Delta\eta| \leq 0.25$, as shown in the right plot of Figure 49. The η of the cluster pair satisfied the requirement is given by the average of the two cluster η.

4. Fill the $\Delta\phi$ of the pair into the corresponding one-dimensional $\Delta\phi$ histogram according to its η, and centrality and reconstructed v_z of the event.

5. Repeat the steps 3 and 4 for all the combinations and step 2 for all the events.

6. After the loop, stack over the $\Delta\phi$ distributions for each tracklet η bin according to the selected region, as the example shown in left plot of Figure 50. The statistic can therefore be increased.

7. The $\Delta\phi$ distribution is composed of two components, the entries of the signal and the contribution of combinatorial background due to incorrect pair formations which results in a bulk underneath the signal. The combinatorial background is estimated by rotating the inner-barrel clusters by π in ϕ angle, as shown in the right plot of Figure 50. The signal is extracted by the subtraction of the two distributions, as shown in Figure 51.

8. The number of tracklets of a given η region is determined by the entries of the subtracted $\Delta\phi$ distribution within the region of 0.021 radians for baseline.

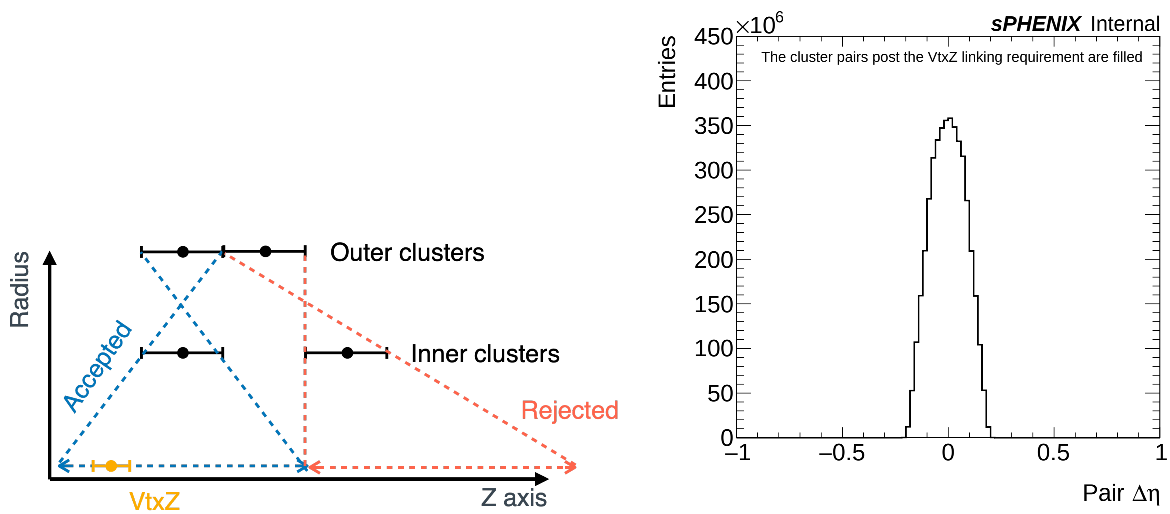

Figure 49: Left: Demonstrating the requirement of cluster pair linking to the reconstructed vertex Z. Right: The $\Delta\eta$ distribution of the cluster pairs satisfied the vertex Z linking requirement.

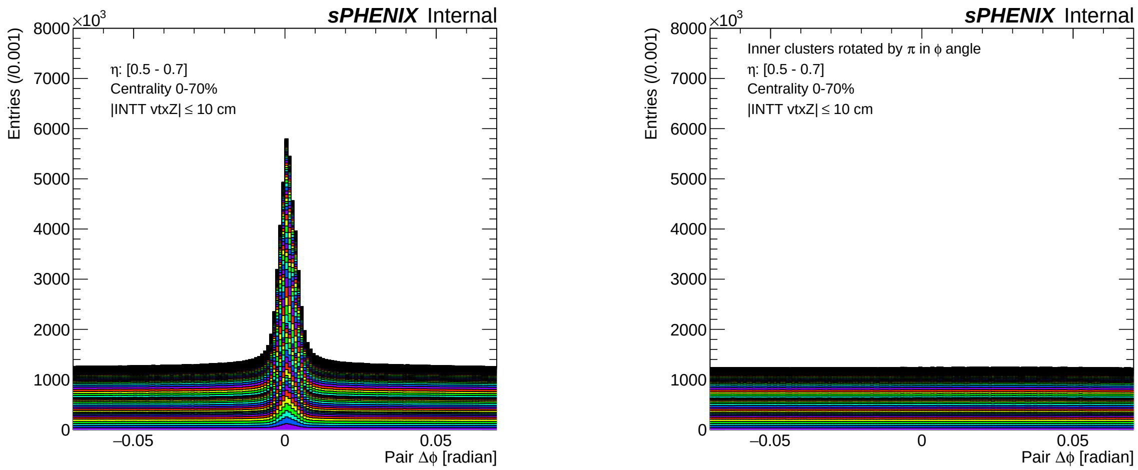

Figure 50: Left: The stacked $\Delta\phi$ distribution in the ranges of $|v_z| \leq 10$ cm, tracklet η 0.5 to 0.7, and centrality 0 to 70 %. Right: The same stacked distribution while having the inner clusters rotated by π in ϕ angle.

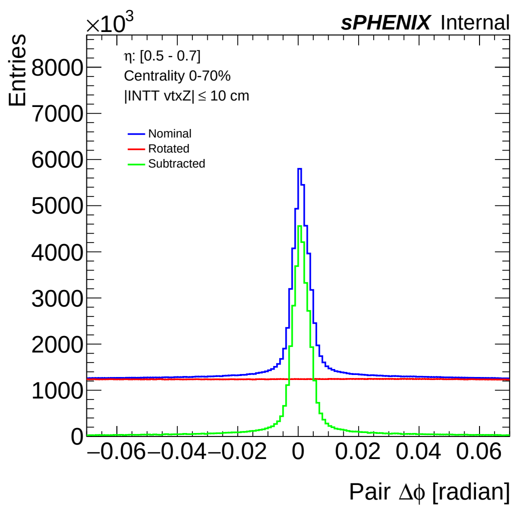

Figure 51: The $\Delta\phi$ distributions of a given region.

The distribution of average number of reconstructed tracklets per event is shown in Figure 52.

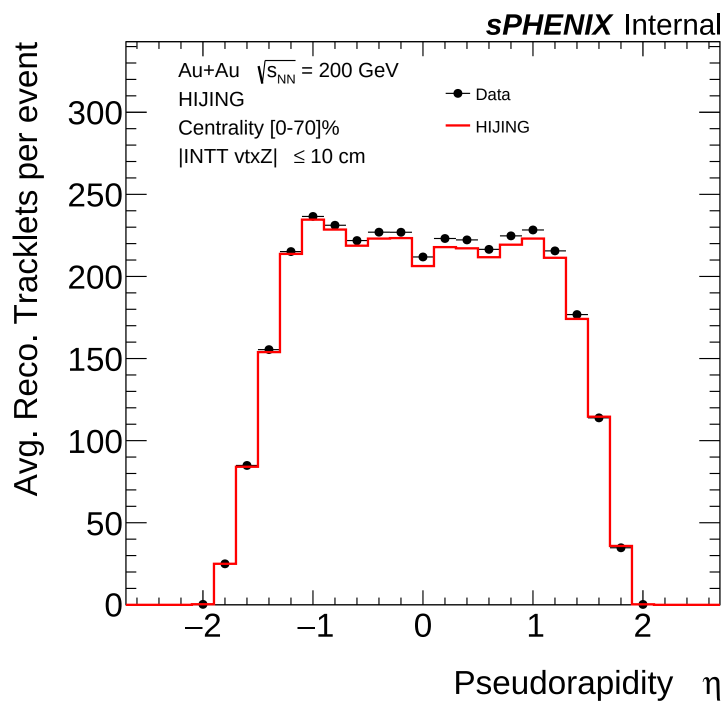

Figure 52: The average number of reconstructed tracklets per event as a function of η.

6.5.2 The closest-match method

This method involves a 3-step process:

1. The cluster η and ϕ are updated based on the reconstructed event vertex (This step is identical as Step 1 in the PHOBOS approach of tracklet reconstruction).

2. In an event, tracklets are formed by pairing one cluster in the inner barrel and one cluster in the outer barrel. Combinations with ΔR (as defined in Eq. 4) less than 0.5 are kept and sorted by ΔR (Note, while the initial pairing step resembles Step 2 in the combinatoric method, the subsequent steps differ significantly).

3. If multiple matches exist for a cluster, the pair with the smallest ΔR is selected to form the final set of reconstructed tracklets.

Figure 53 and 54 show the number of reconstructed tracklets, tracklet ϕ, tracklet η, tracklet $\Delta\phi$, tracklet $\Delta\eta$, and tracklet ΔR.

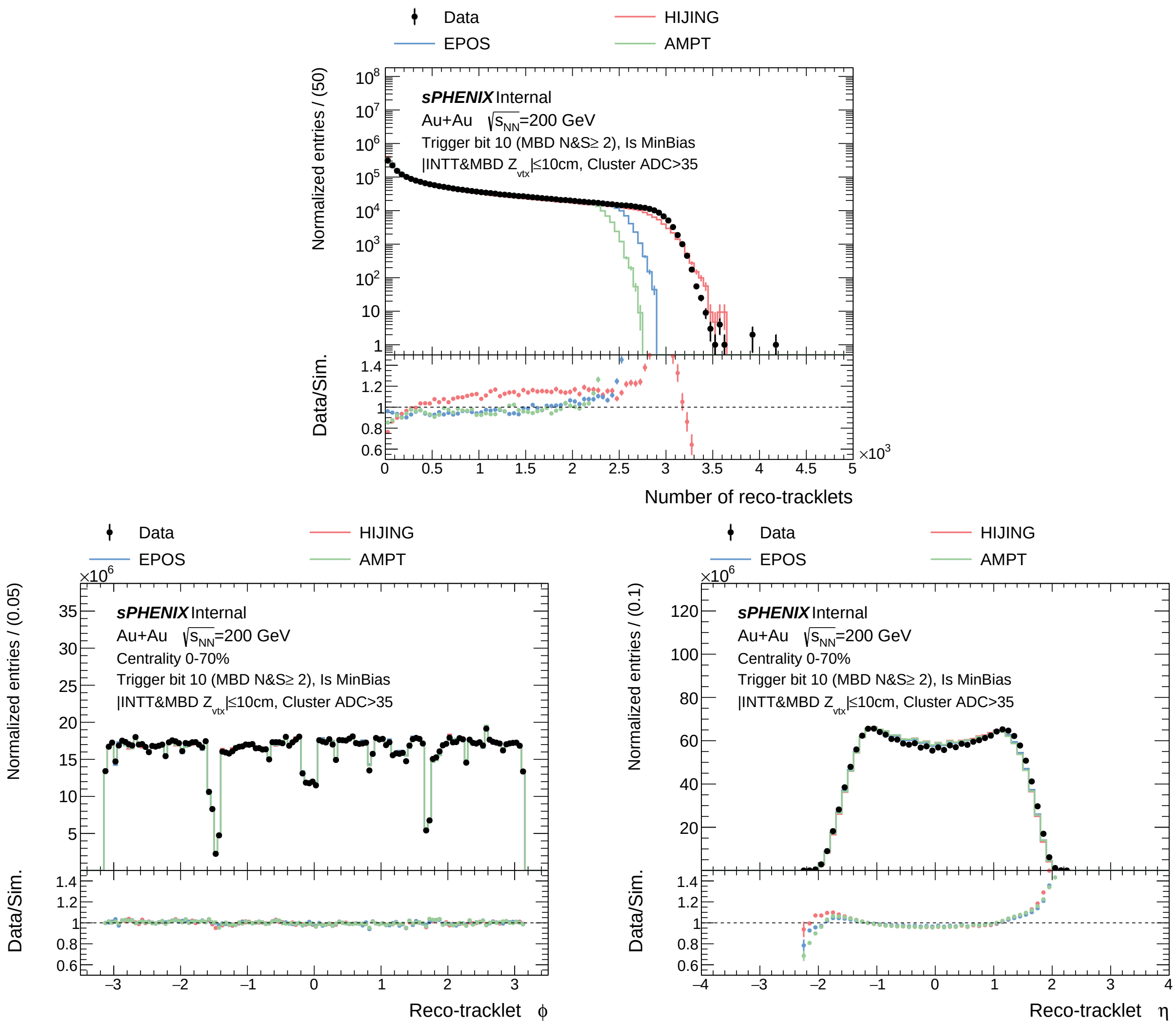

Figure 53: The number of reconstructed tracklets (top), tracklet ϕ (bottom left), tracklet η (bottom right).

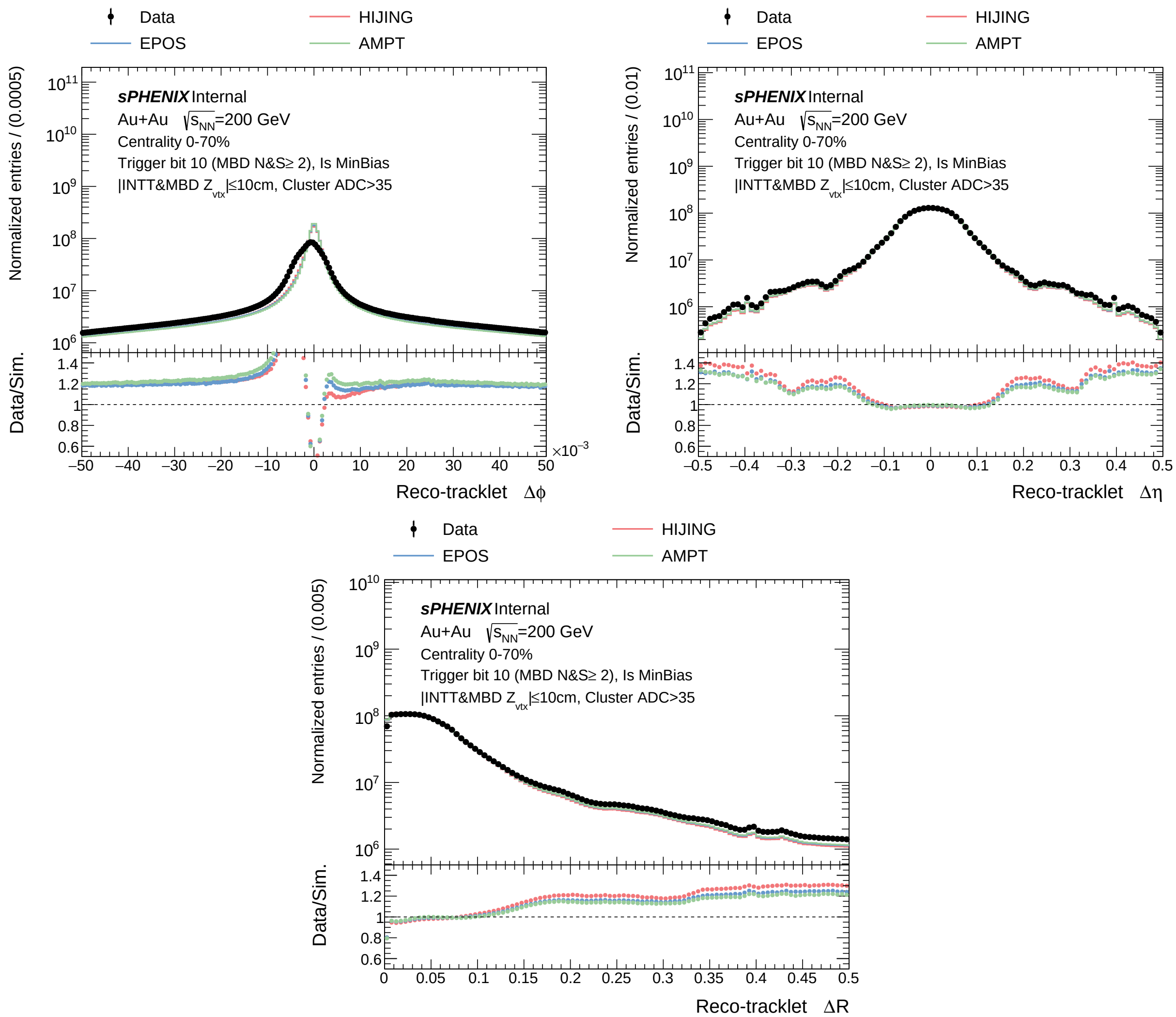

Figure 54: The tracklet $\Delta\phi$ (top left), tracklet $\Delta\eta$ (top right), and tracklet ΔR (bottom).

Figure 55 compares the ϕ-sizes of constituent clusters in tracklets, where the number of tracklets in which both constituent clusters have a ϕ-size of 43 or 46, as well as those where either constituent cluster has a ϕ-size of 43 or 46 are listed in Table 6. Despite the unexpectedly large number of clusters with ϕ-sizes of 43 and 46, the results indicate that only a negligible fraction of tracklets are formed by these large ϕ-size clusters.

Table 6: The number of tracklets in which both constituent clusters have a ϕ-size of 43 or 46, as well as those where either constituent cluster has a ϕ-size of 43 or 46.

Category	Count	Fraction (%)
Total number of tracklets	2.04×10^{9}	–
Number of tracklets in which both constituent clusters have a ϕ-size of 43 or 46	190	9.32×10^{-6}
Number of tracklets in which either constituent cluster has a ϕ-size of 43 or 46	1.70×10^{5}	8.35×10^{-3}

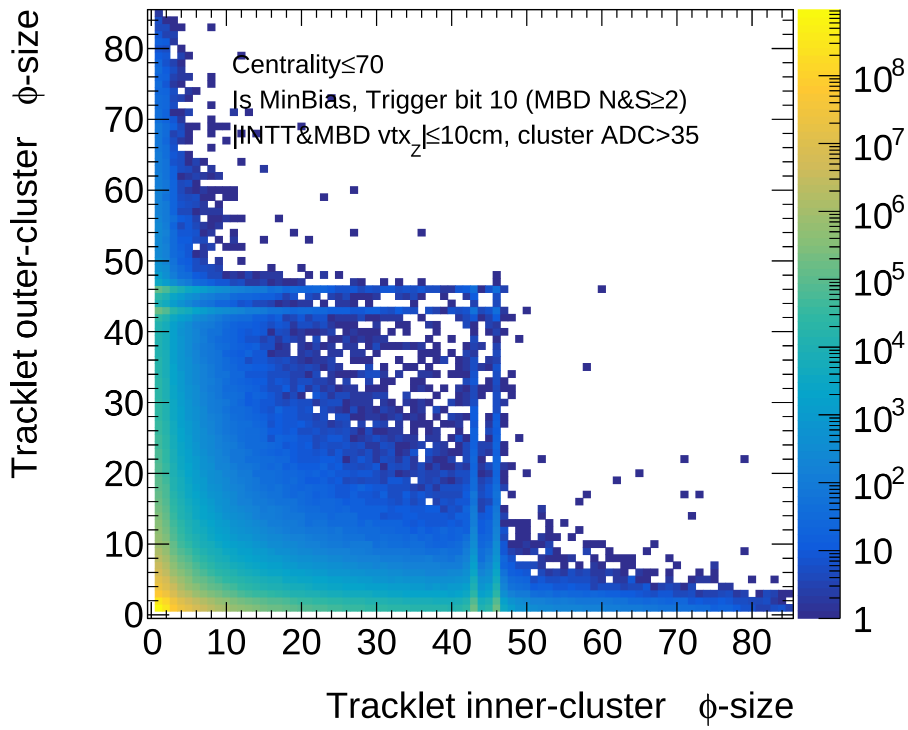

Figure 55: The ϕ-size of constituent clusters on tracklets.

7 Correction factors

Correction factors are applied to correct the reconstructed tracklet spectra to the prompt charged hadron definition (Section 4.3), properly accounting for acceptance and efficiency. The correction factors derived from the HIJING generator are used as the baseline for the final results.

The combinatoric and the closest-match methods differ in the tracklet reconstruction and counting. Consequently, as in the previous section, the correction factors are discussed separately.

7.1 The combinatoric method

Corrections considered in the combinatoric method are summarized here:

1. **Column uniformity corrections**: This performs as a column multiplicity uniformity check after the bad channel masking in the level of cluster as described in 6.5.1.

2. **Acceptance and efficiency corrections**: This accounts for the discrepancies between the number of charged hadrons emitted from the collisions and the number of the reconstructed tracklets, as described in Section 7.1.1.

7.1.1 Acceptance and efficiency correction

This correction accounts for the difference between the number of charged hadrons emitted from the collisions and the number of reconstructed tracklets due to the acceptance and geometry limit of INTT and inefficiencies. In the combinatorial method, the average number of reconstructed tracklets per event is determined in different η bins using the full z-vertex range of the analysis, as shown in Figure 56. The correction factors are then derived by taking the ratio of the number of reconstructed tracklets per event to the number of charged hadrons per event at the generator level in a given centrality interval. Figure 57 illustrates these corrections for the 0–70% centrality interval. These ratios account for both acceptance and efficiency effects. At mid-rapidity, the correction factor is approximately 90%, indicating high reconstruction efficiency. The steep decline at large $|\eta|$ is primarily due to the acceptance limits of INTT, while the slightly lower correction at $\eta = 0$ results from geometric constraints. Figure 58 shows the valid cluster pair multiplicity as a function of pair η and vtx_Z. The tilted pointed-oval structures at $\eta = 0$ across all z-vertex range do not indicate dead acceptance regions; rather, the resolution of tracklet η reconstruction in this region is poor, leading to a near absence of reconstructed tracklets at $\eta \sim 0$. To ensure reliable reconstruction efficiency,η bins with correction factors below 0.5 are excluded from the analysis. Correction factors for different centrality intervals are provided in Appendix H.1.

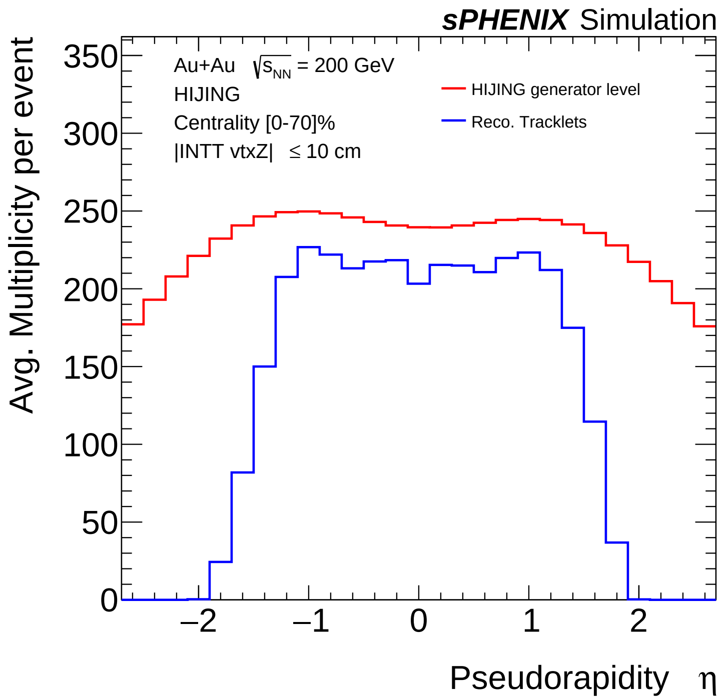

Figure 56: The numbers of reconstructed tracklets and truth hadrons per event for the centrality interval 0-70% as a function of η.

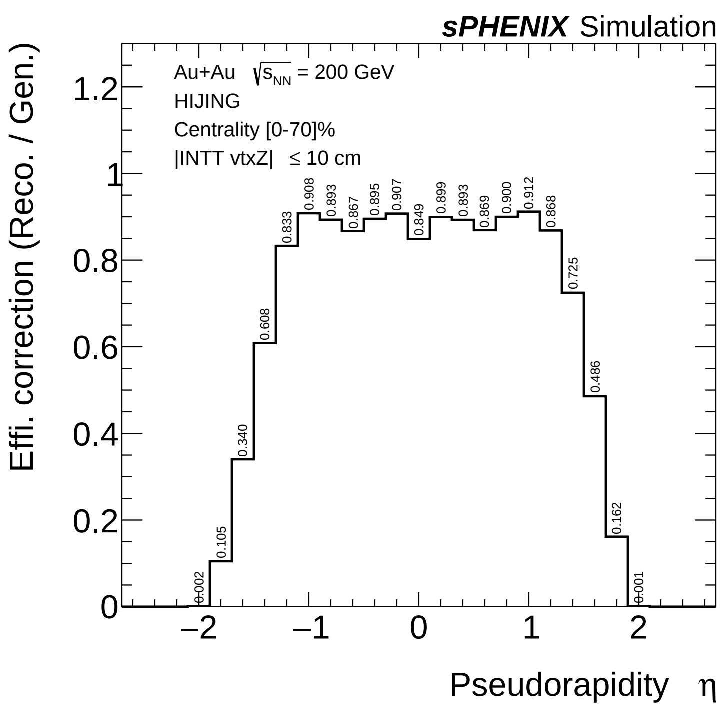

Figure 57: The acceptance and efficiency corrections for the centrality interval 0-70% as a function of η.

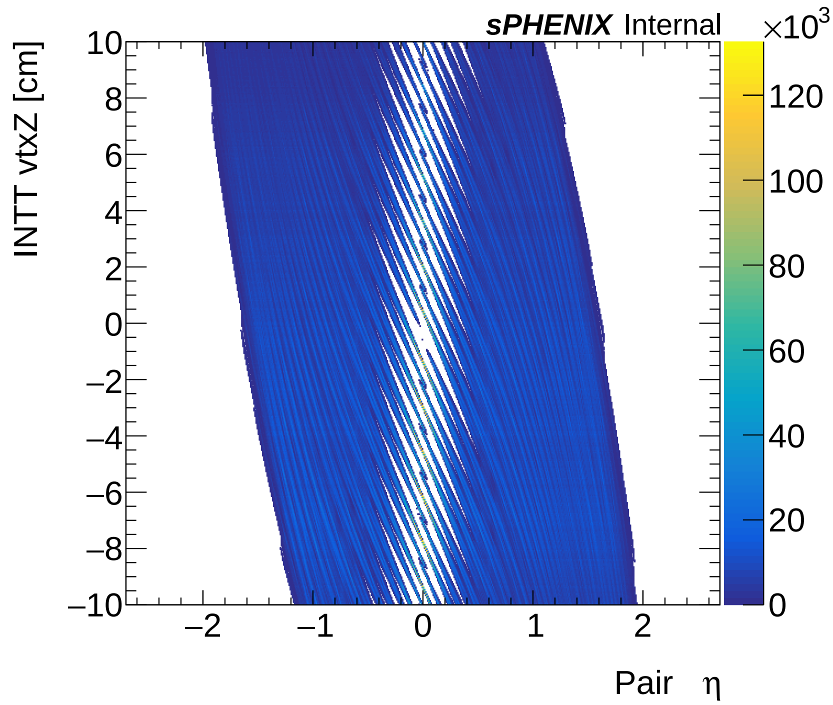

Figure 58: The finely-binned histogram filled by valid cluster pairs.

7.2 The closest-match method

7.2.1 Geometry difference between data and simulation

This correction accounts for the geometry difference between data and simulation. The GEANT4 geometry is modified based on survey measurements, and the reconstruction geometry is built to match the implemented GEANT4 geometry. However, neither geometry perfectly replicates the actual INTT geometry in the physical world. As a result, in simulations, hits are generated and reconstructed using the same geometry, whereas in data, hits are recorded by the detector at physical locations that differ from those reconstructed in the software. This correction factor compensates for the effects of this discrepancy.

The correction is derived in the following steps:

1. Each event is assigned a random vertex Z position, uniformly sampled from -10 to 10 cm. Clusters η and ϕ values are updated accordingly, and "fake" tracklets that do not pass through gaps are reconstructed using the assigned vertex.

2. "Fake" tracklets are filled into a finely binned histogram in the (η, vtx_z) space. Bins containing at least one fake tracklet are set to 1, while empty bins are set to 0.

3. The bins of the histogram are weighted by the vertex distribution in data, and the histograms are re-binned into coarser bins. The final correction factor is calculated as the ratio of the simulation histogram to the data histogram.

Figure 59 shows the correction factor for geometric differences as a function of tracklet η and the event vertex vtx_z. The correction factor remains close to 1 throughout most of the acceptance range, with noticeable deviations near the edges. Regions where the correction factor falls below 0.75 or exceeds 1.25 are excluded from the analysis, as marked by the red lines. This correction factor does not depend on centrality, as it is purely driven by the detector geometry.

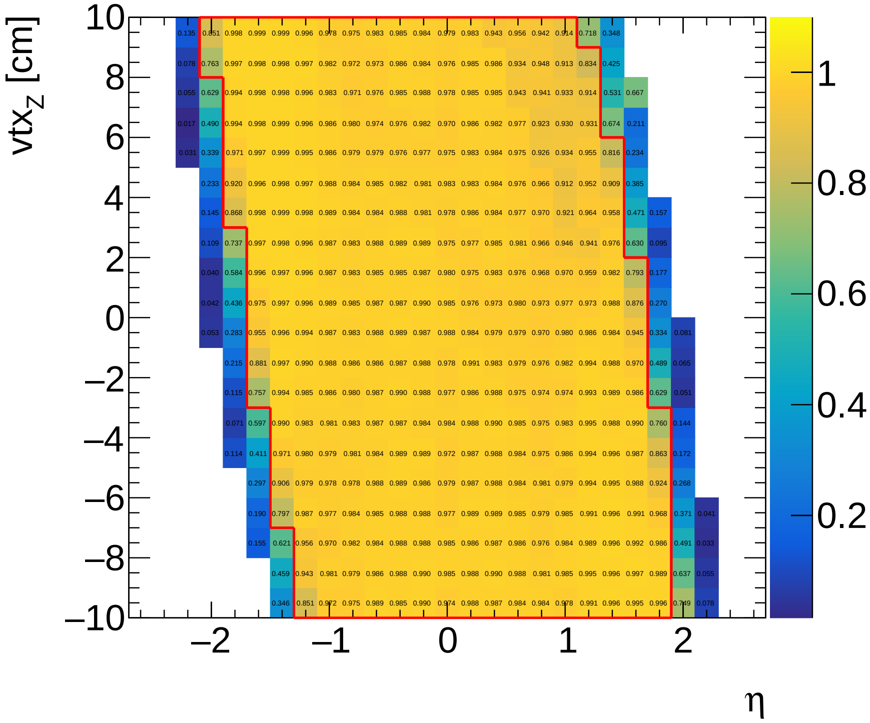

Figure 59: The geometric correction as a function of tracklet η and v_z.

7.2.2 Acceptance and efficiency correction

The reconstructed tracklets are corrected for inefficiencies in the tracklet reconstruction. This correction, referred to as the α factor, is defined as the ratio of the total number of primary charged hadrons in the simulation to the number of uncorrected reconstructed tracklets. In an ideal case where every primary charged hadron is reconstructed as exactly one tracklet, the α factor would be 1. The α factor becomes greater than 1 when there are reconstruction inefficiencies, as the number of reconstructed tracklets is lower than the number of primary charged hadrons. Conversely, if fake tracklets are reconstructed that do not correspond to primary charged hadrons, the α factor becomes less than 1.

To maintain good control over the correction factors, the α factor in each bin is required to satisfy the following conditions :

1. $0 \leq \alpha \leq 3.6$

2. $(\frac{\alpha}{\sigma_\alpha} > 5 \ \&\& \ \alpha < 3) \ || \ (\alpha < 2)$

where σ_α is the statistical error of the α. Regions in the (η, vtx_z) phase space where the α factor does not satisfy these criteria are excluded from the analysis. The acceptance correction accounts for the fact that the detector does not have infinite phase-space coverage. For instance, the length of the INTT ladders provides full acceptance only within $|\eta| \leq 1.2$ for an event vertex at $|\mathrm{vtx}_z| \leq 10$ cm, while clusters with larger $|\eta|$ cannot be recorded when the event vertex is shifted. To derive this correction, a two-dimensional histogram of (η, vtx_z) is first filled with the number of tracklets per vtx_z bin. A second two-dimensional histogram of (η, vtx_z) is then filled with the number of tracklets reconstructed in regions with a valid α factor. The correction factor is calculated by taking the ratio of the two histograms and projecting it into the η dimension.

Since both the tracklet reconstruction efficiency (inefficiency) and fake rate are multiplicity- and centrality-dependent, the α factor is derived separately for each centrality interval. Figure 60 and 61 show the α factor as a function of η and vtx_z and the acceptance correction as a function of η for events in the centrality interval $0-3\%$, $30-35\%$, $65-70\%$, $0-70\%$. Corrections in different centrality intervals can be found in Appendix H.

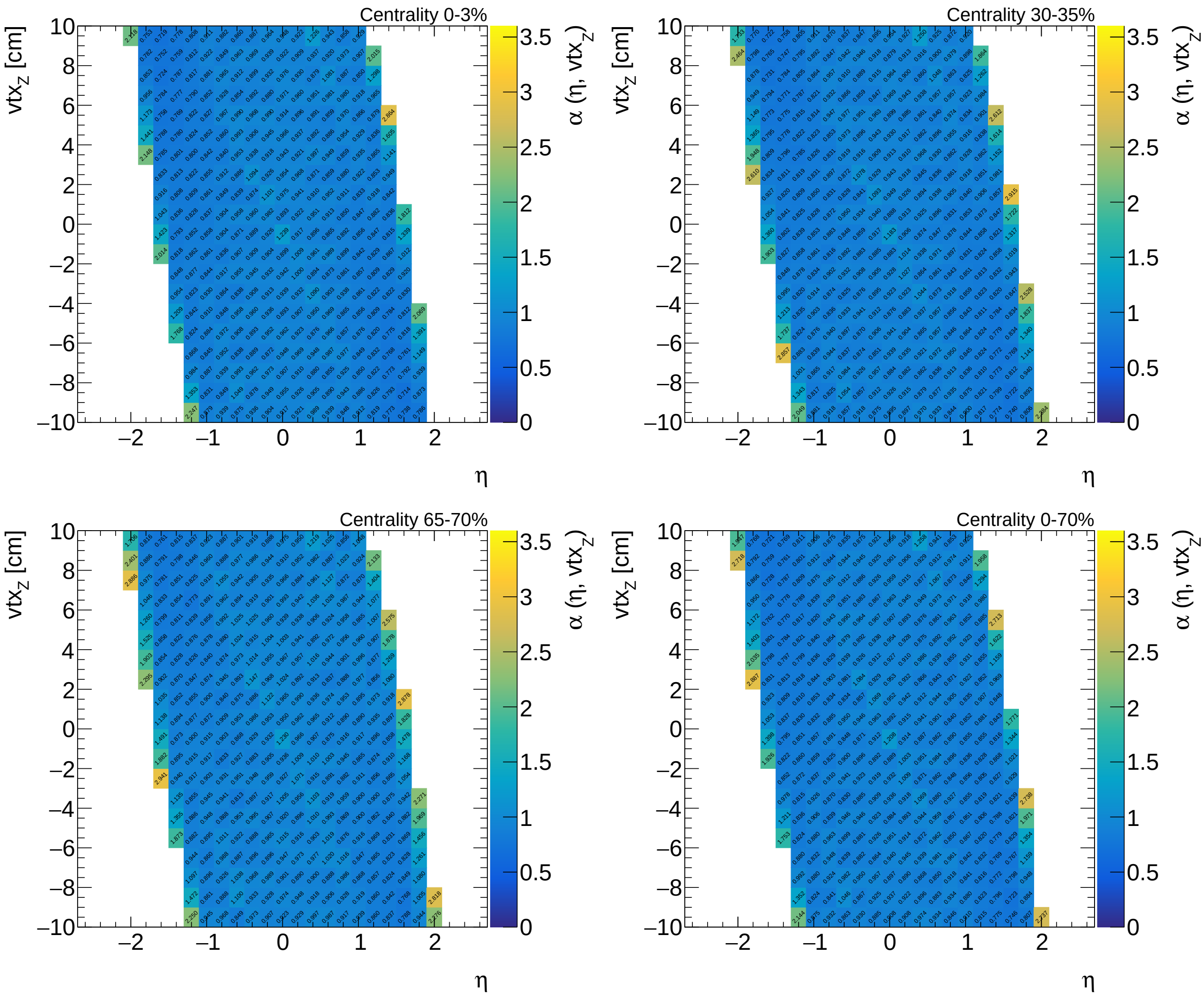

Figure 60: The α factor: $0-3\%$ (top left), $30-35\%$ (top right), $65-70\%$ (bottom left), and $0-70\%$ (bottom right).

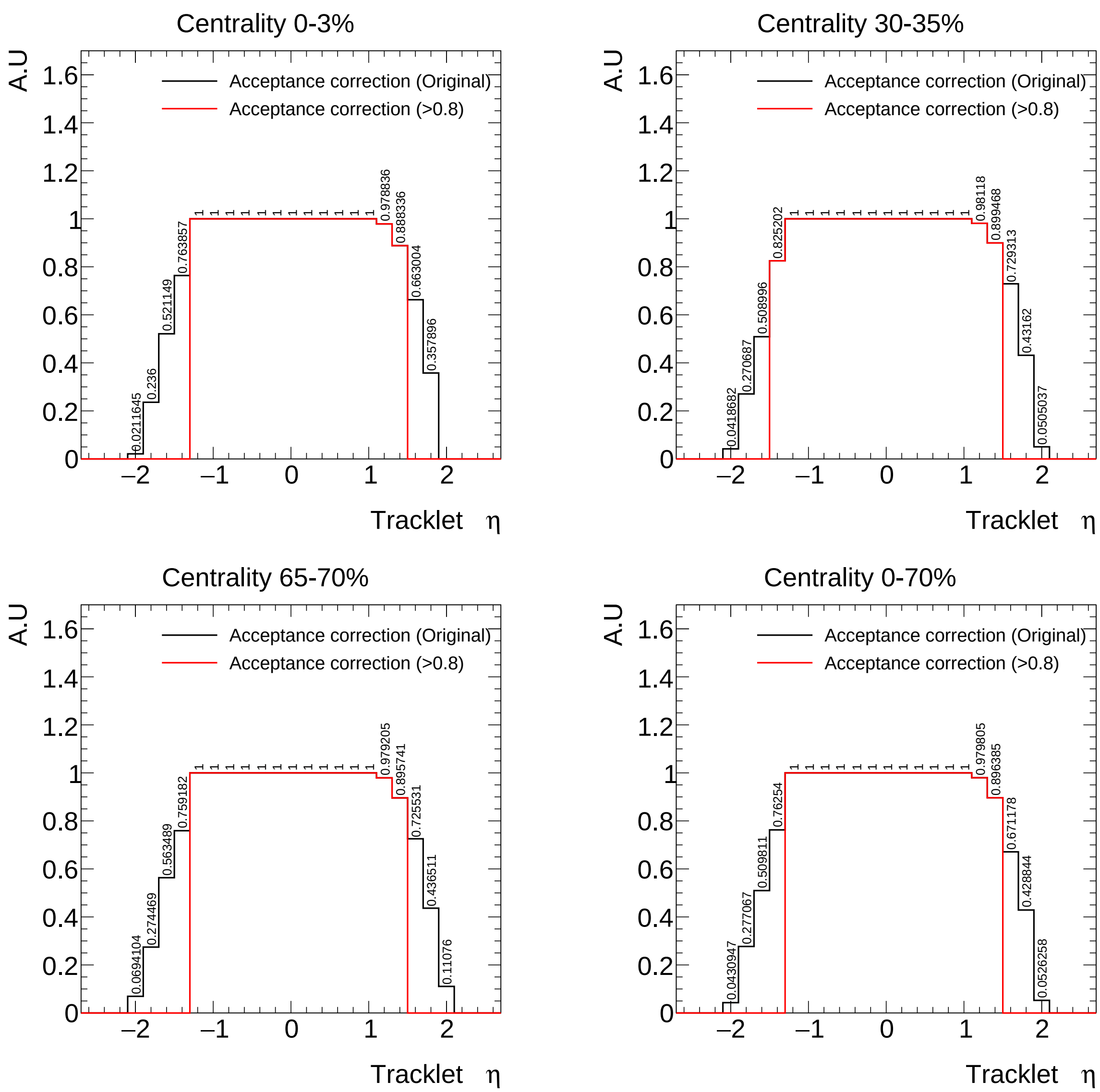

Figure 61: The acceptance correction: $0-3\%$ (top left), $30-35\%$ (top right), $65-70\%$ (bottom left), and $0-70\%$ (bottom right).

8 Systematic uncertainties

Systematic uncertainties considered in the two analyses are discussed separately below.

8.1 The combinatoric method

The following sources of systematic uncertainty are considered:

- **Tracklet counting region.** The tracklet counting region in the subtracted $\Delta\phi$ distribution is varied to $|\Delta\phi|\leq 0.018$, $|\Delta\phi|\leq 0.024$ and $|\Delta\phi|\leq 0.030$. $\mathrm{dN_{ch}}/\mathrm{d}\eta$ results for different $\Delta\phi$ signal counting regions are shown in Figure 62.

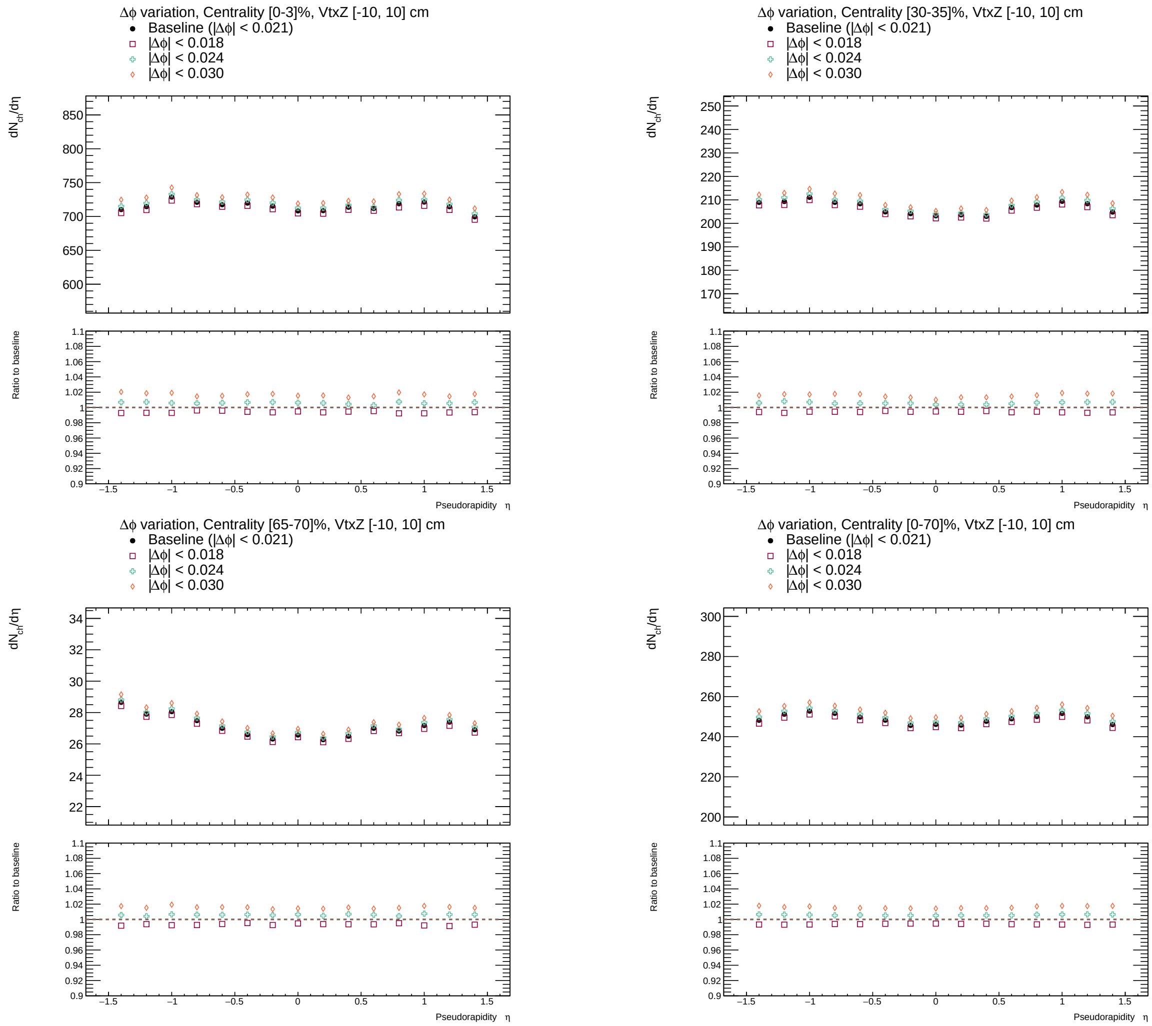

Figure 62: $\mathrm{dN_{ch}/d}\eta$ results for different $\Delta\phi$ signal counting regions in different centrality intervals: $0-3\%$ (top left), $30-35\%$ (top right), $65-70\%$ (bottom left), and $0-70\%$ (bottom right).

- **Cluster ADC cut.** The baseline analysis applies a cluster ADC threshold of > 35. To assess its impact, the selection is modified by either disabling it or increasing the threshold to > 50, and the maximum variation in the final $\mathrm{dN_{ch}/d}\eta$ result is quantified as a systematic uncertainty. This variation is motivated by Figure 93, which shows that cluster ADC values in data are discretized. Specifically, clusters with an ADC of 35 are retained without an ADC cut, while the next discrete value of ADC $= 45$ justifies applying a threshold of ADC > 50. $\mathrm{dN_{ch}/d}\eta$ results for different cluster ADC thresholds are shown in Figure 63.

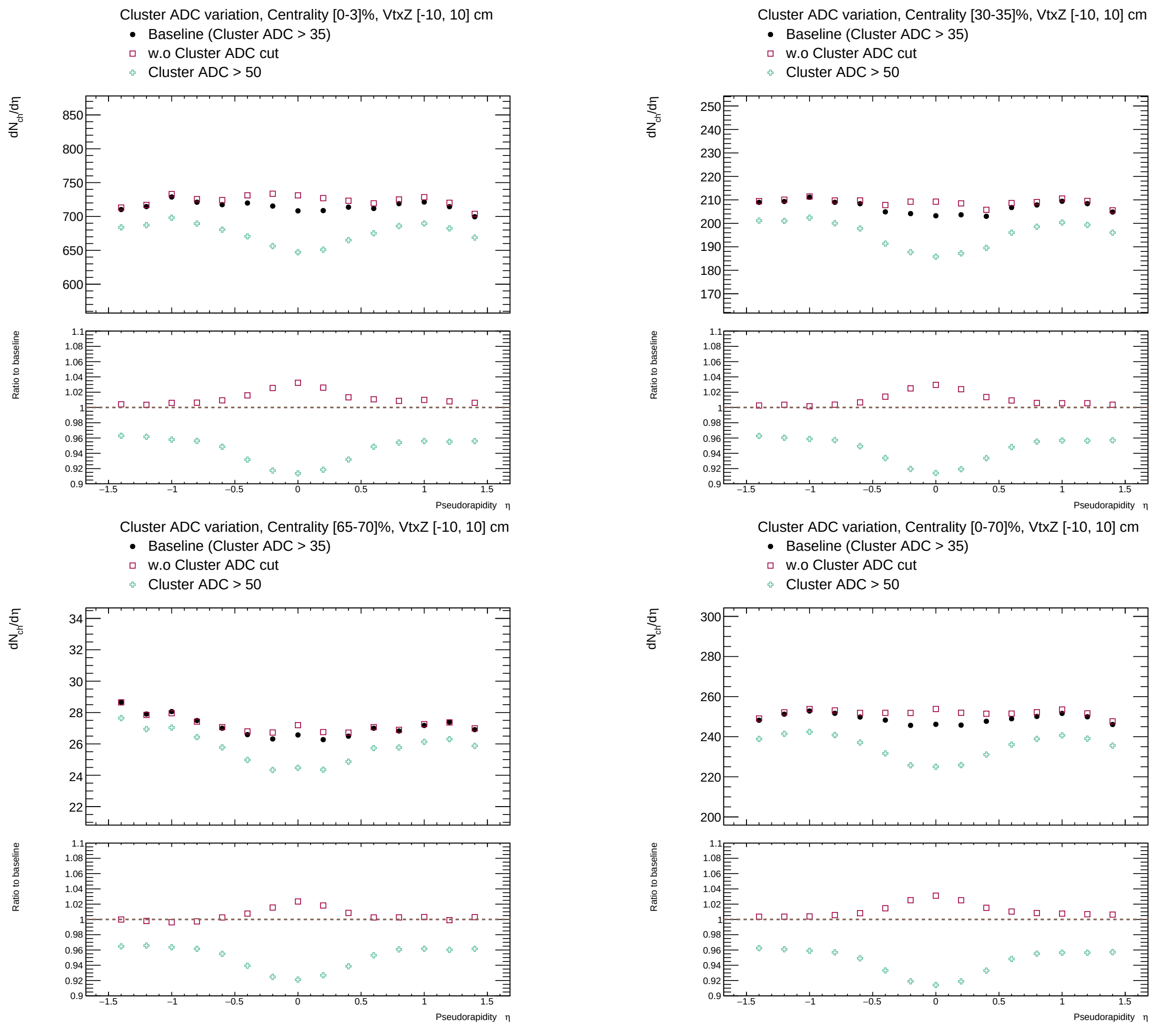

Figure 63: $\mathrm{dN_{ch}/d}\eta$ results for different cluster ADC thresholds in different centrality intervals: $0-3\%$ (top left), $30-35\%$ (top right), $65-70\%$ (bottom left), and $0-70\%$ (bottom right).

- **Cluster ϕ-size cut.** In the baseline analysis, a cluster ϕ-size selection of < 40 is applied. To assess its effect, the selection is removed, and the analysis is repeated. The largest variation in the $\mathrm{dN_{ch}/d}\eta$ distribution is taken as a systematic uncertainty. $\mathrm{dN_{ch}/d}\eta$ results for different cluster ϕ-size cuts are shown in Figure 64.

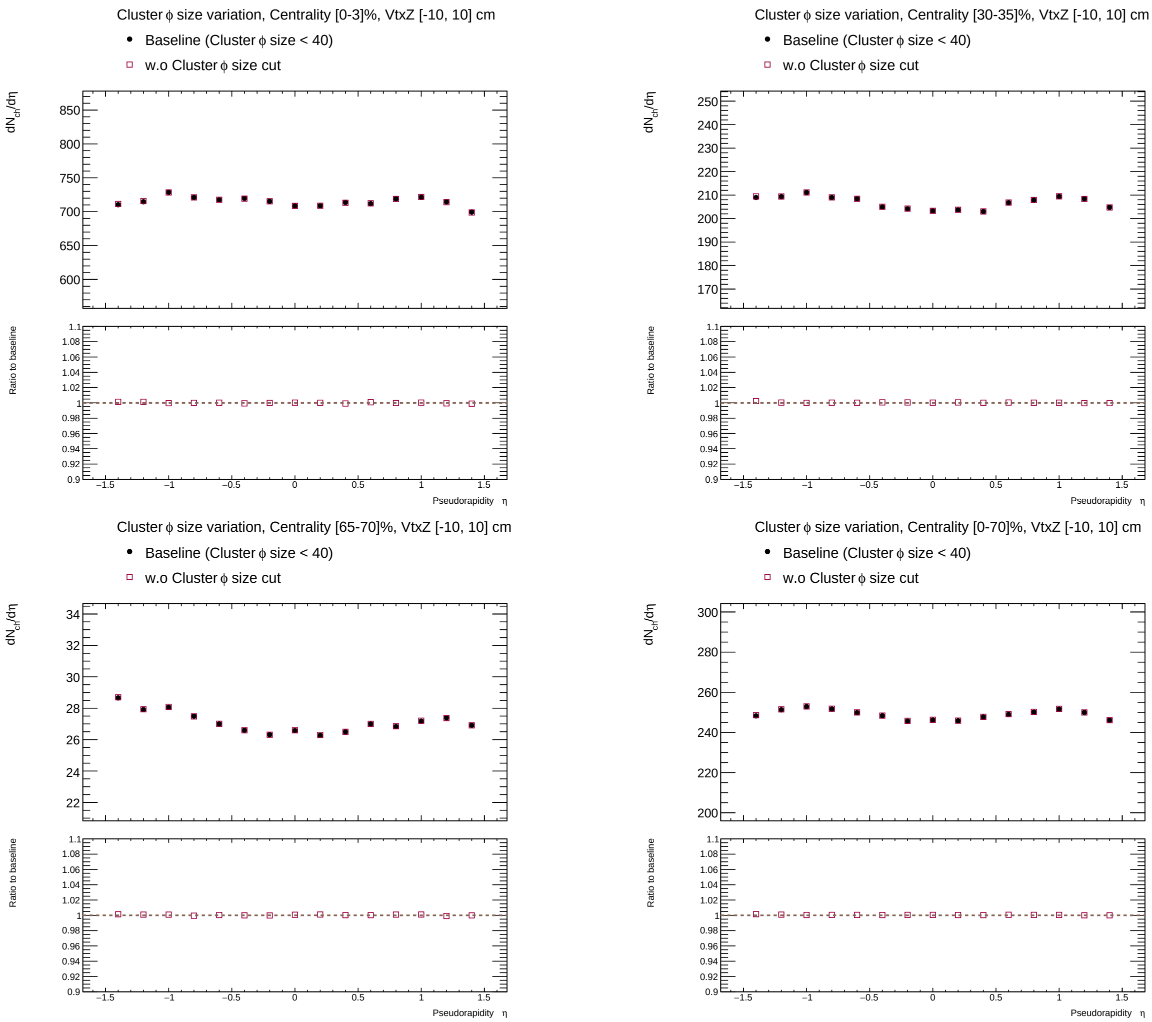

Figure 64: $\mathrm{dN_{ch}}/\mathrm{d}\eta$ results for different cluster ϕ-size cuts in different centrality intervals: $0-3\%$ (top left), $30-35\%$ (top right), $65-70\%$ (bottom left), and $0-70\%$ (bottom right).

- **Run segmentation.** The full set of data DST available is used as the baseline $\mathrm{dN_{ch}}/\mathrm{d}\eta$, while the maximum variation observed in the the segments of first and second 4 million events is quoted as a systematic uncertainty. $\mathrm{dN_{ch}}/\mathrm{d}\eta$ results for different run segments are shown in Figure 65.

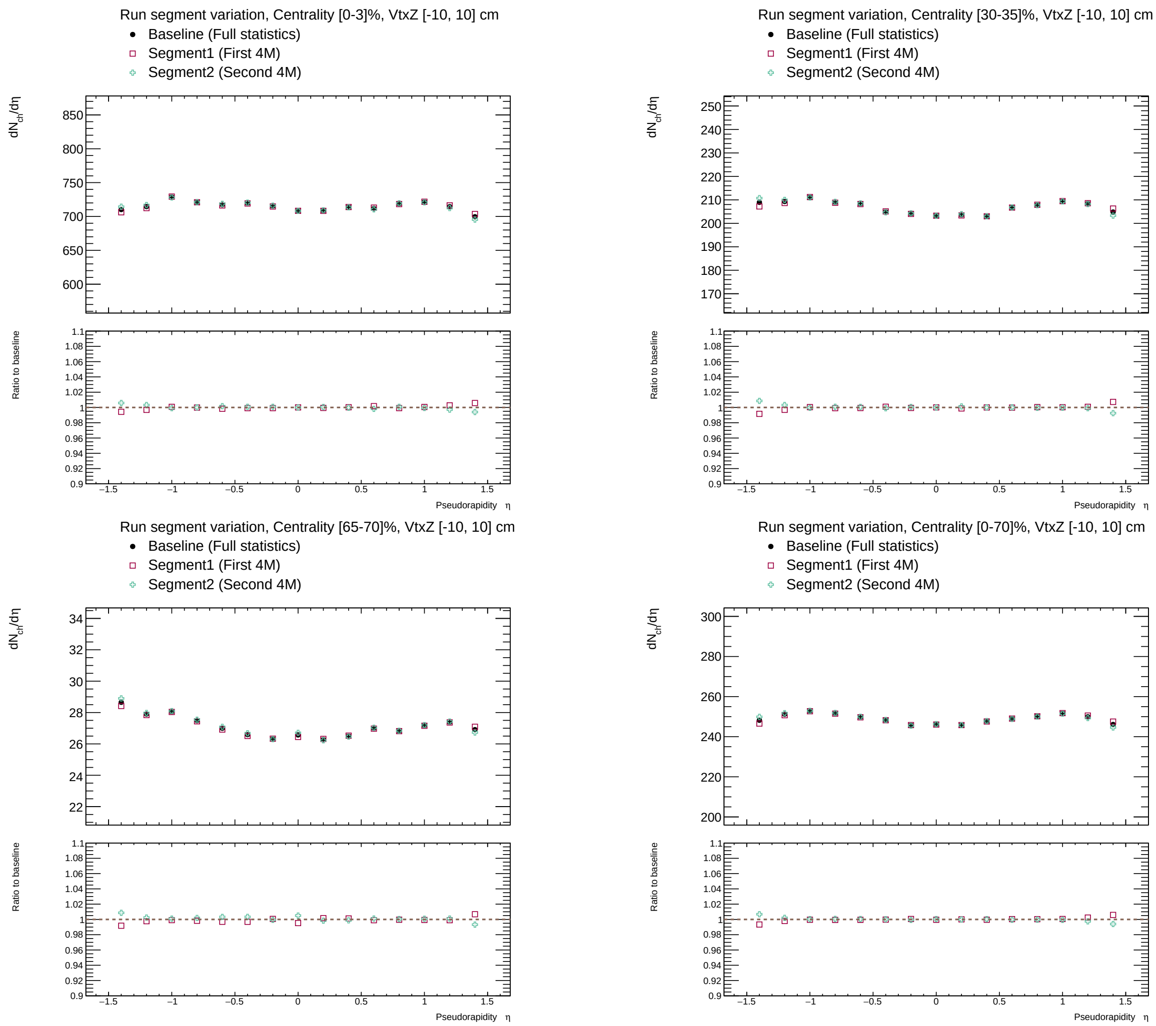

Figure 65: $\mathrm{dN_{ch}}/\mathrm{d}\eta$ results for different run segments in different centrality intervals: $0-3\%$ (top left), $30-35\%$ (top right), $65-70\%$ (bottom left), and $0-70\%$ (bottom right).

- **Geometry misalignment.** This accounts for the remaining misalignment in data. The method is described in Section 8.1.1.

- **Event generator.** The baseline analysis and correction factors are derived using simulation samples generated with `HIJING`. Correction factors will also be derived using samples from `EPOS4` and `AMPT`, and the largest variation in the $\mathrm{dN_{ch}}/\mathrm{d}\eta$ distribution will be quoted as a systematic uncertainty.

- **Strangeness decay.** Decays of strange particles can result in multiple clusters, leading to potential "double/multiple counting" in the $\mathrm{dN_{ch}}/\mathrm{d}\eta$ measurement. The effect is evaluated by varying the fraction of strange particles among primary particles in simulation and assessing the impact on $\mathrm{dN_{ch}}/\mathrm{d}\eta$.[4]

[4] Uncertainties in the event generators and strangeness decays are not included in this version of the paper draft. These uncertainties will be evaluated when the centrality divisions for `EPOS4` and `AMPT` and the `HIJING` with an enhanced strangeness simulations are available.

8.1.1 The uncertainty due to the geometry misalignment

Figure 66 shows the $\Delta\phi$ of cluster pairs as a function of the inner cluster ϕ angle for one of the subsamples in data, where the cluster ϕ angles have been updated based on the assigned beam spot. While a generally flat correlation is observed, ladder-by-ladder fluctuations persist in data. In contrast, no such fluctuations are seen in the simulation, as shown in Figure 35. This is expected since the INTT geometry in GEANT4 and the offline geometry are perfectly aligned in simulation and suggests that the observed fluctuations in data are due to residual misalignment.

To quantify the impact of these residual misalignments, a strategy is implemented that introduces random displacements to cluster positions in simulation, effectively simulating the effects of misalignment in the data. The procedures are outlined as follows:

1. In one trial, introduce displacements in three dimensions (X, Y, Z) to each of 56 ladders. The displacements are randomly and uniformly sampled between ± 250 μm. The clusters in a given ladder are therefore shifted from nominal positions systematically.

2. Process the first thirty thousand events through the full PHOBOS-approach analysis, including event vertex and tracklet reconstructions.

3. Repeat the procedures 500 times to obtain the variation

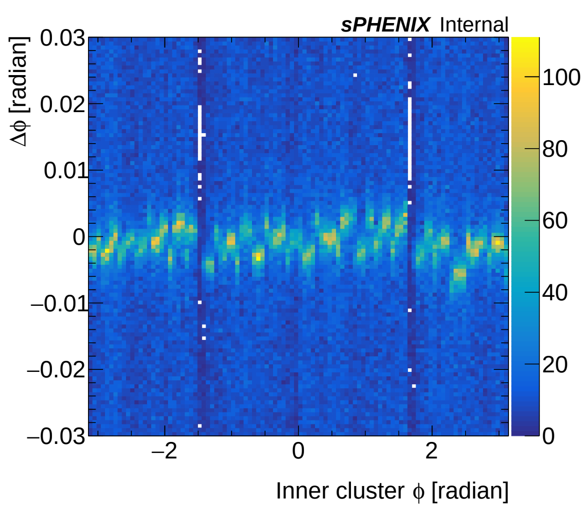

Figure 66: The $\Delta\phi$ of cluster pairs as a function of inner cluster ϕ angle.

Figure 67 shows the distributions of the amount of the introduced offsets to each ladder in all the trials in three dimensions. And the variation of the reconstructed beam spot is shown in Figure 68. The standard deviations of the variation are around 230μm in both axes. Figures 69 and 70 show the variations of the reconstructed vertex Z and $\Delta\phi$ of valid cluster pairs. The $\Delta\phi$ distribution is wider when the offsets are introduced to the offline geometry, which is similar to what observed in data, as shown in Figure 54. Figure 71 shows the variation in the number of reconstructed tracklets due to the random ladder offsets. The maximum difference in $dN_{ch}/d\eta$ resulting from these variation is quoted as the systematic uncertainty.

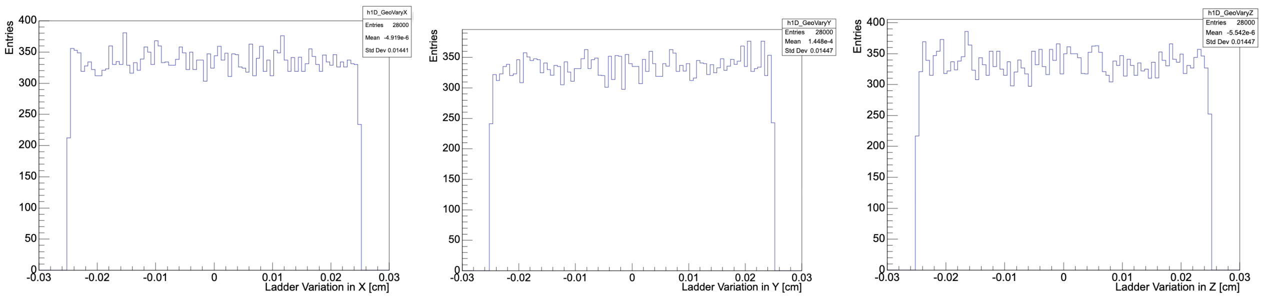

Figure 67: The distributions of introduced offsets to each ladder of all the trials in simulation.

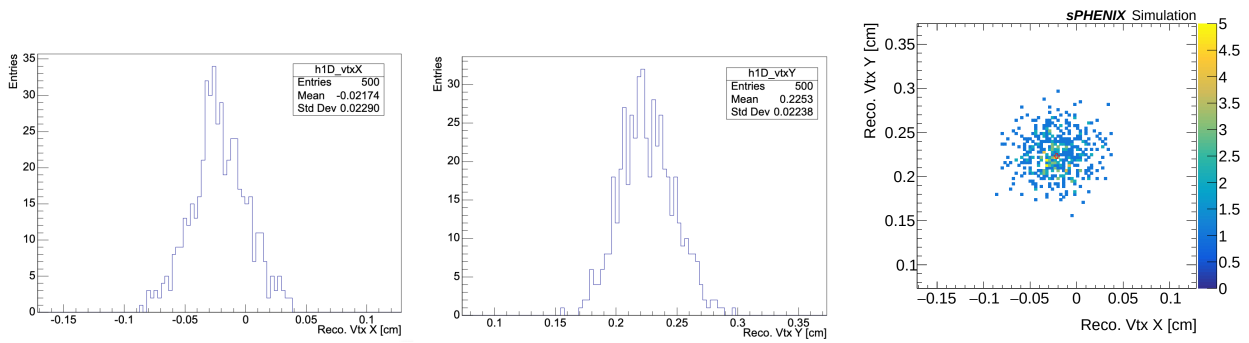

Figure 68: The variation of the reconstructed vertex X (Left) and Y (Middle). Right: The variation of which in 2D. The red cross mark corresponds to the reconstructed beam spot without the offset introduction.

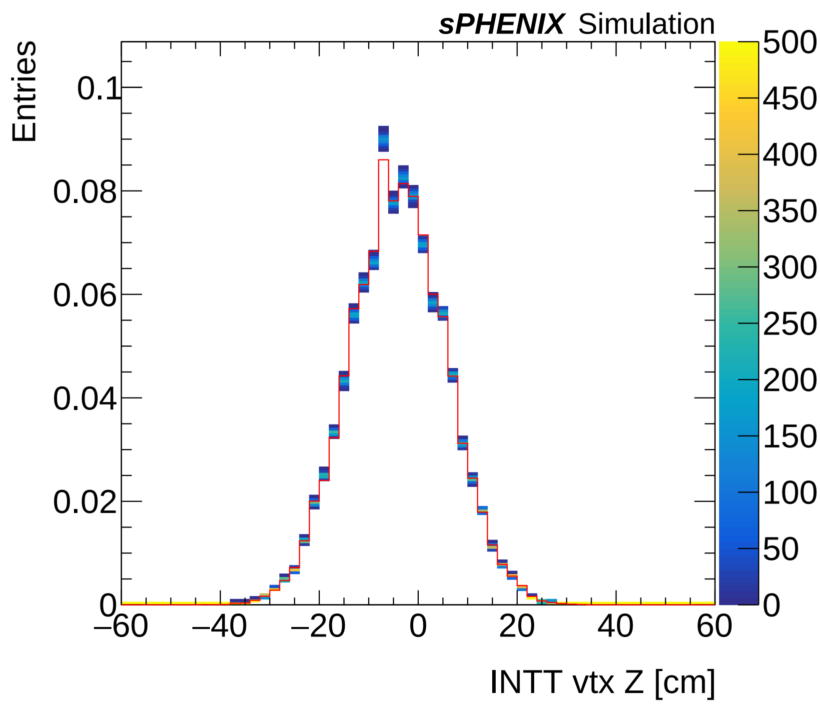

Figure 69: The variation of the reconstructed vertex Z. The distribution in red is without the offset introduction.

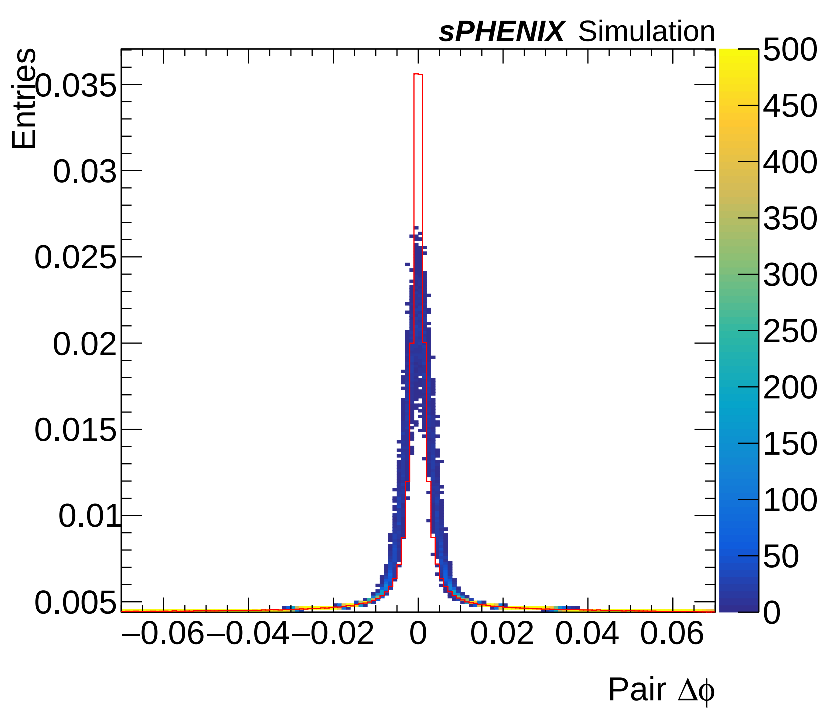

Figure 70: The variation of the $\Delta\phi$ of the valid cluster pairs. The distribution in red is without the offset introduction.

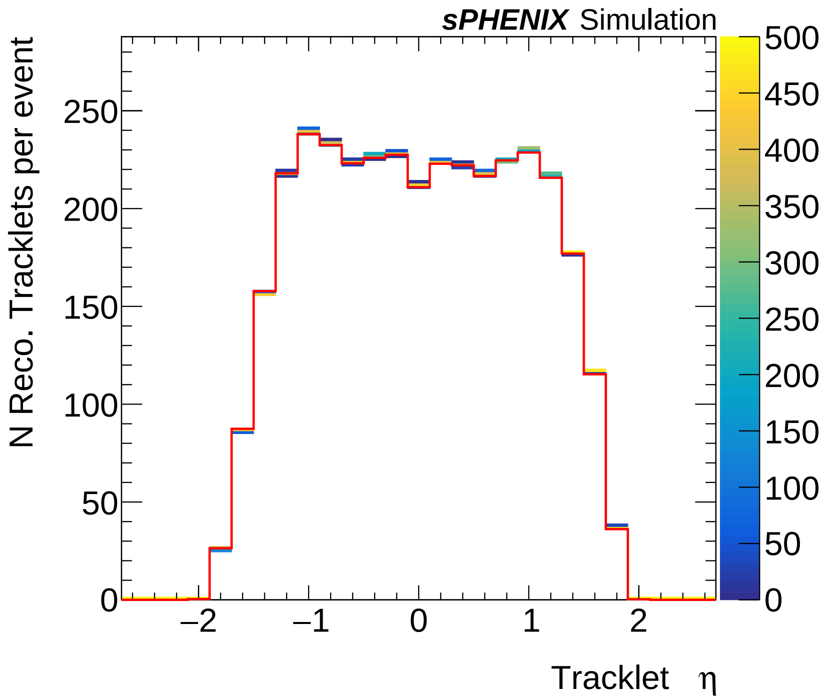

Figure 71: The variation of number of reconstructed tracklets. The distribution in red is without the offset introduction.

The relative variations of the considered systematic uncertainties to the nominal $\mathrm{dN_{ch}/d}\eta$ are shown in Figure 72 for different centrality intervals. The total uncertainties, calculated as the quadrature sum of all individual contributions, are also presented. The systematic uncertainties for different centrality intervals are presented in Appendix J.1.

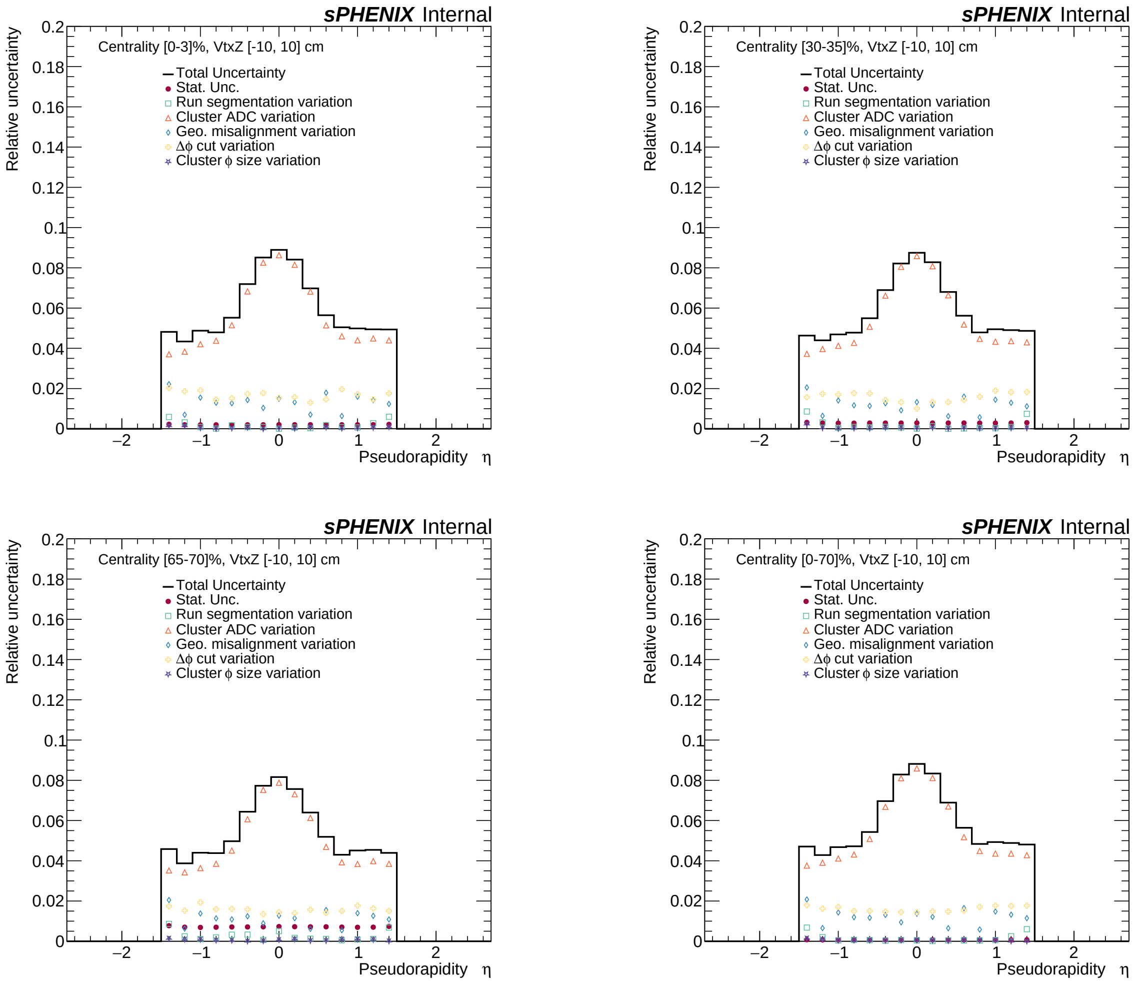

Figure 72: Systematic uncertainties in different centrality intervals: 0−3% (top left), 30−35% (top right), 65 − 70% (bottom left), and 0 − 70% (bottom right).

8.2 The closest-match method

The following sources of systematic uncertainty are considered:

- **Tracklet reconstruction selection**. The tracklet reconstruction selection is varied to $\Delta R < 0.4$ and $\Delta R < 0.6$. The maximum deviation in the final $dN_{ch}/d\eta$ result is taken as a systematic uncertainty. $dN_{ch}/d\eta$ results for different tracklet ΔR cuts are shown in Figure 73.

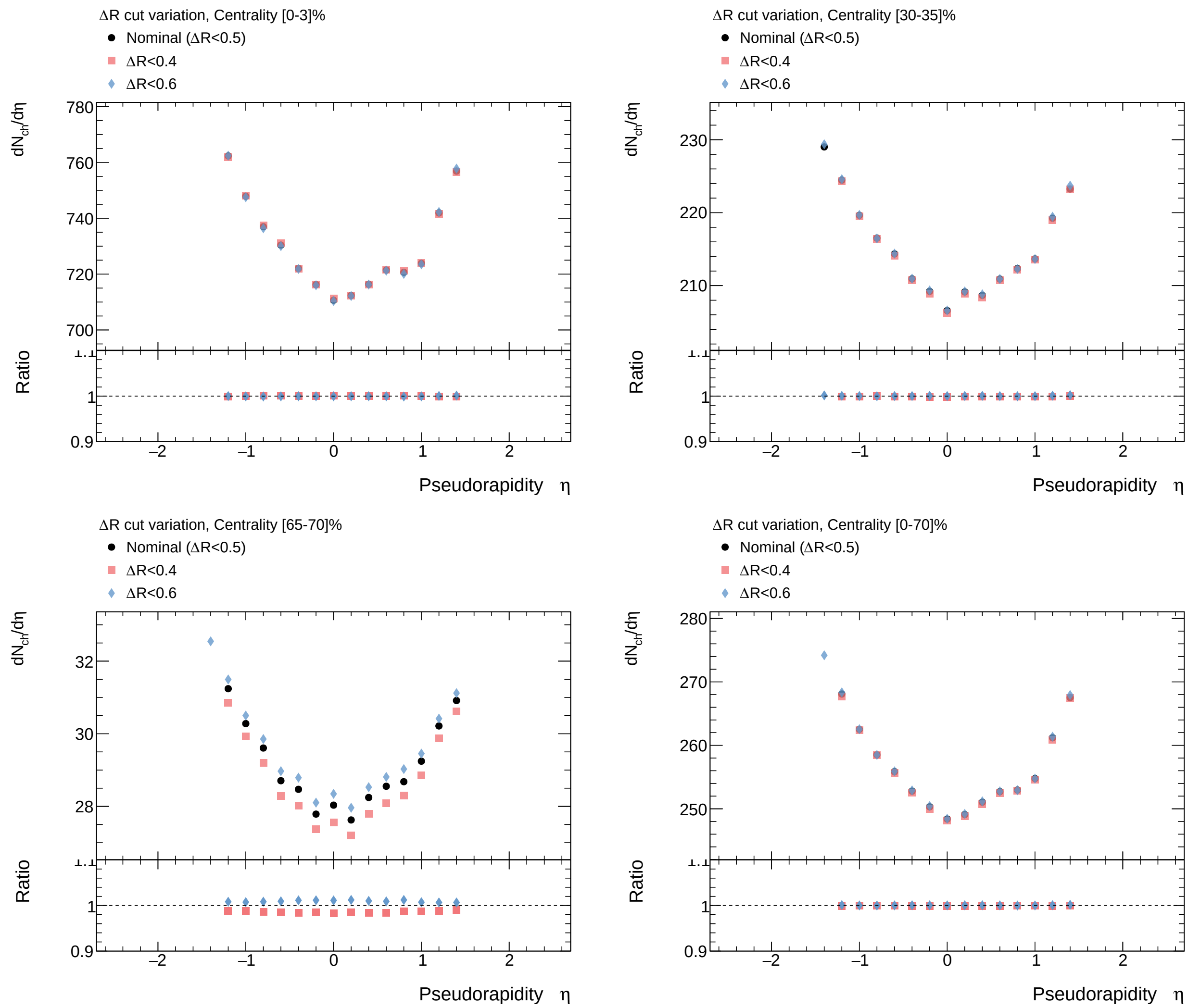

Figure 73: $dN_{ch}/d\eta$ results for different tracklet ΔR cuts in different centrality intervals: $0-3\%$ (top left), $30-35\%$ (top right), $65-70\%$ (bottom left), and $0-70\%$ (bottom right).

In certain centrality intervals, variations in the ΔR cut cause fluctuations in tracklet reconstruction around $\eta \gtrsim 1.4$, resulting in the acceptance correction for those bins failing to meet the required criteria and an unphysical uncertainty of 100%. Consequently, results will be presented only for the range $|\eta| \leq 1.3$.

- **Cluster ADC cut**. Same as described in Section 8.1 $dN_{ch}/d\eta$ results for different cluster ADC thresholds are shown in Figure 74.

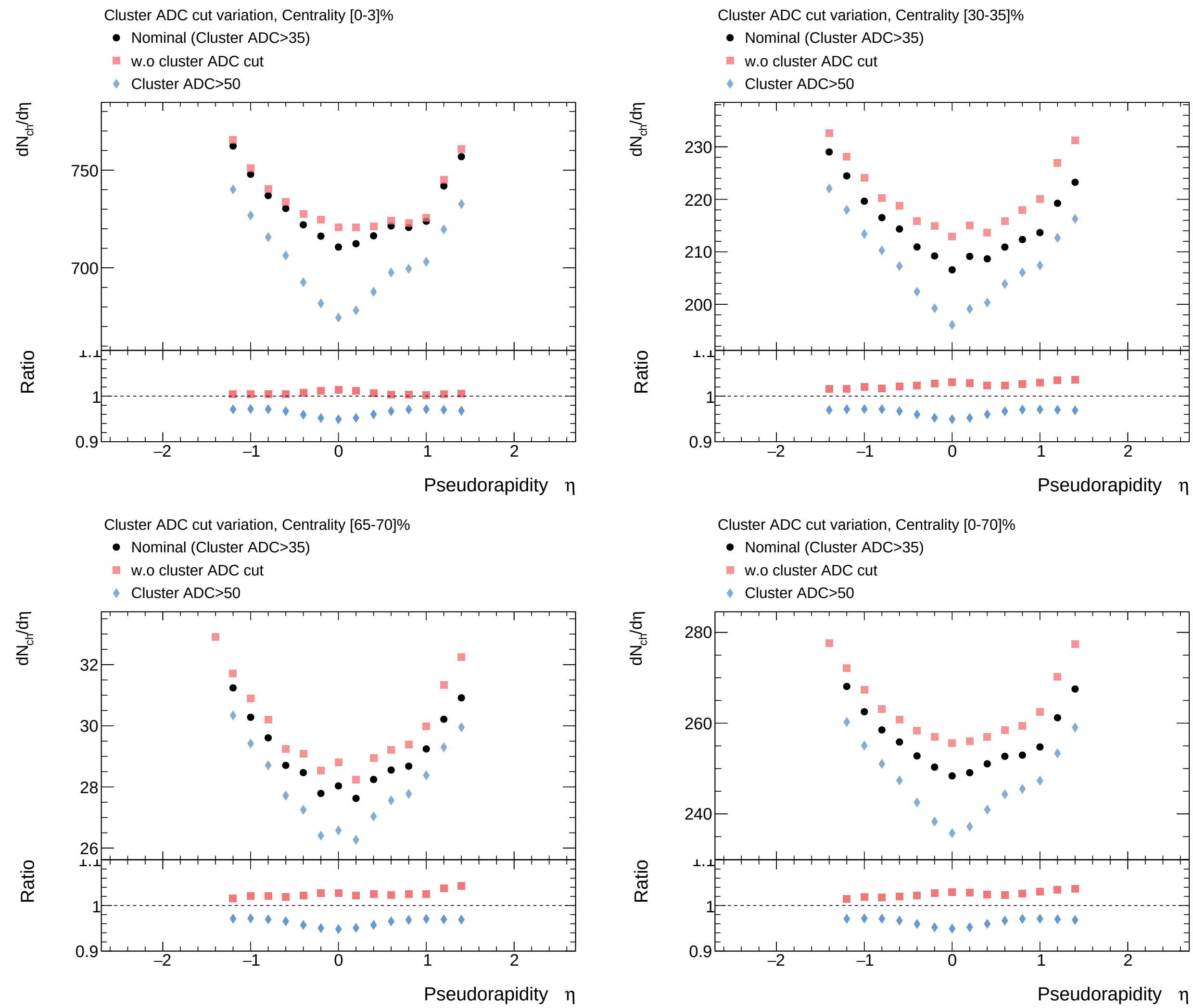

Figure 74: $\mathrm{dN_{ch}/d}\eta$ results for different cluster ADC thresholds in different centrality intervals: $0-3\%$ (top left), $30-35\%$ (top right), $65-70\%$ (bottom left), and $0-70\%$ (bottom right).

A $\sim 5\%$ uncertainty due to variations in the cluster ADC cut can be explained as follows. From Figure 20, applying a cluster ADC cut > 35 removes approximately 4.5% of clusters in simulation (corresponding to the first two non-zero bins) and about 6.5% in data (first non-zero bin). Increasing the cut to ADC > 50 eliminates an additional $\sim 5\%$ of clusters in data (second non-zero bin), which aligns with the observed $\sim 5\%$ uncertainty resulting from this variation.

- **Cluster ϕ-Size cut**. Same as described in Section 8.1 $\mathrm{dN_{ch}/d}\eta$ results for different cluster ϕ-size selections are shown in Figure 75.

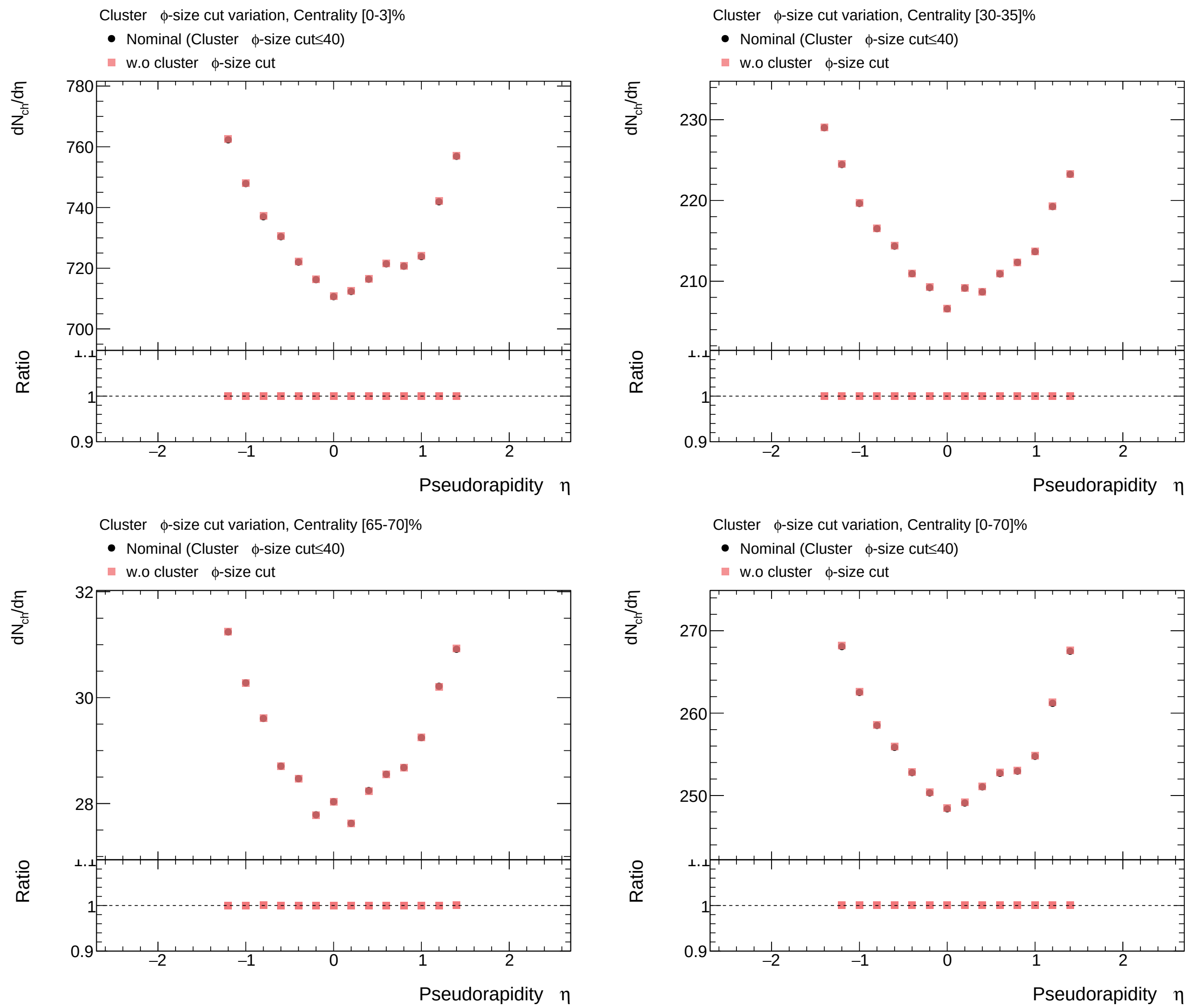

Figure 75: $\mathrm{dN_{ch}}/\mathrm{d}\eta$ results for different cluster ϕ-size selections in different centrality intervals: $0-3\%$ (top left), $30-35\%$ (top right), $65-70\%$ (bottom left), and $0-70\%$ (bottom right).

- **Run segments**. The data DST is divided into six segments, with five containing 1.5 million events each and the sixth containing the remainder. The baseline $\mathrm{dN_{ch}}/\mathrm{d}\eta$ distribution is measured using the first segment, while the maximum variation observed in the other five segments is quoted as a systematic uncertainty. $\mathrm{dN_{ch}}/\mathrm{d}\eta$ results for different segments are shown in Figure 76.

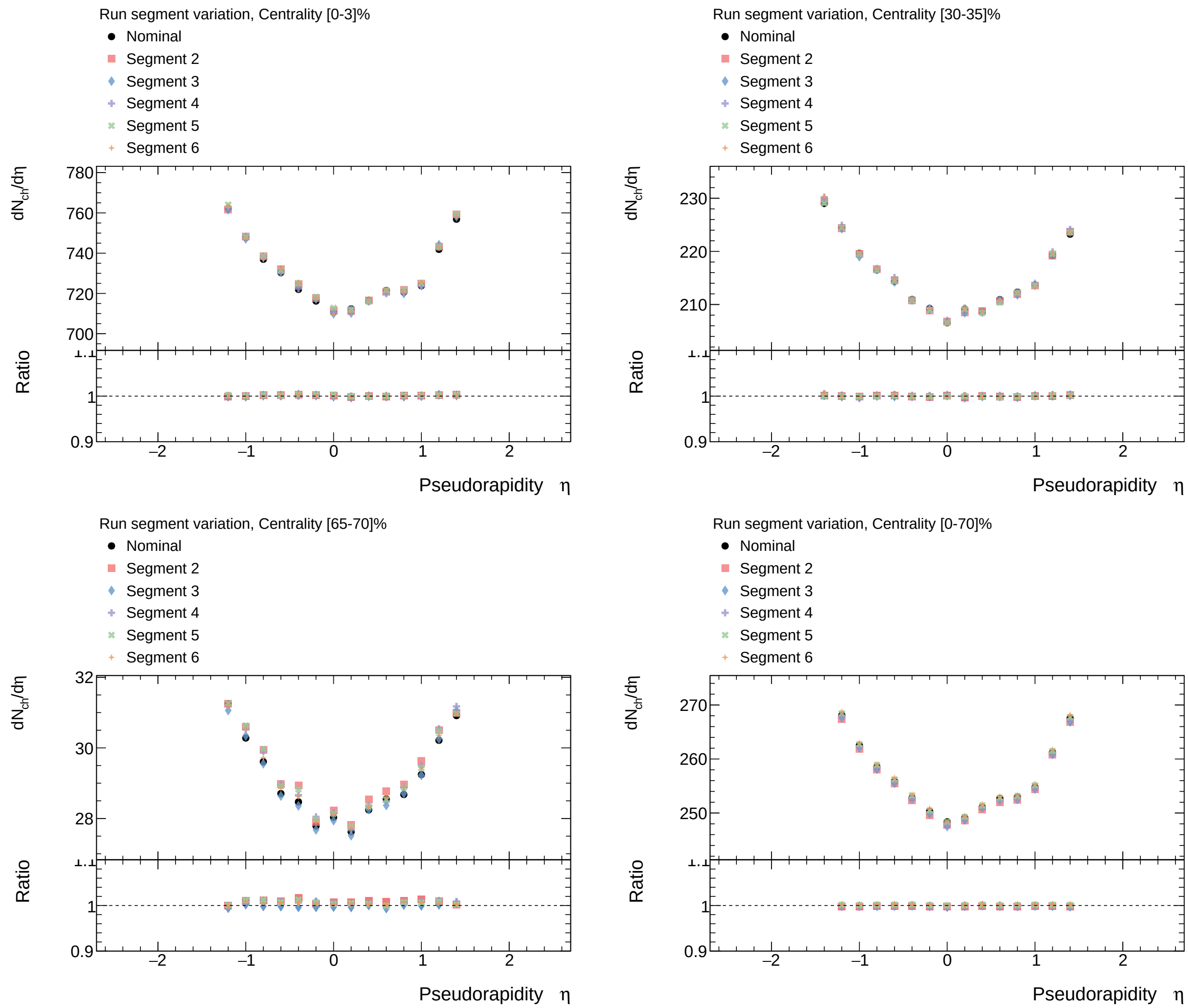

Figure 76: $\mathrm{dN_{ch}}/\mathrm{d}\eta$ results for different segments in different centrality intervals: $0-3\%$ (top left), $30-35\%$ (top right), $65-70\%$ (bottom left), and $0-70\%$ (bottom right).

- **Event generator**. Same as described in Section 8.1.
- **Strangeness decay**. Same as described in Section 8.1.[5]

The relative magnitudes of each systematic uncertainty, defined as the ratio of the variation to the nominal $\mathrm{dN_{ch}}/\mathrm{d}\eta$, are shown in Figure 77 for the centrality interval $0-3\%$, $30-35\%$, $65-70\%$, and $0-70\%$. The total uncertainty, calculated as the quadrature sum of all individual contributions, is also presented.

[5] Uncertainties in the event generators and strangeness decays are not included in this version of the paper draft. These uncertainties will be evaluated when the centrality divisions for `EPOS4` and `AMPT` and the `HIJING` with an enhanced strangeness simulations are available.

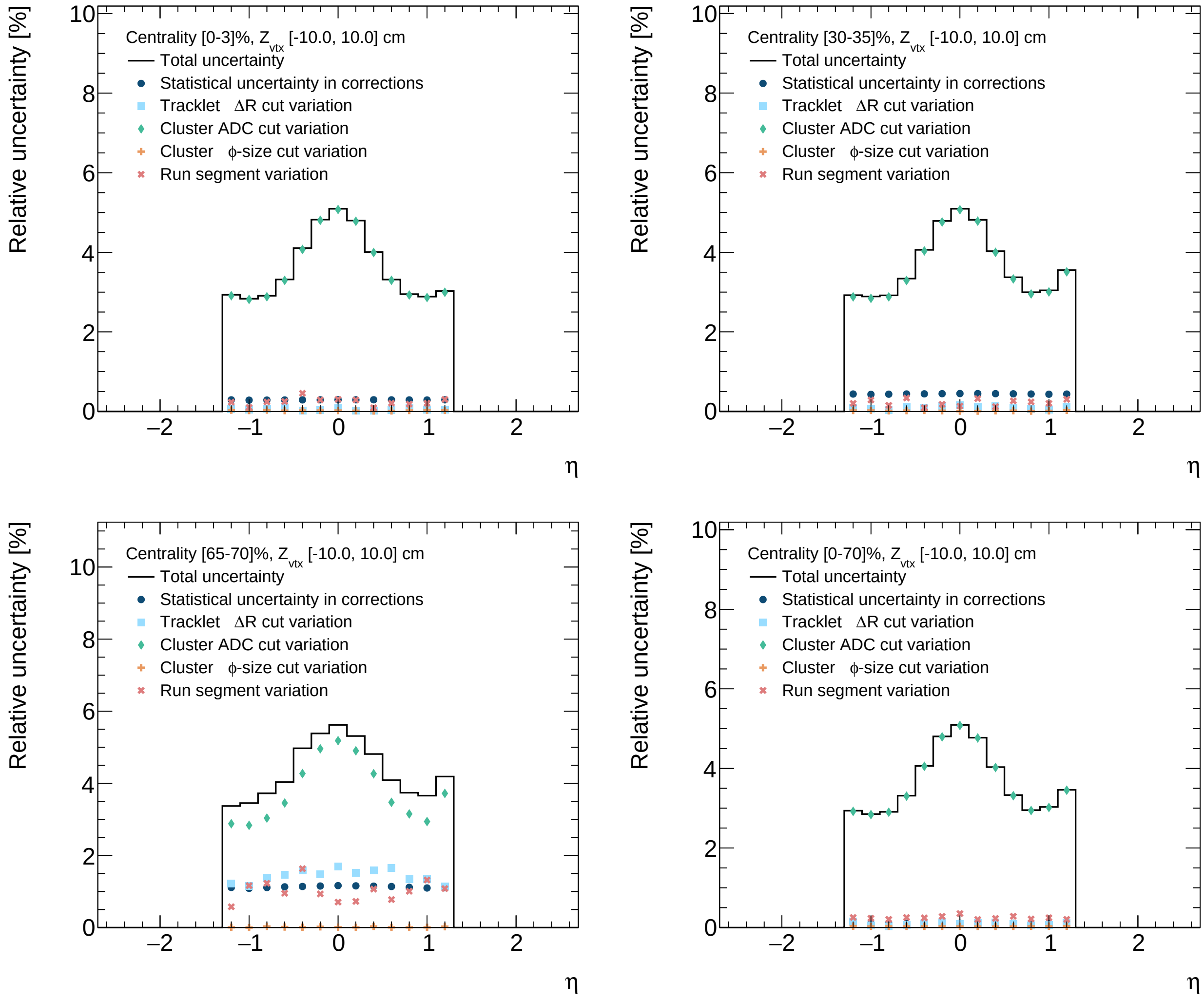

Figure 77: Systematic uncertainties for the centrality interval $0-3\%$ (top left), $30-35\%$ (top right), $65-70\%$ (bottom left), and $0-70\%$ (bottom right).

8.3 Summary of systematic uncertainties

Systematic uncertainties for different centrality intervals are detailed in Appendix J, while Table 7 provides a summary of the uncertainty ranges for each source in both analysis methods. Note that in the closest-match method, this misalignment effect is accounted for using a correction factor that compensates for geometric differences between data and simulation (Section 7.2.1), along with the associated uncertainty. To avoid double counting, this systematic uncertainty is not separately evaluated in the closest-match method.

Table 7: Systematic uncertainties for different sources.

Source	**The combinatoric method** [%]	**The closest-match method** [%]
Corrections	0.2–0.77	0.3–1.2
Tracklet reconstruction	1.0–2.1	3.2×10^{-3}–1.7
Cluster ADC selection	3.4–8.7	2.8–5.2
Cluster ϕ-size selection	1.0×10^{-4}–0.3	2.0×10^{-4}–5.5×10^{-2}
Run segment	1.2×10^{-3}–1.1	9.3×10^{-2}–1.6
Event generator	–	–
Secondaries	–	–
Misalignment	0.6–2.2	–
Total	3.9–9.0	2.8–5.6

Discussion

The systematic uncertainties from different sources exhibit non-trivial correlations between the two analysis approaches, as shown in Figure 78. This arises because both methods share common global objects, such as clusters, and utilize the same binning definitions in the final measurement.

For statistical uncertainties in corrections, the closest-match method incorporates the effect of correcting geometric differences between simulation and data, leading to a slightly larger uncertainty compared to the combinatoric method. Another difference is the segmentation of events – the closest-match method divides events into six segments, whereas the combinatoric method splits them into two segments. The dominant source of uncertainty in both methods is the cluster ADC cut, which impacts tracklet reconstruction differently in each method. The combinatoric method reconstructs all possible cluster pairs, making it more sensitive to a change in the combinatorial background caused by variations in the number of clusters. In contrast, the closest-match method selects only the cluster pair with the smallest ΔR as the final tracklet, making it less susceptible to a change in the cluster multiplicity.

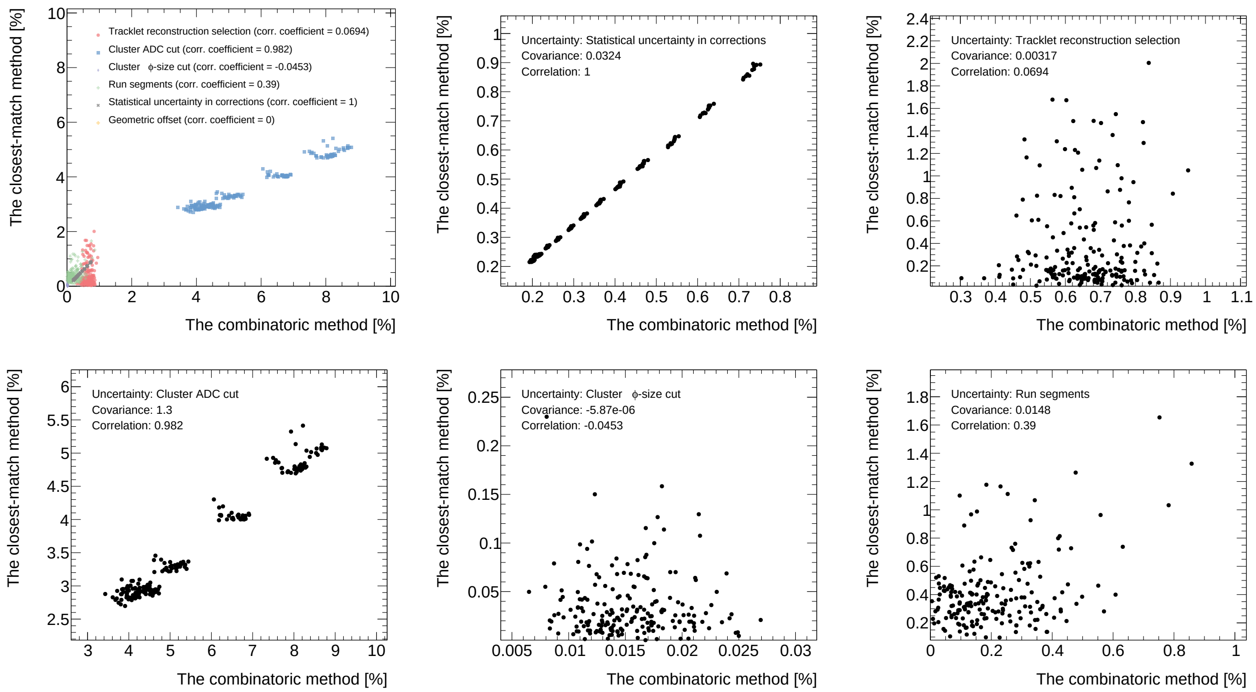

Figure 78: The top-left plot presents all sources of uncertainty on a single canvas, providing a direct comparison of their relative scales. The remaining plots show individual sources of uncertainty separately.

9 Results

Figure 79 shows the $\mathrm{dN_{ch}}/\mathrm{d}\eta$ in data, `HIJING` generator, and `HIJING` simulation closure, and from the PHOBOS measurement [10] in each centrality interval.

Results from the combinatoric and the closest-match methods are statistically combined. Systematic uncertainties are categorized into two groups based on the correlation coefficient: those with a correlation coefficient greater than 0.1 are treated as fully correlated, while those with a correlation coefficient less than 0.1 are considered uncorrelated. The correlated uncertainty on the weighted average result, $\bar{s}$, is calculated:

$$\bar{s} = \frac{\sqrt{\sum_k [(s_{\text{phobos}})_k + (s_{\text{cms}})_k]^2}}{2}$$

The weighted average of the two approaches and the uncorrelated uncertainty on the weighted average result, $\sigma_{X,i}$, are computed as:

$$\bar{X} \pm \sigma_X = \frac{\sum_i w_i X_i}{\sum_i w_i} \pm \left(\sum_i w_i \right)^{-1/2}, \quad \text{where} \quad w_i = \frac{1}{(\sigma_{X,i})^2}$$

where X_i and $\sigma_{X,i}$ represent the value and uncorrelated uncertainty reported by the two approaches. The total uncertainty of the weighted average result is obtained by:

$$\sigma_{\text{total}} = \sqrt{\bar{s}^2 + \sigma_X^2}$$

Figure 81 presents the measured $\mathrm{dN_{ch}}/\mathrm{d}\eta$ spectra in all centrality classes. Results from both analysis methods are compatible with the PHOBOS measurement within uncertainty.

Figure 80 shows the ratio of $\mathrm{dN_{ch}}/\mathrm{d}\eta$ results from both analysis methods for the 20–25% centrality interval, showing consistency with unity within uncertainties. The uncertainty is fully propagated using the covariance matrix[6].

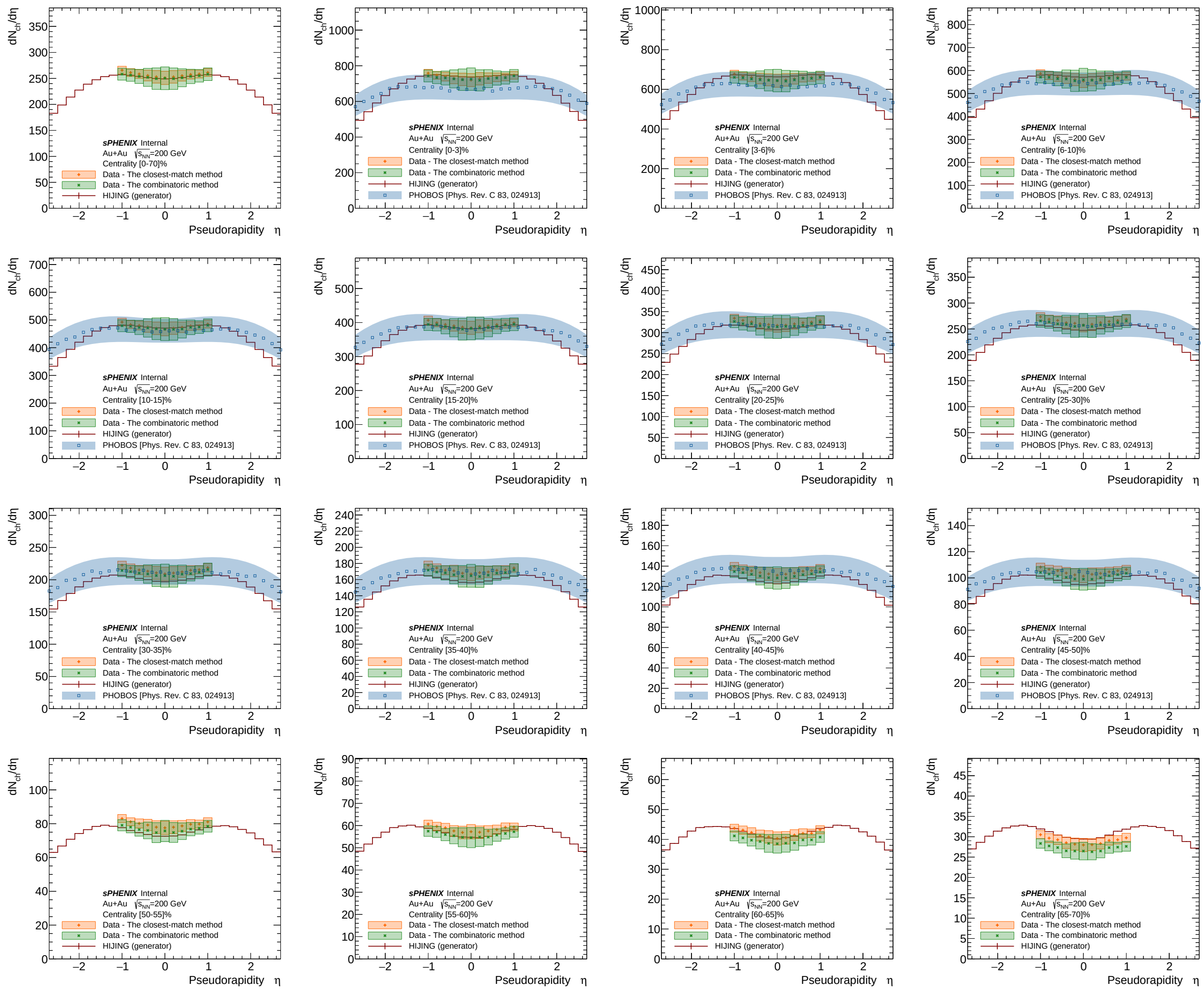

Figure 79: The $\mathrm{dN_{ch}}/\mathrm{d}\eta$ distributions in from `HIJING` generator, simulation closure, data, and the PHOBOS measurement in each centrality interval.

The centrality dependence of the average $\mathrm{dN_{ch}}/\mathrm{d}\eta$ at midrapidity is shown in Figure 82 and is compared to previous measurements at RHIC. The $\mathrm{dN_{ch}}/\mathrm{d}\eta$ normalized by $\langle N_{\mathrm{part}}$ $\rangle$ is also shown as a function of $\langle N_{\mathrm{part}}\ \rangle$ in Figure 82. The midrapidity charged-hadron multiplicities, the number of participants, and the charged hadron multiplicities normalized to the number of participant pairs, $\langle N_{\mathrm{part}}\ \rangle/2$, are summarized in Table 8.

[6]For $f = \frac{A}{B}$, the standard deviation of f, $\sigma_f = \sqrt{(\frac{\sigma_A}{A})^2 + (\frac{\sigma_B}{B})^2 - 2\frac{\sigma_{AB}}{AB}}$, where $\sigma_{AB} = \rho\sigma_A\sigma_B$ and ρ is the correlation coefficient.

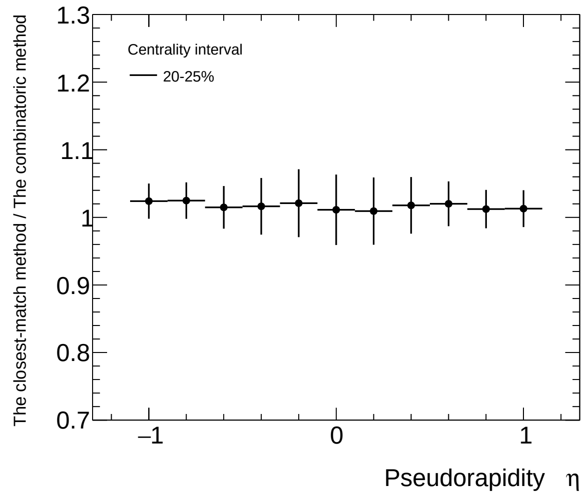

Figure 80: The ratio of $\mathrm{dN_{ch}}/\mathrm{d}\eta$ results from both analysis methods.

Discussion

Results from both the combinatoric and the closest-match methods are consistent with previous measurements within uncertainties. The $\mathrm{dN_{ch}}/\mathrm{d}\eta$ results from the closest-match method align with the trends observed in the cluster- and tracklet-level distributions (Figure 22 and 53), where data show a higher count of clusters and uncorrected tracklets compared to simulation. Since the α correction factors remain approximately uniform across the η range within the defined acceptance (Figure 61), the corrected tracklet and $\mathrm{dN_{ch}}/\mathrm{d}\eta$ distributions are expected to follow the same trend as the uncorrected cluster and tracklet distributions.

10 Conclusion

This note details the measurement of charged-hadron multiplicity per unit pseudorapidity, $\mathrm{dN_{ch}}/\mathrm{d}\eta$, using field-off data from Run 2024 in Au+Au collisions at $\sqrt{s_{NN}} = 200\,\mathrm{GeV}$, collected with the sPHENIX detector. Results are presented as a function of η across different centrality intervals. The $\mathrm{dN_{ch}}/\mathrm{d}\eta$ increases for more central events, and the average $\mathrm{dN_{ch}}/\mathrm{d}\eta$ per participant pair, $N_{\mathrm{part}}/2$, also exhibits a mild increase with increasing N_{part}. Both trends are consistent with previous measurements reported by PHOBOS, PHENIX, and BRAHMS. The sPHENIX measurement, which combines two analysis methods, achieves a [1.6][7]reduction in uncertainty compared to previous RHIC results using the tracklet method, featuring full 2π azimuthal coverage at mid-rapidity and presenting charged particle multiplicity as a function of pseudorapidity. The analysis also serves an essential commissioning purpose, by demonstrating the capabilities of several new detector components and their agreement with established physics results, which will further enable the broader sPHENIX physics program.

[7] This value is based on our current conservative estimate including all sources of uncertainty. The finalized number will be updated when the full set of uncertainties are evaluated and included. The current results are obtained using (1) `HIJING` simulations generated with an older version of the MVTX geometry and (2)

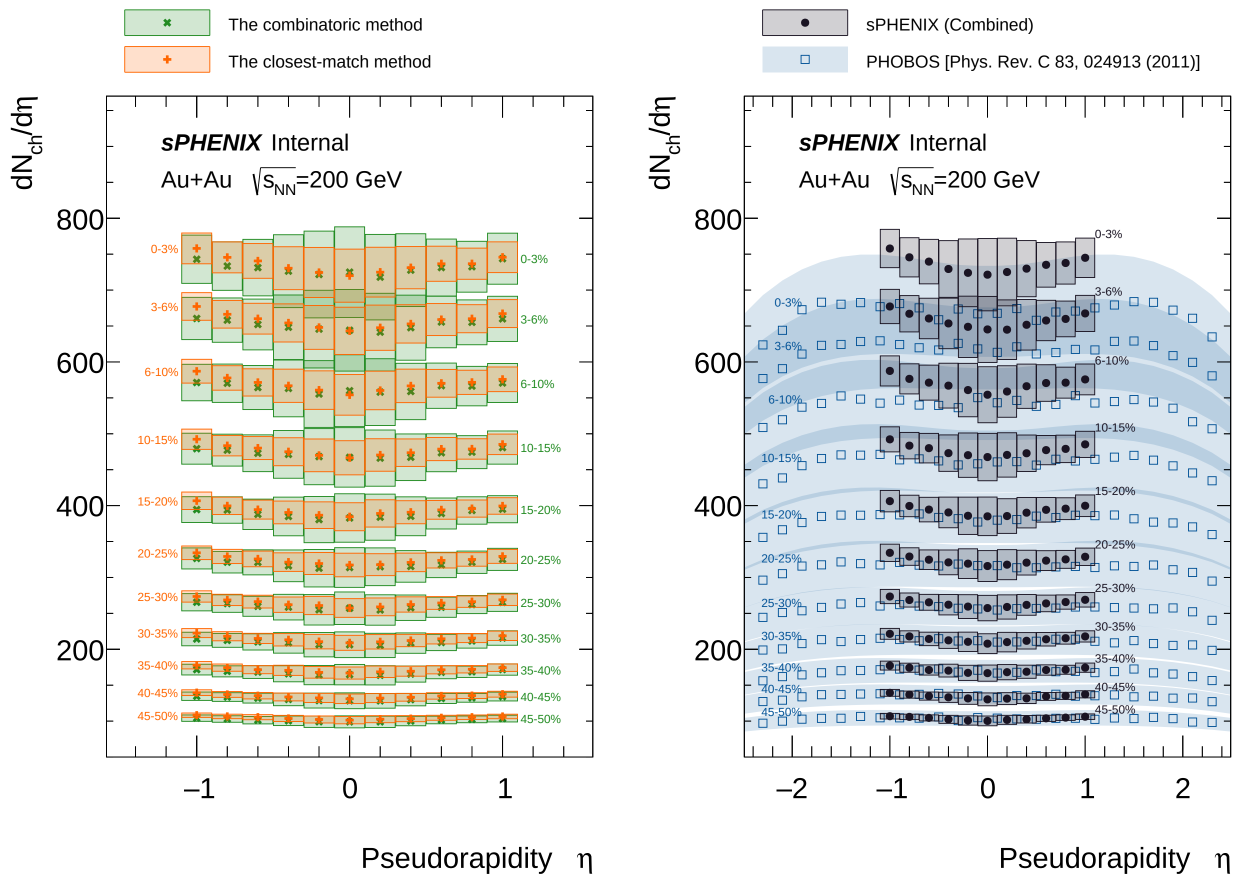

Figure 81: $\mathrm{dN_{ch}/d}\eta$ distributions in different centrality intervals.

a partial set of systematic uncertainties, as noted in the footnotes of previous sections. Full results will be provided for the second circulation.

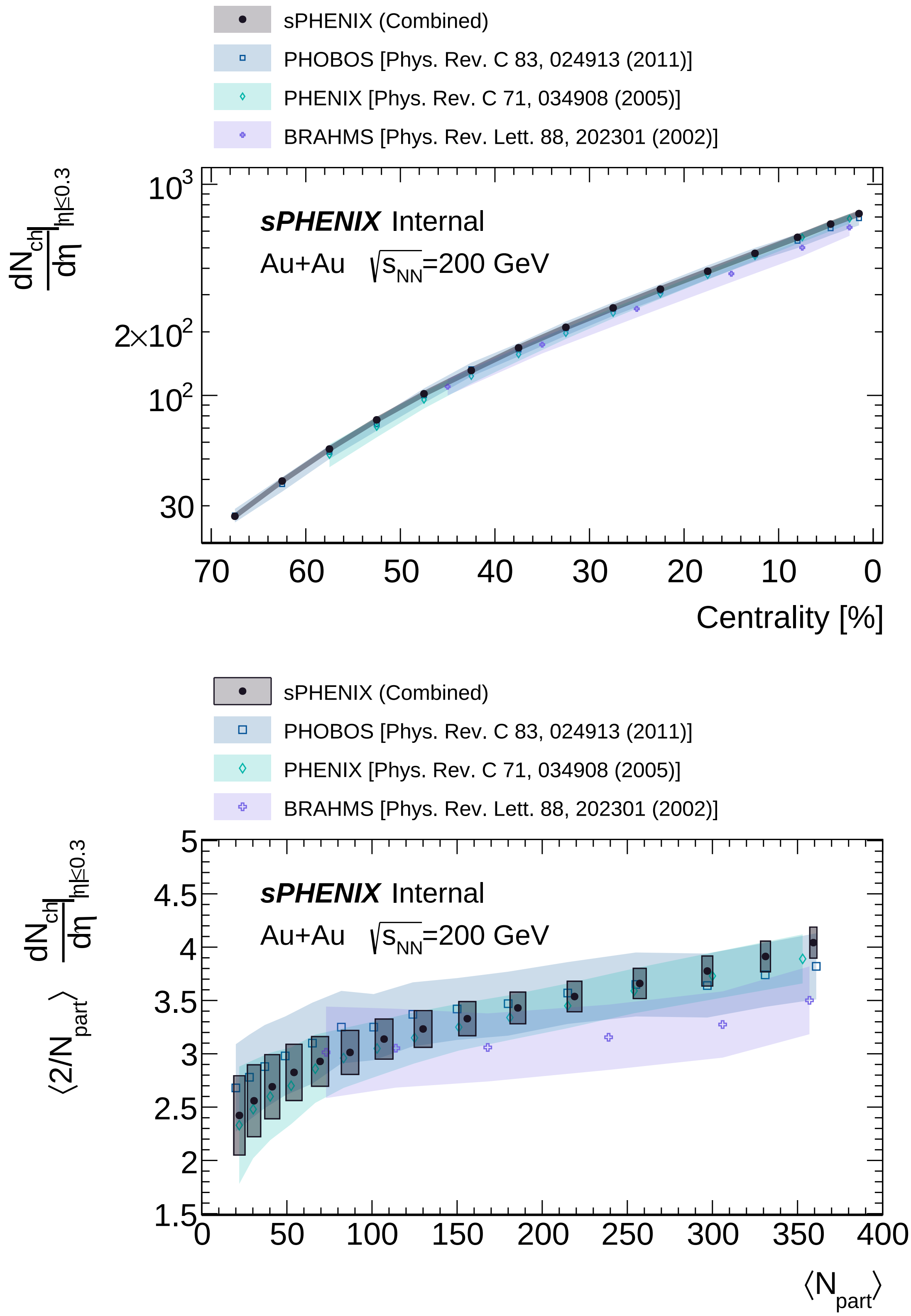

Figure 82: (Top) $dN_{ch}/d\eta$ at midrapidity as a function of centrality intervals. (Bottom) The average $dN_{ch}/d\eta$ at midrapidity normalized by $\langle N_{part} \rangle$ as a function of $\langle N_{part} \rangle$.

Table 8: Summary of the midrapidity charged-hadron multiplicities, the number of participants, and the charged hadron multiplicities normalized to the number of participant pairs $\langle N_{\text{part}} \rangle/2$.

Bin	$\frac{d\mathbf{N_{ch}}}{d\eta}\|_{\|\eta\|\leq 0.3}$	N_{part}	$\frac{\mathrm{dN_{ch}/d}\eta\|_{\|\eta\|\leq 0.3}}{\mathrm{N_{part/2}}}$
0%-3%	726.2 ± 25.8	359.3 ± 2.1	4.0 ± 0.1
3%-6%	647.9 ± 23.2	331.2 ± 2.9	3.9 ± 0.1
6%-10%	560.7 ± 20.0	297.0 ± 3.2	3.8 ± 0.1
10%-15%	470.8 ± 16.9	257.3 ± 3.8	3.7 ± 0.1
15%-20%	387.3 ± 13.7	219.0 ± 4.3	3.5 ± 0.1
20%-25%	318.5 ± 11.3	185.7 ± 4.6	3.4 ± 0.1
25%-30%	259.7 ± 9.3	156.0 ± 5.0	3.3 ± 0.2
30%-35%	210.1 ± 7.4	130.0 ± 5.2	3.2 ± 0.2
35%-40%	168.0 ± 5.9	107.1 ± 5.2	3.1 ± 0.2
40%-45%	131.2 ± 4.7	87.1 ± 5.1	3.0 ± 0.2
45%-50%	101.8 ± 3.5	69.5 ± 5.0	2.9 ± 0.2
50%-55%	76.6 ± 2.7	54.2 ± 4.7	2.8 ± 0.3
55%-60%	55.7 ± 1.9	41.4 ± 4.4	2.7 ± 0.3
60%-65%	39.3 ± 1.4	30.7 ± 3.9	2.6 ± 0.3
65%-70%	26.8 ± 1.0	22.1 ± 3.3	2.4 ± 0.4

References

[1] Wit Busza, Krishna Rajagopal, and Wilke van der Schee. Heavy Ion Collisions: The Big Picture, and the Big Questions. Ann. Rev. Nucl. Part. Sci., 68:339–376, 2018. arXiv:1802.04801, doi:10.1146/annurev-nucl-101917-020852.

[2] Paul Romatschke and Ulrike Romatschke. Relativistic Fluid Dynamics In and Out of Equilibrium. Cambridge Monographs on Mathematical Physics. Cambridge University Press, 5 2019. arXiv:1712.05815, doi:10.1017/9781108651998.

[3] Javier L. Albacete and Cyrille Marquet. Gluon saturation and initial conditions for relativistic heavy ion collisions. Prog. Part. Nucl. Phys., 76:1–42, 2014. arXiv:1401.4866, doi:10.1016/j.ppnp.2014.01.004.

[4] Dmitri Kharzeev and Marzia Nardi. Hadron production in nuclear collisions at RHIC and high density QCD. Phys. Lett. B, 507:121–128, 2001. arXiv:nucl-th/0012025, doi:10.1016/S0370-2693(01)00457-9.

[5] David d'Enterria, Ralph Engel, Tanguy Pierog, Sergey Ostapchenko, and Klaus Werner. Constraints from the first LHC data on hadronic event generators for ultra-high energy cosmic-ray physics. Astropart. Phys., 35:98–113, 2011. arXiv:1101.5596, doi:10.1016/j.astropartphys.2011.05.002.

[6] K. Adcox et al. Centrality dependence of charged particle multiplicity in Au - Au collisions at S(NN)**(1/2) = 130-GeV. Phys. Rev. Lett., 86:3500–3505, 2001. arXiv:nucl-ex/0012008, doi:10.1103/PhysRevLett.86.3500.

[7] S. S. Adler et al. Systematic studies of the centrality and s(NN)**(1/2) dependence of the d E(T) / d eta and d (N(ch) / d eta in heavy ion collisions at mid-rapidity. Phys. Rev. C, 71:034908, 2005. [Erratum: Phys.Rev.C 71, 049901 (2005)]. arXiv:nucl-ex/0409015, doi:10.1103/PhysRevC.71.034908.

[8] A. Iordanova et al. U+U and Cu+Au results from PHENIX. Journal of Physics: Conference Series, 458(1):012004, aug 2013. URL: https://dx.doi.org/10.1088/1742-6596/458/1/012004, doi:10.1088/1742-6596/458/1/012004.

[9] B. B. Back et al. Charged particle multiplicity near mid-rapidity in central Au + Au collisions at $S^{(1/2)}$ = 56-A/GeV and 130-A/GeV. Phys. Rev. Lett., 85:3100–3104, 2000. arXiv:hep-ex/0007036, doi:10.1103/PhysRevLett.85.3100.

[10] B. Alver et al. Phobos results on charged particle multiplicity and pseudorapidity distributions in Au+Au, Cu+Cu, d+Au, and p+p collisions at ultra-relativistic energies. Phys. Rev. C, 83:024913, 2011. arXiv:1011.1940, doi:10.1103/PhysRevC.83.024913.

[11] I. G Bearden et al. Charged particle densities from Au+Au collisions at s(NN)**(1/2) = 130-GeV. Phys. Lett. B, 523:227–233, 2001. arXiv:nucl-ex/0108016, doi:10.1016/S0370-2693(01)01333-8.

[12] I. G. Bearden et al. Pseudorapidity distributions of charged particles from Au+Au collisions at the maximum RHIC energy. Phys. Rev. Lett., 88:202301, 2002. arXiv:nucl-ex/0112001, doi:10.1103/PhysRevLett.88.202301.

[13] C. Adler et al. Multiplicity distribution and spectra of negatively charged hadrons in Au+Au collisions at s(NN)**(1/2) = 130-GeV. Phys. Rev. Lett., 87:112303, 2001. arXiv:nucl-ex/0106004, doi:10.1103/PhysRevLett.87.112303.

[14] K Aamodt et al. First proton-proton collisions at the LHC as observed with the ALICE detector: Measurement of the charged particle pseudorapidity density at s**(1/2) = 900-GeV. Eur. Phys. J. C, 65:111–125, 2010. arXiv:0911.5430, doi:10.1140/epjc/s10052-009-1227-4.

[15] K. Aamodt et al. Charged-particle multiplicity measurement in proton-proton collisions at $\sqrt{s}$ = 0.9 and 2.36 TeV with ALICE at LHC. Eur. Phys. J. C, 68:89–108, 2010. arXiv:1004.3034, doi:10.1140/epjc/s10052-010-1339-x.

[16] K. Aamodt et al. Charged-particle multiplicity measurement in proton-proton collisions at $\sqrt{s}$ = 7 TeV with ALICE at LHC. Eur. Phys. J. C, 68:345–354, 2010. arXiv:1004.3514, doi:10.1140/epjc/s10052-010-1350-2.

[17] Jaroslav Adam et al. Pseudorapidity and transverse-momentum distributions of charged particles in proton–proton collisions at $\sqrt{s}$ = 13 TeV. Phys. Lett. B, 753:319–329, 2016. arXiv:1509.08734, doi:10.1016/j.physletb.2015.12.030.

[18] Jaroslav Adam et al. Charged-particle multiplicities in proton–proton collisions at $\sqrt{s}$ = 0.9 to 8 TeV. Eur. Phys. J. C, 77(1):33, 2017. arXiv:1509.07541, doi:10.1140/epjc/s10052-016-4571-1.

[19] S. Acharya et al. Charged-particle multiplicity distributions over a wide pseudorapidity range in proton-proton collisions at $\sqrt{s}$ = 0.9, 7, and 8 TeV. Eur. Phys. J. C, 77(12):852, 2017. arXiv:1708.01435, doi:10.1140/epjc/s10052-017-5412-6.

[20] Shreyasi Acharya et al. Pseudorapidity distributions of charged particles as a function of mid- and forward rapidity multiplicities in pp collisions at $\sqrt{s}$ = 5.02, 7 and 13 TeV. Eur. Phys. J. C, 81(7):630, 2021. arXiv:2009.09434, doi:10.1140/epjc/s10052-021-09349-5.

[21] K Aamodt et al. Charged-particle multiplicity density at mid-rapidity in central Pb-Pb collisions at $\sqrt{s_{NN}}$ = 2.76 TeV. Phys. Rev. Lett., 105:252301, 2010. arXiv:1011.3916, doi:10.1103/PhysRevLett.105.252301.

[22] Jaroslav Adam et al. Centrality Dependence of the Charged-Particle Multiplicity Density at Midrapidity in Pb-Pb Collisions at $\sqrt{s_{\rm NN}}$ = 5.02 TeV. Phys. Rev. Lett., 116(22):222302, 2016. arXiv:1512.06104, doi:10.1103/PhysRevLett.116.222302.

[23] Shreyasi Acharya et al. Centrality and pseudorapidity dependence of the charged-particle multiplicity density in Xe–Xe collisions at $\sqrt{s_{\rm NN}}$ =5.44TeV. Phys. Lett. B, 790:35–48, 2019. arXiv:1805.04432, doi:10.1016/j.physletb.2018.12.048.

[24] CMS Collaboration. Study of Charged Hadron Multiplicity in Minimum Bias p+p Collisions at $\sqrt{s} = 0.9$ and 10 TeV. Technical report, CERN, Geneva, 2009. URL: https://cds.cern.ch/record/1194513.

[25] Vardan Khachatryan et al. Transverse Momentum and Pseudorapidity Distributions of Charged Hadrons in pp Collisions at $\sqrt{s} = 0.9$ and 2.36 TeV. JHEP, 02:041, 2010. arXiv:1002.0621, doi:10.1007/JHEP02(2010)041.

[26] Vardan Khachatryan et al. Transverse-momentum and pseudorapidity distributions of charged hadrons in pp collisions at $\sqrt{s} = 7$ TeV. Phys. Rev. Lett., 105:022002, 2010. arXiv:1005.3299, doi:10.1103/PhysRevLett.105.022002.

[27] Vardan Khachatryan et al. Charged Particle Multiplicities in pp Interactions at $\sqrt{s} = 0.9$, 2.36, and 7 TeV. JHEP, 01:079, 2011. arXiv:1011.5531, doi:10.1007/JHEP01(2011)079.

[28] Serguei Chatrchyan et al. Measurement of pseudorapidity distributions of charged particles in proton-proton collisions at $\sqrt{s} = 8$ TeV by the CMS and TOTEM experiments. Eur. Phys. J. C, 74(10):3053, 2014. arXiv:1405.0722, doi:10.1140/epjc/s10052-014-3053-6.

[29] Vardan Khachatryan et al. Pseudorapidity distribution of charged hadrons in proton-proton collisions at $\sqrt{s} = 13$ TeV. Phys. Lett. B, 751:143–163, 2015. arXiv:1507.05915, doi:10.1016/j.physletb.2015.10.004.

[30] Albert M Sirunyan et al. Pseudorapidity distributions of charged hadrons in proton-lead collisions at $\sqrt{s_{\mathrm{NN}}} = 5.02$ and 8.16 TeV. JHEP, 01:045, 2018. arXiv:1710.09355, doi:10.1007/JHEP01(2018)045.

[31] Serguei Chatrchyan et al. Dependence on pseudorapidity and centrality of charged hadron production in PbPb collisions at a nucleon-nucleon centre-of-mass energy of 2.76 TeV. JHEP, 08:141, 2011. arXiv:1107.4800, doi:10.1007/JHEP08(2011)141.

[32] CMS Collaboration. Pseudorapidity distributions of charged hadrons in PbPb collisions at $\sqrt{s_{\mathrm{NN}}} = 5.36$ TeV. Technical report, CERN, Geneva, 2023. URL: https://cds.cern.ch/record/2871619.

[33] Albert M Sirunyan et al. Pseudorapidity distributions of charged hadrons in xenon-xenon collisions at $\sqrt{s_{\mathrm{NN}}} = 5.44$ TeV. Phys. Lett. B, 799:135049, 2019. arXiv:1902.03603, doi:10.1016/j.physletb.2019.135049.

[34] Georges Aad et al. Measurement of the centrality dependence of the charged-particle pseudorapidity distribution in proton–lead collisions at $\sqrt{s_{\mathrm{NN}}} = 5.02$ TeV with the ATLAS detector. Eur. Phys. J. C, 76(4):199, 2016. arXiv:1508.00848, doi:10.1140/epjc/s10052-016-4002-3.

[35] Georges Aad et al. Measurement of the centrality dependence of the charged particle pseudorapidity distribution in lead-lead collisions at $\sqrt{s_{NN}} = 2.76$ TeV with the ATLAS

detector. Phys. Lett. B, 710:363–382, 2012. arXiv:1108.6027, doi:10.1016/j.physletb.2012.02.045.

[36] Alexander Milov. Charged particle multiplicity measurement in Au-Au collisions using the Pad Chambers of the PHENIX detector at RHIC , May 2002. doi:10.5281/zenodo.3983557.

[37] C.-W. Shih. The commissioning status of the intermediate silicon tracker of sPHENIX. EPJ Web Conf., 296:02006, 2024. doi:10.1051/epjconf/202429602006.

[38] James R. Hoff, Tom N. Zimmerman, Raymond J. Yarema, Jon S. Kapustinsky, and Melynda L. Brookes. Fphx: A new silicon strip readout chip for the phenix experiment at rhic. In 2009 IEEE Nuclear Science Symposium Conference Record (NSS/MIC), pages 75–79, 2009. doi:10.1109/NSSMIC.2009.5401873.

[39] sPHENIX INTT detector group. The ladder and readout cables of intermediate silicon strip detector for sphenix. Draft on sPHENIX INVENIO, 2024. URL: https://sphenix-invenio.sdcc.bnl.gov/communities/sphenixcommunity/requests/af9ca02b-78ed-4155-a2fd-a183073b063a.

[40] Joaquin Hoya. FELIX: first operational experience with the new ATLAS readout system and perspectives for HL-LHC. Technical report, CERN, Geneva, 2024. URL: https://cds.cern.ch/record/2871991, doi:10.1051/epjconf/202429502012.

[41] sPHENIX Collaboration. Commissioning status: August 2023, 2023. Indico: https://indico.bnl.gov/event/20373/attachments/49393/84311/Commissioning_Status_August_2023.pdf.

[42] sPHENIX INTT group. INTT FELIX. INTT FELIX twiki page, 2024. URL: https://wiki.sphenix.bnl.gov/index.php?title=INTT_FELIX.

[43] sPHENIX Collaboration. sPHENIX Centrality Calibration for Run-24 Au+Au Collisions at $\sqrt{s_{NN}}$ =200 GeV, 2025. sPHENIX note on Invenio: https://sphenix-invenio.sdcc.bnl.gov/records/qzphw-g0h72.

[44] Hao-Ren Jheng et al. INTT survey geometry. Analysis report on sPHENIX Indico, 2024. URL: https://indico.bnl.gov/event/22918/#16-intt-survey-geometry.

[45] Hao-Ren Jheng et al. MVTX geometry. Analysis report on sPHENIX Indico, 2024. URL: https://indico.bnl.gov/event/24940/#14-mvtx-geometry-update.

[46] T. Miao, H. Wenzel, F. Yumiceva, and N. Leioatts. Beam position determination using tracks, 8 2007.

[47] sPHENIX Collaboration. INTT vertex reconstruction, 2024. sPHENIX note on Invenio: https://sphenix-invenio.sdcc.bnl.gov/communities/sphenixcommunity/requests/717c5d51-65dc-4a5b-877b-bc19789f21f7.

Appendices

A INTT bad channel masks

This section shows the supporting plots for the INTT hot, dead, and cold channel masks. Figure 83–86 show the distributions of channels classified as hot, dead, cold, and good, respectively.

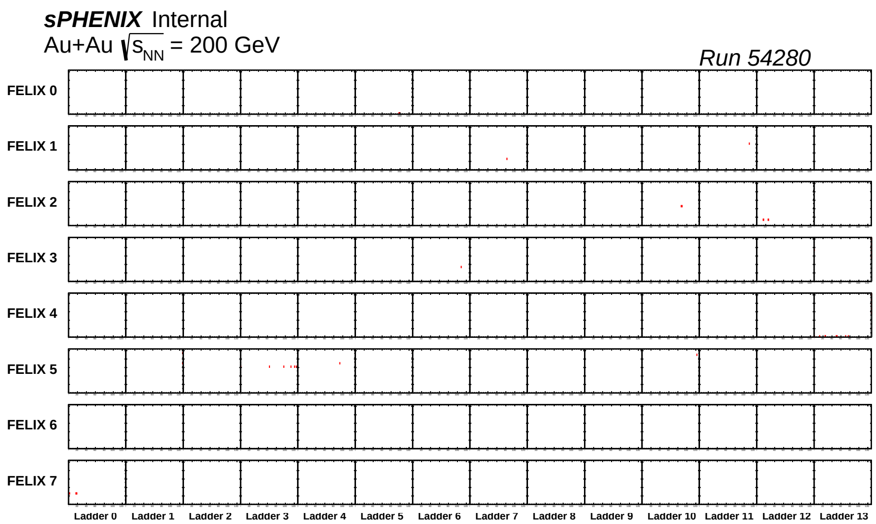

Figure 83: The map of hot channels of run 54280.

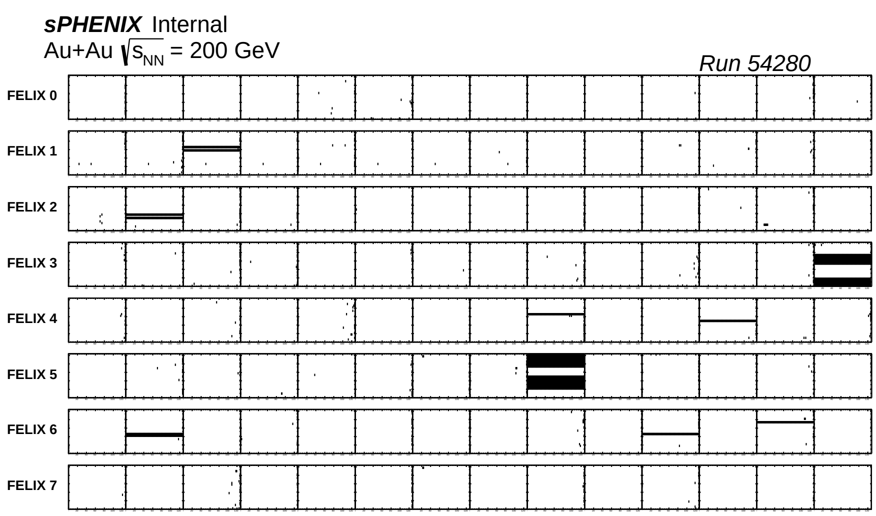

Figure 84: The map of dead channels of run 54280.

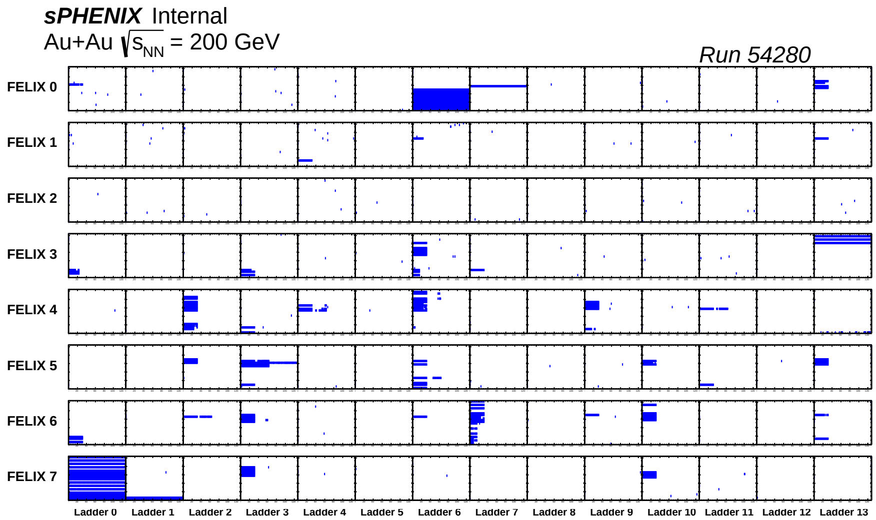

Figure 85: The map of cold channels of run 54280.

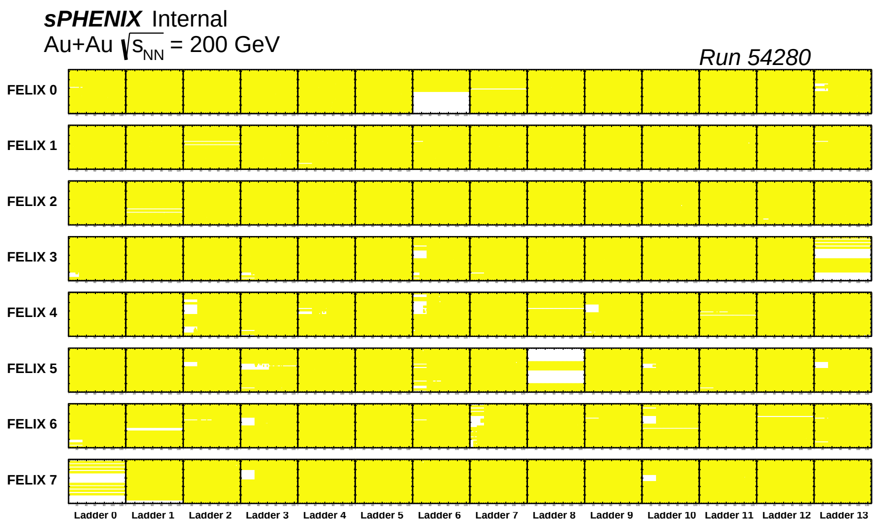

Figure 86: The map of good channels of run 54280.

B INTT geometry with survey measurement

(Numbers are quoted with 4 significant figures for consistency throughout this section.)

The survey measurement performed after the installation of INTT indicated a gap between two INTT half barrels. This gap is reflected as dips in the azimuthal angle distribution of the INTT strips, as shown in Figure 87.

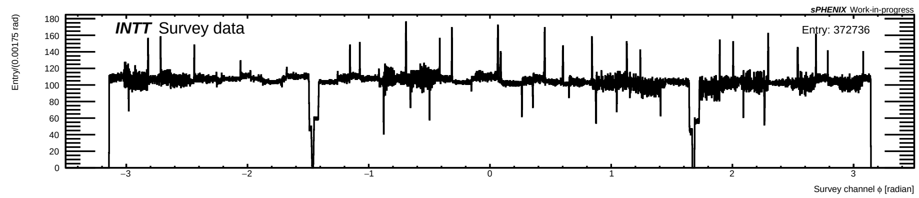

Figure 87: Azimuthal angle distribution of INTT channels, calculated from the survey measurement.

The INTT Geant4 geometry model is modified accordingly to account for the acceptance difference between ideal and misaligned detector placement. The following list describes the modifications:

1. The dimensions of the Geant4 volume representing the space between the active area and the stave peek are updated from an incorrect default value of 7.622 mm to 0.8000 mm based on the production design.

2. The equivalent specifications of the metal and carbon support rings representing the INTT stave peek and the INTT ladder support structure at both ends of INTT barrel are updated from 0.5000 cm to 0.7500 cm and from 0.7500 cm to 0.3125 cm in length respectively. The radii of both rings are updated such that an equivalent material budget as the production design is achieved. The detail is shown in Figure 88.

3. The physical position along the sPHENIX Z-axis of both support rings is automatically adjusted by accurately setting the values of their lengths (see item 2).

4. The center position of both support rings and the inner and outer barrel support skins with respect to the sPHENIX origin is adjusted according to the averaged X and Y positions of all INTT ladders based on the survey, which corresponds to 0.4025 mm and -2.886 mm in both X and Y axes, respectively.

5. The sensor's positions and rotations relative to the ladder remain unchanged with the default ideal geometry. The translations and rotations of the sensor relative to the sPHENIX coordinates are adjusted according to the survey measurement of the physical ladder to which the sensor belongs. These adjustments include (a) the translation in the X and Y directions of the individual ladder, (b) the average translation in the Z direction of all ladders, and (c) the rotation around the Z-axis of the ladder (which is parallel to the sPHENIX Z-axis).

6. A shift in the Z direction with respect to the sPHENIX origin is applied to both support rings and the inner and outer barrel support skins according to the average translation in the Z direction of all ladders.

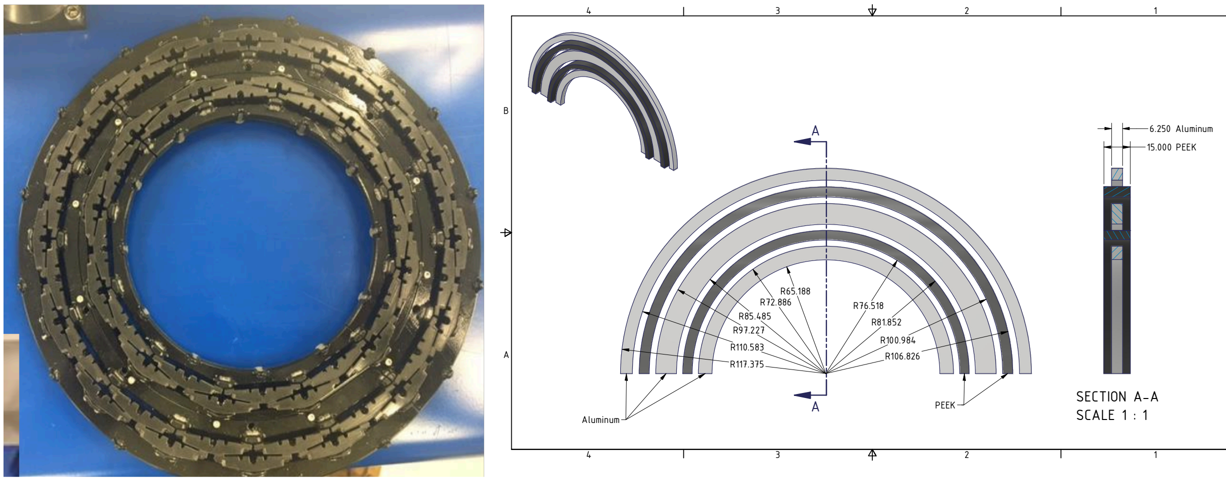

Figure 88: (Left) Mock module of the INTT endcap support structure. (Right) Simplified GEANT4 volume design of the INTT endcap support structure.

An offset is applied to account for various factors when translating the survey measurement to the X and Y coordinates of the GEANT4 physical volume placement for the INTT ladder. This offset encompasses the point where the survey probe touches the ladder's surface (illustrated by the dashed green line in Figure 89), as well as the thicknesses of the sensor (the bottom red box in Figure 89), glue, high-density interface (the blue box above the sensor), and carbon fiber plate (the grey shape above the high-density interface). A 0.2282 mm radially inward is given to the offset, derived by subtracting the distance of 2.386 mm between the survey measurement point and the bottom of the sensor from the 2.158 mm between the center of the INTT GEANT4 physical volume and the sensor's bottom.

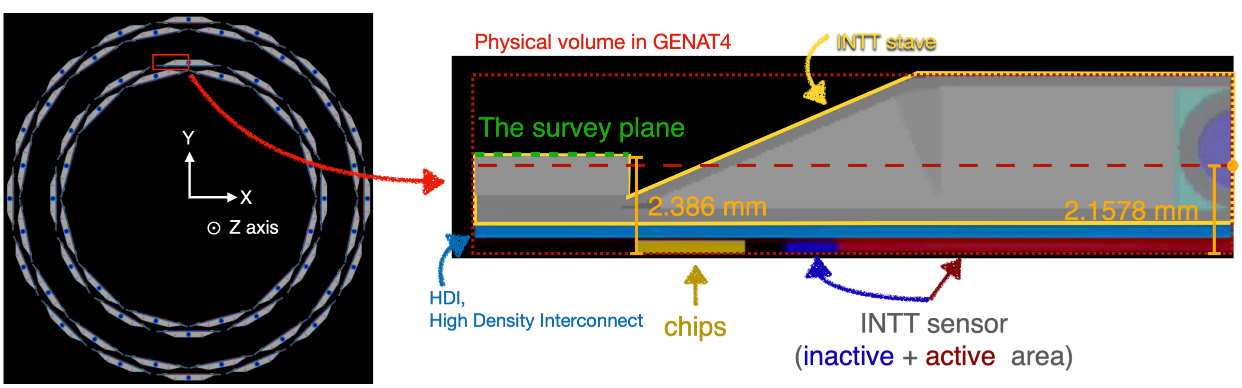

Figure 89: The drawing presents the amount of correction.

The center of INTT half barrels on the transverse plane is determined by averaging the X and Y positions of the ladders obtained from the survey measurement and found to be shifted to (0.4027 mm, −2.887 mm) relative to the ideal position at (0.000 mm, 0.000 mm). Figure 90 shows the center position of ladders in the ideal GEANT4 geometry (in red) and as measured from the survey (in blue).

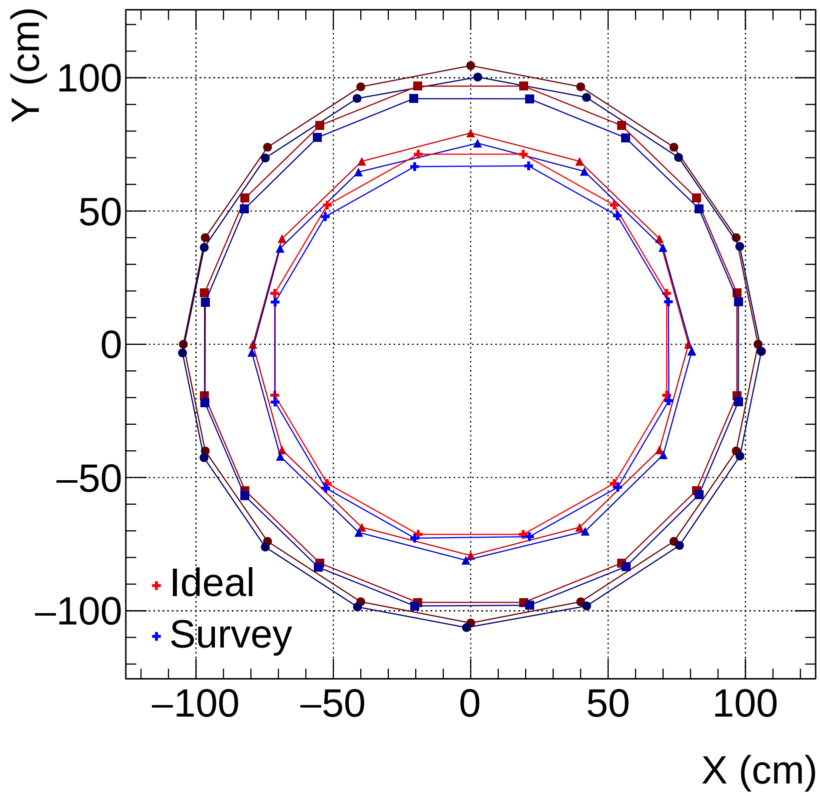

Figure 90: The center position of ladders in the ideal GEANT4 geometry (in red) and as measured from the survey (in blue).

The INTT ladders are shifted individually along the sPHENIX Z-axis, as shown in Figure 91, resulting in an average displacement of −4.724 mm relative to the nominal position at 0 mm. The standard deviation of these longitudinal shifts is 0.1904 mm, an order of magnitude smaller than the mean shift. Consequently, a uniform translation in the Z position of the sensor is applied, as outlined in item 5 of the preceding list.

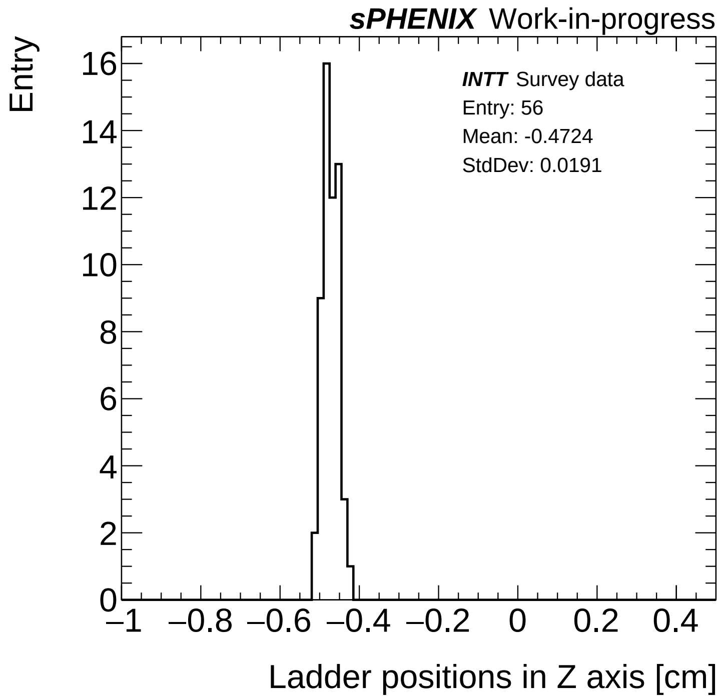

Figure 91: Center positions in the Z direction of all ladders according to the survey.

A sample of 100 simulated events is generated using the single-particle generator in the sPHENIX simulation production framework to verify the updated geometry. Within each event, 2000 charged pions are uniformly sampled in $-\pi \leq \phi \leq \pi$ and $-1 \leq \eta \leq 1$. The resulting ϕ and η distributions of reconstructed clusters, referred to as TrkrCluster in the sPHENIX software, are shown in Figure 92. The visible dips in the cluster ϕ distribution are consistent with those shown in Figure 87.

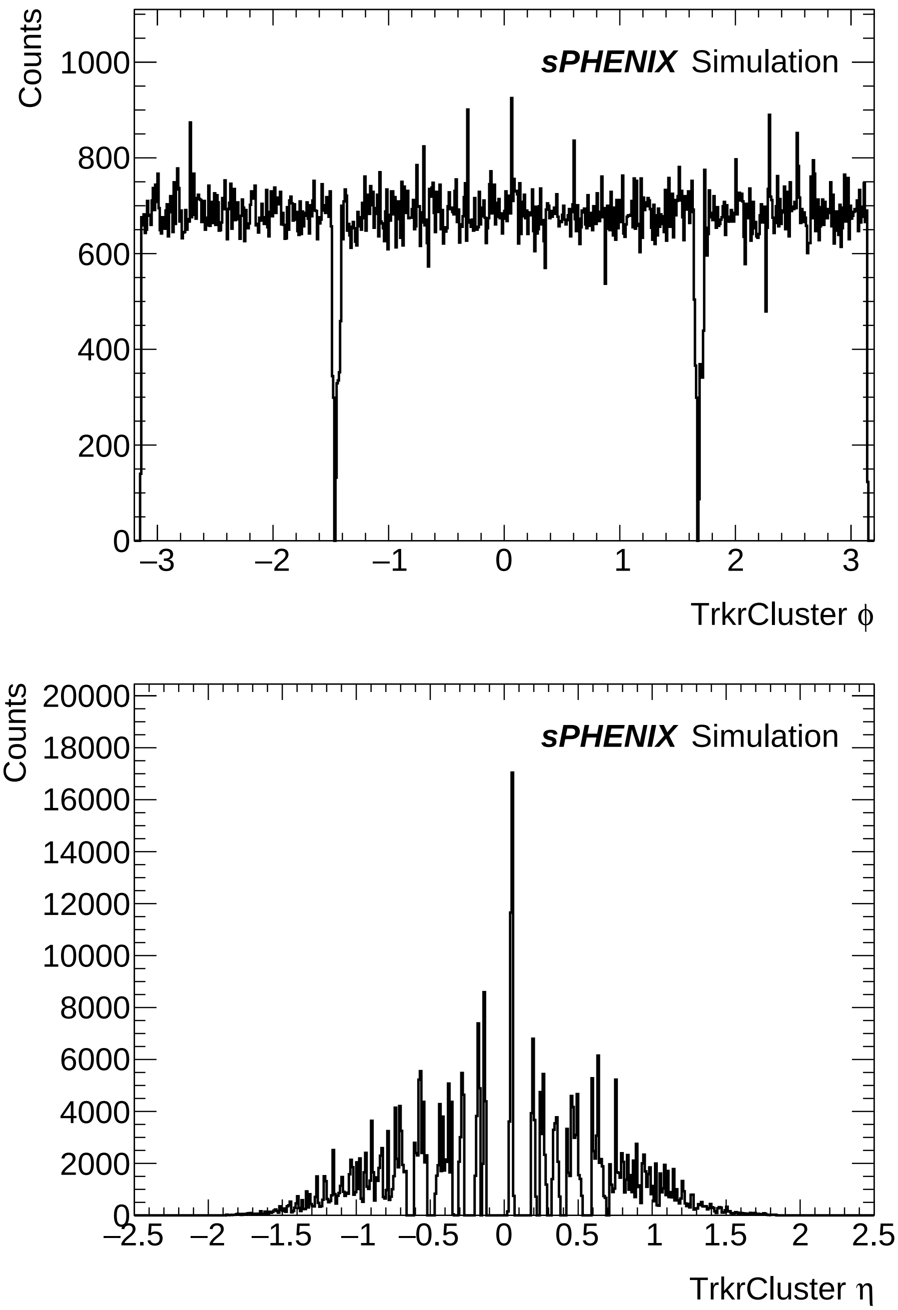

Figure 92: The cluster ϕ and η distributions of single-particle events.

The final implementation can be found at the sPHENIX GitHub coresoftware repository. Packages that are modified for the final deployment of the updated geometry include:

- simulation/g4simulation/g4intt: https://github.com/sPHENIX-Collaboration/coresoftware/tree/master/simulation/g4simulation/g4intt
- offline/packages/intt: https://github.com/sPHENIX-Collaboration/coresoftware/tree/master/offline/packages/intt

- offline/packages/trackreco: https://github.com/sPHENIX-Collaboration/coresoftware/tree/master/offline/packages/trackreco

Two pull requests for integrating the modifications into the sPHENIX software framework are

- sPHENIX-Collaboration/macros: https://github.com/sPHENIX-Collaboration/macros/pull/790

- sPHENIX-Collaboration/coresoftware: https://github.com/sPHENIX-Collaboration/coresoftware/pull/2595

sPHENIX Jenkins continuous integration system performs various quality assurance tests. The resulting build and test reports include diagnostic plots for QA, which can be accessed from the links provided.

C Supplementary plots for cluster distributions

This section presents additional cluster distributions in data and simulation. The selection criteria have been slightly relaxed, with no cuts applied to the cluster ϕ-size and ADC.

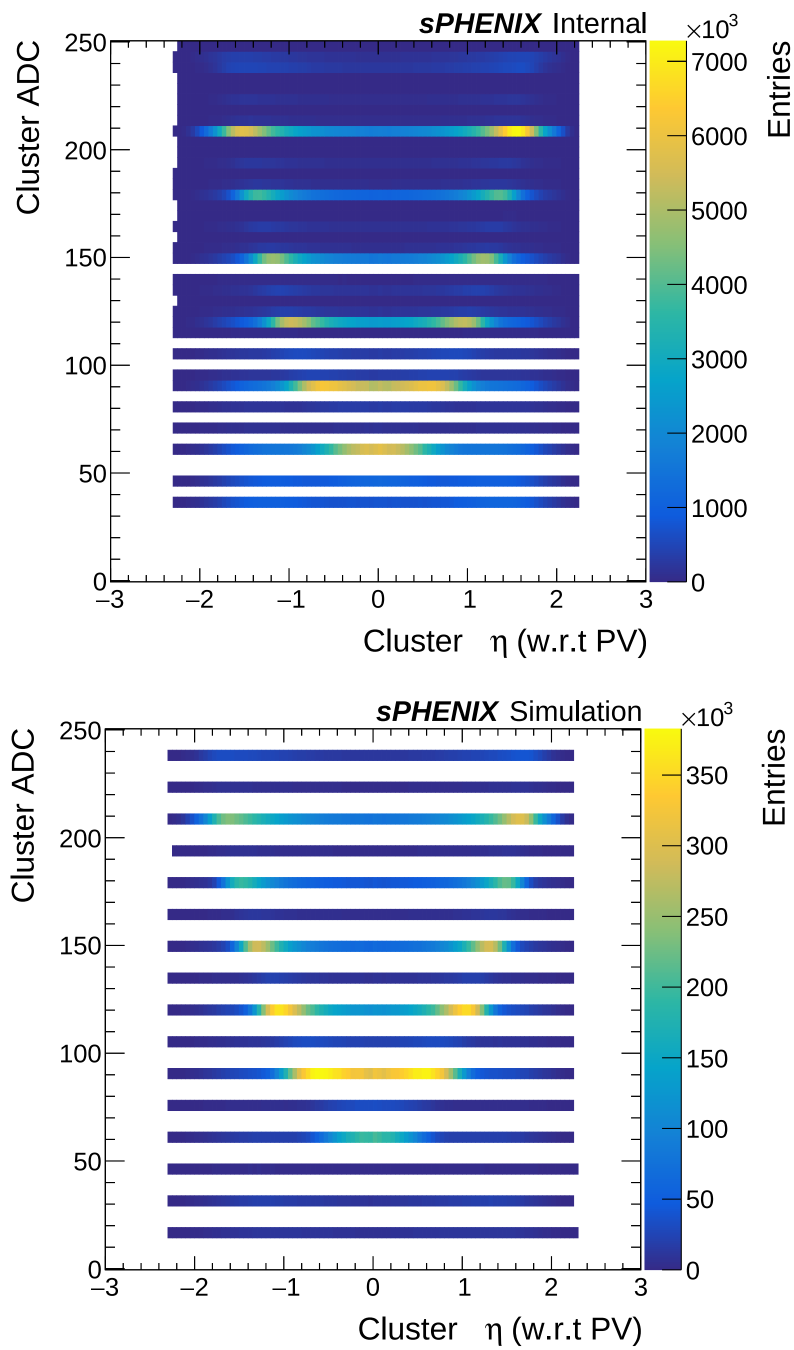

Figure 93: The cluster η versus cluster ADC in data (top) and simulation (bottom).

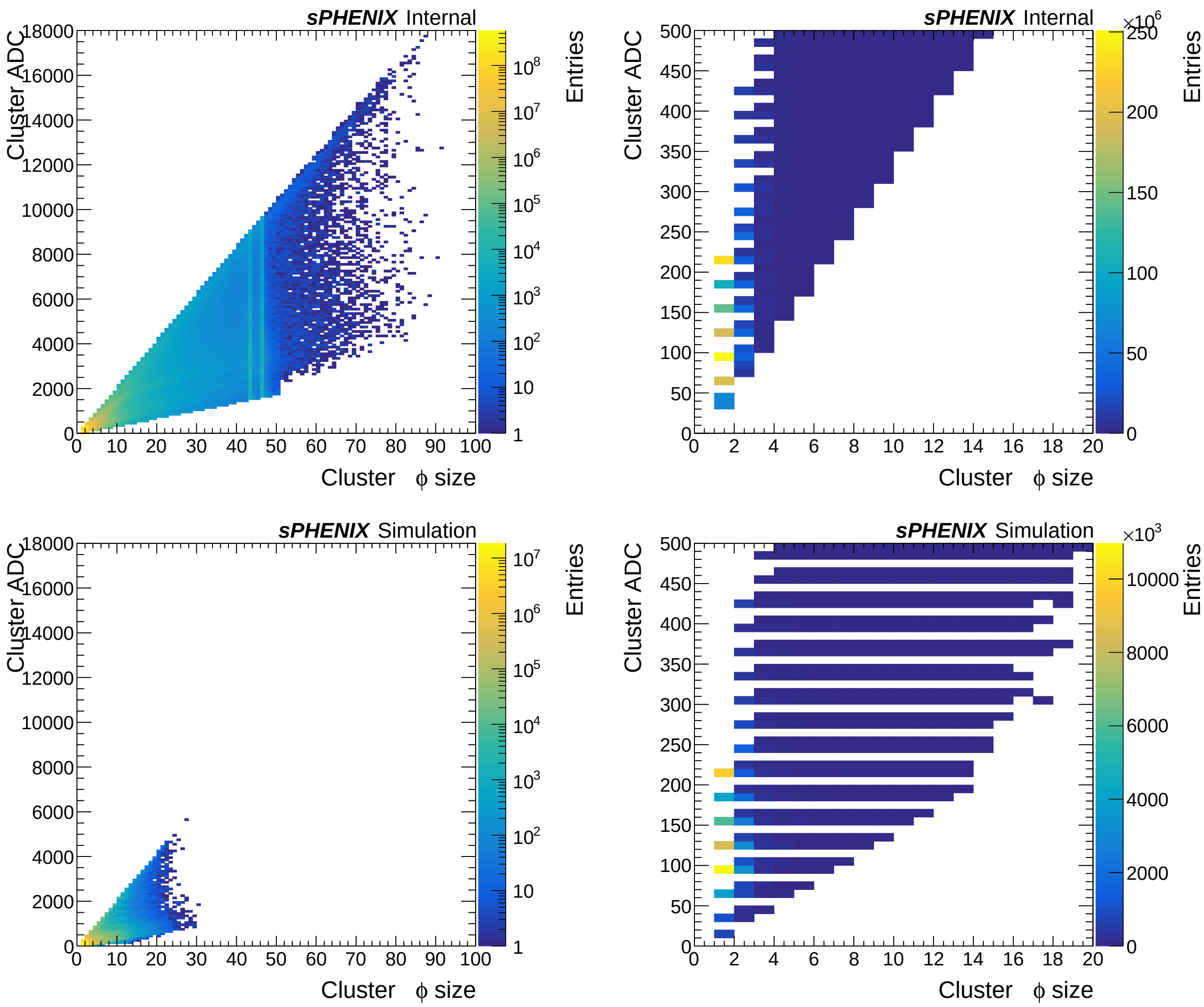

Figure 94: The cluster ϕ-size versus cluster ADC distributions are shown for data (top) and simulation (bottom). The plots on the left display a wider axis range, while those on the right provide a zoomed-in view.

D Discrepancy in cluster ϕ-size and ADC distributions between data and simulation

A simplified model is implemented in the Fun4All module, PHG4InttHitReco, to approximate charge diffusion in silicon. For each charged particle passing through the active region, a column with a fixed radius, referred to as the diffusion radius, is defined to represent the range of charge diffusion. A check is then performed to determine whether this column overlapped with a strip and to calculate the overlapping area. This overlap is used to assign the energy deposit to the strip, assuming a uniform energy profile across the column's cross-section. After the charge diffusion step, clustering is performed by grouping adjacent strips with non-zero energy deposits. The cluster ϕ-size is determined as the number of strips with non-zero energy deposits within a cluster, while the cluster ADC is calculated as the sum of the ADC values of those strips.

A control sample of clusters is defined and constructed to enable a fair comparison between data and simulation and to ensure that the selected clusters primarily originate from collisions rather than beam background. First, hits are clustered using the standard Z-clustering algorithm. From the resulting collection of clusters, those with a pseudorapidity $|\eta| < 0.1$ and a cluster Z-size of 1 are selected. These criteria ensure that the selected clusters are most likely produced by particles incident perpendicularly to the INTT strips.

Figure 95 compares the cluster ϕ-size and ADC distributions of the control sample in data against simulations using different diffusion parameters. The distributions of data without Z-clustering are normalized to 1, while the distributions with Z-clustering are scaled based on the ratio of their integral to the non-Z-clustered data. In simulations with a large diffusion radius, the cluster ϕ-size and ADC values can extend to the maximum observed in the data. However, the shapes of the simulated distributions deviate from the data in the intermediate region. In addition, the data-to-simulation ratios for both cluster ϕ-size and ADC deviate from 1, indicating that none of the tested diffusion radii in the simulation fully reproduce the observed behavior in data.

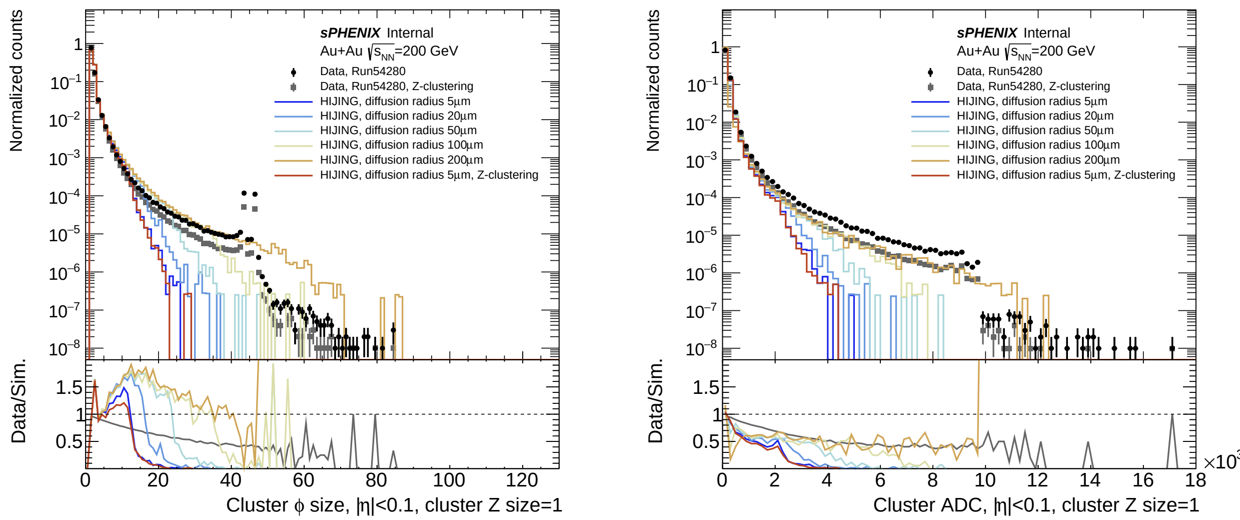

Figure 95: The cluster ϕ-size (left) and ADC (right) distributions of the selected control sample in data and simulations with different diffusion parameters.

The beamspot, event vertex, and tracklet reconstructions in the closest method are performed on simulation samples with different diffusion radii. Figure 96 presents the cluster η and the reconstructed tracklet distributions in data and simulations with varying diffusion parameters. Notably, the shapes of the distributions for simulations with large diffusion radii differ significantly from those with smaller diffusion parameters. This difference can be explained by the fact that, for a large diffusion radius, a particle in the simulation spreads its energy deposits across multiple strips. As a result, the constant cluster ADC cut disproportionately impacts the low-η region, leading to a distorted distribution.

The substantial difference in the tracklet η distributions for simulations with a large diffusion radius introduces significant variation in the correction factor compared to simulations with smaller diffusion parameters. This variation results in a large systematic effect when the diffusion parameter is varied. Consequently, the baseline analysis uses simulations with the default diffusion parameter of 5μm.

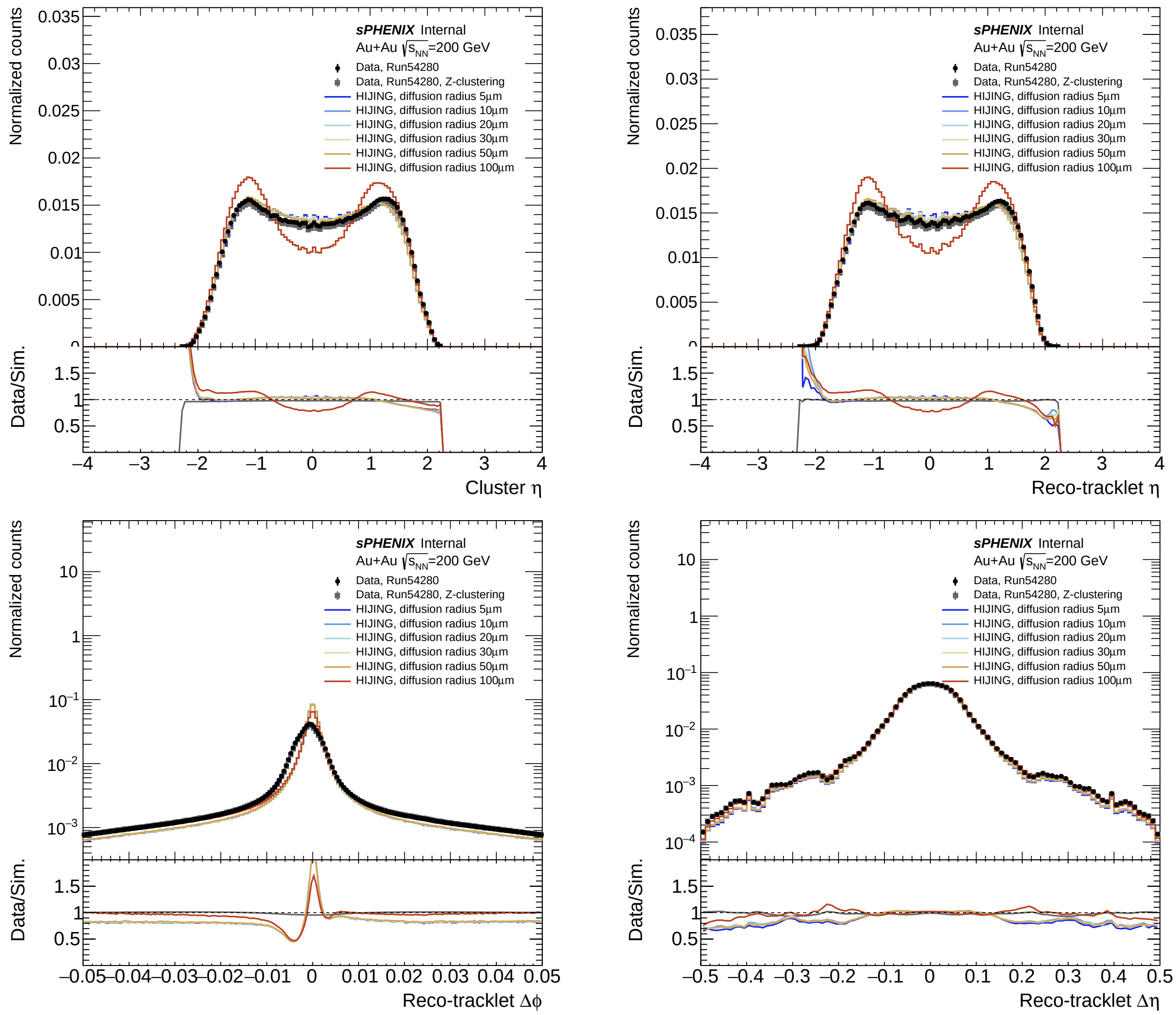

Figure 96: The cluster η (top left) reconstructed tracklet η (top right), $\Delta\phi$ (bottom left), and $\Delta\eta$ (bottom right) distributions in data and simulations with different diffusion parameters.

E Supplementary plots for vertex reconstruction in the combinatoric method

The $\Delta\phi$ and DCA cuts used in proto-tracklets selection for vertex Z reconstruction are 0.6 degrees and 0.1 cm, respectively. This is supported by the previous cut scan study with the simulation sample of run 20869, as shown in Figure 97.

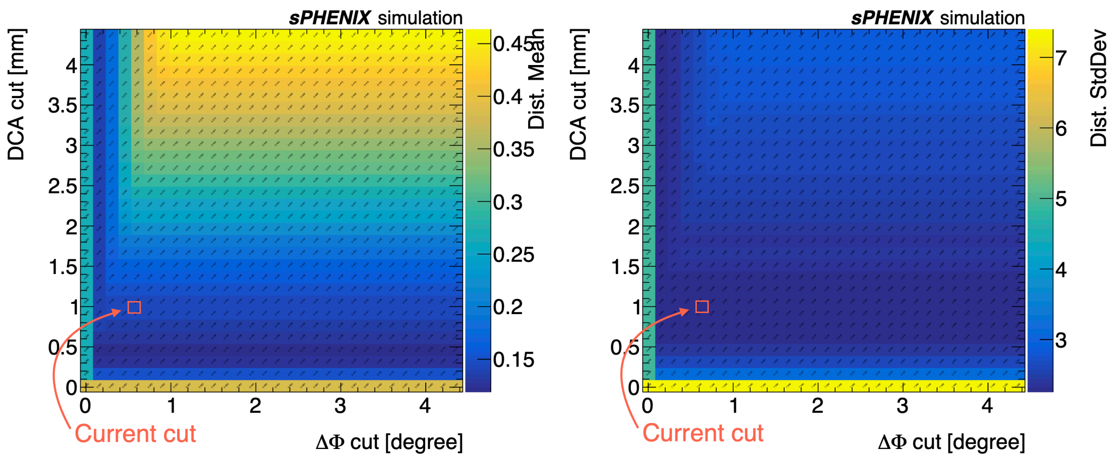

Figure 97: The mean (left) and standard deviation (right) of the ΔZ distribution as a function of $\Delta\phi$ and DCA cuts, where ΔZ is the difference between INTT vtxZ and truth vertex Z.

The vertex Z reconstruction performance is studied with simulation sample of run 54280, as shown in Figure 98, and Figure 99 for the high multiplicity events. The wiggling structure observed in the correlation between ΔZ, the difference between INTT vtxZ and truth vertex Z, and truth vertex Z is expected to be due to the intrinsic INTT sensor geometry. The vertex Z reconstruction resolution of 0.15 mm is measured for the high-multiplicity events, which is more than one order of magnitude smaller than the INTT strip length, 1.6 or 2.0 cm. The INTT vertex Z reconstruction efficiency is shown in Figure 100, where the efficiency is defined as the fraction of the number of events with $\Delta Z < 1$ cm. The efficiency of vertex Z reconstruction is consistently at unity up to centrality 70%.

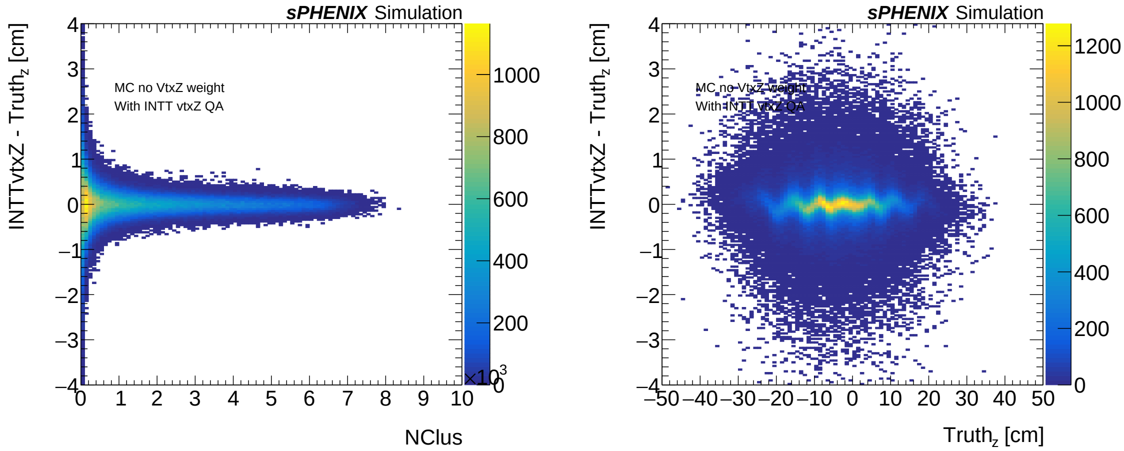

Figure 98: Left: The ΔZ as a function of number of INTT clusters. Right: The ΔZ as a function of truth vertex Z.

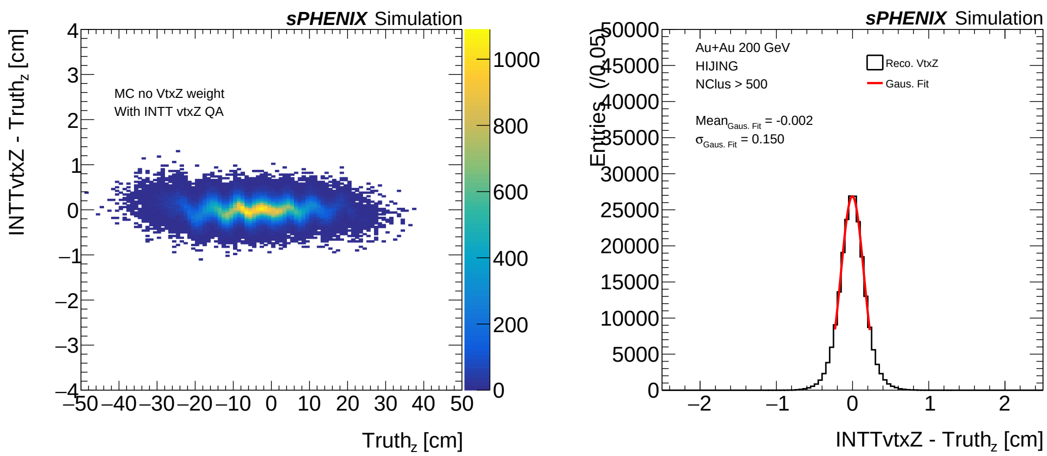

Figure 99: Left: The ΔZ as a function of truth vertex Z for the events with numbers of INTT clusters > 500. Right: The vertex Z reconstruction resolution for the high-multiplicity events.

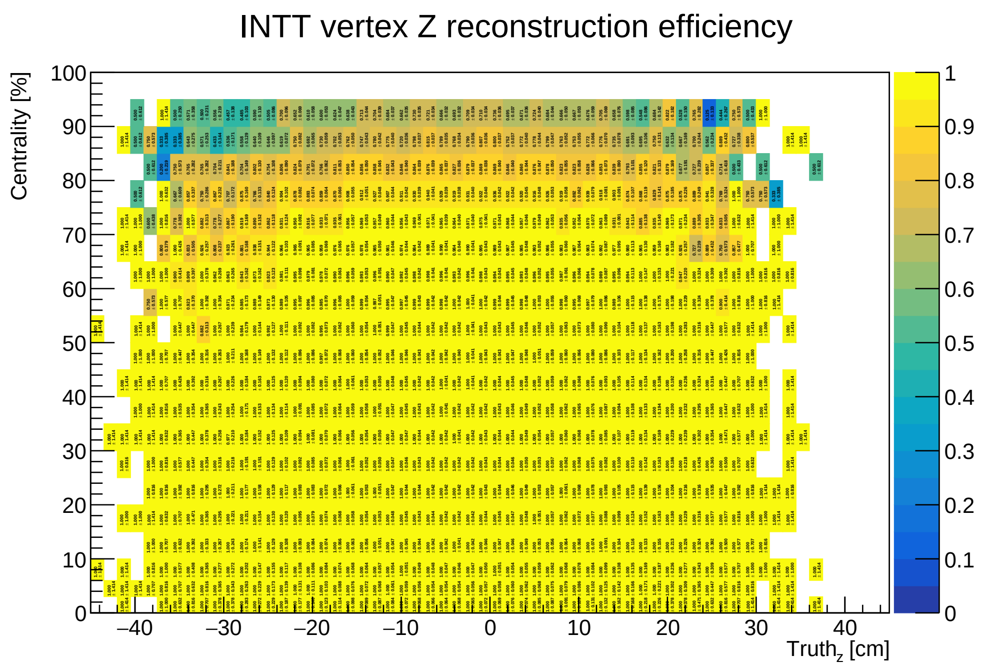

Figure 100: The vertex Z reconstruction efficiency as a function of centrality bin and truth vertex Z.

In data, the correlation of vertex Z reconstructed by INTT and MBD is checked, as shown in Figure 101. A positive correlation is identified indicating the reliability of the algorithm developed. The cause of the two satellite groups along the major correlation is under investigation. It is expected to be due to the MBD calibration. The two satellite groups are discarded in the analysis of the combinatoric method, as mentioned in Section 6.4.

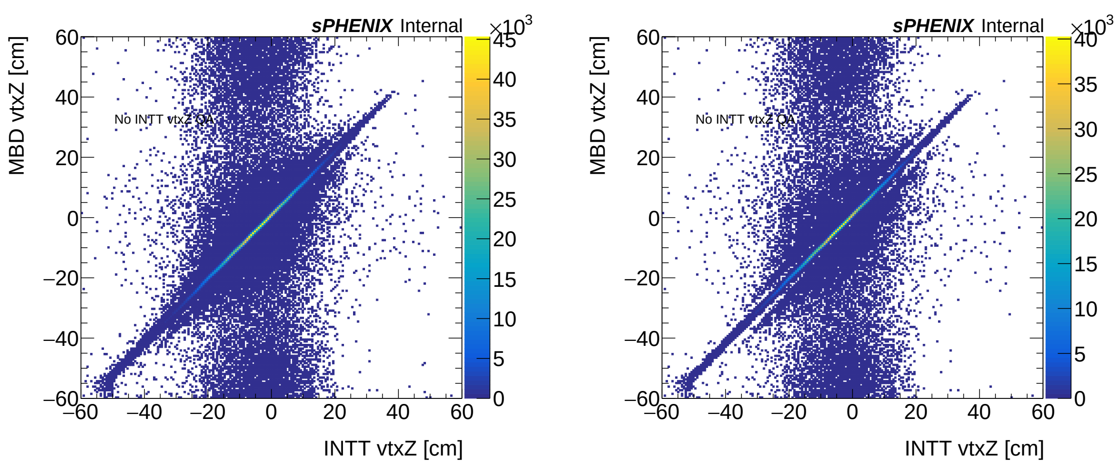

Figure 101: The correlation of vertex Z reconstructed by INTT and MBD for centrality interval $0 - 70\%$ (left) and the events with numbers of INTT clusters > 500 (right).

In data, the reconstructed vertex Z distribution for each centrality interval is compared to that for the centrality interval 0-70% for the reliability study, as shown Figure 102. The good agreement is observed up to the centrality interval of 70–80%.

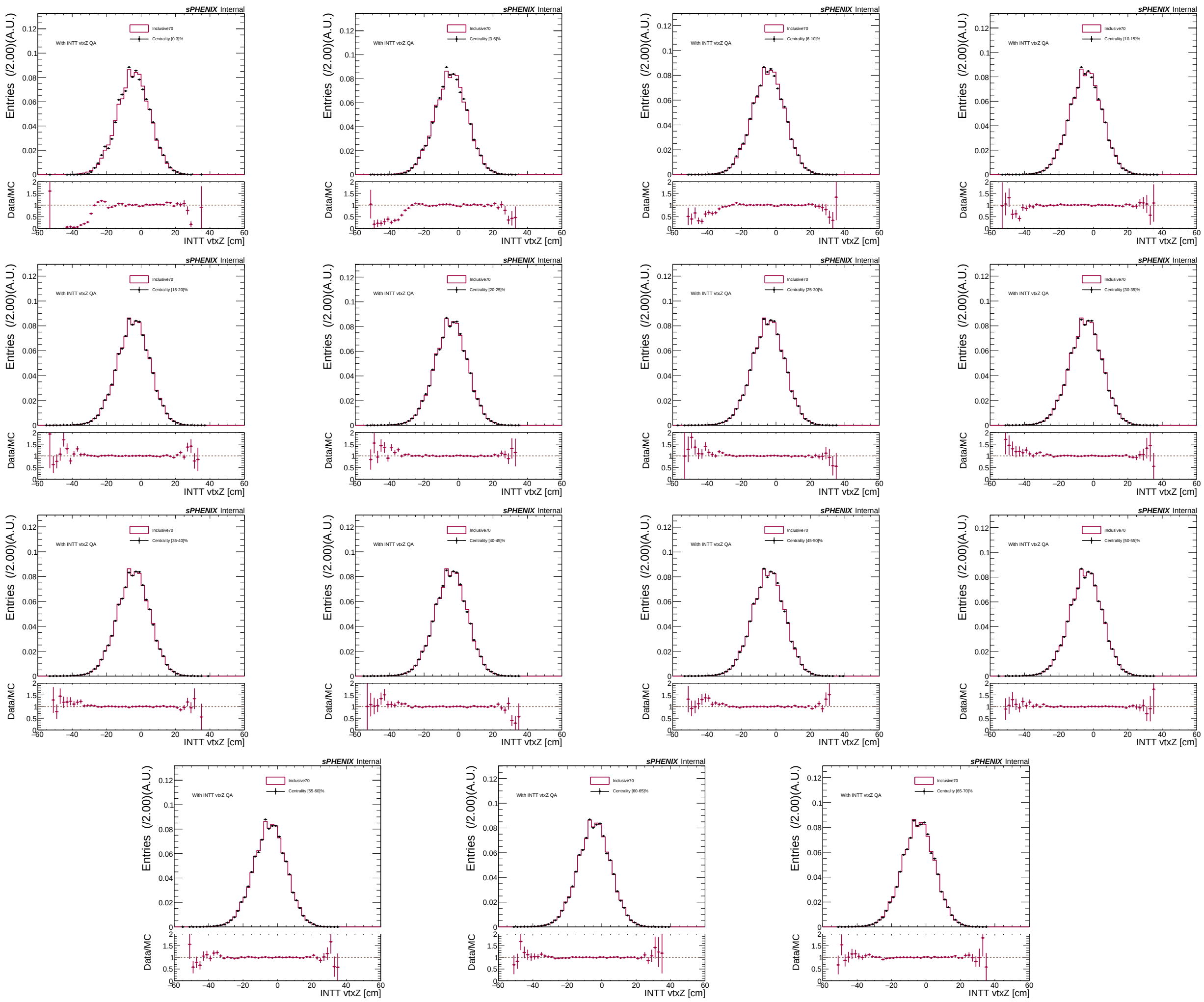

Figure 102: In data, the reconstructed vertex Z distribution for each centrality interval comparing to that of for the centrality interval 0-70%.

E.1 INTT z-vertex quality checks

In a single event, after stacking the trapezoidal shapes formed by all valid cluster pairs, the resulting distribution is fitted with seven Gaussian functions, each with a different fit range. An example from a data event is shown in Figure 103. The z-vertex is then determined as the average of the fitted Gaussian means.

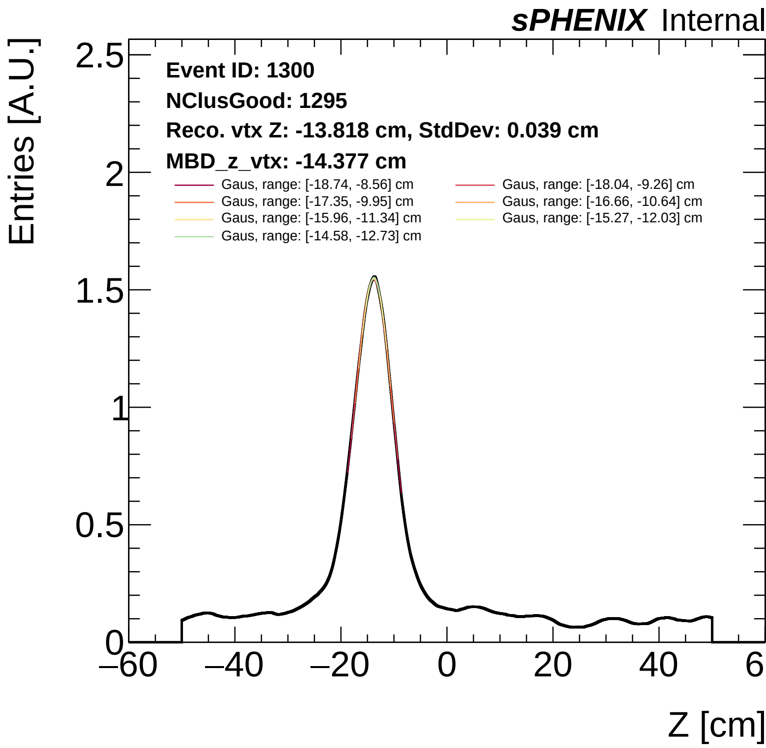

Figure 103: The probability distribution of the z-vertex in a single event by stacking up the trapezoidal shapes formed by the valid cluster pairs.

Three properties are evaluated and shown in Figure 104: the width of the fitted Gaussian distribution, the full width at half maximum (FWHM) of the distribution, and the difference between the INTT and MBD z-vertices. Table 9 summarizes examples of selection criteria for each property, and the distributions after applying the quality selections are presented in Figure 105.

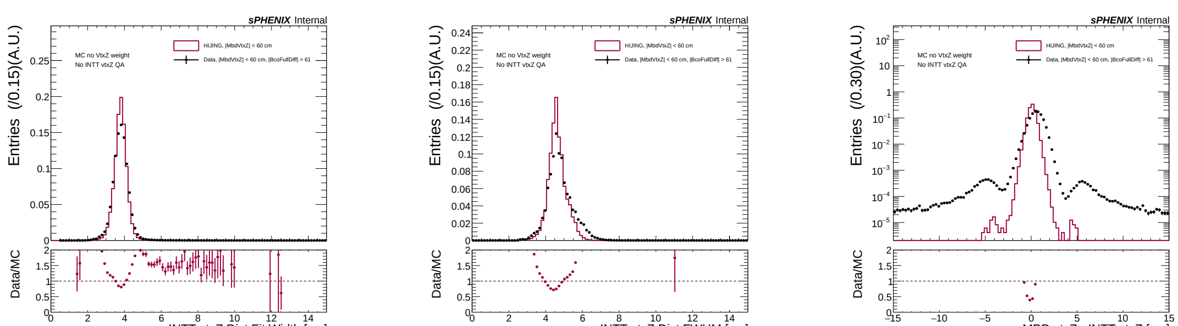

Figure 104: The properties of the reconstructed z-vertex before the quality check. (Left) The fit Gaussian width of the distribution. (Middle) The FWHM of the distribution. (Right) The z-vertex difference between the INTT and MBD.

Table 9: The selections used in the INTT vtx_z quality check.

Property	Cut Minimal [cm]	Cut Maximal [cm]
Fit Gaussian Width	1.5	10
FWHM	2	14
$\Delta(\mathrm{vtx}_Z^{\mathrm{INTT}}, \mathrm{vtx}_Z^{\mathrm{MBD}})$	-3.5	4.5

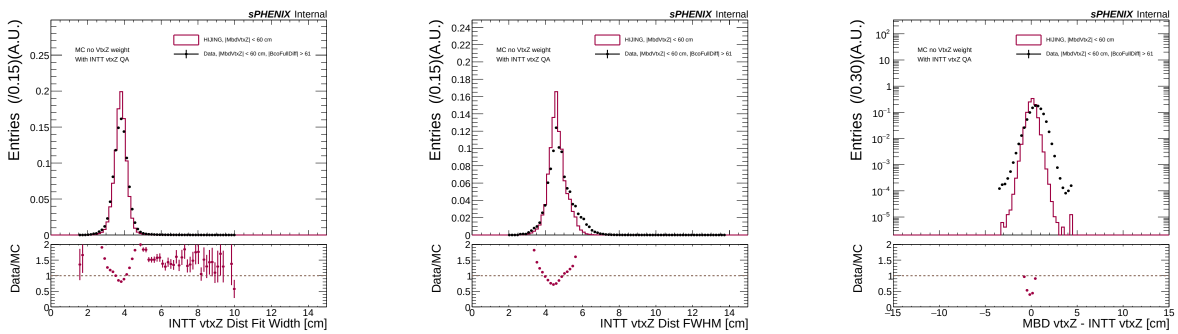

Figure 105: The properties of the reconstructed z-vertex after the quality check. (Left) The fit Gaussian width of the distribution. (Middle) The FWHM of the distribution. (Right) The z-vertex difference between the INTT and MBD.

The standard deviation of the reconstructed INTT z-vertex is examined and presented in Figure 106. The long tail in the distribution is significantly reduced after applying the selection, improving the agreement between data and simulation distributions.

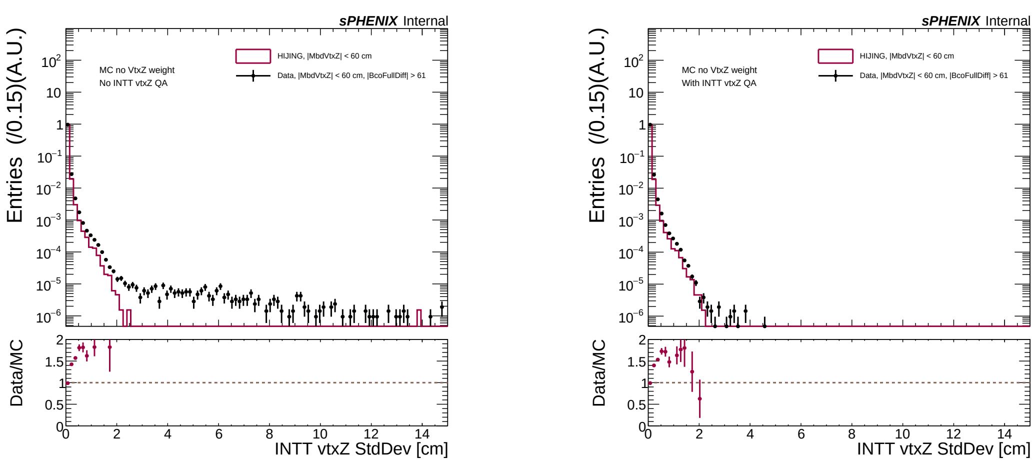

Figure 106: The distribution of the standard deviation of the reconstructed INTT z-vertex before the QA selection (Left) and after the QA selection (Right).

E.2 Per-event vertex X/Y position reconstruction

(This section presents a feasibility study of reconstructing the beam spot width performed in Run2023.)

With the average-vertex XY and the per-event vertex Z in place, the per-event vertex XY position reconstruction can be feasible. The limit of INTT is therefore extended forward. Note that reconstructing the event-by-event vertex XY is mainly for obtaining the beam spot size and vertex-position stability. The idea is similar to the 2D tracklet fill method as described in Section 6.4.2. On the contrary, the events with high multiplicities are expected to have higher precision as more information can be included in the reconstruction. The steps are described in the following:

1. Define the dimensions and center of a finely-binned 2D histogram. The central point is determined by the average vertex XY position. In the standard configuration, this corresponds to a 5 mm $\times$ 5 mm square with bin sizes of 50 μm $\times$ 50 μm.

2. In an event, start with a cluster in the inner layer and loop over the clusters in the outer layer. The combinations with cluster $\Delta\phi < 5$ degrees and the strip Z positions able to link to the reconstructed per-event vertex Z position are kept. Move to the next inner-layer cluster, and repeat the procedure.

3. Populate the trajectories of the combinations into the 2D histogram. The example is shown in Figure 107.

4. Remove the background of the histogram.

5. The per-event vertex XY are obtained by taking the averages on both axes of the histogram, as shown in Figure 107.

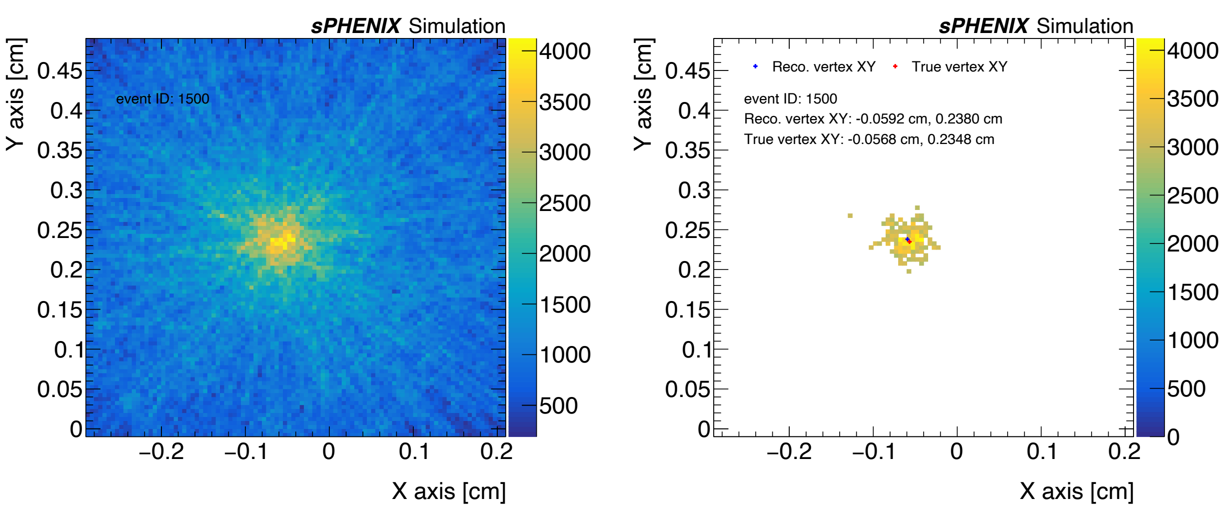

Figure 107: 2D histogram filled by the trajectories of combinations (left) and post background removal (right). The red and blue full cross marks are true and reconstructed vertex XY, respectively.

The reconstructed per-event vertex XY is compared with the true vertex XY in the simulation. Figure 108 and 109 show the correlations and deviations between true and reconstructed vertices for both axes. The correlations described by linear fits are consistent with unity, indicating good reliability of the current reconstruction method. In general, the resolution is 30 μm for the high-multiplicity events.

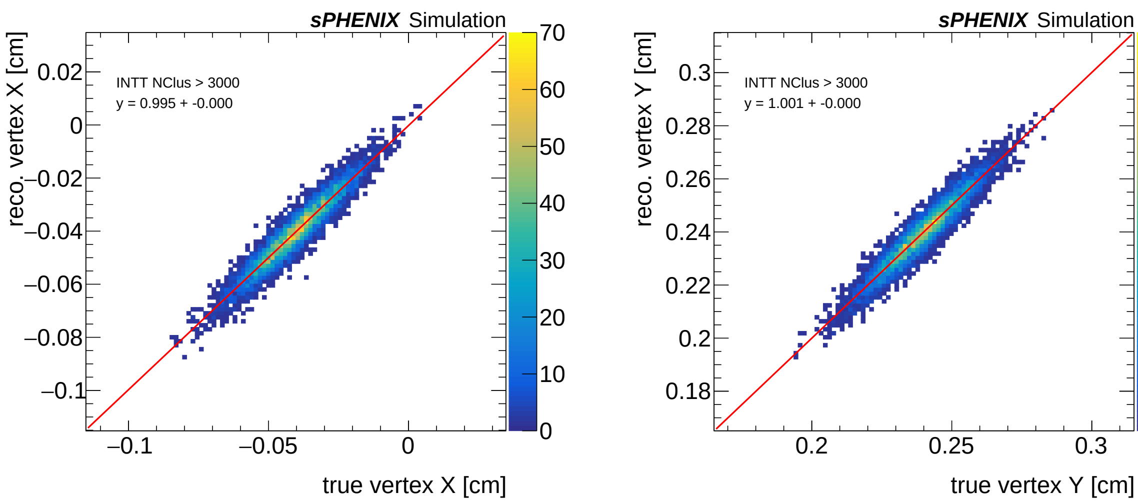

Figure 108: Correlation between the true vertex and reconstructed vertex for X (left) and Y (right) axes. The events with number of clusters > 3000 are shown.

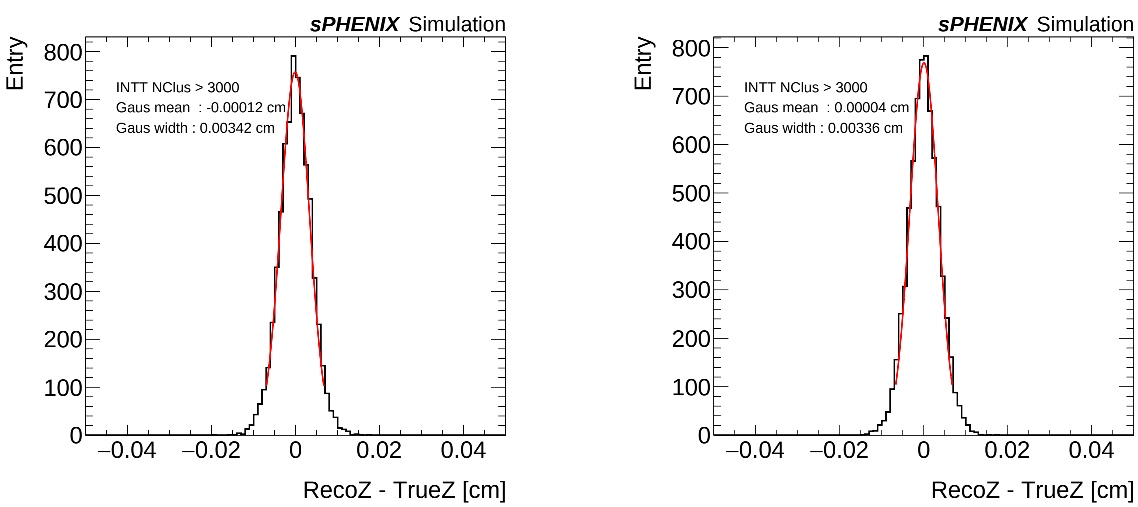

Figure 109: Difference between the true vertex and reconstructed vertex for X (left) and Y (right) axes. The events with number of clusters > 3000 are shown.

To obtain the beam spot size in data, the average vertices are obtained as the first step, which are (-0.191 mm, 2.621 mm) and (-0.277 mm, 2.576 mm), respectively. The discrepancy of the vertices between the two approaches can be explained by the detector misalignment, as described in Chapter 8.1.1. The average of the two vertices, (-0.234 mm, 2.599 mm), is used in the per-event vertex XY position reconstruction. The beam spot sizes for both axes are shown in Figure 110. The beam spot size is ~ 1 mm for both axes. In addition, the beam position stability is studied, as shown in Figure 111. The observed consistency in the vertex position over the run suggests a stable behavior. Consequently, the average vertex position in the XY plane demonstrates the adequacy for being utilized in the tracklet reconstruction.

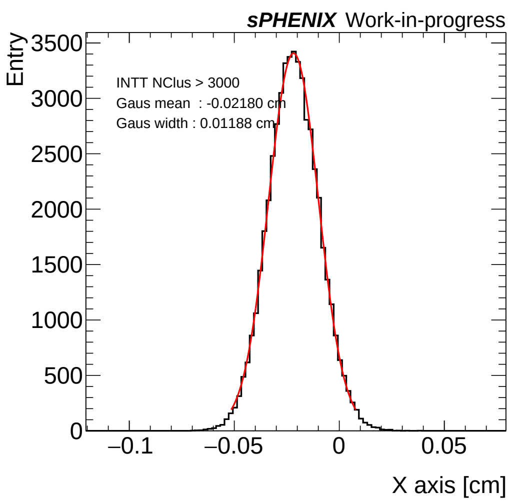

Figure 110: Distributions of the beam spot size in X (left) and Y (right) axes with run 20869.

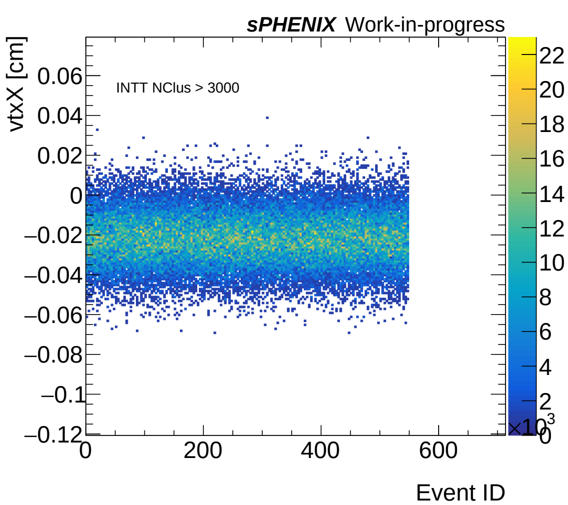

Figure 111: Vertex Position as a function of event index for X (left) and Y (right) axes with run 20869.

F Supplementary plots for vertex reconstruction in the closest-match method

The mean and sigma values of the Gaussian fit to the difference in Z position between the truth vertex and the reconstructed vertex, $\Delta(\mathrm{vtx}_z^{\mathrm{Reco}}, \mathrm{vtx}_z^{\mathrm{Truth}})$, are shown as functions of $\Delta\phi_{\mathrm{cut}}$ and $\mathrm{DCA}_{\mathrm{cut}}$ in Figure 112. The resolution is quantified using the effective width, defined as the minimal range containing 68.5% of the distribution. The distribution of $\Delta(\mathrm{vtx}_z^{\mathrm{Reco}}, \mathrm{vtx}_z^{\mathrm{Truth}})$ and its dependence on the number of clusters in the inner layer, with the optimized parameters $\Delta\phi_{\mathrm{cut}} = 0.3$ degrees and $\mathrm{DCA}_{\mathrm{cut}} = 0.15\,\mathrm{cm}$, are shown in Figure 113.

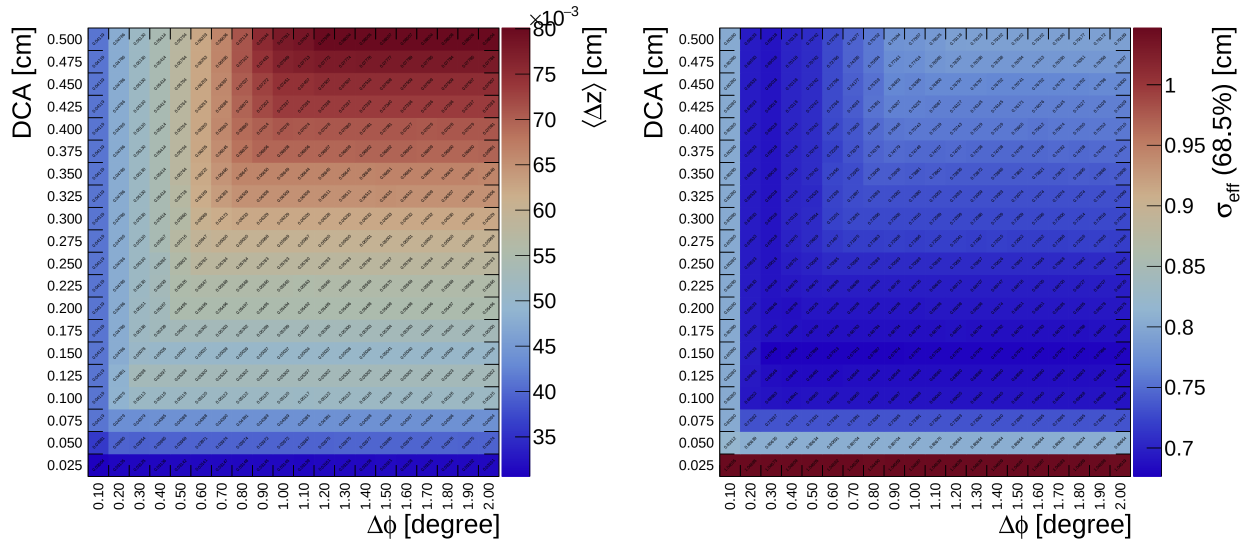

Figure 112: The mean (left) and sigma (right) of the Gaussian fit to $\Delta(\mathrm{vtx}_z^{\mathrm{Reco}}, \mathrm{vtx}_z^{\mathrm{Truth}})$ as a function of $\Delta\phi_{\mathrm{cut}}$ and $\mathrm{DCA}_{\mathrm{cut}}$.

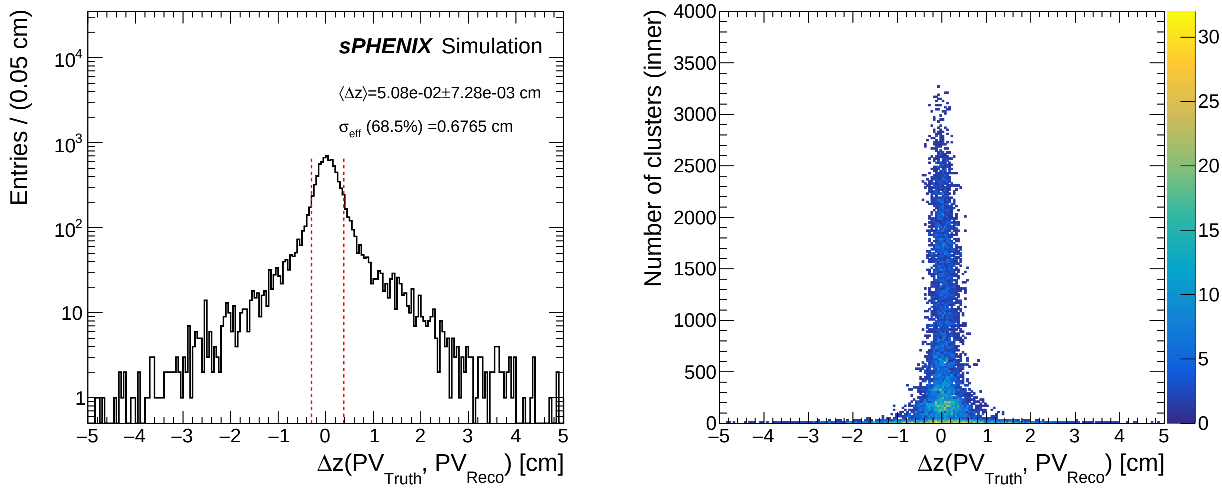

Figure 113: The distribution of $\Delta(\mathrm{vtx}_z^{\mathrm{Reco}}, \mathrm{vtx}_z^{\mathrm{Truth}})$ (left) and $\Delta(\mathrm{vtx}_z^{\mathrm{Reco}}, \mathrm{vtx}_z^{\mathrm{Truth}})$ v.s number of clusters in the inner layer (right) with the optimized $\Delta\phi_{\mathrm{cut}} = 0.3$ degree and $\mathrm{DCA}_{\mathrm{cut}} = 0.15\,\mathrm{cm}$.

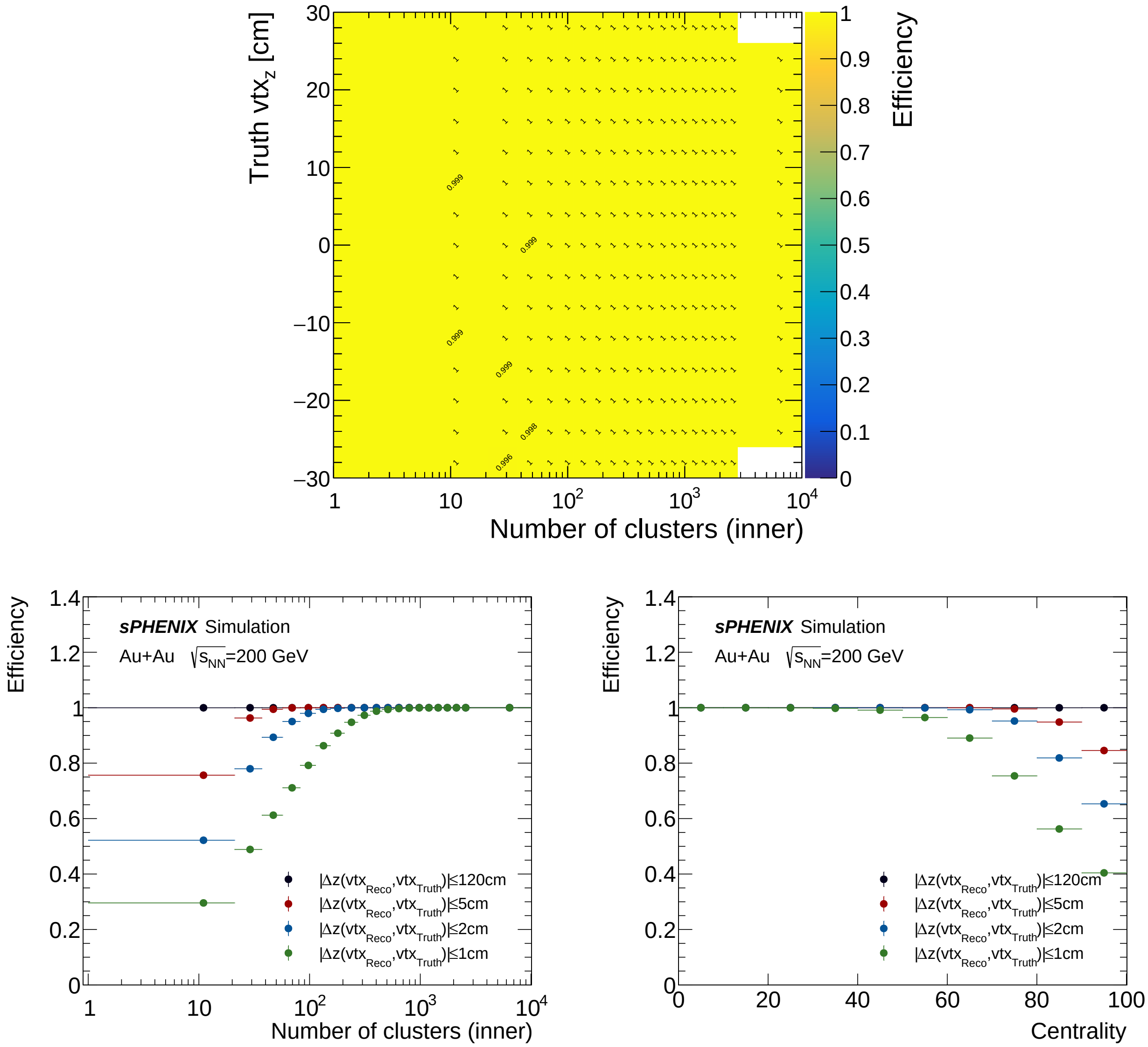

Figure 114: (Top) The vertex reconstruction efficiency as a function of cluster multiplicity and $\mathrm{vtx}_z^{\mathrm{Truth}}$). The vertex reconstruction efficiency with different quality cut values as a function of cluster multiplicity (bottom left) and centrality interval (bottom right).

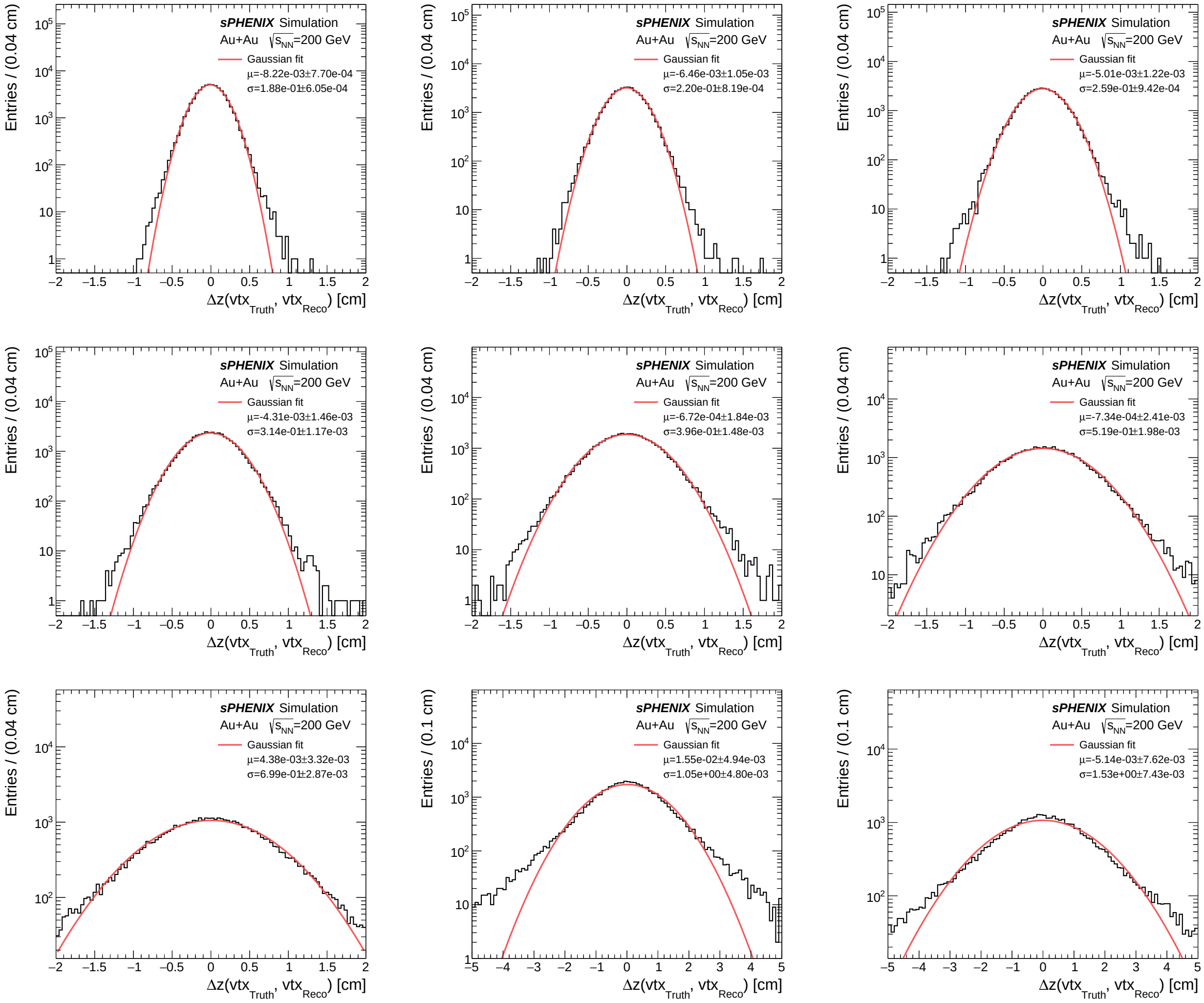

Figure 115: $\Delta(v_z^{\mathrm{Reco}}, v_z^{\mathrm{Truth}})$ and the Gaussian fit.

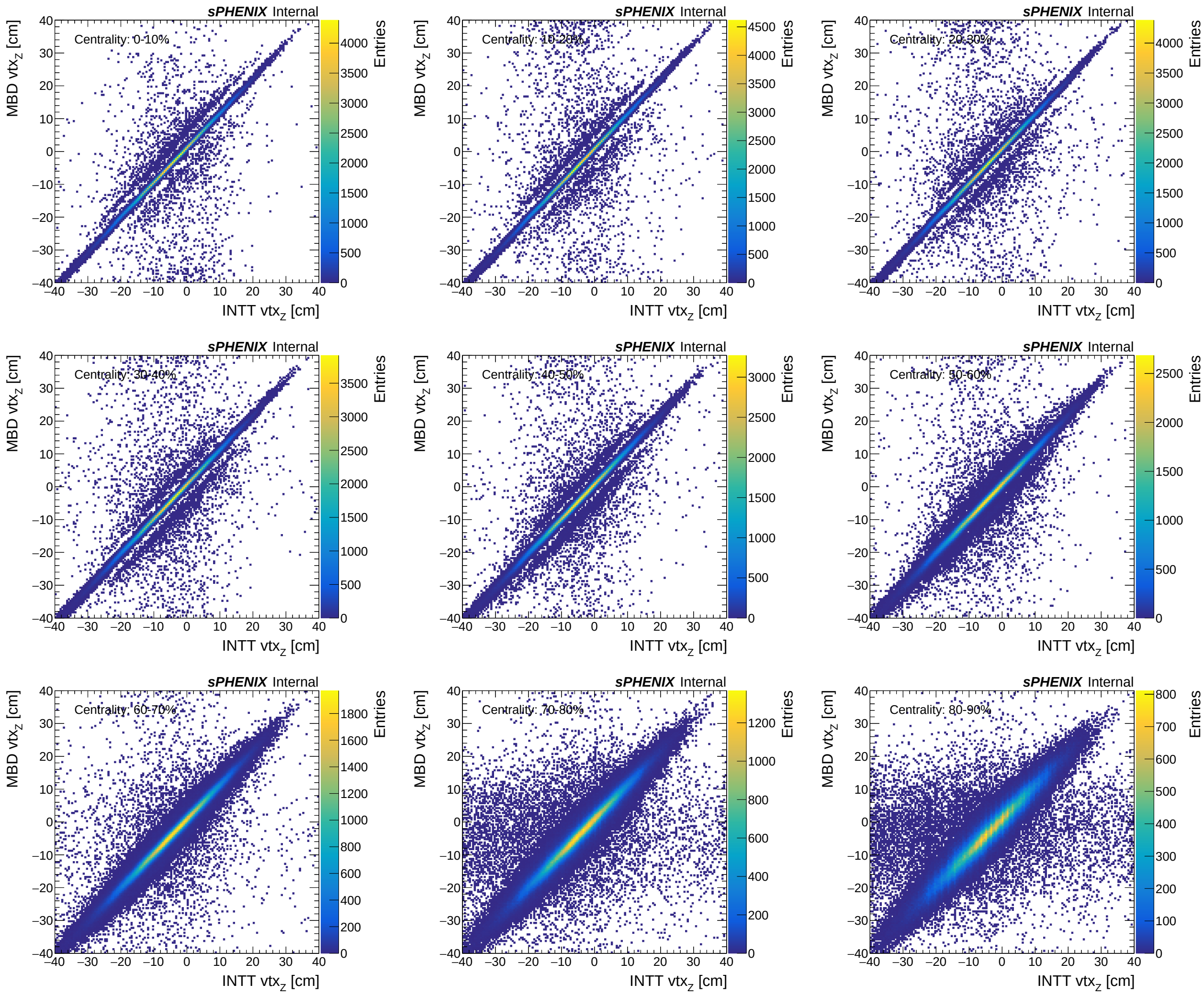

Figure 116: Comparisons between the INTT tracklet vertex Z reconstruction and the MBD vertex determination in different centrality intervals.

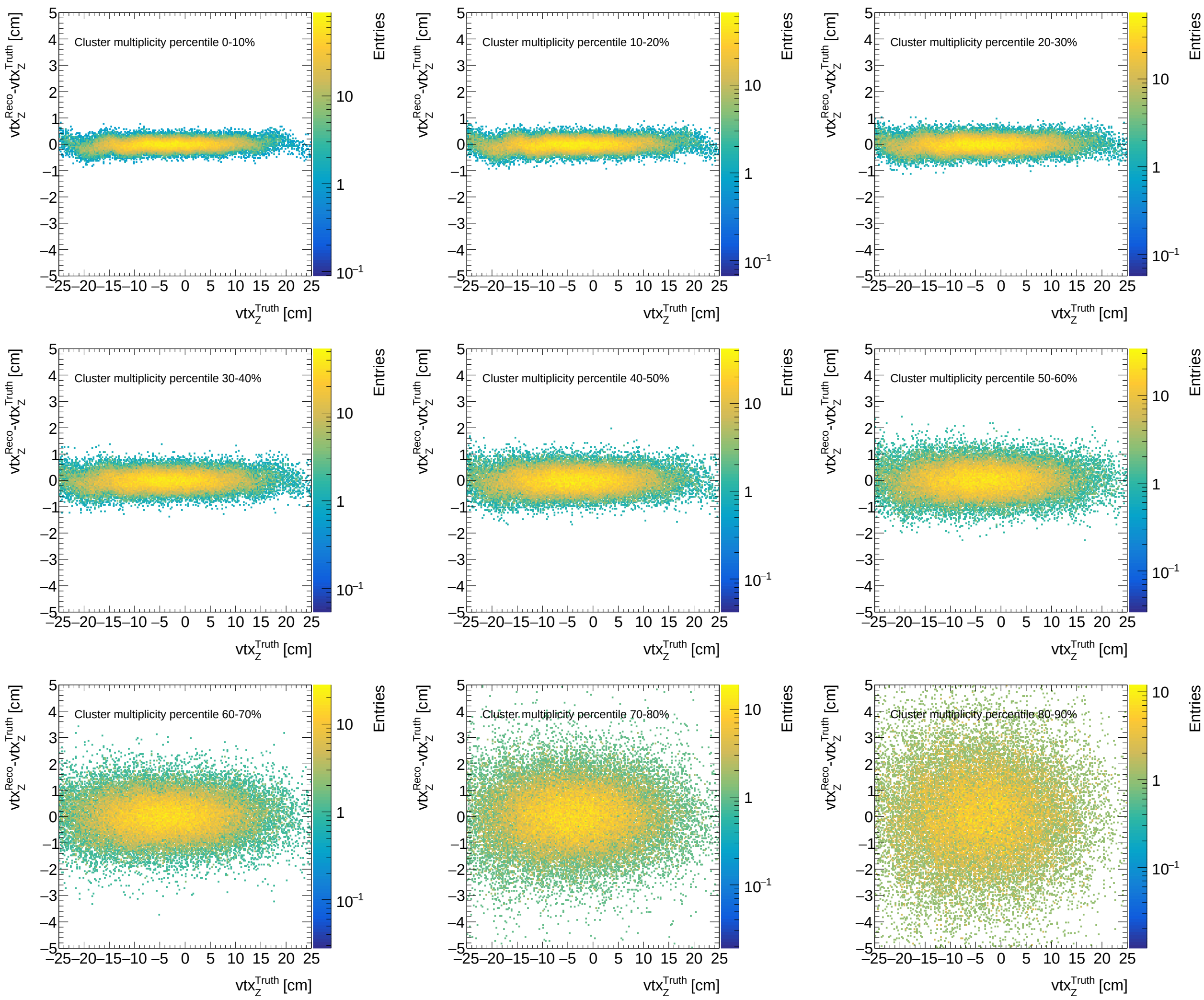

Figure 117: Comparisons of the reconstructed and truth vertex Z position in simulation in different centrality intervals.

G Supplementary plots for the tracklet reconstruction

In the closest method, reconstructed tracklets are matched to the generator truth object, PHG4Particle (referred to as G4P in the following figures), to evaluate the purity of tracklet reconstruction. The matching procedure is as follows. In simulated events, each cluster is matched to a truth-level PHG4Particle that contributes the maximum energy to it. Each PHG4Particle has a unique identifier, referred to as track ID, and thus each tracklet has a pair of track IDs of PHG4Particle corresponding to its constituent clusters. Next, all reconstructed tracklets are checked to determine whether their constituent clusters are associated with the same PHG4Particle. Specifically, if the matched PHG4Particle for both clusters has the same track ID, the tracklet is labeled as matched; otherwise, it is classified as not matched. For tracklets that are matched to a PHG4Particle, an additional classification is performed based on the track ID. A positive track ID indicates that the PHG4Particle is a primary particle, while a negative track ID means that it is a secondary particle originating from material interactions or decays. Note that, for the truth-matching study, the $\Delta \mathrm{R}$ criterion used in tracklet reconstruction is effectively removed.

The matching procedure is applied to a dedicated simulation sample generated using the single-particle generator within the sPHENIX simulation framework. Figure 118 presents key tracklet variables, categorized based on different matching criteria. The truth-matching procedure indicates that tracklets associated with primary particles typically exhibit $\Delta\phi \lesssim 0.2$, $\Delta\eta \lesssim 0.35$, and $\Delta \mathrm{R} \lesssim 0.4$. The large tails observed in all tracklet kinematic distributions are primarily attributed to secondary particles and combinatorial backgrounds. The matching study also validates the tracklet selection criterion of $\Delta \mathrm{R} < 0.5$ in the baseline analysis, ensuring that tracklets originating from primary particles are retained with minimal inefficiency while maintaining relatively low contamination from combinatorial backgrounds.

A metric, defined as the ratio of the number of generated hadrons matched with a reconstructed tracklet to the total number of generated hadrons, quantifies the fraction of truth-generated hadrons that can be reconstructed as tracklets and is shown in Figure 119 as a function of the truth hadron ϕ and η. This ratio remains mostly uniform across η, while the two dips in ϕ coincide with the known gaps between INTT barrels, as discussed in Section B. It is important to note that this fraction should not be interpreted as tracking efficiency - tracklets are formed by pairing only two INTT clusters, whereas a full track is reconstructed by combining clusters from all sPHENIX tracking detectors, MVTX (3 layers), INTT (2 layers), Time Projection Chamber TPC (48 layers), and Time Projection chamber Outer Tracker TPOT (1 layer), making it significantly more robust against fakes and combinatorial backgrounds.

Figure 120 shows an example of tracklets grouped by matching criteria in both the transverse and Z-ρ planes, providing a clear visual representation of the tracklet reconstruction and truth-matching process. The same event is shown in Figure 120 in the $\eta-\phi$ phase space, overlaid with primary PHG4Particles. Tracklets matched to PHG4Particles with positive and negative track IDs are displayed separately.

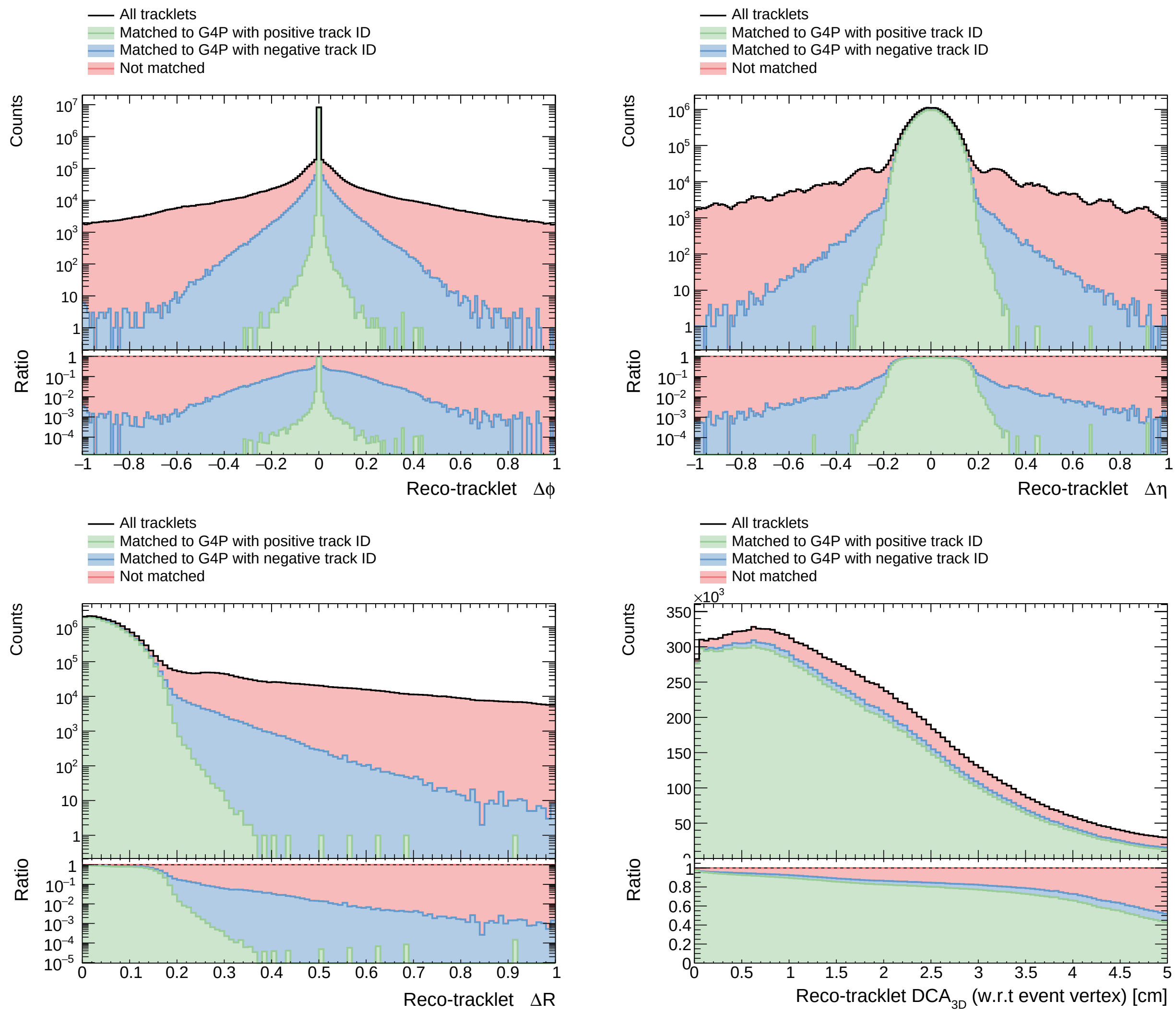

Figure 118: The tracklet $\Delta\phi$ (top left), tracklet $\Delta\eta$ (top right), tracklet ΔR (bottom left), and tracklet DCA with respect to the event vertex (bottom right).

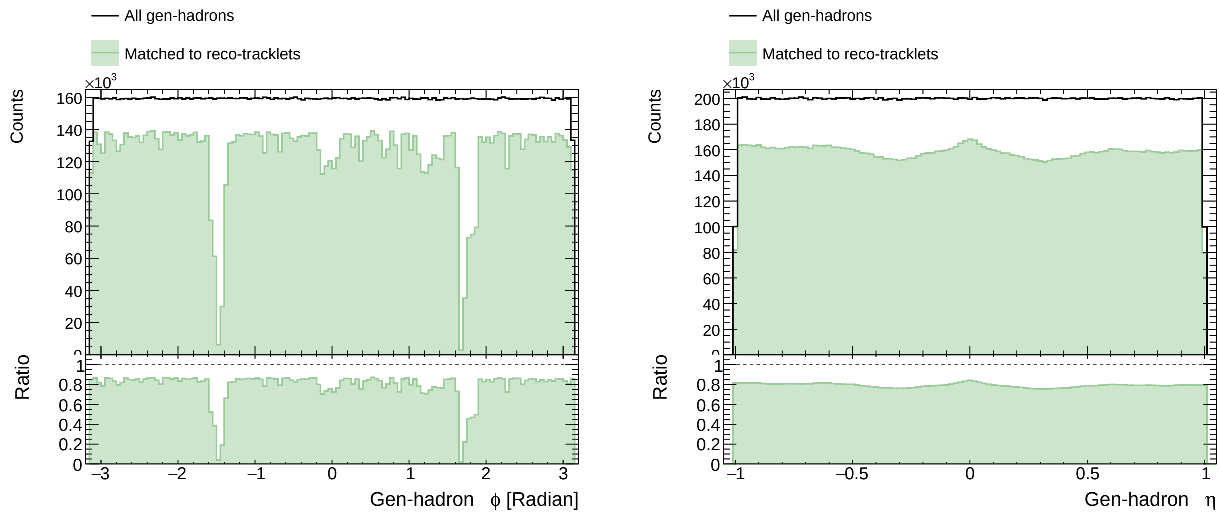

Figure 119: An example of tracklets grouped by the matching criteria in the transverse (Top) and Z-ρ planes (Bottom).

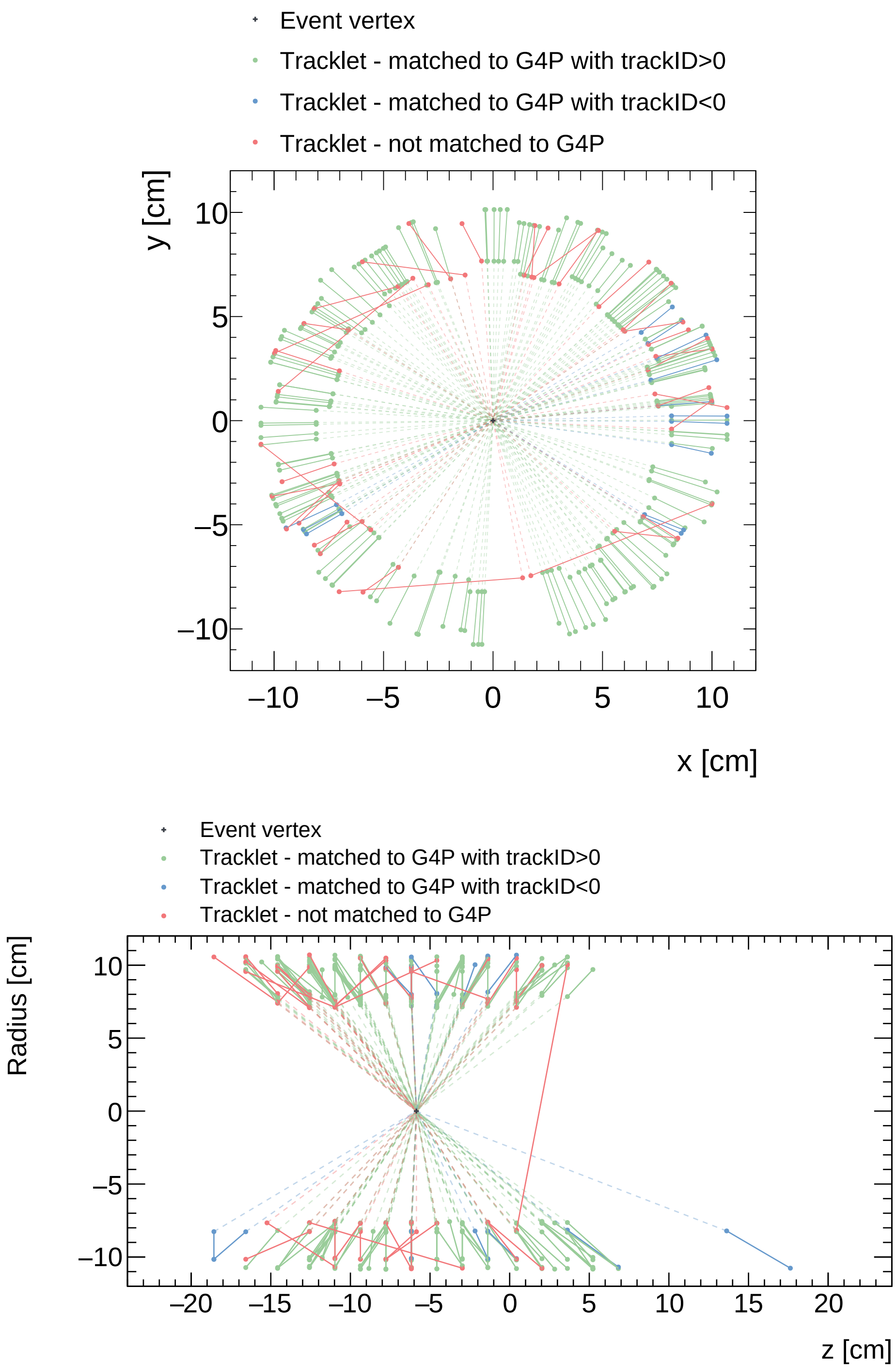

Figure 120: An example of tracklets grouped by the matching criteria in the transverse (Top) and Z-ρ planes (Bottom).

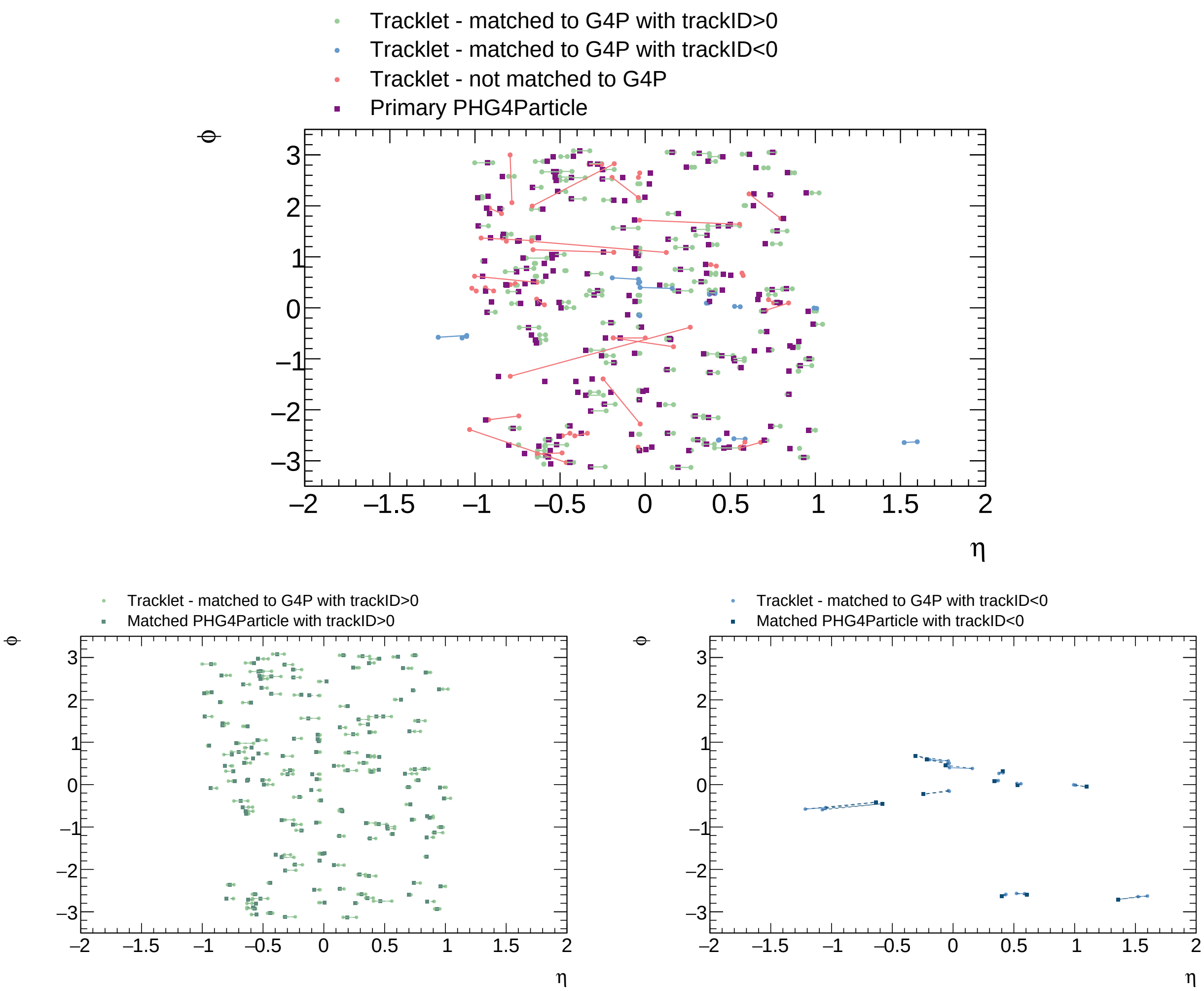

Figure 121: Tracklets grouped by the matching criteria in the $\eta - \phi$ phase space, overlaid with primary PHG4Particles.

H Supplementary plots for the correction factors

Corrections factors in each centrality interval are shown in this section.

H.1 The combinatoric method

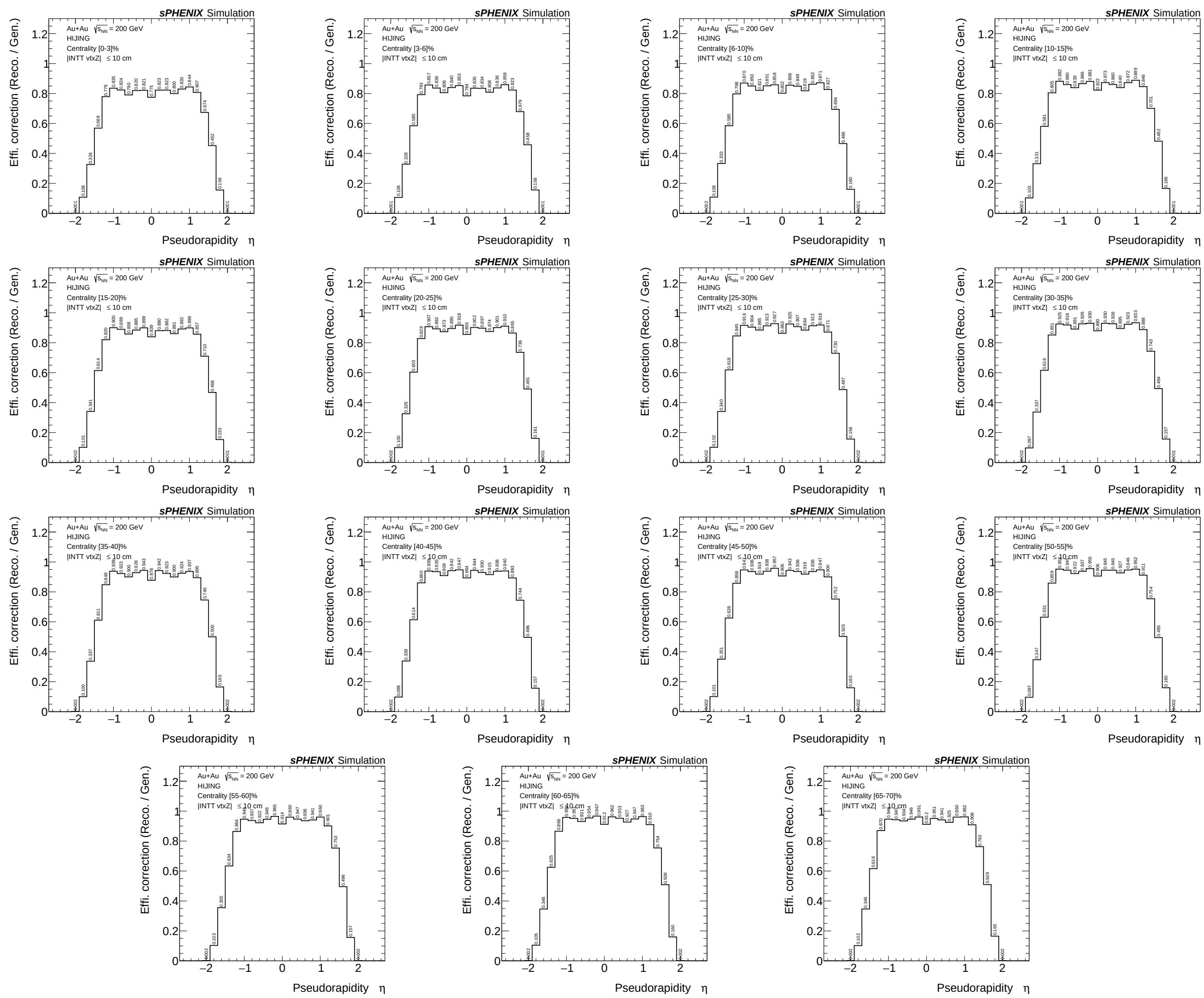

Figure 122: The acceptance and efficiency correction for each centrality interval.

H.2 The closest-match method

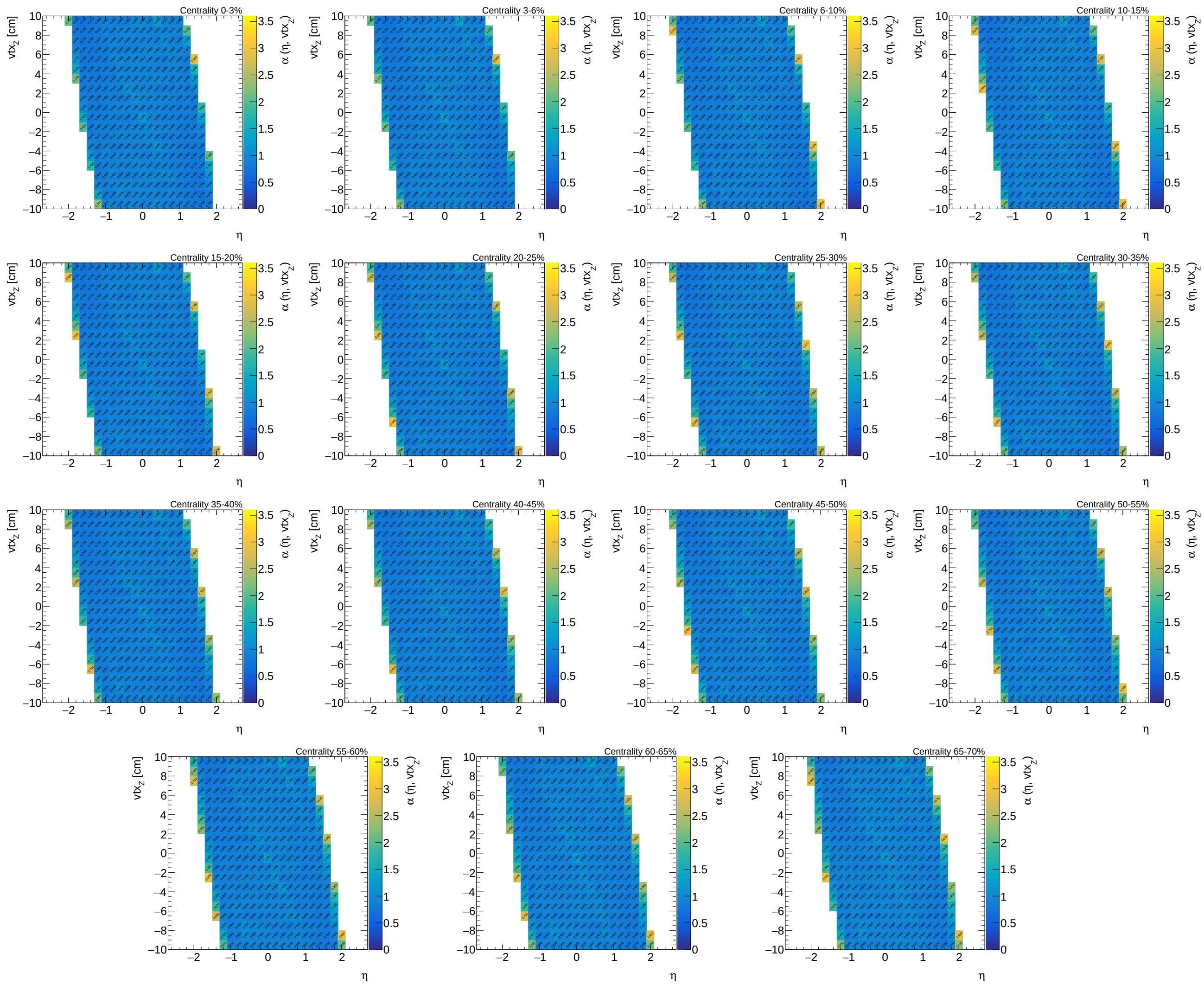

Figure 123: The α factor for each centrality interval.

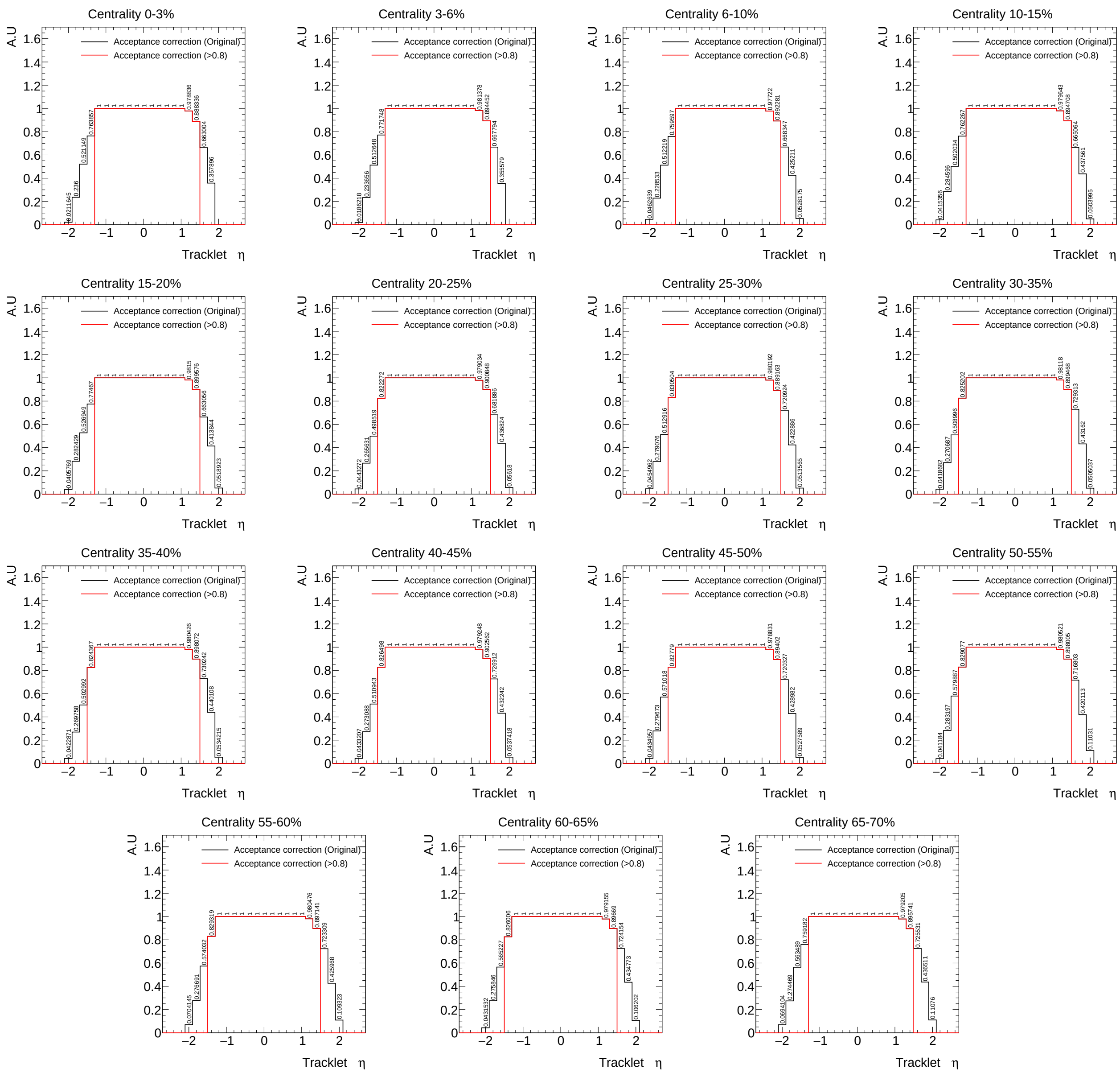

Figure 124: The acceptance correction for each centrality interval.

I Strangeness fraction in simulation

The Fun4All simulation framework, particularly the HepMCNodeReader module, is modified and expanded to allow the enhancement of strange particle fractions. Key modifications include methods for defining enhancement fractions, lists of particle IDs and production probabilities based on the existing measured quantity, and assigning unique identifiers to newly added particles. Static functions for the fitted distributions allow the sampling of kinematic variables, while the fraction of additional strange particles could be dynamically specified through Fun4All macro G4_Input.C. The full implementation can be found at https://github.com/sPHENIX-Collaboration/coresoftware/blob/master/simulation/g4simulation/g4main/HepMCNodeReader.cc and the corresponding pull request https://github.com/sPHENIX-Collaboration/coresoftware/pull/3349.

The functions used to sample the particle kinematics, p_T and η, are derived by fitting the generator truth distributions of K_s^0 meson from the Pythia8 simulation. The p_T distribution is modeled using an Exponentially-Modified Gaussian (EMG) function, defined as:

$$f(x;\mu,\sigma,\lambda) = \frac{\lambda}{2} e^{\frac{\lambda}{2}(2\mu+\lambda\sigma^2-2x)} \operatorname{erfc}\left(\frac{\mu+\lambda\sigma^2-x}{\sqrt{2}\sigma}\right),$$

where μ and σ are the mean and standard deviation of the Gaussian component, λ is the rate parameter of the exponential component, and $\operatorname{erfc}(z)$ is the complementary error function. The η distribution is modeled as the sum of two Gaussian functions, with equal fractions, sharing the same standard deviation, but with distinct mean values. The generator truth distributions for p_T and η, along with their respective fits, are shown in Figure 125.

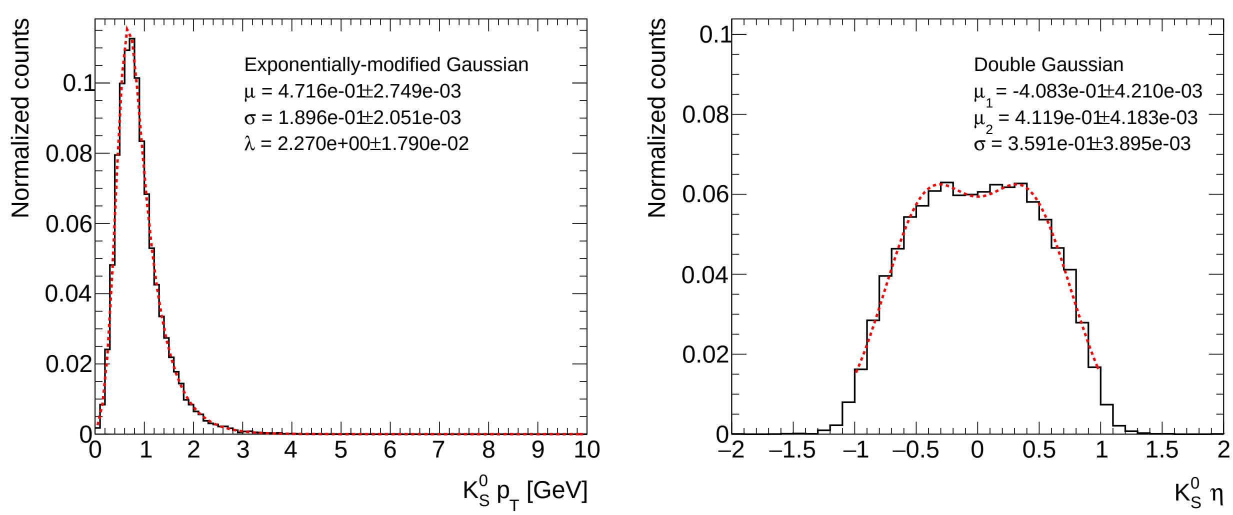

Figure 125: The generator truth distributions of p_T and η and their corresponding fit

A standalone test was performed to sample p_T and η using the EMG and double Gaussian functions, with parameters set according to the fit results, and ϕ uniformly sampled from $-\pi$ to π. A comparison between the truth and sampled distributions of the total momentum p and its z-component p_z is shown in Figure 126, while the two-dimensional distributions of

p_{T} and η from the truth and sampled data are presented in Figure 127. A good agreement between the truth and sampled kinematics ensures that the additional particles introduced in the simulation are consistent with the underlying kinematic properties.

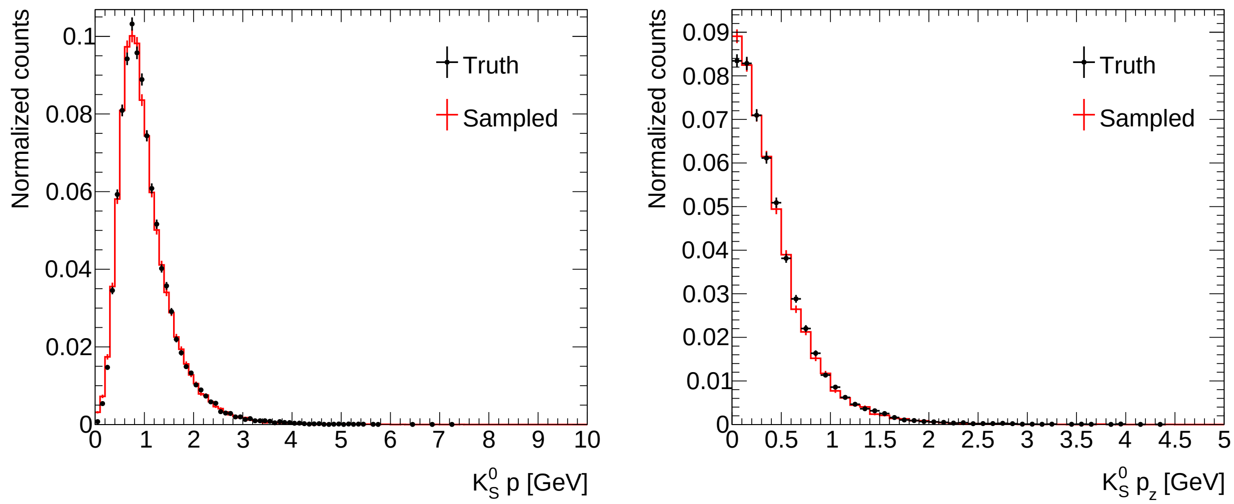

Figure 126: The truth and sampled distributions of the total momentum p (left) and its z-component p_z (right).

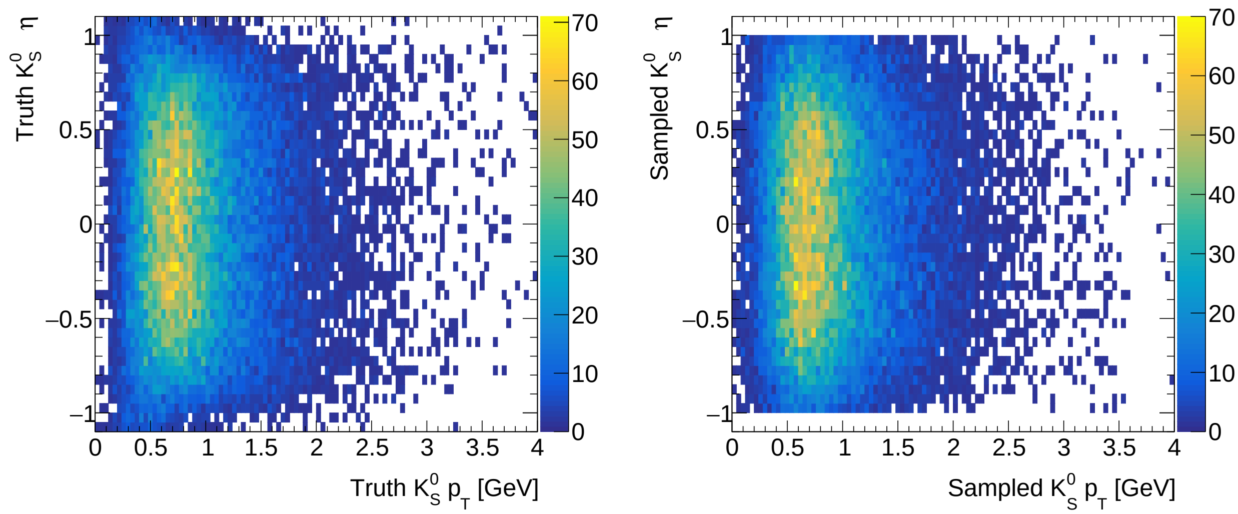

Figure 127: The two-dimensional distributions of p_{T} and η from the truth (left) and sampled (right) particles.

Validation of the implementation was performed using two sets of `HIJING` minimum bias simulations with enhancement fractions of 40% and 100%, respectively, each containing 500 events. For both validation samples, the additional particles were restricted to K_s^0 mesons and Λ baryons. The top plot in Figure 128 shows the number of K_s^0 mesons and Λ baryons at the HepMC-particle and PHG4Particle stages, confirming that the additional particles were correctly added to the PHG4Particle collection without altering the HepMC record. Marginal differences in the p_T and η distributions of PHG4Particle, shown in the bottom plots of Figure 128, indicate that the introduction of additional particles did not significantly distort the overall event kinematics.

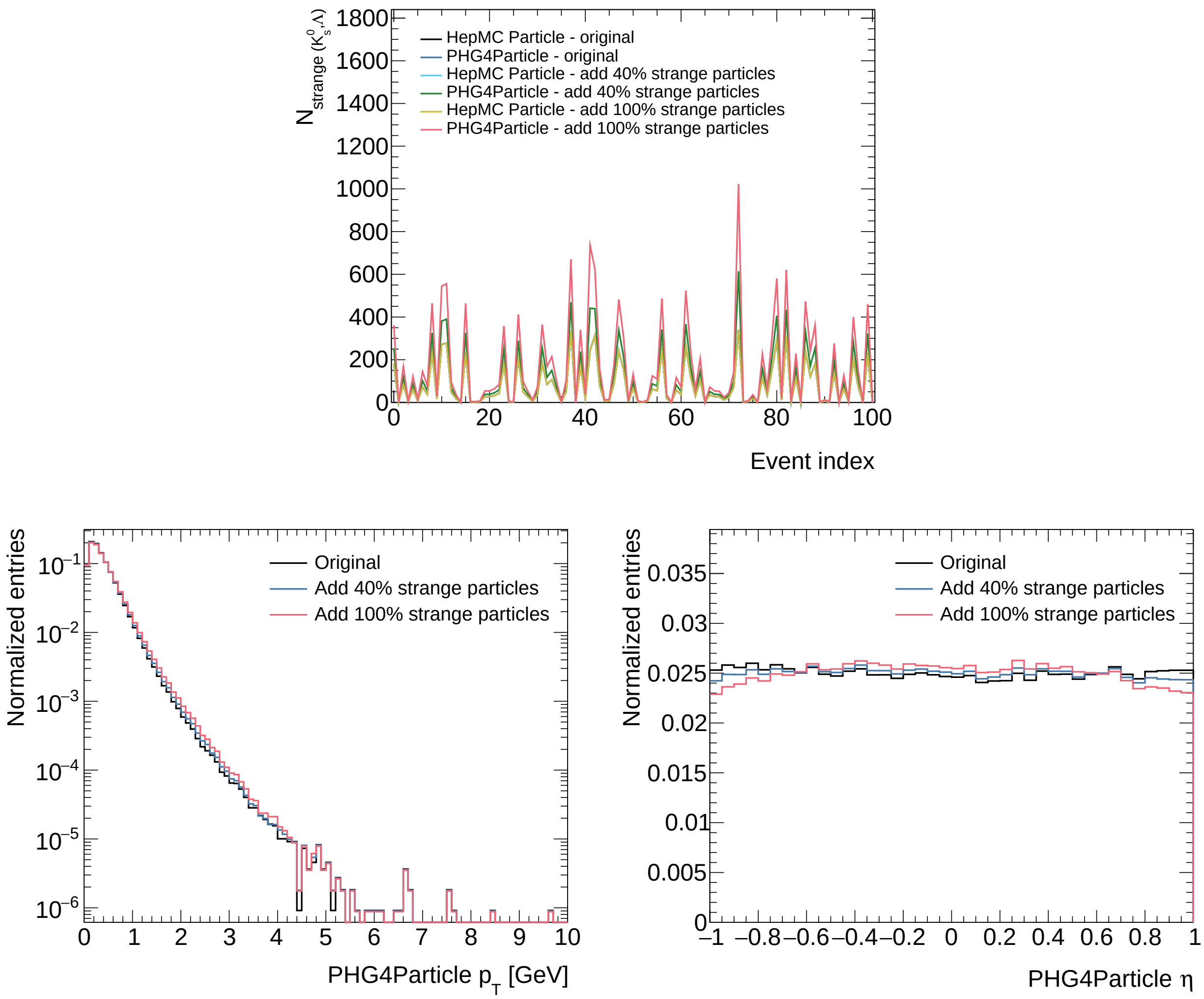

Figure 128: The number of K_s^0 mesons and Λ baryons at the HepMC-particle and PHG4Particle stages (top), the p_T (bottom left) and η (bottom right) distributions of PHG4Particles with additional strange particles.

J Supplementary plots for the systematic uncertainty

Systematic uncertainties in each centrality interval are shown in this section.

J.1 The combinatoric method

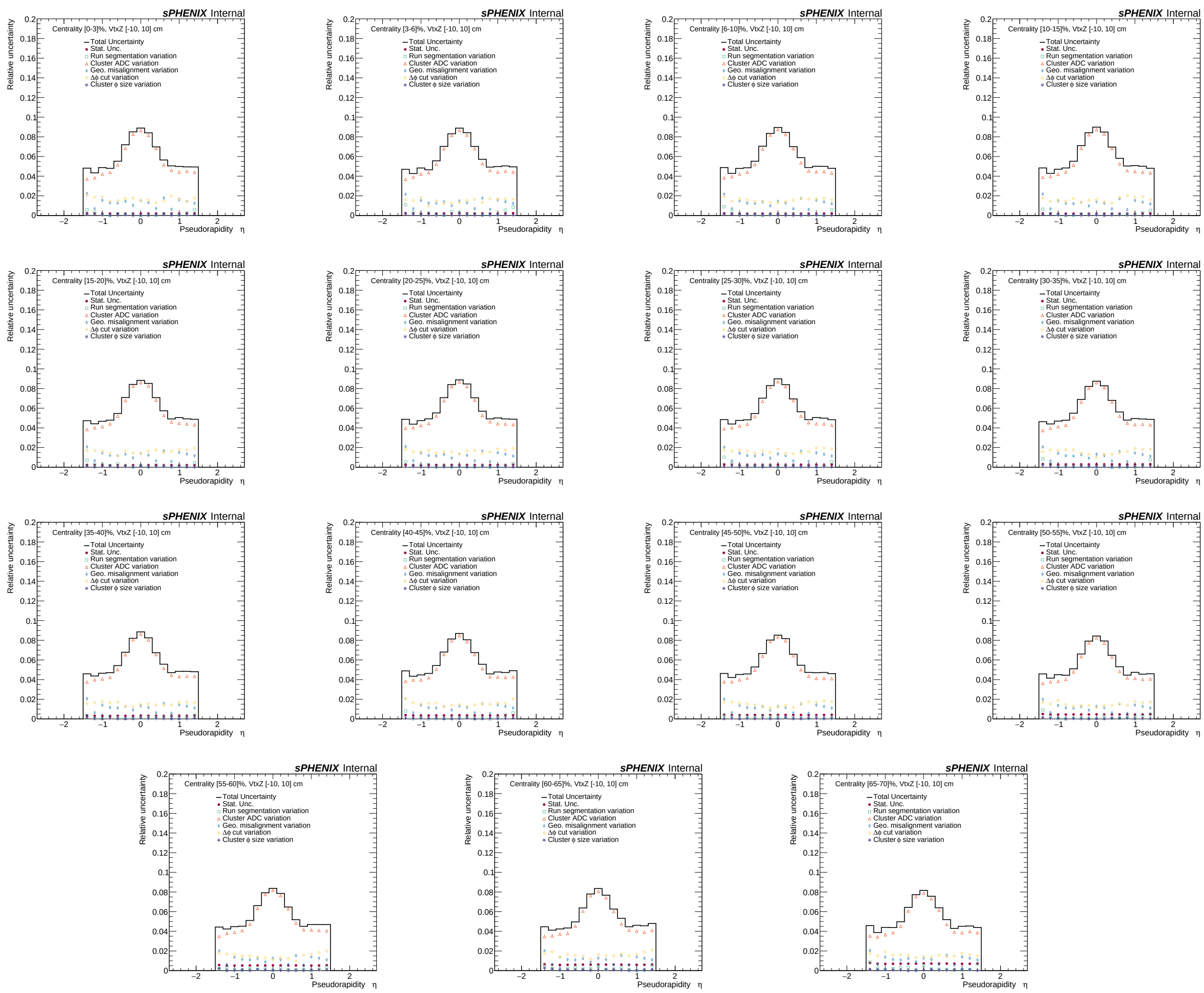

Figure 129: Systematic uncertainties in different centrality intervals.

J.2 The closest-match method

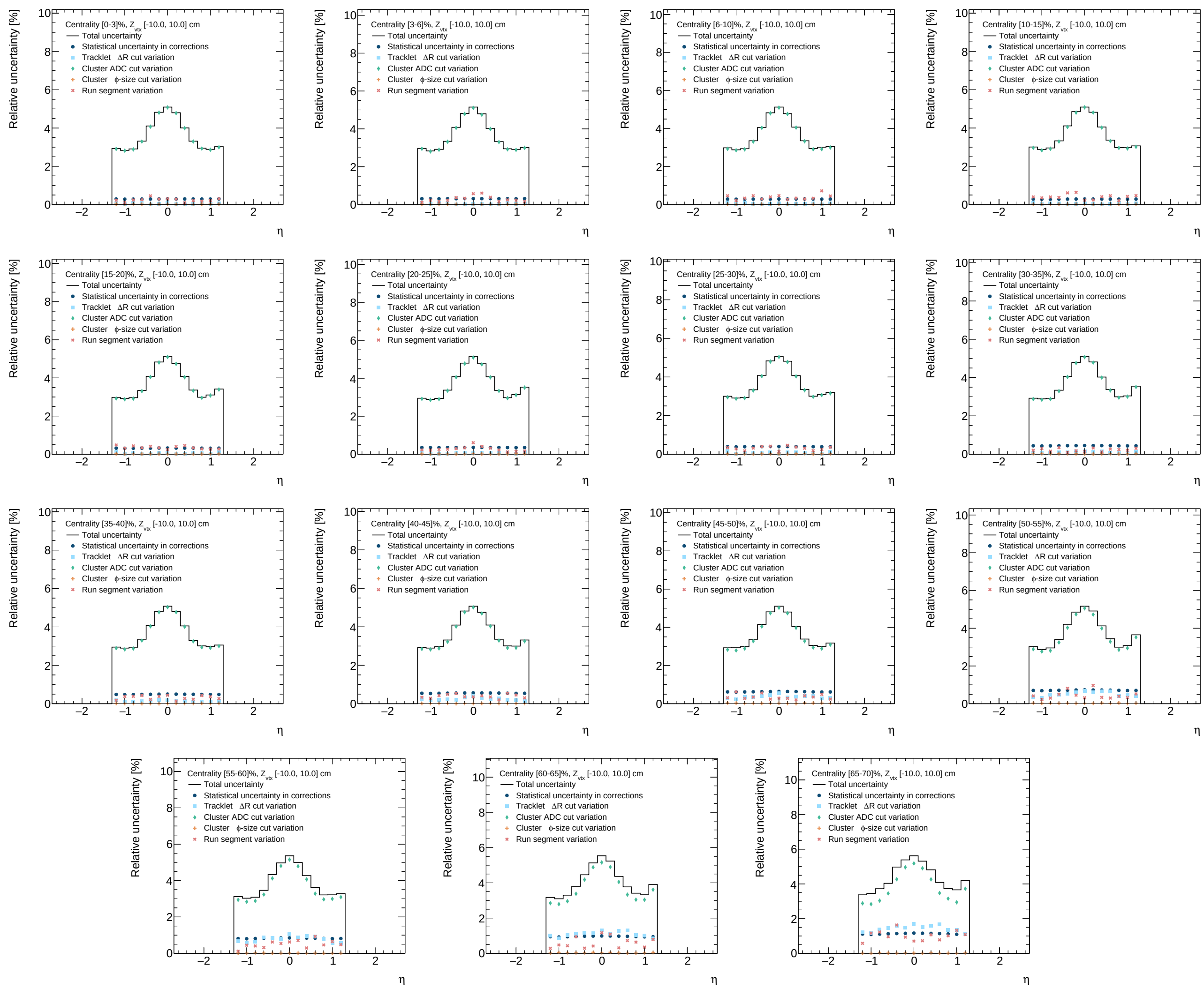

Figure 130: Systematic uncertainties in different centrality intervals.

K Statistical combination of measurement results

Three methods are tested for combining results from the combinatoric and the closest-match methods. Two of these involve standard statistical techniques: the least squares (LS) method and the profile likelihood method, both of which incorporate uncertainty correlations between the two analysis approaches into the covariance matrix, ensuring they are properly accounted for in the final combination. The third method is based on and adapted from the combination procedure outlined in the CMS publication [31].

K.1 The least square method

Given a set of measured values, $y_1, \cdots, y_N$, with corresponding uncertainties $\sigma_1, \cdots, \sigma_N$ at points $x_1, \cdots, x_N$, the true value λ_i of y_i is assumed to follow a functional form $\lambda_i = \lambda(x_i, \boldsymbol{\theta})$. The optimal λ is determined by minimizing the generalized χ^2 function

$$\chi^2(\lambda) = \sum_{i,j=1}^{N} (y_i - \lambda)(V^{-1})_{ij}(y_j - \lambda)$$

which is achieved by solving the derivative of $\chi^2(\lambda)$ with respect to λ equals zero. The covariance matrix takes the form

$$V = \begin{bmatrix} V_{11} = \sum_k \sigma_{1,k}^2 & V_{12} = \sum_k \rho_k \sigma_{1,k}\sigma_{2,k} \\ V_{21} = \sum_k \rho_k \sigma_{1,k}\sigma_{2,k} & V_{22} = \sum_k \sigma_{2,k}^2 \end{bmatrix}$$

where

$$\begin{aligned} \sigma_{1,k} &: \text{ the } k\text{-th systematic uncertainty of measurement 1,} \\ \sigma_{2,k} &: \text{ the } k\text{-th systematic uncertainty of measurement 2,} \\ \rho_k &: \text{ the correlation coefficient of the } i\text{-th uncertainties between the two measurements} \end{aligned}$$

The combined measurement is then given by

$$\bar{y} = \frac{y_1 V_{22} + y_2 V_{11} - (y_1 + y_2)V_{12}}{V_{11} + V_{22} - 2V_{12}}$$

with the one standard deviation uncertainty given by

$$\sigma_y = \sqrt{\frac{V_{11}V_{22} - V_{12}^2}{V_{11} + V_{22} - 2V_{12}}}$$

Figure 131 presents the results from both analysis approaches and the combined measurement using the LS method in three different centrality intervals. Notably, the combined value can sometimes exceed both input measurements, which is not physically meaningful.

This occurs when the covariance is large due to a strong correlation in one of the systematic uncertainties (e.g $\rho_k \simeq 1$), leading to an unphysical combined results.

To verify this effect, Figure 132 shows the impact of artificially reducing the correlation of the cluster ADC uncertainty from its original value of 0.986 to 0.5. With this modified correlation, the combined result falls between the two input measurements, supporting the interpretation that a high correlation artificially inflates the combined value.

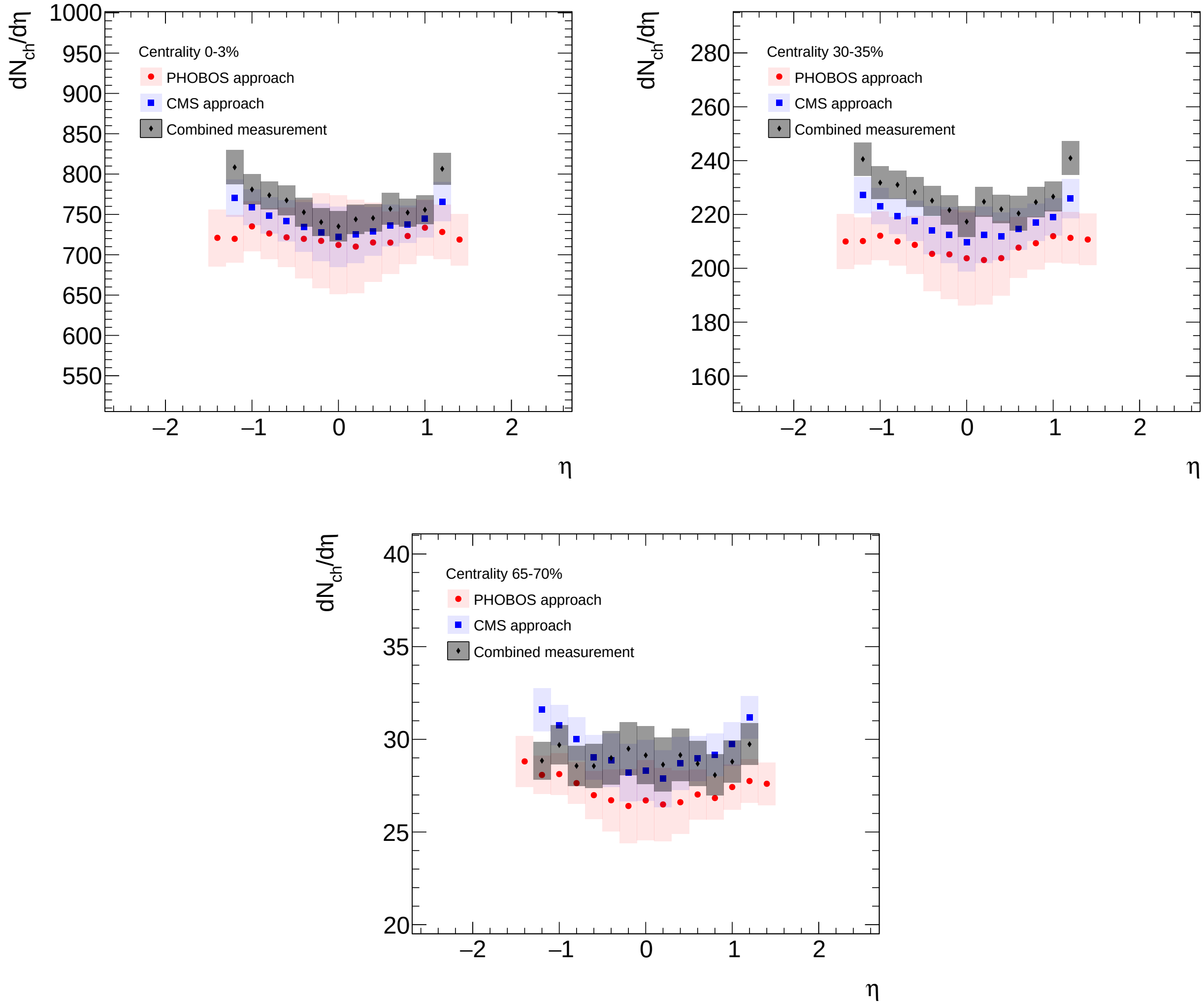

Figure 131: The results from both analysis approaches and the combined measurement with the LS method in three different centrality intervals. (Top left) centrality interval 0–3%, (Top right) centrality interval 30–35%, (Bottom) centrality interval 65–70%

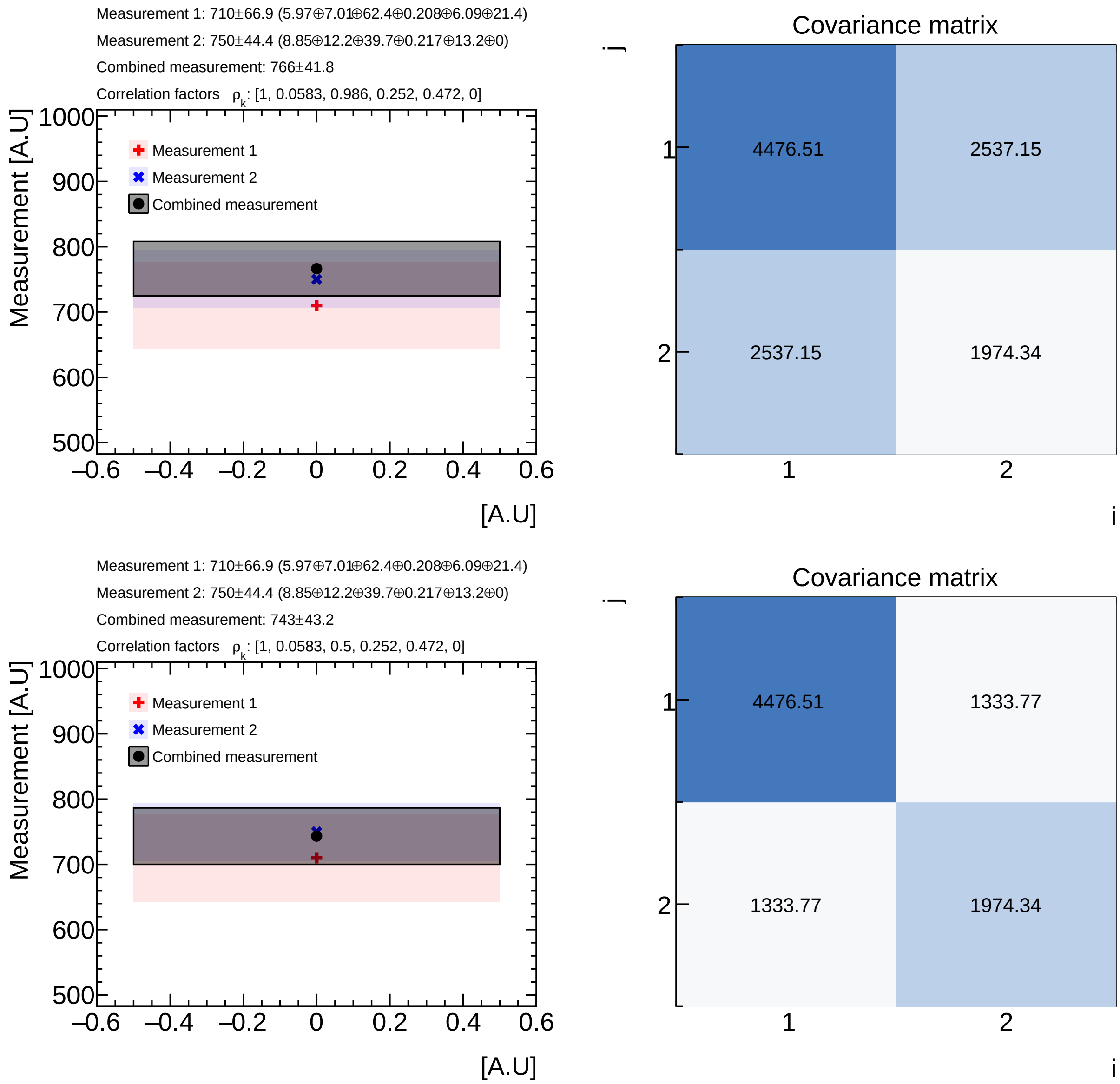

Figure 132: The impact of artificially reducing the correlation of the cluster ADC uncertainty from its original value of 0.986 (top) to 0.5 (bottom).

K.2 The profile likelihood method

Assuming the measurement uncertainties follow Gaussian distribution, the joint probability (likelihood) of obtaining the measurements 1 and 2 given a true value λ is described by a multivariate Gaussian distribution:

$$L(\lambda) = \frac{1}{2\pi\sqrt{\det(V)}} \exp\left[-\frac{1}{2}\,\mathbf{d}^T V^{-1}\mathbf{d}\right],$$

where

$$\mathbf{d} = \begin{pmatrix} y_1 - \lambda \\ \\ y_2 - \lambda \end{pmatrix}$$

is the difference vector between the observed values and the hypothesized true value, and V^{-1} is the inverse of the covariance matrix,

$$\det(V) = V_{11}V_{22} - V_{12}^2,$$

$$V^{-1} = \frac{1}{\det(V)} \begin{pmatrix} V_{22} & -V_{12} \\ \\ -V_{12} & V_{11} \end{pmatrix}.$$

The exponent in Equation K.2 then becomes:

$$-\frac{1}{2}\,\mathbf{d}^T V^{-1}\mathbf{d} = -\frac{1}{2}\left[(y_1-\lambda)^2\,\frac{V_{22}}{\det(V)} - 2(y_1-\lambda)(y_2-\lambda)\,\frac{V_{12}}{\det(V)} + (y_2-\lambda)^2\,\frac{V_{11}}{\det(V)}\right].$$

The best estimate $\hat{\lambda}$ is defined as the value that maximizes $L(\lambda)$, obtained by scanning over the parameter of interest λ and computing the likelihood $L(\lambda)$ given the data and the constructed covariance matrix.

To quantify the uncertainty in $\hat{\lambda}$, one uses the likelihood ratio test statistic

$$\Delta\chi^2(\lambda) \equiv -2\ln\frac{L(\lambda)}{L(\hat{\lambda})}.$$

With Wilks' theorem, $\Delta\chi^2(\lambda)$ approximately follows a χ^2 distribution with one degree of freedom in the limit of a large sample size. This property allows for defining a confidence interval for λ. For example, a threshold of $\Delta\chi^2 = 1.0$ corresponds roughly to a 68.3% confidence interval, $\Delta\chi^2 = 2.71$ corresponds to about 90%, and $\Delta\chi^2 = 3.84$ corresponds to roughly 95% confidence.

Figure 133 presents the results obtained using the profile likelihood method. The combined uncertainty (confidence interval) appears to be overly optimistic, potentially underestimating the true uncertainty rather than providing a more conservative estimate.

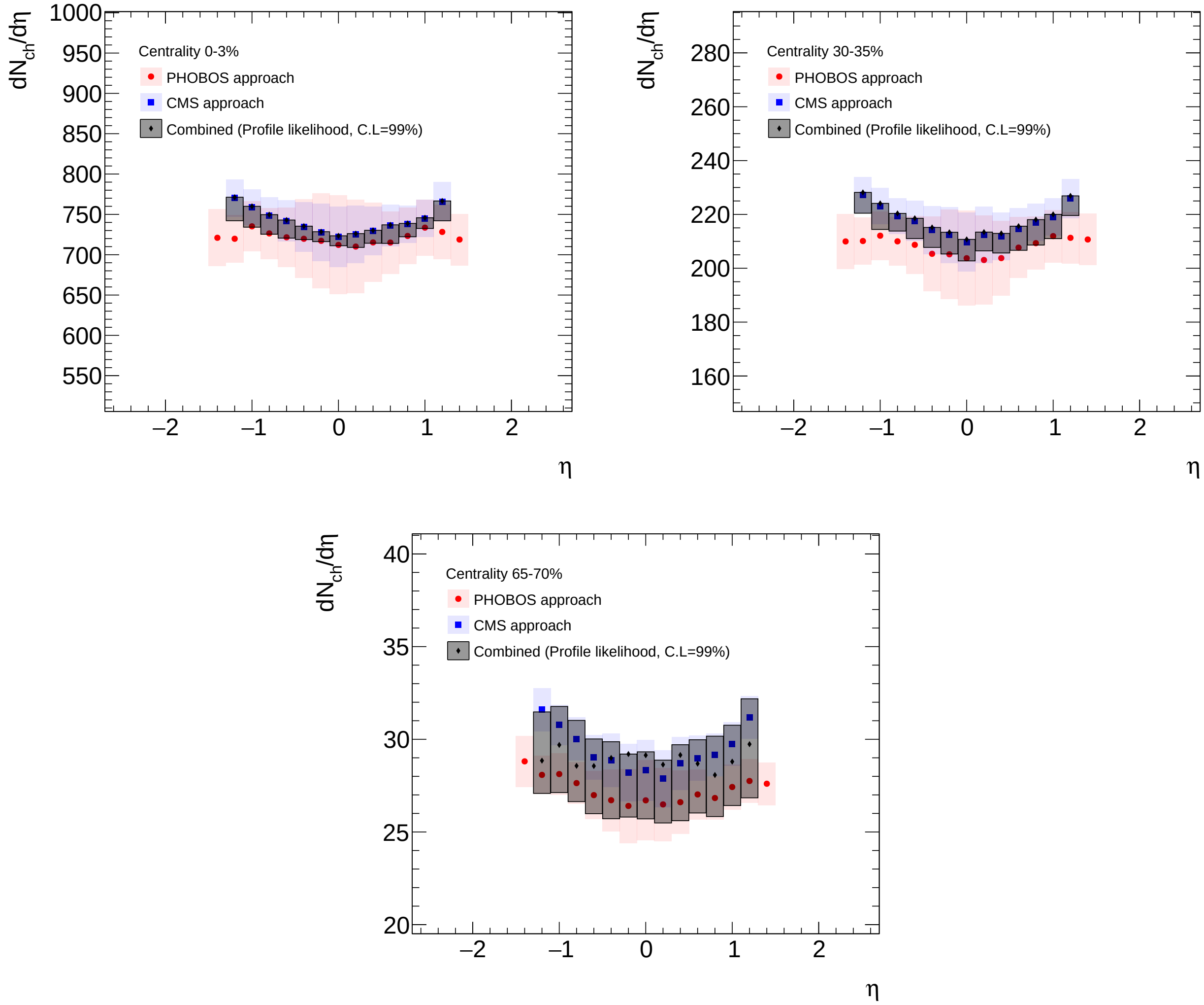

Figure 133: The results from both analysis approaches and the combined measurement with the profile likelihood method in three different centrality intervals. (Top left) centrality interval 0–3%, (Top right) centrality interval 30–35%, (Bottom) centrality interval 65–70%

K.3 The adapted combination procedure from the CMS publication

The results from the two analyses are consistent within uncertainties and are therefore averaged using the arithmetic mean. Uncertainties are categorized into two groups based on the magnitude of the correlation coefficient: those with a correlation coefficient greater than 0.1 are treated as fully correlated, while those with a correlation coefficient less than 0.1 are considered uncorrelated. The correlated and uncorrelated uncertainties of the average result, $\bar{s}$ and $\bar{\sigma}$, are calculated as

$$\bar{s} = \frac{\sqrt{\sum_k \left[(s_{\mathrm{phobos}})_k + (s_{\mathrm{cms}})_k\right]^2}}{2}$$

$$\bar{\sigma} = \frac{\sqrt{\sum_k \left[(\sigma_{\text{phobos}})_k^2 + (\sigma_{\text{cms}})_k^2\right]}}{2}.$$

The total systematic uncertainty is then given by

$$\bar{\sigma}_{\text{total}} = \sqrt{\bar{\sigma}^2 + \bar{s}^2}.$$

This procedure can be heuristically understood as follows. Correlated uncertainties are treated as fully correlated, meaning the off-diagonal elements of the covariance matrix are always the product of the uncertainties from the two approaches. When calculating the total variance, this results in an expression of the form $\sigma_1^2 + 2 \times 1 \times \sigma_1\sigma_2 + \sigma_2^2 = (\sigma_1 + \sigma_2)^2$, giving the square of the sum of the correlated uncertainties. In our case, since the dominant uncertainty accounts for more than 90% of the total uncertainty and is almost fully correlated between the two approaches (the cluster ADC uncertainty has a correlation coefficient of 0.986 between two approaches), computing the correlated uncertainty as the squared sum may not introduce significant issues.

Figure 134 presents the results obtained using the adapted combination procedure from the CMS publication.

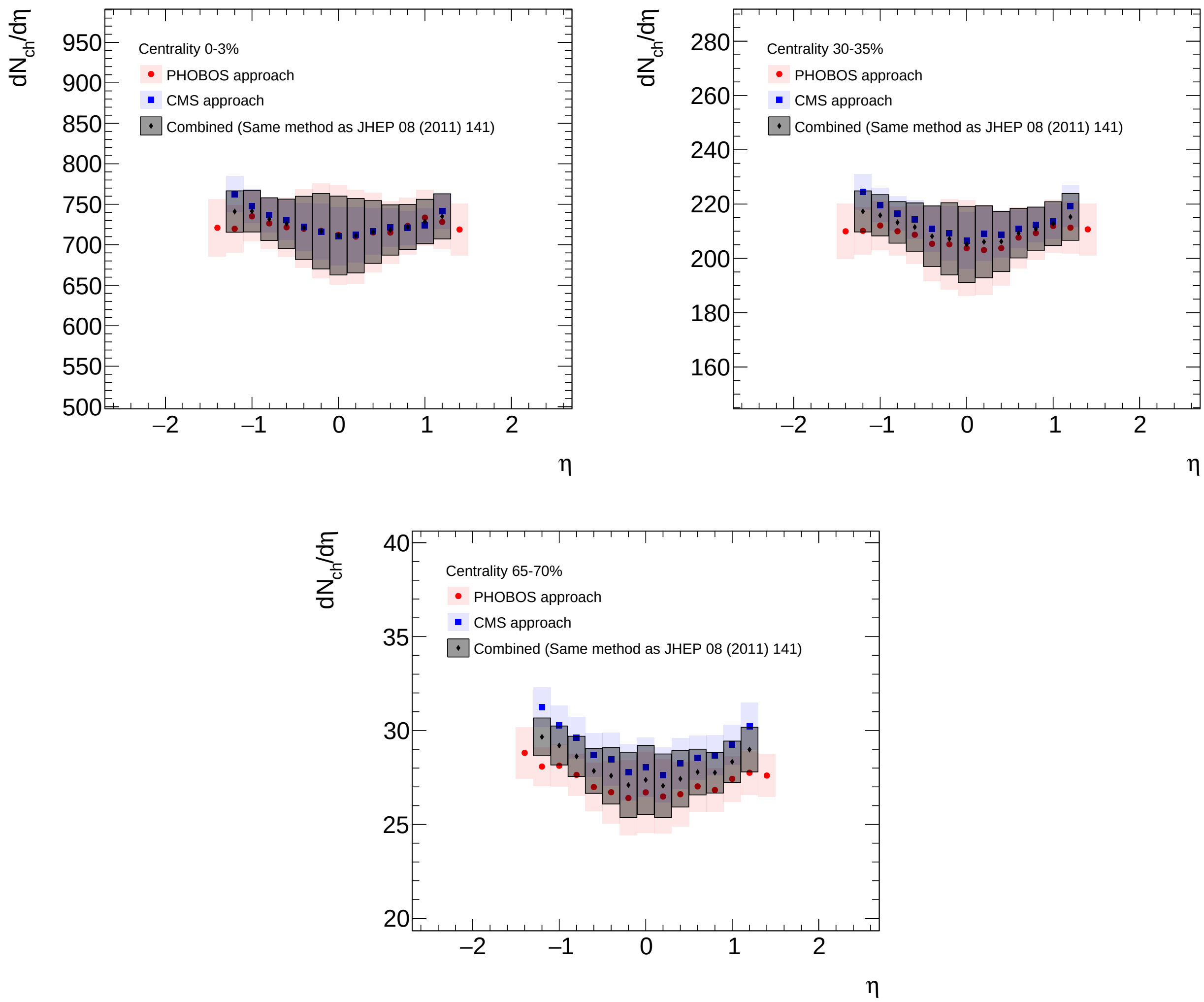

Figure 134: The results from both analysis approaches and the combined measurement with the adapted procedure from the CMS publication [31]. (Top left) centrality interval 0–3%, (Top right) centrality interval 30–35%, (Bottom) centrality interval 65–70%